



A University of Sussex DPhil thesis

Available online via Sussex Research Online:

<http://sro.sussex.ac.uk/>

This thesis is protected by copyright which belongs to the author.

This thesis cannot be reproduced or quoted extensively from without first obtaining permission in writing from the Author

The content must not be changed in any way or sold commercially in any format or medium without the formal permission of the Author

When referring to this work, full bibliographic details including the author, title, awarding institution and date of the thesis must be given

Please visit Sussex Research Online for more information and further details



Investigation of Rim Seal Exchange and Coolant Re-
Ingestion in Rotor Stator Cavities Using Gas
Concentration Techniques

DANIEL EASTWOOD

Submitted for the degree of Doctor of Philosophy, School of Engineering and
Informatics, University of Sussex, June 2014



DECLARATION

I hereby declare that this thesis has not been and will not be, submitted in whole or in part to another University for the award of any other degree.

Daniel Eastwood

June 2014

PREFACE

The work described in this thesis was conducted at the Thermo-Fluid Mechanics Research Centre, University of Sussex as part of the MAGPI "Main Annulus Gas Path Interactions" European Union funded research project. Experimental investigations were carried out at the TSW "Turbine Stator Well" test facility at the University of Sussex. Under the guidance of principle investigator Dr. C. A. Long and previously Professor. P.R.N. Childs, a number of researchers have conducted experiments on the rig in support of MAGPI activities; including Dr. N. R. Atkins, Dr. D. D. Coren, J. R. Turner and the author. In order to support the results and findings of this thesis it is necessary to describe the test facility fully as well as to describe results obtained and published by the research group. Sections of this thesis pertaining to collective work are indicated at the beginning of each relevant Chapter.

UNIVERSITY OF SUSSEXInvestigation of Rim Seal Exchange and Coolant Re-Ingestion in Rotor Stator Cavities Using Gas Concentration Techniques

DANIEL EASTWOOD

Submitted for the degree of Doctor of Philosophy, School of Engineering and Informatics, University of Sussex, June 2014

Summary

Gas turbine engine performance requires effective and reliable internal cooling over the duty cycle of the engine. Understanding the effectiveness of cooling flows when making life predictions for rotating components subject to the main gas path temperatures is crucial. A test facility has been developed at the University of Sussex incorporating a two stage turbine designed to support a European funded research project with the objective of enhancing the understanding of interactions between main annulus gas paths and secondary air systems. This thesis describes the specific contribution of the author to the research conducted at the test facility.

Non-invasive gas seeding and concentration measurement techniques together with hot geometry displacement measurements have been developed to meet three distinct objectives: to determine inter-stage seal flows between rotor disc cavities; to provide data to quantify rim seal exchange flows between rotor stator cavities and the main annulus gas path for both bulk ingestion and egress conditions; and, to provide data to quantify the re-ingestion of cooling air egressed into the main annulus gas path. Detailed knowledge of these flows is vital to understanding the flow structures within rotor stator cavities and to optimise coolant delivery methods.

Experimental results are presented for a number of cooling flow supply geometries and flow rates. The gas concentration measurement techniques developed and the results obtained are compared to traditional measurements as well as numerical simulations carried out by research project partners. This work develops the measurement techniques of rotor stator cavity flows and provides data suitable for the validation of improved thermo-mechanical and CFD codes, beneficial to the engine design process.

ACKNOWLEDGEMENTS

I would like to thank my supervisor Dr C.A. Long and my previous supervisors Prof P.R.N. Childs and Dr N.R. Atkins for their help and support. I would also like to thank Dr D.D Coren for his continued guidance.

Thanks are also given to J.R. Turner, S. Davies (University of Sussex), J. A. Dixon, T.J. Scanlon, and A. Guijarro-Valencia, (RollsRoyce Plc).

The present investigations were supported by the European Commission within the Framework 6 Programme, Research Project ‘Main Annulus Gas Path Interactions (MAGPI)’, Grant No.AST5-CT-2006-030874. This financial support is gratefully acknowledged.

Contents

1	Introduction	1
2	Review of Previous Work	6
2.1	Introduction	6
2.2	The Free Disc	6
2.3	Shrouded Rotor Stator Cavities in a Quiescent Environment	8
2.4	Shrouded Rotor Stator Cavities with an External Flow	12
2.5	Interstage Labyrinth Seals	22
2.6	Concentration Measurement Techniques	30
2.7	Summary	35
3	Test Facility Overview	36
3.1	Introduction	36
3.2	Test Facility External Systems	37
3.3	Test Section Air Supply	38
3.4	Drive Train and Dynamometer	39
3.5	Test Rig Internal Components and Systems	44
3.5.1	Test Section Air Supply Paths	45
3.6	Test Section Features	46
3.7	Coolant Delivery Geometries	49
3.8	Rotor Blades and NGV Geometry	52
3.9	Test Facility Design Point Summary	52
3.10	Temperature Measurements	53
3.11	Test Section Pressures Measurements	60
3.12	Control and Data Acquisition Overview	63
3.13	Labview VI	66
3.14	Summary	71
4	Test Facility Instrumentation	72
4.1	Introduction	72
4.2	Thermocouple Manufacturing Process	72
4.3	Initial Thermocouple Calibration Investigation	74
4.4	Stationary Thermocouple Cold Junction	78
4.5	Cold Junction PRT Calibration	80
4.6	Stationary Thermocouple Calibration	87
4.7	Stationary Thermocouple Installation	91
4.8	Rotating Thermocouple Calibration	95
4.9	Rotating Thermocouple Installation	99
4.10	Temperature Measurement Uncertainty	103
4.11	Pressure Transducer Calibration	105
4.12	Pressure Tap Installation	107
4.13	Pressure Tube Manufacturing Faults	108
4.14	Flow Meters Calibration	109
4.15	Summary	110
5	Rig Operation Procedure	111
5.1	Introduction	111
5.2	Rig Pre-Start Up Procedure	111

5.3	Rig Start Up Procedure.....	116
5.4	Operating conditions.....	121
5.5	Data Settling.....	123
5.6	Changing of Flow Rates.....	125
5.7	Rig Shut Down Procedure.....	126
5.8	Data Processing.....	127
5.9	Summary.....	128
6	Gas Concentration Experiments.....	129
6.1	Introduction.....	129
6.2	Interstage Seal Flow Experiment.....	129
6.3	Rim Seal Exchange Experiment.....	132
6.4	Re-Ingestion Experiment.....	135
6.5	Gas Concentration Instrumentation.....	137
6.6	Carbon Dioxide Supply.....	139
6.7	Carbon Dioxide Flow Meter.....	140
6.8	In-Line Heater.....	141
6.9	Gas Analyser.....	142
6.10	Solenoid Measurement Locations.....	143
6.11	Gas Concentration System Commissioning.....	145
6.12	Uncertainty of Gas Concentration Experiments.....	148
6.13	Gas Concentration Experimental Procedure.....	149
6.13.1	Interstage Seal Flow Experimental Procedure.....	149
6.13.2	Rim Seal Exchange Experimental Procedure.....	151
6.13.3	Re-Ingestion Experimental Procedure.....	151
6.14	Summary.....	153
7	Hot Geometry and Seal Flow Study.....	154
7.1	Introduction.....	154
7.2	Mechanics of Seal Movement.....	154
7.3	Displacement Sensor Selection.....	155
7.4	Calibration and Installation.....	157
7.5	Thermo-Mechanical Modelling of Seal Movement.....	160
7.6	Installation of Radial Sensor.....	165
7.7	Full Structural Model for Seal Movement Calibration.....	166
7.8	Test Matrix Seal Movement Calculations.....	168
7.9	Test Matrix Seal Flow Calculation.....	171
7.10	Summary.....	173
8	Results - Stator Well Temperature.....	174
8.1	Introduction.....	174
8.2	Main Annulus Pressure.....	174
8.3	Cooling Flow Rates.....	176
8.4	Normalised Temperature Methodology.....	178
8.5	Upstream Wheelspace Temperatures.....	179
8.5.1	Normalised Rotating Upstream Stator Well Temperatures.....	183
8.5.2	Normalised Stationary Upstream Stator Well Temperatures.....	187
8.5.3	Comparison of Phase 1 Drive Arm Configurations.....	190
8.5.4	Comparison of Phase 1 Lock Plate Configurations.....	193
8.5.5	Comparison of 39 Drive Arm Holes with Angled Inserts.....	196

VIII

8.5.6	Comparison of Drive Arm and Deflector Plate geometries.....	199
8.6	Summary.....	202
9	Results - Concentration Measurements.....	204
9.1	Introduction.....	204
9.2	Interstage Seal Flow Experimental Results.....	205
9.3	Rim Seal Exchange.....	207
9.3.1	Dilution Ratio Measurements.....	209
9.3.2	Summation Results.....	215
9.4	Re-Ingestion Experimental Results.....	217
9.5	Summary.....	225
10	Conclusions.....	227
10.1	Interstage Seal Flow.....	227
10.2	Rim Seal Exchange Experiment.....	228
10.3	Re-Ingestion Experiment.....	228
10.4	The Use of Concentration Measurements.....	229
10.5	Recommendations for Further Work.....	230
11	References.....	232
	Appendix A	238
	Appendix B	244
	Appendix C.....	249

FIGURES

Figure 1-1 AE3007 axial gas turbine engine with compressor bleed takeoff, Rolls-Royce (2005).....	1
Figure 1-2 AE 3007 turbine cooling circuit, Rolls-Royce (2005).....	2
Figure 1-3 Typical turbine stator well flows, Dixon et al (2012).....	3
Figure 2-1 A rotating disc in an initially stationary fluid, Schlichting (1979).....	7
Figure 2-2 Simple rotor stator cavity.....	10
Figure 2-3 Simple axial and radial seal geometry.....	11
Figure 2-4 Instantaneous velocity vector map in rotor disc cavity, Roy et al (2007)....	15
Figure 2-5 Sealing effectiveness, ingress and egress with imposed sealing flow, Owen (2009a).....	16
Figure 2-6 Variation of sealing effectiveness with imposed sealing flow, Owen (2009b).....	17
Figure 2-7 Contours of static pressure at 5% annulus height, Zhou et al (2011b).....	19
Figure 2-8 Comparison of sealing effectiveness for externally and rotationally induced ingestion, Sangan et al (2011b).....	20
Figure 2-9 Re-ingestion between two turbine stages, Guijarro Valencia et al (2012)...	21
Figure 2-10 Interstage labyrinth seal application in a three-shaft turbine, Rolls-Royce (2005).....	22
Figure 2-11 Basic straight through labyrinth seal geometry.....	24
Figure 2-12 Discharge coefficients for seals with greater than 2 fins, Zimmerman and Wolff (1998).....	25
Figure 2-13 Discharge coefficients for 1 and 6 fin straight through seals, Wittig et al (1987).....	25
Figure 2-14 Discharge coefficient with pressure ratio and clearance, Kim (2009).....	27
Figure 2-15 Discharge coefficient with fin number and tip clearance, PR = 1.5 bar, Kim (2009).....	27
Figure 2-16 Rotational effects on the discharge coefficients as a function of Re, Waschka (1992).....	29
Figure 2-17 Rotational effects on the discharge coefficients as a function of the ratio Ta/Re , Waschka (1992).....	29
Figure 2-18 Sealing effectiveness with radial location r/b	33
Figure 2-19 Concentration measurement locations of four experimental test facilities	34
Figure 3-1 Test facility major component overview.....	38
Figure 3-2 Heenan and Froude DPY590 dynamometer cross section.....	40
Figure 3-3 Dynamometer water circuit.....	40
Figure 3-4 Gnome reduction gearbox internals, Stefanis (2007).....	42
Figure 3-5 Gnome gearbox external oil circuit (Courtesy of Rolls-Royce plc).....	43
Figure 3-6 TSW facility test cell arrangement.....	43
Figure 3-7 Cross section of TSW test facility.....	44
Figure 3-8 TSW facility test section air supply paths.....	45
Figure 3-9 Test section main features.....	47
Figure 3-10 Major test section dimensions in terms of main annulus outer radius h , Eastwood (2012).....	48
Figure 3-11 Stator well dimensions in terms of the rotor stator spacing s , Eastwood (2012).....	48
Figure 3-12 Drive arm coolant supply path.....	50

Figure 3-13	Lock plate slot delivery path.....	51
Figure 3-14	Deflector plate geometry.....	52
Figure 3-15	Stator 1 temperature measurements.....	54
Figure 3-16	Stator 2 temperature measurements.....	55
Figure 3-17	Rotor 1 temperature measurements.....	56
Figure 3-18	Rotor 2 temperature measurements.....	58
Figure 3-19	Main annulus temperature measurements.....	59
Figure 3-20	Stator 1 pressure measurements.....	60
Figure 3-21	Stator 2 pressure measurements.....	61
Figure 3-22	Main annulus pressure measurements.....	62
Figure 3-23	Data acquisition system, Coren et al (2010).....	64
Figure 3-24	Temperature controlled instrumentation cabinets.....	65
Figure 3-25	Temperature controlled instrumentation enclosure.....	65
Figure 3-26	Test Rig Operator Terminal.....	66
Figure 3-27	Labview VI rig operator system.....	67
Figure 4-1	Thermocouple bead types.....	73
Figure 4-2	Traditional thermocouple calibration technique.....	75
Figure 4-3	Initial thermocouple calibration.....	76
Figure 4-4	Initial thermocouple batch calibration.....	77
Figure 4-5	Standard NI card cold junction measurement.....	78
Figure 4-6	NI-SCXI-1303 machined ready for new spreader plate.....	79
Figure 4-7	Copper spreader plate prior to installation.....	79
Figure 4-8	Open NI SCXI-1303 with spreader plate and PRTs attached.....	80
Figure 4-9	Stationary thermocouple cold junction PRT calibration.....	81
Figure 4-10	Cold junction PRT calibration, Turner et al (2008).....	82
Figure 4-11	SXCI-1303 card connected to SXCI-1000 chassis.....	82
Figure 4-12	Infrared image of NI-SCXI-1303 card.....	83
Figure 4-13	SXCI-1303 card casing attached to modified NI lead.....	85
Figure 4-14	Modified SCXI 1303 with top casing removed.....	85
Figure 4-15	SCXI-1303 card in isothermal box.....	86
Figure 4-16	SCXI-1303 cold junction temperature variation.....	87
Figure 4-17	Stationary thermocouple calibration instrumentation path.....	88
Figure 4-18	Isotech bath layout.....	89
Figure 4-19	Isotech liquid bath temperature set points, Turner et al (2008).....	90
Figure 4-20	Stationary thermocouple voltage output, Turner et al (2008).....	90
Figure 4-21	Deviation of post processed thermocouple temperature data from reference temperature, Turner et al (2008).....	91
Figure 4-22	Stator 1 thermocouple installation.....	92
Figure 4-23	NGV 1 air thermocouples.....	93
Figure 4-24	NGV 2 air thermocouple installation.....	93
Figure 4-25	Female vane mould and clamp system.....	94
Figure 4-26	Re-profiled NGV 1 vane.....	94
Figure 4-27	NGV2 in stator 2 assembly.....	95
Figure 4-28	PRT installed in telemetry unit cap.....	96
Figure 4-29	Rotating PRT calibration points, Turner et al (2008).....	96
Figure 4-30	Rotating frame PRTs deviation from reference PRT, Turner et al (2008).....	97
Figure 4-31	Rotating thermocouple calibration instrumentation path.....	98

Figure 4-32	Deviation of post processed thermocouple temperature data from reference temperature, Turner et al (2008).....	98
Figure 4-33	Rotating thermocouple embedding.....	99
Figure 4-34	Rotating thermocouple rig routing.....	100
Figure 4-35	Upstream internal face, rotor 1 thermocouple routing.....	101
Figure 4-36	Rear face tracks, rotor 1.....	101
Figure 4-37	Assembled rotating section.....	102
Figure 4-38	Telemetry unit to rotating thermocouple installation.....	103
Figure 4-39	Angle sensitivity test, Turner et al (2008).....	105
Figure 4-40	Angle sensitivity study results, Turner et al (2008).....	106
Figure 4-41	NGV 1 total pressure taps.....	107
Figure 4-42	Pressure tap lead out.....	108
Figure 4-43	Manufacturing defect in pressure lead out tubing.....	108
Figure 4-44	Hot Film Flow Meter installed in cooling air line.....	110
Figure 5-1	Telemetry cooling supply path.....	113
Figure 5-2	Rig speed steps during standard start up process.....	117
Figure 5-3	Rotating section bearing operating temperature history.....	117
Figure 5-4	Bearing life prediction for three bearing arrangements, Coren et el (2012)	119
Figure 5-5	Main annulus static pressure.....	120
Figure 5-6	Upstream wheel-space stationary metal temperatures.....	120
Figure 5-7	Test section air mass flows.....	122
Figure 5-8	Upstream wheel-space static pressure.....	122
Figure 5-9	Stationary stator well temperatures at a near settled condition.....	124
Figure 5-10	Rotating stator well temperatures at near settled condition.....	124
Figure 5-11	Test section air mass flows.....	125
Figure 5-12	Upstream wheel-space stationary metal temperatures.....	126
Figure 5-13	Test data storage structure.....	128
Figure 6-1	Interstage seal experimental flows.....	131
Figure 6-2	Simple seal flow case.....	131
Figure 6-3	Rim seal experimental flows.....	132
Figure 6-4	Comparison of summation and concentration approach.....	134
Figure 6-5	Re-ingestion experimental flows.....	136
Figure 6-6	Gas concentration supply and measurement system.....	138
Figure 6-7	Carbon dioxide supply.....	139
Figure 6-8	Carbon dioxide mass flow meter.....	140
Figure 6-9	Seeding gas temperature variation.....	141
Figure 6-10	Basic NDIR sensor fundamental operation.....	142
Figure 6-11	TSW gas analyser unit.....	143
Figure 6-12	Gas concentration seeding and measurement radial and axial locations..	144
Figure 6-13	Gas concentration seeding and measurement circumferential locations.	144
Figure 6-14	Pipe test gas seeding experiment.....	145
Figure 6-15	Pipe test gas seeding experiment results.....	146
Figure 6-16	Seeded coolant rig flood test.....	147
Figure 7-1	Interstage seal area.....	154
Figure 7-2	Cross section of test rig sensor locations.....	155
Figure 7-3	Thermal calibration drift check.....	158

Figure 7-4	U6 axial sensor calibration process.....	158
Figure 7-5	U6 axial sensor calibration results.....	159
Figure 7-6	SO5 radial sensor and target.....	159
Figure 7-7	SO5 radial sensor calibration results.....	160
Figure 7-8	Basic geometry model of test section.....	161
Figure 7-9	Contours of temperature on displaced model.....	162
Figure 7-10	Component displacement and seal movement at 9589 rpm.....	163
Figure 7-11	Component displacement and seal movement at 10630 rpm.....	164
Figure 7-12	Radial sensor installed in stator foot.....	165
Figure 7-13	Full radial displacement calibration model.....	166
Figure 7-14	Comparison of predicted thermo-mechanical model and measured interstage seal radial clearance change.....	167
Figure 7-15	Deformed seal shape.....	168
Figure 7-16	Displacement results for 39 lock plate slot geometry with a cooling flow rate of 55 gs^{-1}	169
Figure 7-17	Radial seal displacement measurement for 26 drive arm holes with deflector plate installed.....	170
Figure 7-18	Seal flow parameter measurement locations.....	172
Figure 7-19	Comparison of CFD and calculated seal flows using a $CD = 0.48$, Eastwood et al (2012).....	173
Figure 8-1	Test section inlet total pressure measurement locations.....	175
Figure 8-2	Total pressure asymmetry at test section inlet.....	175
Figure 8-3	Normalised temperature reference model points.....	179
Figure 8-4	Upstream wheel-space normalised model point locations.....	180
Figure 8-5	Normalised temperatures for 26 straight drive arm inserts and deflector plate.....	180
Figure 8-6	Normalised Temperature on front face of Rotor 1 for 26 drive arm inserts and deflector plate.....	182
Figure 8-7	Rotor 1 rear face normalised temperature locations.....	183
Figure 8-8	Rotor 1 rear face normalised metal temperature for all tested geometries and cooling flow rates.....	186
Figure 8-9	Normalised temperature locations on front face of Stator 2.....	187
Figure 8-10	Stator 2 front face normalised metal temperature for all tested geometries and cooling flow rates.....	189
Figure 8-11	Rotor 1 rear face normalised metal temperature for all Phase 1 straight drive arm geometries and cooling flows.....	191
Figure 8-12	Adiabatic flow visualisation of coolant delivery through 39 and 13 drive arm holes at $0.63 \text{ Cw}_{\text{ent}}$ (Coren et al 2011).....	192
Figure 8-13	Stator 2 front face normalised metal temperature for all Phase 1 straight drive arm geometries and cooling flows.....	193
Figure 8-14	Rotor 1 rear face normalised metal temperature for all Phase 1 lock plate geometries and cooling flows.....	195
Figure 8-15	Stator 2 front face normalised metal temperature for all Phase 1 lock plate geometries and cooling flows.....	196
Figure 8-16	Rotor 1 rear face normalised metal temperature for all angled 39 drive arm insert geometries and cooling flows.....	197
Figure 8-17	Stator 2 front face normalised metal temperature for all angled 39 drive arm insert geometries and cooling flows.....	198

Figure 8-18 RotPathlines of cooling effectiveness, Axial insert geometry, 30 gs ⁻¹ , Dixon et al (2012).....	199
Figure 8-19 Rotor 1 rear face normalised metal temperature for 39 and 26 drive arm insert geometries, with and without deflector.....	200
Figure 8-20 Stator 2 front face normalised metal temperature for 39 and 26 drive arm insert geometries, with and without deflector.....	201
Figure 9-1 Labyrinth seal flow experimental measurement points.....	206
Figure 9-2 Concentration measurements made for 39 DAH, 26 DAH and 13 DAH, for 40 gs-l cooling flow at interstage seal exit and downstream cavity.....	206
Figure 9-3 Carbon dioxide concentration plume.....	207
Figure 9-4 Rim seal exchange flows, Eastwood (2012).....	208
Figure 9-5 Dilution Ratio η for 39 and 26 Drive Arm Hole Geometries, & for 39 and 26 Simulated Lock Plate Slot Geometries.....	210
Figure 9-6 Cavity streamlines for 39 drive arm configuration coloured by normalised absolute frame total temperature, Coren et al (2011).....	211
Figure 9-7 Dilution ratio for axially angled drive arm and Deflector Plate Geometries.....	213
Figure 9-8 Path lines of cooling effectiveness, Deflector plate geometry, 30 gs ⁻¹ , Dixon et al (2012).....	215
Figure 9-9 Indicated upstream stator well rim seal ingestion m_i and egress rate m_e ...	217
Figure 9-10 Re-ingestion experimental flows.....	218
Figure 9-11 Re-ingestion rates calculated from concentration measurements made in the upstream and downstream stator wells.....	219
Figure 9-12 Re-ingestion as a fraction of interstage seal flow	220
Figure 9-13 Re-ingestion as a fraction of wheelspace supply rate.....	221
Figure 9-14 Streamlines of wheelspace egress, Eastwood et al (2012).....	222
Figure 9-15 Streamlines of seeded coolant, Guijarro Valencia et al (2012).....	224
Figure 9-16 Upstream stator well ingress streamlines for steady and unsteady solutions, Guijarro Valencia et al (2012).....	225

TABLES

Table 3-1: Drive arm coolant delivery geometries	50
Table 3-2: Lock plate slot geometries.....	51
Table 3-3: Blade and NGV geometry, Stefanis (2007).....	52
Table 3-4: Facility Design Point Conditions Summary	53
Table 3-5: Stator 1 temperature measurement locations.....	54
Table 3-6: Stator 2 temperature measurement locations.....	55
Table 3-7: Rotor 1 temperature measurement locations	57
Table 3-8: Rotor 2 temperature measurement locations	58
Table 3-9: Main annulus temperature measurement locations	59
Table 3-10: Stator 1 pressure measurement locations	60
Table 3-11: Stator 2 pressure measurement locations	61
Table 3-12: Main annulus pressure measurement locations	62
Table 3-13: Critical rig parameters.....	67
Table 4-1: Sources of Temperature Measurement Uncertainty	103
Table 4-2: Main annulus supply venturi parameters.....	109
Table 6-1: Contributions to gas concentration measurement uncertainties	148
Table 7-1: Material properties for SC03 model, Touloukian (1975).....	161
Table 7-2: Change in interstage seal radial clearance [mm] (* calculated from SC03 model).....	171
Table 7-3: Interstage seal flow rates for all cooling flow supply geometries	172
Table 8-1: Phase 1 augmented cooling flow rates.....	177
Table 8-2: Phase 2 measured cooling flow rates	177
Table 8-3: Rotor 1 rear face measurement locations	183
Table 8-4: Stator 2 upstream face measurement location.....	187
Table 9-1: Work package partner CFD solution details, Guijarro Valencia et al (2012).....	223

NOMENCLATURE

a	disc inner radius
A_{SEAL}	circumferential seal area
b	disc outer radius
c	concentration
c_o	concentration of cooling air
c_a	concentration of ambient air
c_m	measured concentration
c_s	concentration of seeded cooling air
C_D	seal discharge coefficient
$C_{d,i}$	ingress discharge coefficient
$C_{e,i}$	egress discharge coefficient
g	acceleration due to gravity
Gc	gap ratio
h	main annulus outer radius
\dot{m}	mass flow rate
\dot{m}_{IDEAL}	ideal mass flow rate
\dot{m}_l	labyrinth seal mass flow
\dot{m}_g	mass flow of seeding gas
\dot{m}_0	mass flow of cooling/sealing air
\dot{m}_s	mass flow of seeded cooling/sealing air
\dot{m}_w	mass flow of seeded cooling air to wheelspace
\dot{m}_c	mass flow into stator well cavity
\dot{m}_i	mass flow ingress

\dot{m}_e	mass flow egress
M	windage torque
P	static pressure
P_0	total pressure
r	local radius
r_l	labyrinth seal radius
R	gas constant
s	axial rotor-stator spacing
s_c	seal clearance
T	static temperature
T_o	total temperature
T_M	measured temperature
T_H	hot reference temperature
T_C	cold reference temperature
t	interstage seal fin tip to tip distance
U_ϕ	uncertainty in normalised temperature
U_{T_M}	uncertainty in metal temperature
U_{T_C}	uncertainty in coolant temperature
U_{T_H}	uncertainty in hot gas temperature
u	velocity
V_ϕ	tangential core velocity
w	labyrinth seal fin tip width
y	labyrinth seal fin height
z	labyrinth seal fin tip clearance

Greek Symbols

α	thermal expansion coefficient
ε	sealing effectiveness
ε_c	sealing efficiency, derived from concentration
μ	dynamic viscosity
ν	kinematic viscosity
ν_φ	tangential velocity component
ρ	density
γ	ratio of specific heats
ω	angular velocity
λ_T	turbulent flow parameter
Φ_0	non-dimensional sealing parameter
ϕ	normalised temperature
η	dilution ratio

Dimensionless

β	swirl ratio
β^*	swirl ratio (β when $C_w = 0$)
C_m	momentum coefficient
$C_{m,f}$	momentum coefficient of a free disc
C_w	non-dimensional throughflow
$C_{w,0}$	nondimensional supplied cooling/sealing flow
$C_{w,f}$	nondimensional entrainment of a free disc
$C_{w,ent}$	nondimensional entrainment of a partial disc
$C_{w,min}$	minimum nondimensional flow to seal cavity

$C_{w,i}$	nondimensional ingress flow
$C_{w,e}$	nondimensional egress flow
G_c	gap ratio
Re_ϕ	rotational Reynolds number
Re_w	axial flow Reynolds number
T_a	Taylor number

Subscripts

0	sealing/cooling flow value
1	upstream statorwell
2	downstream statorwell
e	egress flow value
ent	entrainment of a partial disc
i	ingress flow value
min	minimum sealing requirement
r	radial
z	axial

Abbreviations

AXL	axial
CFD	computational fluid dynamics
CIR	circumferential
CMM	coordinate measuring machine
DEF	deflector plate
DR	dilution ration

<i>DVM</i>	digital volt meter
<i>GC</i>	gas concentration
<i>NDIR</i>	non-dispersive infrared sensor
<i>NGV</i>	nozzle guide vane
<i>PIV</i>	particle imaging velocimetry
<i>PRT</i>	Platinum resistance thermometer
<i>STR</i>	straight
<i>TFMRC</i>	Thermo-fluid Mechanics Research Centre
<i>TSW</i>	turbine stator well

1 Introduction

Since their inception the efficiency of gas turbines has improved dramatically, however, the pressure to optimise these engines further through development and research is likely only to increase. This push for improvement, as with most technologies, is partly due to commercial and competition considerations. The main factor driving this need for improvement however, is the increasing cost of non-renewable resources and the resulting operational costs over the life of an engine. Improvements are also driven by the need to reduce emissions to meet legislation targets.

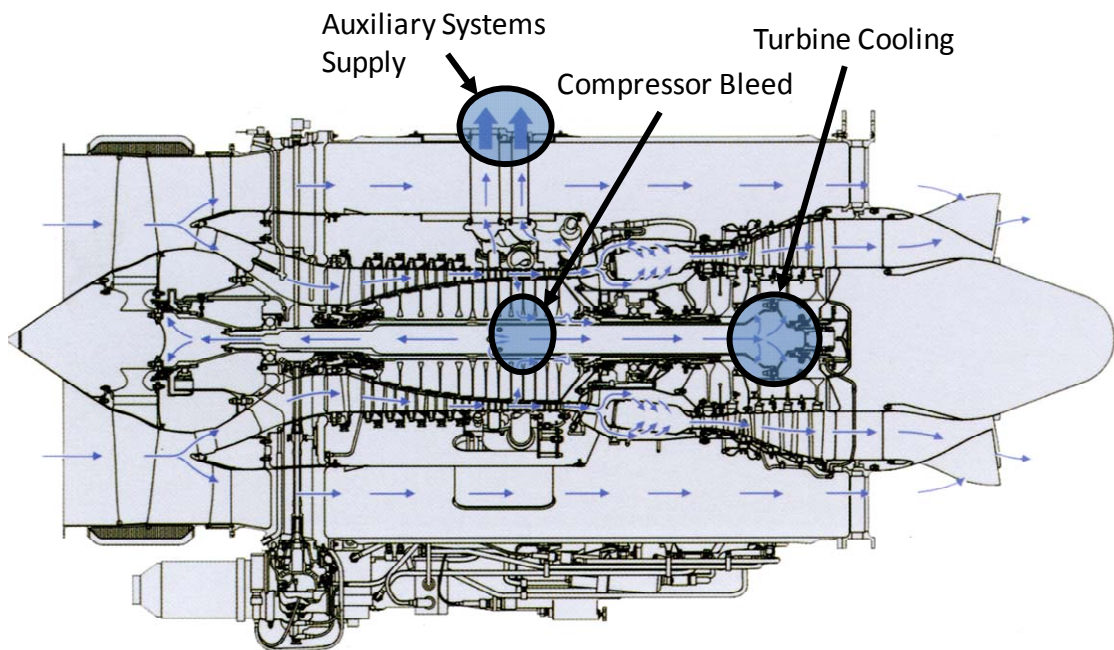


Figure 1-1: AE3007 axial gas turbine engine with compressor bleed takeoff, Rolls-Royce (2005)

Figure 1-1 shows a cut away view of an axial gas turbine engine. The figure shows air being taken from a high pressure compressor stage and then passed along the central shaft for use in the engines secondary air system. Secondary air systems are required for a number of operations within gas turbines, including provision of sealing and

cooling air to the turbine, shown towards the rear of the central shaft, as well as powering auxiliary aircraft systems.

Figure 1-2 shows a cross section of a two stage turbine where air from a compressor bleed provides internal cooling of turbine components. The turbine stator well (also referred to as rotor disc cavity) is cooled by the compressor bleed air by both sealing the rotor disc cavity from hot main annulus gas ingestion and also by removing heat from component surfaces by heat transfer. Within this thesis both 'cooling flow' and 'sealing flow' are used interchangeably to describe this flow.

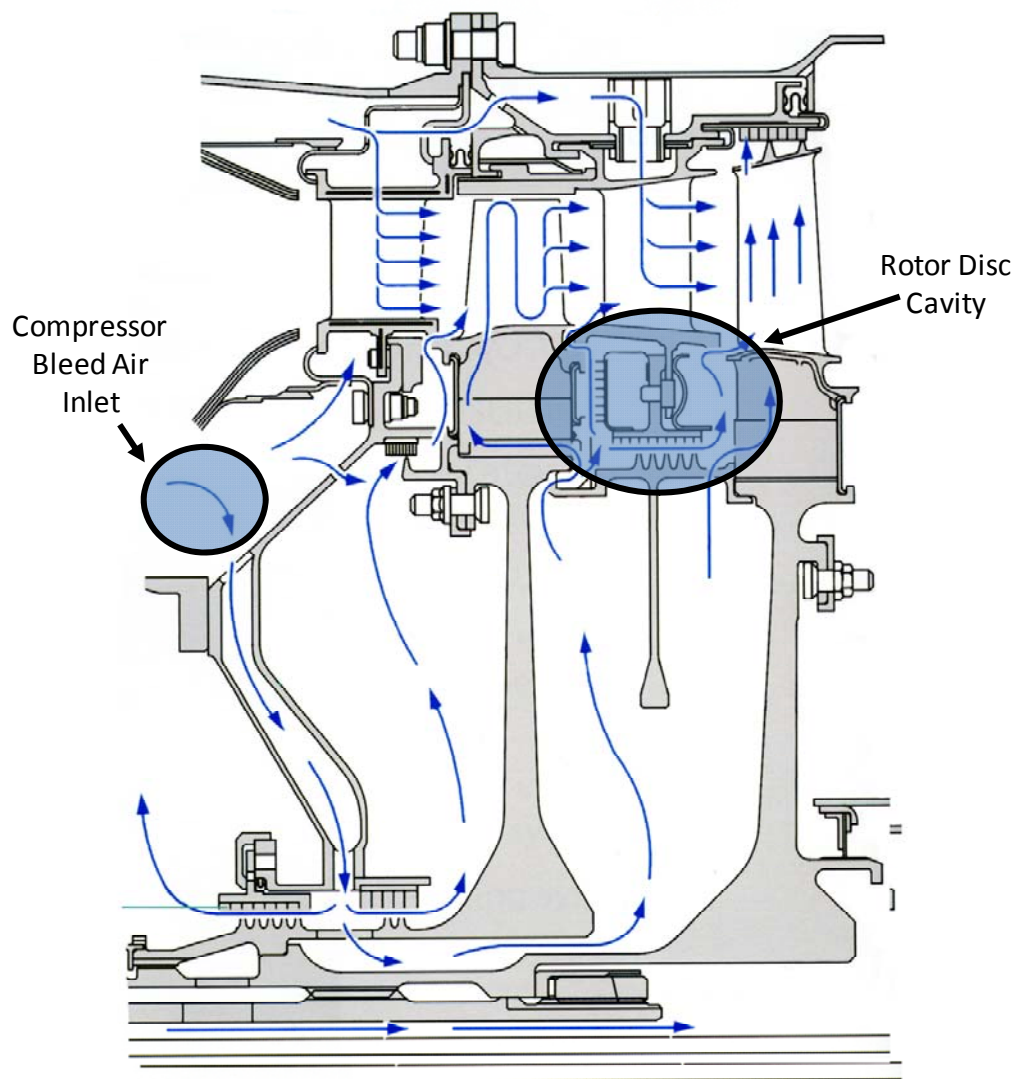


Figure 1-2: AE 3007 turbine cooling circuit, Rolls-Royce (2005)

The internal cooling and the prevention of hot main annulus ingestion is necessary to prevent overheating of turbine discs, which can lead to reduced component life and component failure. The use of compressor bleed air to perform this function however, has a detrimental effect on the cycle performance of the engine therefore reduction of the cooling flow requirement is of great interest to gas turbine manufacturers. In order to optimise the cooling flow detailed knowledge of the flow structures within turbine stator wells and the interaction with main annulus gas path flows is required.

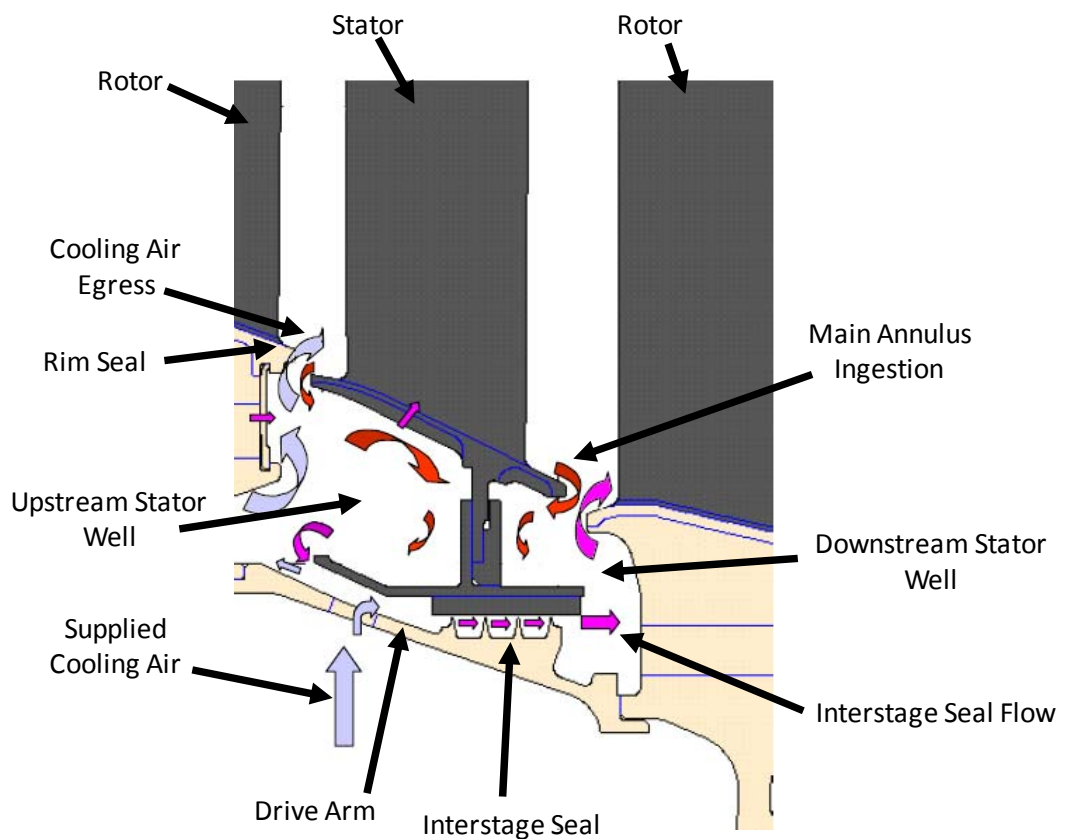


Figure 1-3: Typical turbine stator well flows, Dixon et al (2012)

Figure 1-3 shows the flows associated with a typical turbine stator well. The supplied cooling air can be seen entering the stator well radially through a component joining the two rotors, referred to as the drive arm. A proportion of the cooling air flow enters the upstream stator well where it mixes with ingested main annulus gas. Some of the cooling air may pass through the rim seal into the main annulus. The process through

which the cooling air is egressed and the main annulus air ingressed through the seal is referred to as rim seal exchange. This can be driven by rotationally driven flow structures within the stator well or by asymmetric pressure profiles in the main annulus. The mixture of ingested main annulus gas and cavity cooling air is then seen to pass through the interstage seal into the downstream stator well. The pressure drop and flow rate through the interstage seal affect the flow structure in the upstream stator well. Under certain conditions it is possible for cooling air egressed into the main annulus from the upstream stator well to contribute to the flow ingested into the downstream stator well. This is referred to as re-ingestion.

This thesis describes the contribution of the author to research conducted on a two stage axial turbine test facility, designed for further understanding of the interaction of turbine stator well flows with the main annulus gas path. Both rim seal exchange and coolant re-ingestion are known to contribute to the flows within turbine stator wells however, these flows are difficult to capture with traditional measurement methods. The flows are also often complex and unsteady making modelling of the effects challenging. The authors research aims to describe the use of three distinct concentration measurement experiments where flows are seeded with a tracer gas, together with displacement measurements, to meet the following experimental objectives:

- Investigate to what extent gas concentration measurements can be used to describe and quantify these flows
- To provide experimental data for the calibration and development of modelling techniques

- Provide hot running clearances of test facility internal seals
- Provide data to quantify interstage seal flows for a range of rig operating conditions and coolant supply geometries
- Provide data to determine rim seal exchange flows for both bulk ingress and egress conditions for a range of rig operating conditions and coolant supply geometries
- Provide data to quantify the extent to which egressed cooling air is re-ingested into downstream cavities

Literature describing the mechanisms through which ingestion and egress take place in stator well cavities and the associated flow structures are reviewed in Chapter 2. The use of concentration measurements in experimental facilities is also discussed. The TSW "Turbine Stator Well" experimental facility located at the Thermo-fluids Research Centre at the University of Sussex on which the experimental investigations were conducted as well as the calibration and installation of instrumentation is described in Chapter 3 and Chapter 4. The test facility operation and data acquisition system are described in Chapter 5. The gas concentration experimental methodology, instrumentation calibration and measurement uncertainty are described in Chapter 6. The measurement and thermo-mechanical modelling of the test facility hot geometry is describe in Chapter 7. Temperature measurements and results obtained from the gas concentration experiments are described in Chapter 8 and Chapter 9 where results are presented for a number of cooling flow delivery geometries. The extent to which the research aims were met is described in Chapter 10, including recommendations for future work.

2 Review of Previous Work

2.1 Introduction

This chapter reviews previous studies of the flow behaviour in rotor-stator cavities, the interaction with main annulus flows and also the use of instrumentation and measurement techniques in similar experimental facilities.

The review is primarily concerned with the mechanisms of ingestion through which main annulus gas can enter rotor-stator cavities. The primary flows are discussed, including the basic 'free disc' and shrouded 'rotor-stator' geometries. The effects of rim seal ingress and egress, main annulus conditions and inter-stage labyrinth seal demand are also discussed. The use of tracer gas as a non invasive sealing effectiveness measurement technique is also reviewed.

2.2 The Free Disc

The Free Disc model refers to a disc of radius b rotating at ω (rad/s) in a fluid of density ρ and dynamic viscosity μ , described by Dorfman (1963). Figure 2-1 shows the flows associated with a free disc, the most noteworthy being the "pumped" radial outflow and the corresponding balancing axial inflow. Assuming a no-slip condition at the disc surface the shear between the disc and fluid causes radial outflow in the boundary layer of velocity u_r . By consideration of conservation mass, a flow in the axial direction of velocity u_z must be entrained onto the disc in order to supply the radial outflow.

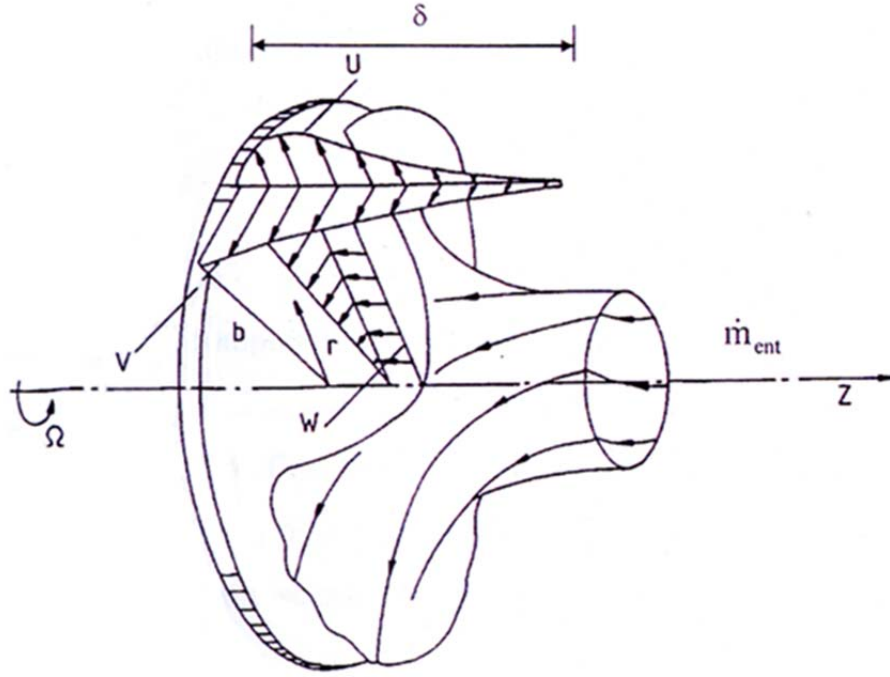


Figure 2-1: A rotating disc in an initially stationary fluid, Schlichting (1979)

The value of the rotational Reynolds number, given in equation 2-1 is used as the criterion for transition from laminar to turbulent flow. For flow over a free disc this is considered turbulent for $Re_\phi > 3 \times 10^5$.

$$Re_\phi = \frac{\rho \omega b^2}{\mu} \quad \text{Equation 2-1}$$

The entrained (or any other supplied) mass flow can be expressed in dimensionless form as:

$$C_w = \frac{\dot{m}}{\mu b} \quad \text{Equation 2-2}$$

The non-dimensional moment coefficient C_m can be expressed as:

$$C_m = \frac{M}{\frac{1}{2} \rho \omega^2 b^5} \quad \text{Equation 2-3}$$

Von Karman (1921) solved Navier-Stokes equations for the free disc. Boundary conditions were applied and a one-seventh power law for the velocity profile to

produce four ordinary differential equations for an axisymmetric incompressible flow, producing the solutions for the free disc entrainment rate and momentum coefficient.

$$C_{w,f} = 0.219 Re_\phi^{0.8} \quad \text{Equation 2-4}$$

$$C_{m,f} = 0.146 Re_\phi^{-0.2} \quad \text{Equation 2-5}$$

Chew (1998) provided a relationship which allows the flow entrained by a partial disc with an inner radius a and outer radius b , could be related to the entrainment of a free disc.

$$C_{w,ent} = C_{w,0} \left[1 - \left(\frac{a}{b} \right)^5 \right] \quad \text{Equation 2-6}$$

2.3 Shrouded Rotor Stator Cavities in a Quiescent Environment

Rotor stator cavities exist where a rotating disc is faced by a stationary disc, offset along the axis of rotation. The behaviour of rotor stator cavities are analogous to rotor disc cavities and are useful when describing the flows in cooled turbine disc cavities. Figure 2-2 shows the basic configuration of a shrouded rotor stator system, where the rotor has an angular velocity ω . A rotor stator cavity is said to be in a quiescent environment where there is no external flow above the shroud or seal. The basic geometry of the rotor stator is defined by the cavity outer radius b , the rotor stator axial gap s , and the seal clearance s_c . Sealing flow is supplied to the rotor stator cavity at a non-dimensional rate $C_{w,0}$. The flow is entrained into the rotor boundary layer where it is pumped radially outward. Some of the sealing air then passes through the seal clearance to the external environment. For cases where the sealing flow $C_{w,0}$ is less than the minimum sealing flow requirement to seal the rotor stator cavity $C_{w,min}$, the

resultant pressure in the cavity due to the rotational effects can cause external air to be ingested into the cavity. This is referred to as rotationally induced ingress. The ingested air travels down the face of the stator and from mass conservation this air can pass across the rotor stator gap into the rotor boundary layer. In rotor stator configurations where $s/b > 0.1$ this results in a 2D core region with distinct and separate rotor and stator boundary layers. Daily and Nece (1960) calculated the swirl ratio β of the core to be in the region of 0.4 relative to the rotor where:

$$\beta = \frac{V\phi}{\omega r} \quad \text{Equation 2-7}$$

Daily et al (1964) gave a correlation for the core velocity of a shrouded rotor stator cavity with a superimposed flow, where $\beta^* = \beta$ when the flow $C_{w,0} = 0$.

$$\frac{\beta}{\beta^*} = \left(1 + 12.74 \frac{\lambda_T}{(r/b)^{\frac{13}{5}}} \right)^{-1} \quad \text{Equation 2-8}$$

The turbulent flow parameter λ_T describes the effect of the superimposed flow $C_{w,0}$ on the core, where the flow structure is rotationally dominated for low values of $C_{w,0}$, and imposed flow dominated at high values of $C_{w,0}$. The turbulent flow parameter was defined by Owen and Rogers (1989) as:

$$\lambda_T = \frac{C_w}{Re_\phi^{0.8}} \quad \text{Equation 2-9}$$

A sink region exists in the vicinity of the clearance gap where mixing of the sealing flow and ingressed flow occurs, meaning that the fluid re-circulating around the cavity can be a mixture of the two flows.

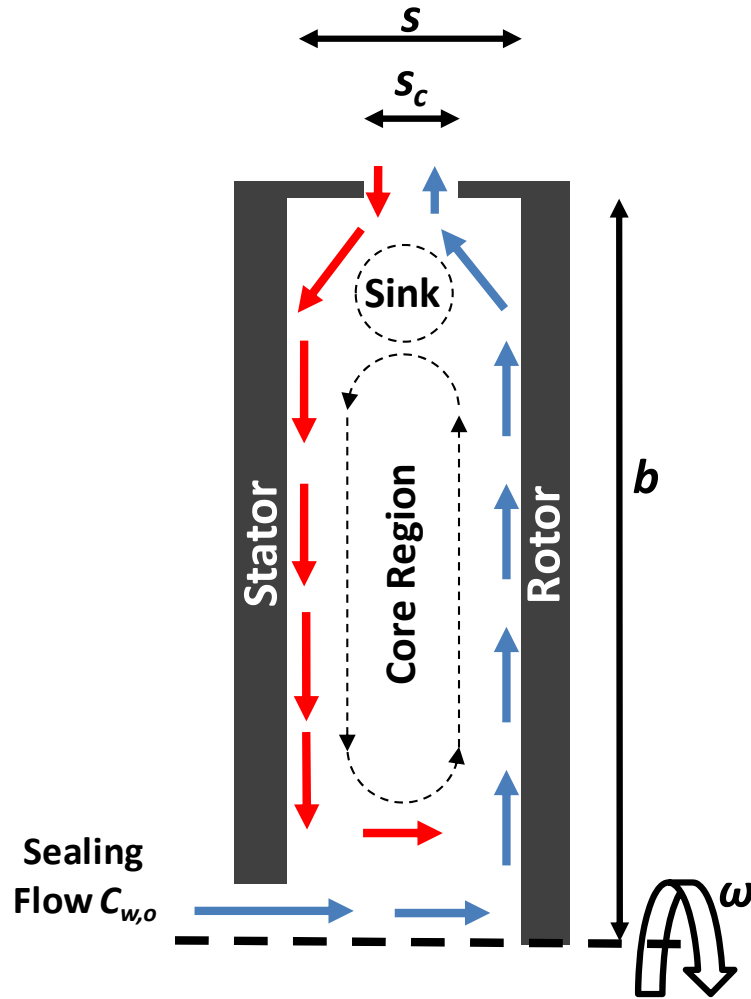


Figure 2-2: Simple rotor stator cavity

Bayley and Owen (1970) conducted experimental investigations of sealing air requirements of a shrouded rotor stator cavity with a simple axial gap seal within a quiescent environment, where there is no influence of an external flow, for rotational Reynolds numbers $\leq 4 \times 10^6$. A relationship was given relating the minimum sealing flow requirement to the axial seal gap, disc radius and rotational Reynolds number, shown in equation 2-10, where the gap ratio $G_c = s_c/b$.

$$C_{w,min} = 0.61 G_c Re_\phi \quad \text{Equation 2-10}$$

Phadke and Owen (1980) offered a correlation resulting from a similar study for a larger range of seal gap ratios G_c , up to a rotational Reynolds number of $Re_\phi \leq 1 \times 10^6$.

$$C_{w,min} = 0.14 G_c^{0.66} Re_\phi \quad \text{Equation 2-11}$$

Phadke and Owen (1983) extended this work to include radial seals which compared with axial seals were found to require a lower value of $C_{w,min}$. This was explained by a pressure inversion effect where increased rotational speed was found to increase pressure in the rotor stator cavity. This effect was attributed to an impinging jet across the seal. Figure 2-3 shows both an axial and radial seal with simplified geometry. The axial seal has a seal gap parallel to the axis of rotation while a radial seal has a seal gap perpendicular to the axis of rotation. Phadke and Owen (1988a) conducted a number of studies of the sealing characteristics of shrouded rotor stator cavities. In the first part of this series of investigations a rotor stator system was studied within a quiescent environment for a number of clearance ratios and rotational Reynolds numbers. The minimum sealing requirement for seven seal types were given. The results of this investigation were then compared to sealing air requirements in the presence of both axisymmetric and non axisymmetric external flow in Phadke and Owen (1988b) and Phadke and Owen (1988c).

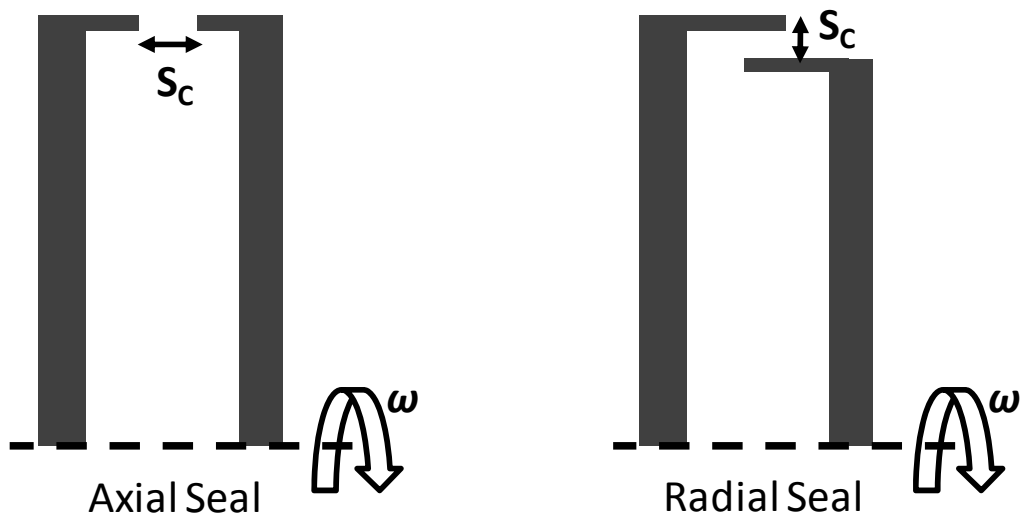


Figure 2-3: Simple axial and radial seal geometry

2.4 Shrouded Rotor Stator Cavities with an External Flow

Although the case of shrouded rotor stator cavities in a quiescent environment is useful when describing the flows within a gas turbine engine rotor disc cavity, in practise the cavities will be subject to an external main annulus flow. A consequence of the presence of NGVs "Nozzle Guide Vanes" and rotor blades in the main annulus is complex three-dimensional flows which cause unsteady non-axisymmetric pressure profiles above rotor disc cavity rim seals. These pressure profiles drive externally induced ingestion. It is useful therefore to use shrouded rotor stator cavity models with external flows to examine the effects of this external pressure profile.

Useful nondimensional flow rates for the study of rotor stator systems with an external flow include nondimensional ingress $C_{w,i}$ and nondimensional egress $C_{w,e}$. The extent to which an imposed sealing flow $C_{w,o}$ prevents ingestion into a rotor stator cavity can be described by the sealing effectiveness parameter:

$$\varepsilon = \frac{C_{w,o}}{C_{w,e}} \quad \text{Equation 2-12}$$

In the second part of their investigation Phadke and Owen (1988b) conducted sealing experiments where the rotor stator cavity was subject to an external, near axisymmetric axial flow. This study did not attempt to recreate the main annulus flow feature associated with blade and nozzle rows. For all seal geometries tested it was shown that two ingress regimes existed. This effect was described by the ratio of the external flow axial Reynolds number to the in cavity rotational Reynolds number, Re_w/Re_ϕ . For low values of Re_w/Re_ϕ the ingress was said to be rotationally dominated. For larger values of Re_w/Re_ϕ the ingress was said to be externally induced. The value of Re_w/Re_ϕ at which ingestion became externally dominated varied with seal geometry.

Abe et al (1979) conducted experimental investigations of externally induced ingress in a half stage axial turbine rig. It was shown that for externally induced ingress, the ingress rate was determined by the ratio of sealing air and main annulus flow velocities, the rim seal type and clearance.

Dadkhah et al (1992) conducted experimental sealing effectiveness measurements in a axial turbine test facility with external flow. The test facility included two radial clearance seals, one with the stator upstream and a second with the rotor upstream. In each case the upstream component's shroud overlapped the downstream shroud. The test facility included guide vanes but did not include blade rows. Measurements showed that the minimum sealing flow requirement $C_{w,min}$ was lower with the upstream stator configuration. However, where $C_{w,o}$ was less than $C_{w,min}$ the ingress levels were seen to be lower with the upstream rotor seal.

Green and Turner (1994) conducted further experiments using this facility with the addition of rotor blades. It was observed that to completely seal a rotor stator cavity the in-cavity pressure needed to be equal to the maximum main annulus pressure occurring at the rotor blade leading edge. It was found however that the inclusion of the rotor blades improved sealing effectiveness. Bohn et al (2000) observed a similar effect, but for a different seal configuration found the opposite was true where the inclusion of rotor blades reduced sealing effectiveness. Gentilhomme et al (2003) conducted experimental and CFD "Computational Fluid Dynamics" investigations of ingestion in a single stage axial turbine rig showing that for low sealing flow values the ingestion of high swirl main annulus air could increase swirl within the rotor stator cavity.

Roy et al (2007) conducted an investigation into the flow fields above rim seals which result in simultaneous ingress and egress from rotor stator cavities through experimental and CFD studies of a single stage axial turbine. The rotor stator cavity included blade and NGV row together with a radial overlap rim seal. Cavity sealing requirement measurements were made in the presence of an external axial flow. Figure 2-4 shows a PIV "particle image velocimetry" image of instantaneous velocity vectors for a quadrant of the rotor stator cavity, 2.8 mm from the stator disc. The locations of the rim seal are shown by the dotted lines at the outer radius. The blade and NGV positions are indicated outside the rim seal. High tangential velocities of 55 rad/s were measured at the outer radius near the rim seal, fluctuating circumferentially with blade passing events. It was suggested that these areas of high tangential velocities resulted from ingested main annulus flow entering the rim seal area. The areas of lower tangential velocity near the rim seal were attributed to egressed air from the rotor stator cavity.

Zhou et al (2009) continued work on this experimental facility testing a number of different aspect ratio rotor stator cavities, b/s . Multiple regions of ingress and egress were observed through PIV measurements and concentration measurements showed that ingestion decreased with decreasing cavity aspect ratio. The results obtained from flow visualization techniques and concentration measurements were compared to three dimensional CFD solutions. It was found that the model under predicted ingestion which was attributed to the sector model failing to capture circumferentially rotating, low pressure areas in the vicinity of the rim seal.

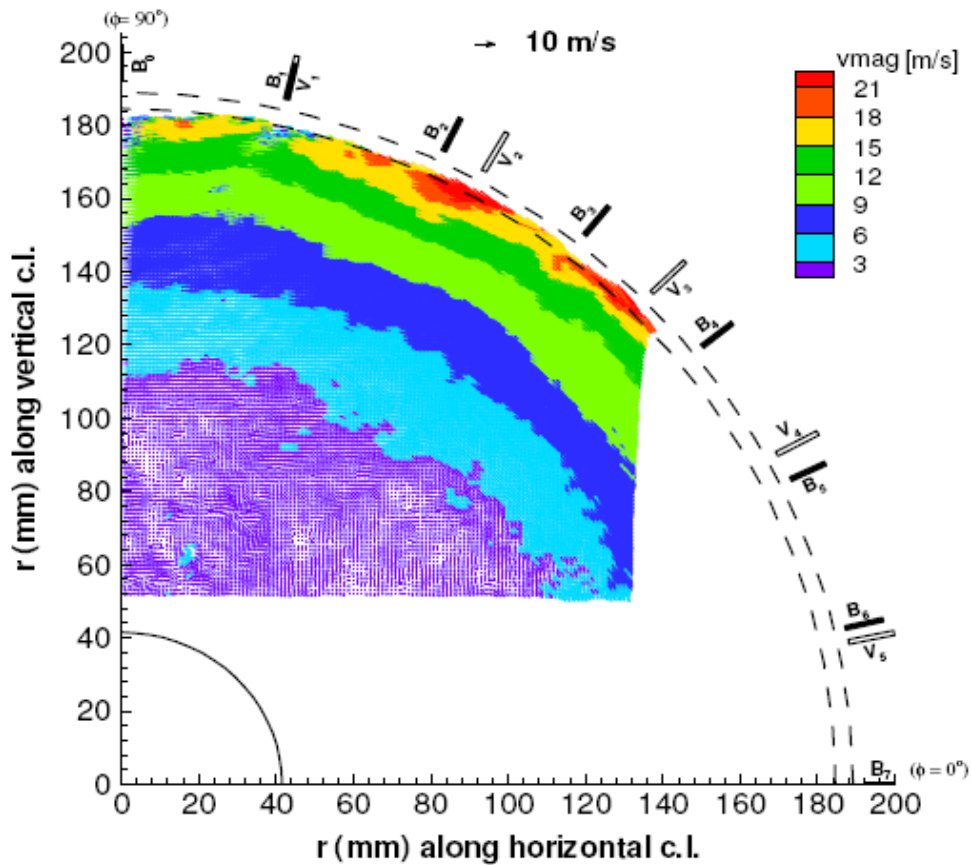


Figure 2-4: Instantaneous velocity vector map in rotor disc cavity, Roy et al (2007)

Mirzamoghadam et al (2008) conducted a CFD investigation of ingestion through a rotor stator cavity for a single stage turbine using engine representative geometry for $Re_w/Re_\phi = 0.42$. It was shown that the model predicted ingestion driven by main annulus pressure asymmetries even at high sealing flows. Design correlations predicted ingestion rates 18% lower than those shown by the CFD model. Rabs et al (2009) conducted a study of external rim seal ingestion driven by Kelvin-Helmholtz vortices which had been noted under certain conditions at rotor stator gaps in the absence of NGVs and blade rows. CFD studies were conducted on a 1.5 stage axial turbine based on an experimental facility. It was found that the inclusion of NGVs and rotor blades prevented the formation of the vortices except at high rates of imposed sealing air. For large values of $C_{w,o}$ the effects were seen but greatly reduced when compared to those in the absence of NGVs and blade rows.

Owen (2009a) solved incompressible orifice flow equations for the case of rotationally induced ingress. Figure 2-5 was presented by Owen showing the variations in sealing effectiveness ϵ , nondimensional egress $C_{w,e}$ and nondimensional ingress $C_{w,i}$ with imposed flow $C_{w,o}$. This is presented for the case where there is zero external swirl and the discharge coefficient for the ingress and egress paths through the rim seal are equal. For zero imposed flow, where the sealing effectiveness is zero, the rates of ingress and egress are equal and due purely to the external pressure asymmetry. As the imposed flow increases, the sealing effectiveness and egress rate are seen to increase until they reach unity as the imposed sealing flow reaches the entrainment rate. The ingress is seen to reduce to zero. Owen compared the experimental data of Graber et al (1987) to effectiveness and theoretical values obtained from the flow equations. The theoretical values showed close agreement for lower values of sealing effectiveness, however, at higher values they were found to over predict the sealing effectiveness. This was attributed to the effects of molecular and turbulent diffusion at low ingress rates. It was noted that the model may not be applicable for certain seal geometries and that further experimental data would be required to further test the model.

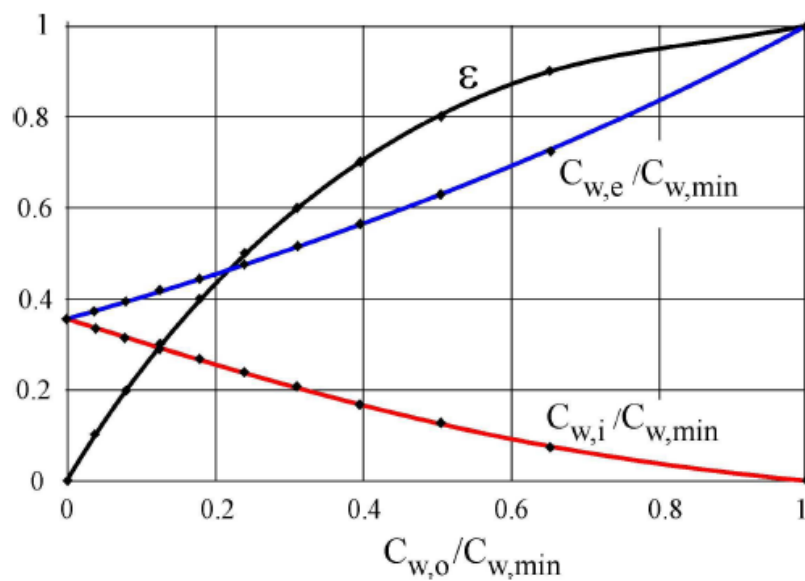


Figure 2-5: Sealing effectiveness, ingress and egress with imposed sealing flow, Owen (2009a)

In part 2 of this publication Owen (2009b) solved the incompressible orifice equations for nonaxisymmetric externally-induced ingress and for combined internal and externally induced ingress, using a saw tooth model to represent external circumferential variations in pressure and radial velocity. Figure 2-6 shows the variation in modelled effectiveness for both rotationally induced (solid lines) and combined internally and externally induced (dotted lines) cases for three values of the ingress to egress discharge coefficient ratio $C_{d,i}/C_{d,e}$.

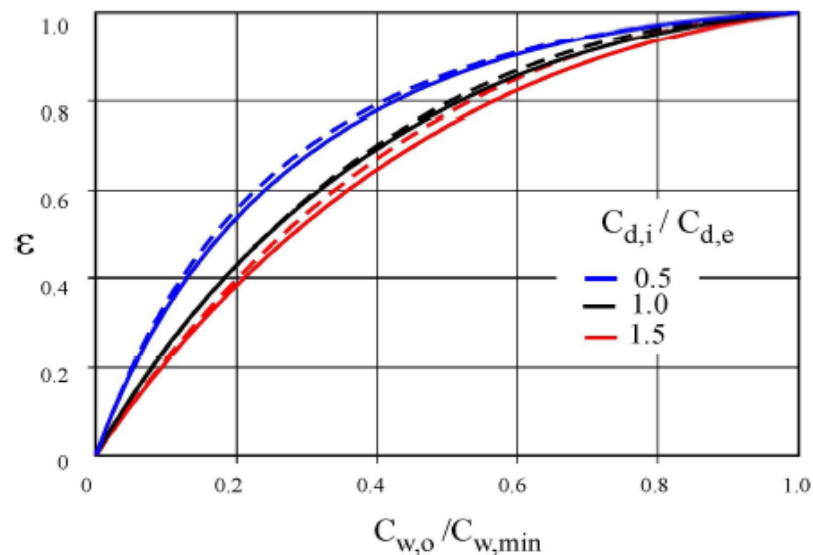


Figure 2-6: Variation of sealing effectiveness with imposed sealing flow, Owen (2009b)

Good agreement was found between the saw tooth externally induced ingress model and the data of Johnson et al (2006) and Johnson et al (2008). It was concluded that where the egress discharge coefficient was equal to the ingress discharge coefficient the modelled values of effectiveness were in good agreement with published externally induced ingestion data, however more data was required to validate the suitability of the model to predict combined internally and externally induced ingress.

Zhou et al (2011a) used the orifice flow models described by Owen (2009) to estimate sealing effectiveness at engine conditions. The calculated effectiveness based on the models of Owen vary with the discharge coefficient ratio and the minimum required sealing flow parameter, the values of which were determined statistically to best match empirical effectiveness data. It was shown that for rotationally induced ingress the values of the two parameters used by Zhou showed better agreement with the data of Graber et al (1987). For the case of externally induced ingress, good agreement was found between Zhou's calculated value of effectiveness, the data of Owen et al (2010) and the data of Johnson et al (2008).

Zhou et al (2011b) also conducted CFD studies of ingestion through axial clearance rim seals. The results of these studies were compared to the sealing effectiveness number generated from orifice flow models and were found to support the orifice model assumption that ingress and egress is driven by pressure asymmetries in the main annulus. Figure 2-7 shows line contours of static pressure across the modelled turbine stage for two locations of the rotor blades with respect to the NGV row. Filled contours of radial velocity are also shown in the seal gap clearance between the blade and NGV rows. Red contours lines of high static pressure and red contour areas of negative radial velocity in the seal gap indicate ingestion, while blue contours lines of lower pressure and blue contour areas of positive radial velocity indicate egress. For the image on the left, where the leading edge of the rotor blade and the trailing edge of the NGV are axially adjacent the high peak pressures are seen to be prominent. In the right hand image where the centre of the suction side of the blade is in line with the trailing edge of the NGV the areas of high pressure are greatly reduced.

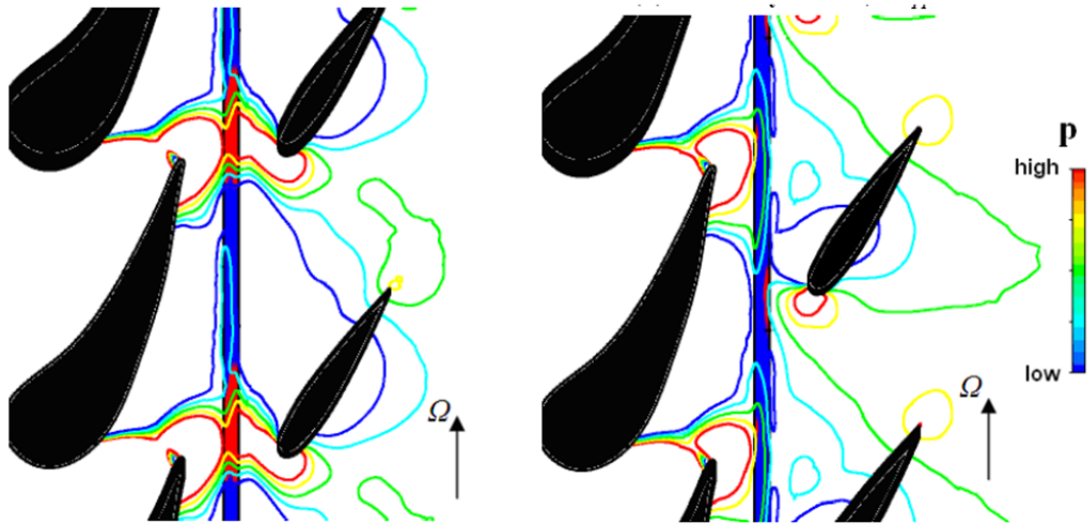


Figure 2-7: Contours of static pressure at 5% annulus height, Zhou et al (2011b)

Sangan et al (2011a) conducted an experimental investigation of externally induced ingress for both an axial and radial seal. Concentration and pressure measurements were made in a test facility, comprising of a single turbine stage and rotor stator cavity, to determine sealing effectiveness. Orifice model calculated values of minimum sealing flow requirement correlated well to the experimentally obtained values. Sangan et al (2011b) also conducted experimental studies of rotationally induced ingress. Figure 2-8 shows experimentally obtained values of sealing effectiveness plotted against values obtained from orifice models for both externally and rotationally induced ingestion against the nondimensional sealing parameter, defined in equation 2-13. In both cases the radial seal was shown to require lower sealing flows to prevent ingestion.

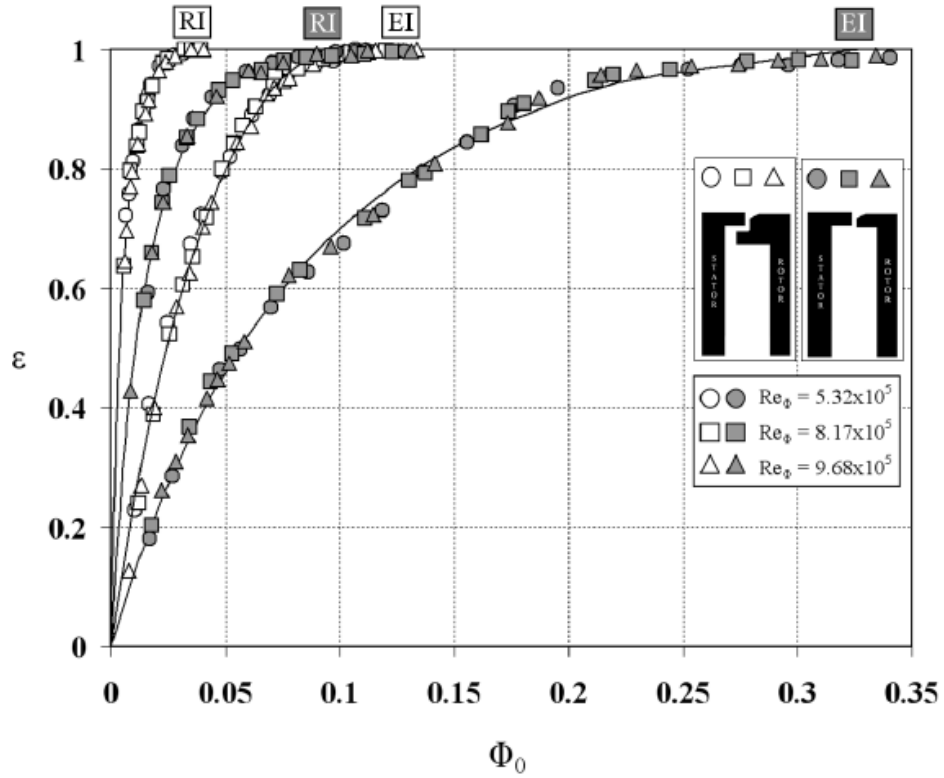


Figure 2-8: Comparison of sealing effectiveness for externally and rotationally induced ingestion, Sangan et al(2011b)

$$\Phi_0 = \frac{C_{w,o}}{2\pi G_c Re_\phi} \quad \text{Equation 2-13}$$

In multistage turbines, where sealing air is used to seal rotor disc cavities and is egressed into the main annulus flow, re-ingestion of this sealing air from the main annulus into a downstream seal can have a significant effect on the system performance. Figure 2-9 shows the paths of these flows between two rotor disc cavities, where the stationary stator row components are shown in dark green and the rotating section in yellow. Fluid egressed from the downstream seal of the first stator row can be seen mixing with hot main annulus gas and entering the upstream seal of the downstream stator. The rotor blades have been omitted for clarity.

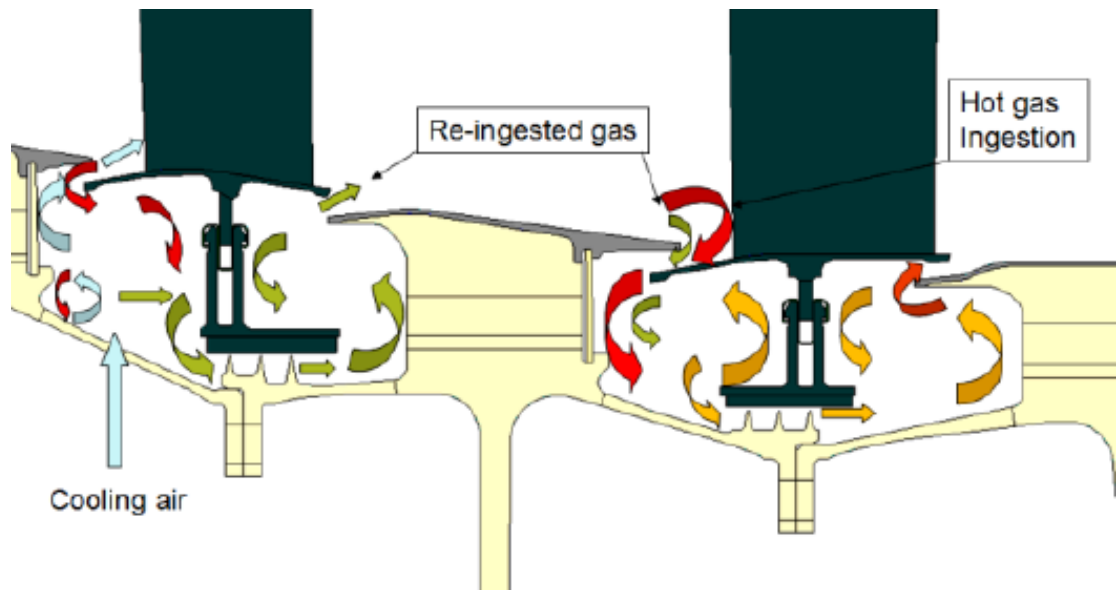


Figure 2-9: Re-ingestion between two turbine stages, Guijarro Valencia et al (2012)

The effect of the re-ingestion of sealing air from upstream cavities was investigated by Georgakis et al. (2007). A CFD study was conducted where sealing air was egressed from an upstream wheelspace at a rate of 1-2% of the external main annulus flow. It was shown that re-ingestion of upstream egress provided a significant contribution to downstream stator well cooling, which was quantified as improving thermal effectiveness on the downstream cavity walls by 4-5%. In general the egress of sealing air into the main annulus is detrimental to the overall performance of a gas turbine, however, it can be advantageous if geometry and flow rates can be optimised to encourage re-ingestion of this sealing air back into a downstream stage.

2.5 Interstage Labyrinth Seals

The primary function of the labyrinth seal is to limit flow from a high to low pressure cavity, where contact is not permitted due to high speed differentials between two components. Labyrinth seals are used in many gas turbine applications, where good sealing characteristics are required between rotating and stationary discs, the primary factors influencing the seal performance being seal clearance and the number of sealing fins. In multistage turbines interstage labyrinth seals are a common solution for controlling flow from upstream to downstream rotor disc cavities. Figure 2-10 shows the use of axial labyrinth seals in a section of a three-shaft turbine. The blue shaded sections represent the rotating components of the turbine while the grey shaded sections represent stationary components associated with the NGV rows. Three fin labyrinth seals can be seen at the lower radius of the grey stationary components at the interface with the rotating section.

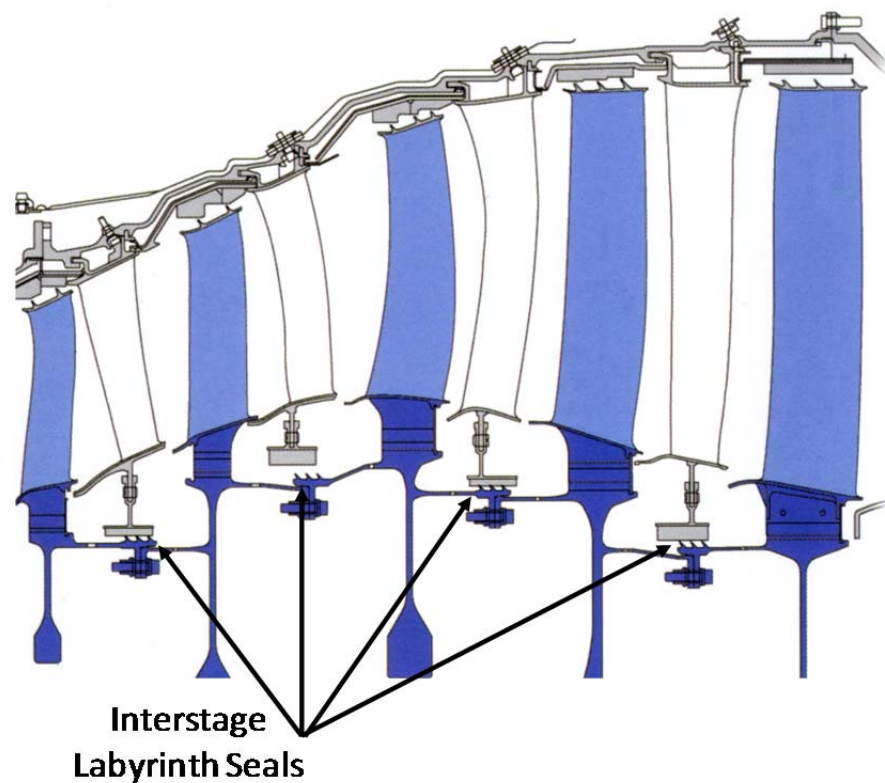


Figure 2-10: Interstage labyrinth seal application in a three-shaft turbine, Rolls-Royce (2005)

The St. Venant (1871) Equations, with an appropriate discharge coefficient can be used to calculate seal mass flow rates through interstage labyrinth seals (Equation 2.14), Wittig et al (1987). The discharge coefficient C_D is required to account for the fact that the St. Venant Equation was derived for use with a single circular cross section orifice.

$$\dot{m} = C_D \frac{P_1 A}{\sqrt{T_0}} \left(\frac{P_2}{P_1} \right)^{\frac{1}{\gamma}} \sqrt{\frac{2\gamma}{R(\gamma-1)} \left[1 - \left(\frac{P_2}{P_1} \right)^{\frac{\gamma-1}{\gamma}} \right]} \quad \text{Equation 2-14}$$

Egli (1935) described an ideal labyrinth flow as the case where the kinetic energy of the leakage flow through the seal is zero at the downstream cavity, which can be considered similar to a single circular cross section orifice. The discharge coefficient therefore gives the ratio of the flow through a given labyrinth seal to the flow through an ideal labyrinth seal where the C_D value accounts for the dependent parameters such as sealing fin geometry and number, shown in Equation 2-15.

$$C_D = \frac{\dot{m}}{\dot{m}_{IDEAL}} \quad \text{Equation 2-15}$$

The interstage labyrinth seal axial flow Reynolds and Taylor number are defined by the following expressions:

$$Ta = \frac{\omega \times 2 \times z}{\nu} \sqrt{\frac{z}{r_l}} \quad \text{Equation 2-16}$$

$$Re = \frac{\dot{m}_l}{\mu \times \pi \times r_l} \quad \text{Equation 2-17}$$

Zimmermann and Wolff (1998) provided a review of seal discharge coefficients. Data was presented for a variety of configurations including number of sealing fins for 'straight through' seals, the use of grooves at sealing fin tips, the use of honeycomb

structures on the sealing face as well as variation in sealing fin geometry and the use of stepped seals. Figure 2-11 shows a basic labyrinth seal with a twin fin configuration. This seal type can be considered a 'straight through' seal where the stationary surface of the seal is flat and does not contain pockets or grooves, the fins are of equal height y , and where the seal tip clearance z (when s is seen on figures in Section 2.5 this should be taken as z) and the fin tip thickness w (when b seen on figures in Section 2.5 this should be taken as w) are consistent for each fin.

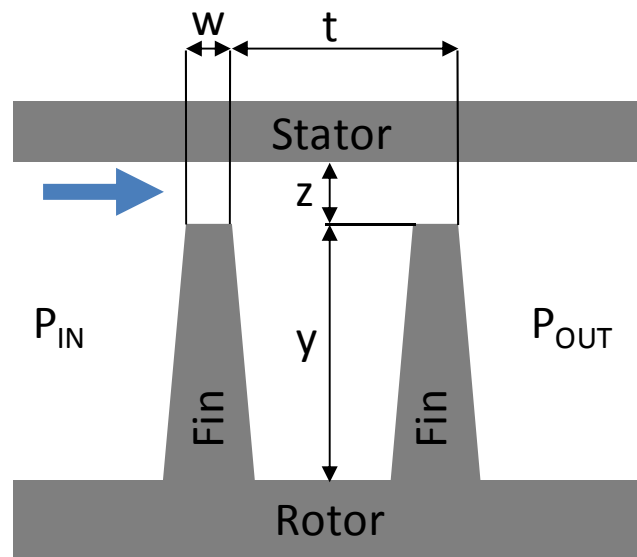


Figure 2-11: Basic straight through labyrinth seal geometry

Figure 2-12 shows discharge coefficient data presented for straight through seals with two or more sealing fins, for three values of the clearance ratio z/w . The discharge coefficients are given against the axial Reynolds number. It was shown that the effect of the clearance ratio z/w was only evident below $Re_w = 2 \times 10^4$ except for the case of very small seal clearances.

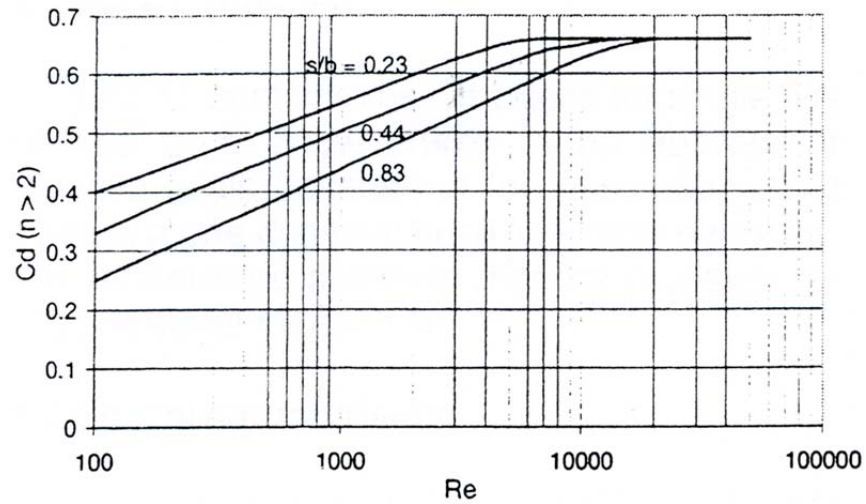


Figure 2-12: Discharge coefficients for seals with greater than 2 fins, Zimmerman and Wolff(1998)

Wittig et al (1987) examined the use of two dimensional numerical calculations to solve the time averaged Navier-Stokes equations. These calculations were compared to experimental results obtained from a test facility, including both a straight through and stepped seal arrangement. Figure 2-13 shows the results obtained for the straight through seal configuration with 1 and 6 fins for a range of seal clearance values and pressure ratios. Numerically calculated results are shown with solid symbols, while experimental data is shown with open symbols.

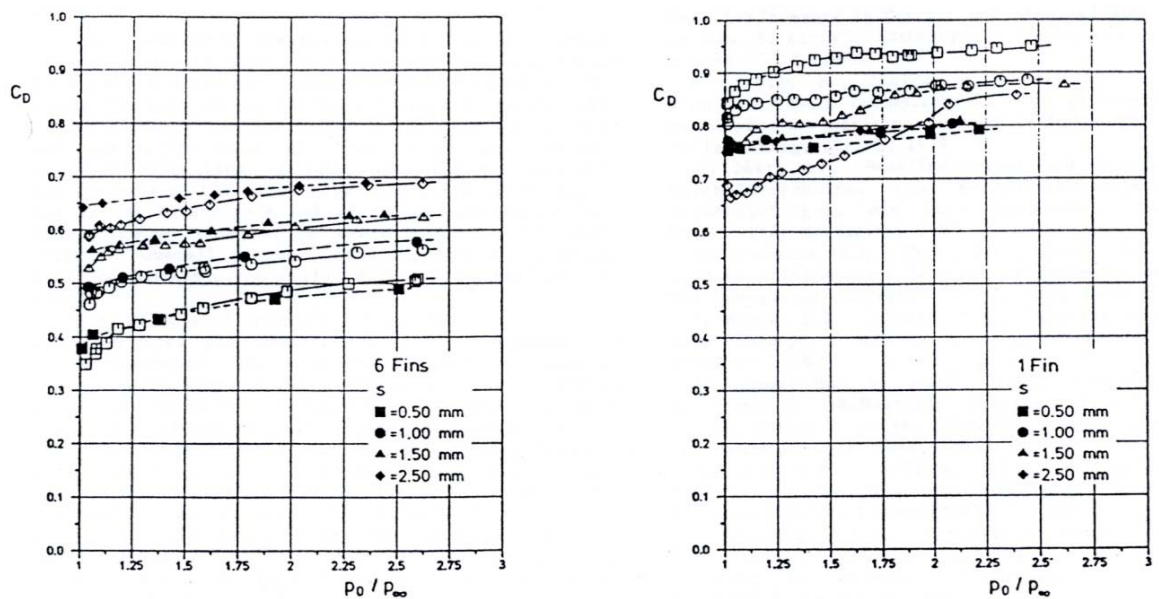


Figure 2-13: Discharge coefficients for 1 and 6 fin straight through seals, Wittig et al (1987)

Good agreement was found between the multi fin experimental and calculated discharge coefficients. Calculated results for one and two fin seals showed little variation with seal gap when compared to the experimental values. This was attributed to the modelling of the intake to the seal having a much larger influence over the flow when compared to the multi fin models. It was also observed that the effects of rotation were only significant for small Reynolds numbers and high Taylor numbers.

Gamal and Vance (2007) conducted studies on a number of labyrinth seal configurations on a test rig consisting of a high pressure supply flow of up to 6.89 bar, an external stationary seal and an internal rotating journal with a nominal diameter of 101.6mm. The number, thickness and profiles of the sealing fin were altered and measurements of seal leakage rate and cavity pressure made. It was found that leakage rates could be reduced by up to 20% by doubling the thickness w of the sealing fins. The effect of the fin tip profile design of sealing performance was found to be largely influenced by the fin seal clearances. The effects of seal eccentricity were also studied, where it was found that increased eccentricity reduced sealing performance. Gamal and Vance (2007) provided summarised C_D values for a number of 6, 8 and 12 fin seal configurations based on the publications of Shultz (1996), Gamel et al (2006) and Ertas (2005).

Kim and Cha (2009) compared experimental data to CFD and a numerical analytical tool for both straight through and stepped configuration seals for a range of seal clearances. It was found that the CFD model more accurately predicted the seal behaviour in both configurations than the analytical tool. It was also noted that although the step seal performed better for larger clearances, this advantage diminished as the seal clearance reduced. Figure 2-14 shows discharge coefficient data presented

for a six fin straight through seal for a range of tip clearances. The discharge coefficient was seen to increase with both increased seal clearance and pressure ratio. Both Experimental and CFD data is given.

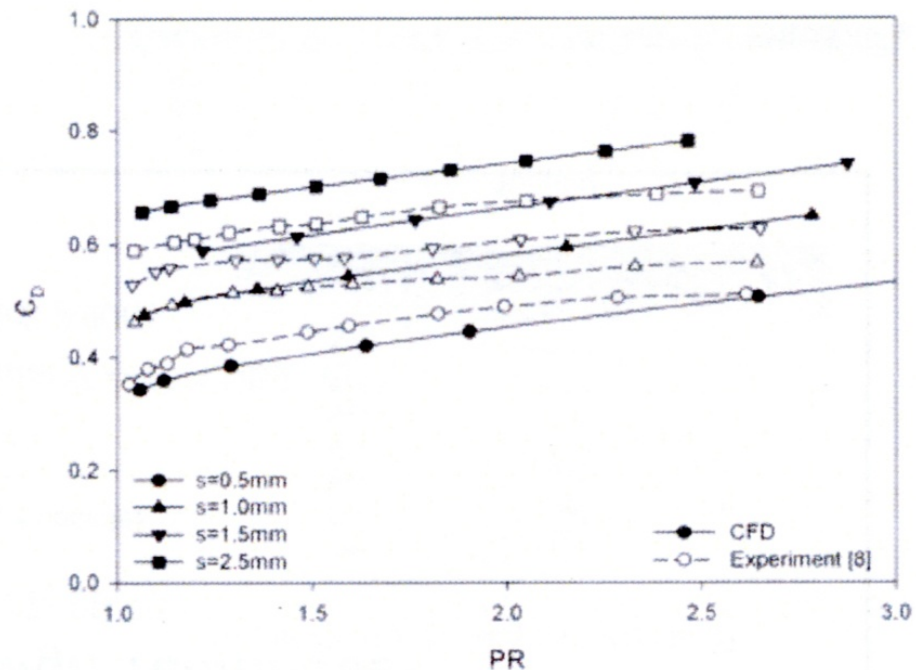


Figure 2-14: Discharge coefficient with pressure ratio and clearance, Kim (2009)

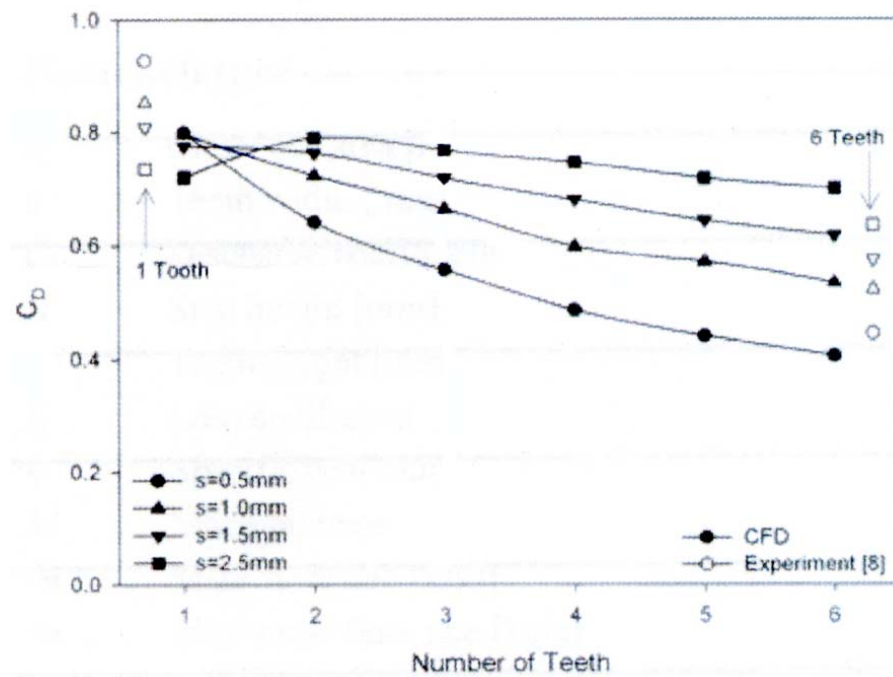


Figure 2-15: Discharge coefficient with fin number and tip clearance, PR = 1.5 bar, Kim (2009)

Figure 2-15 shows discharge coefficients for a straight through seal with one to six sealing fins. Both experimental and CFD data is presented for a number of tip clearances, at a seal pressure ratio of 1.5 bar. The discharge coefficient was seen to reduce with increased number of fins indicating increased sealing performance.

Waschka et al (1992) conducted a number of experimental investigations into the effect of high rotational speeds on the discharge coefficient of straight through labyrinth seals. A number of tip clearances were tested across a range of Taylor and Reynolds numbers. The rotational effect was described by the ratio of these numbers, defined in equation 2-16 and equation 2-17. This ratio describes the relationship between the axial and peripheral moment of flow through a seal.

Figure 2-16 shows results obtained for the effect of rotational speed for a range of Reynolds numbers for a fin tip clearance of 0.5 mm. It was found that at lower Reynolds numbers the discharge coefficient reduced with increased rotational speed. The rotational effect was seen to reduce with increasing Reynolds number. For the range of tip clearances measured it was found that the limiting Reynolds number for rotational effects ranged from 5000 to 10,000. Figure 2-17 shows the effect of the ratio Ta/Re on the discharge coefficient for a range of pressure ratios for a tip clearance of 0.5 mm. For all clearances tested a critical ratio of $Ta/Re \approx 0.2$ was found at which the discharge coefficient starts to dramatically reduce. Waschka et al (1992) attributed this to rotational effects becoming dominant, increasing flow resistance through the seal.

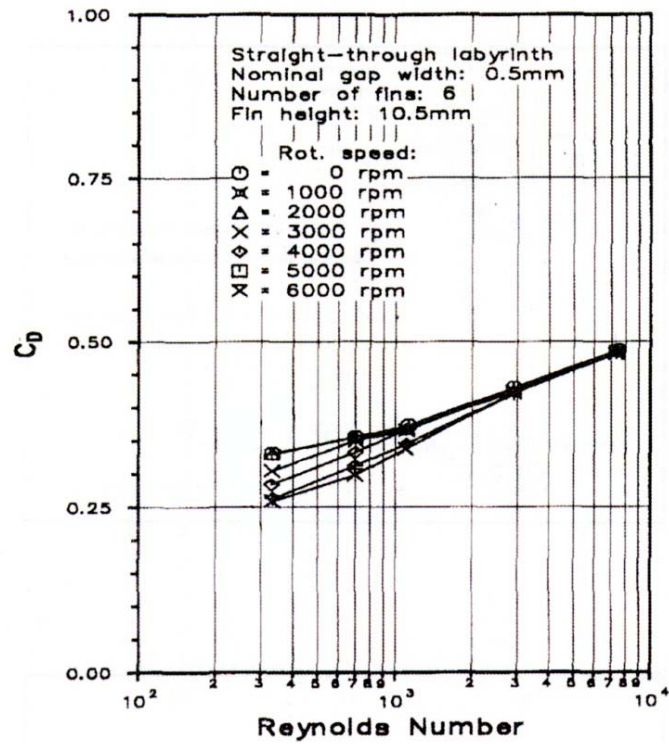


Figure 2-16: Rotational effects on the discharge coefficients as a function of Re, Waschka (1992)

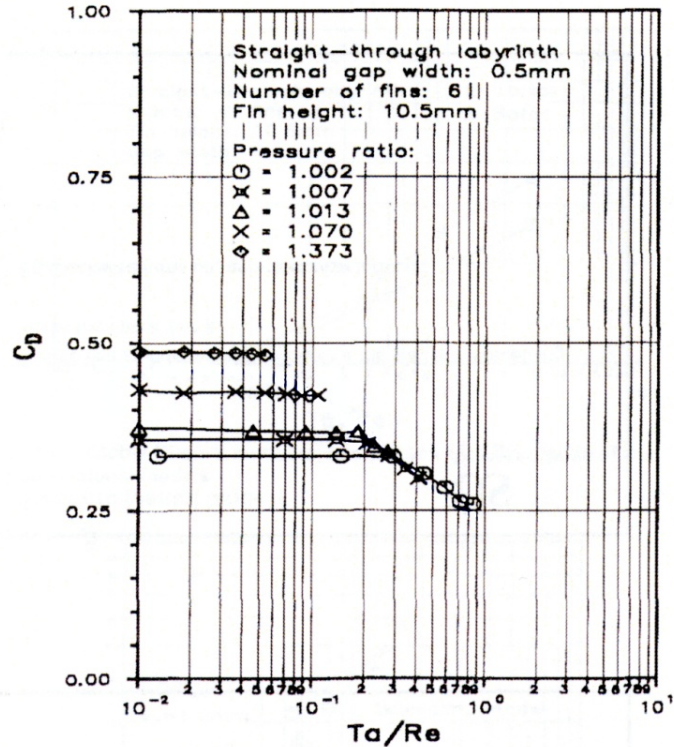


Figure 2-17: Rotational effects on the discharge coefficients as a function of the ratio Ta/Re , Waschka (1992)

2.6 Concentration Measurement Techniques

In order to measure sealing effectiveness in rotor stator cavities a range of experimental techniques have been developed. The most commonly used techniques are temperature measurements, pressure measurement, flow visualisation and concentration measurements. Temperature measurements have been used to indicate ingress where a change in temperature indicates the presence of ingested hot gas. The process does however, present many challenges due to heat transfer between the rotor and stator surfaces and the cavity air. The effects of windage and frictional heating must also be accounted for. Pressure measurement can indicate ingestion, when the pressure inside the cavity is less than the pressure outside the rim seal. However, due to the complexity of the pressure profiles in the vicinity of the rim seal, capturing the unsteady variations is difficult and often requires additional numerical investigation. Flow visualisation techniques such as PIV offer insight into the complex flow structures in the vicinity of the rim seal, where a laser sheet is used to illuminate particles seeded into sealing or external flow. The presence of seeded gas in the cavity can also be used to indicate ingestion and hence identify $C_{w,min}$. The technique does not however offer the ability to directly quantify the rate of ingestion. Gas concentration measurements, where either the sealing air or external air is seeded with a tracer gas, offer the most direct method for quantifying sealing effectiveness. Where the imposed sealing flow $C_{w,o}$ is seeded with tracer gas the sealing effectiveness is calculated from the concentration of the sealing flow c_o , the measured concentration c_m and the ambient concentration c_a :

$$\varepsilon_c = \frac{c_m - c_a}{c_o - c_a} \quad \text{Equation 2-18}$$

Phadke and Owen (1988a) conducted a number of experimental concentration measurements. A traverse probe was located in the rotor-stator wheel-space through

which the concentration measurements were taken. The tracer gas, nitrous oxide, could be supplied to the rig through either the sealing flow, or to the external air outside the rim seal. In order to obtain $C_{w,min}$ the sealing air was supplied with a known concentration of nitrous oxide. The rotational speed of the rig was then increased while keeping the coolant flow constant, until the concentration measured by the probe was seen to drop, indicating the point at which the supplied sealing air was insufficient to seal the wheel-space. The commissioning of the concentration instrumentation included testing of the time response of the infra-red gas analyser. It was found that reducing the bore of the sampling pipe reduced the response time of the analyser.

Phadke (1988) investigated the effect of gas velocity through the analyser with two commissioning tests using a 50mm diameter pipe. The pipe was supplied with air of a known concentration of nitrous oxide. Concentration measurements were then taken using the experimental apparatus. For the first test, the sample gas velocity was said to be isokenetic. This is the case where gas passing through the analyser has the same velocity as that of the mean stream velocity being sampled. Measurements were taken from the centre of the pipe flow over a number of concentration levels. The results showed close agreement between the known seeding levels and the measured concentration. For the second test the 50mm pipe was supplied with a constant concentration level at three different sampling velocities, 0.4, 1.0 and 4.0 times the isokinetic velocity. Samples for each case were taken across the diameter of the pipe. The results showed that for a homogeneous mixture the measured concentration was independent of sampling velocity.

Dadkhah (1992) made gas concentration measurements via a traverse within the wheel-space at four radial locations, $r/b = 0.163, 0.411, 0.658, 0.905$, using nitrous oxide as a tracer gas seeded into the sealing air. The concentration measurements were used to determine the amount of main annulus gas ingested as well as the distribution of the ingested gas in the wheel-space. The study showed, from the resulting concentration measurements, where ingestion was present. The ingested gas entering the wheel-space was entrained onto the stator where it then proceeded down the face of the stator. The ingested gas then moved across the core of the wheel-space into the rotor boundary layer. The study showed that the highest dilution levels occurred at the higher radius of the wheel-space. Ingress mass flows were estimated by integration of the mean gas concentration levels.

Gentilhomme et al (2003) introduced sealing air to the rotor cavity at a radius of $r/b = 0.55$. Seeding gas was introduced to the sealing air prior to the cavity. Two operating conditions were tested, corresponding to in cavity rotational Reynolds numbers of $Re_\phi = 2.83 \times 10^6$ and $Re_\phi = 9.04 \times 10^5$. Nitrous oxide was used as the seeding gas for the higher Reynolds number condition and carbon dioxide for the lower Reynolds number condition. Concentration measurements were made at cavity radii of $r/b = 0.4, 0.71, 0.88$ and 0.92 . Nitrous oxide and carbon dioxide concentration was measured using infrared gas analysers. Concentration measurements were then used to calculate sealing efficiency.

Dunn et al (2010) conducted concentration measurements in a single stage model gas turbine. Numerical simulations were compared to experimental results taken at a main annulus flow of Reynolds number $Re_w = 7.86 \times 10^4$ and a rotational Reynolds number

of $Re_\phi = 8.74 \times 10^5$. Carbon dioxide was used as a tracer gas to measure ingestion levels. The purge air was seeded with carbon dioxide upstream of the injection point into the rotor-stator cavity. The injection point was at a radius of $r/b = 0.78$, below a rim seal consisting of two axially overlapping seals, the lower seal located on the rotor at a radius of $r/b = 0.85$. The purge air, pre injection into the cavity was kept at a constant volumetric concentration of 4.0 %. Concentration measurements were taken in the cavity at $r/b = 0.22, 0.40, 0.55, 0.71, 0.88$ (mid rim seal) and 0.93 (above rim seal). The uncertainty for the concentration measurements made by a NDIR gas analyser was given as ± 0.11 %. Sealing effectiveness was then calculated.

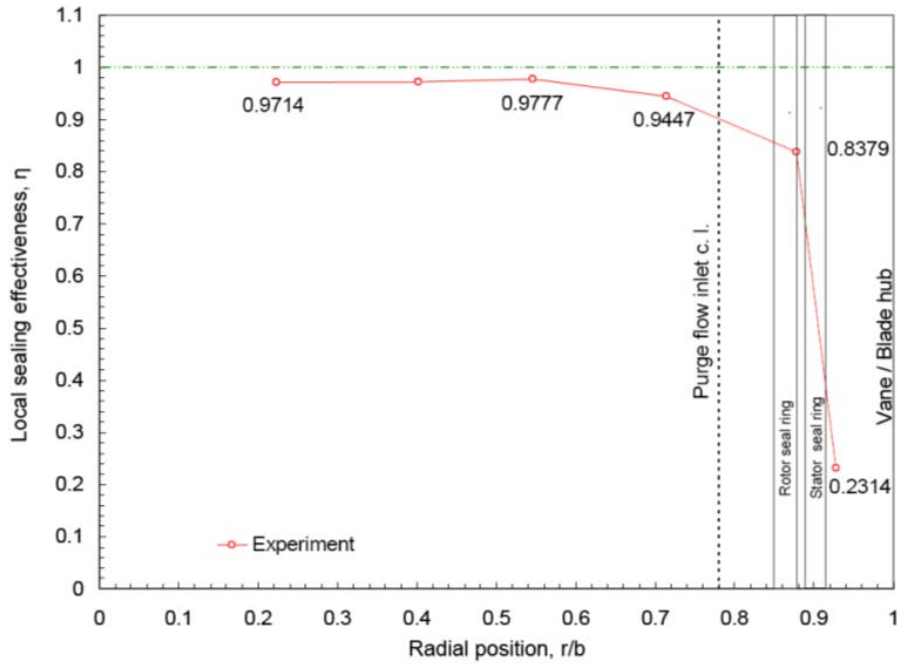


Figure 2-18: Sealing effectiveness with radial location r/b

Figure 2-18 shows the local sealing effectiveness calculated for the six concentration measurement locations. The effectiveness at $r/b = 0.93$ of 0.23 suggests that purge air was present outside of the cavity and had passed through the rim seal. Similarly the sealing effectiveness of 0.9447 at $r/b = 0.71$ shows main annulus flow has reached the higher radius areas of the cavity, indicating that a rim seal exchange is taking place including local mixing between the main and purge flow in the vicinity of the rim seal.

Figure 2-19 shows the test facilities of Phadke and Owen (1988a), Dadkhah (1992), Gentilhomme et al (2003) and Dunn et al (2010). For each test facility the main external flow is indicated with a red arrow. The supply path of cooling/purge air is indicated with a blue arrow. Sampling locations are indicated with green dots and labelled with radial positions r/b . The test facilities of Phadke and Owen (1988a) and Dadkhah (1992) took samples via a traverse, indicated by the joining together of the sampling locations with a green line. Gentilhomme et al (2003) and Dunn et al (2010) used single point sampling locations located on the stator face of their respective test sections.

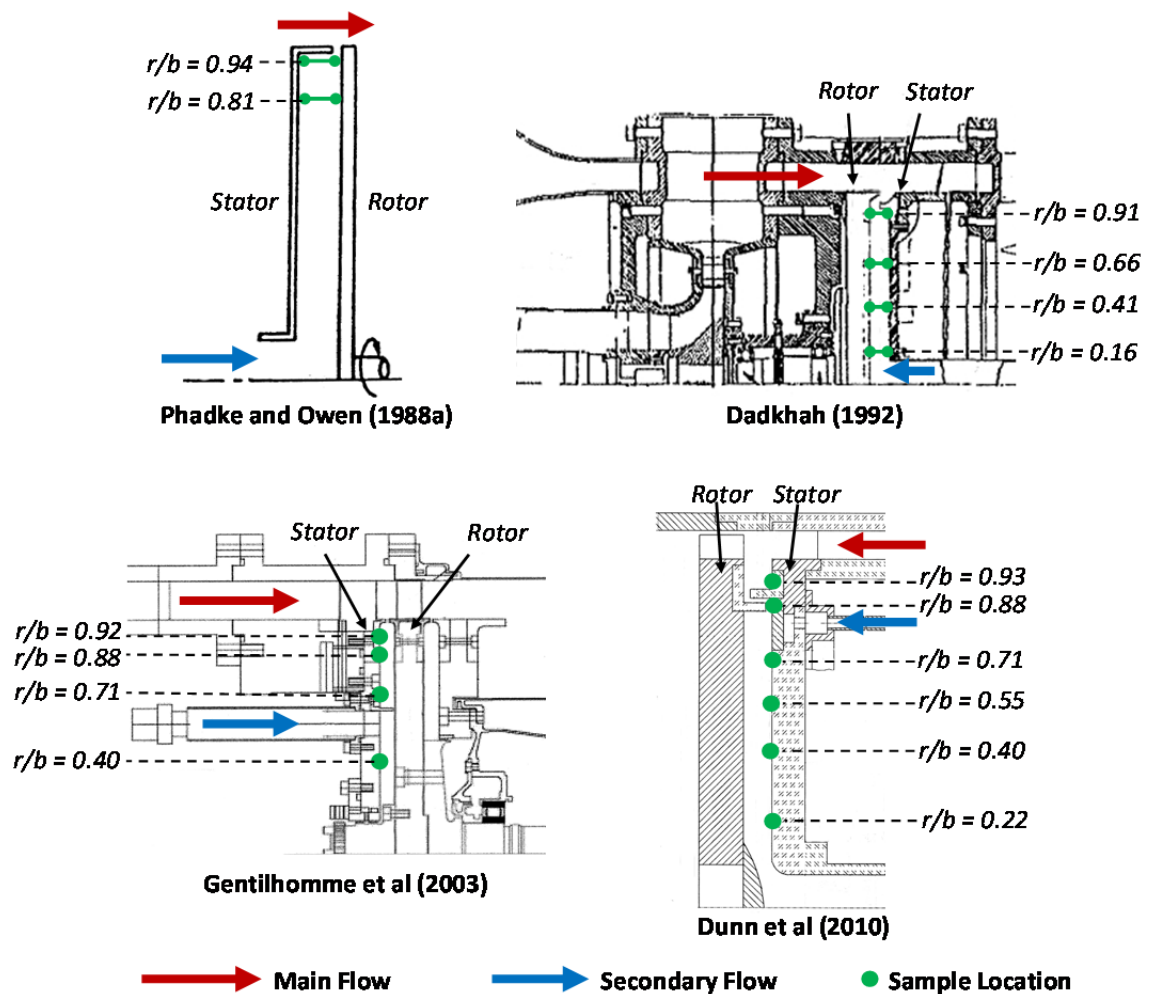


Figure 2-19: Concentration measurement locations of four experimental test facilities

2.7 Summary

The mechanisms through which the exchange of main annulus and rotor disc cavity sealing air takes place are generally understood. Through the use of rotor stator models analogous to rotor disc cavities the behaviour of such systems, including rotationally and externally induced ingestion, can largely be described through numerical models. However, for more complex, engine representative geometries and operating conditions, where both rotationally and externally induced ingestion can occur simultaneously, experimental data is required for validation of theoretical models. The most directly comparable experimental measurements of sealing efficiency and ingestion are obtained through concentration measurements as described in Section 2.6.

The work presented by the author describes ingestion experiments conducted on a two stage axial turbine rig. The experimental rig is considered engine representative in terms of both geometry and operating conditions. This was achieved by careful consideration of the aerodynamic design of the test facility, reported by Woollatt (2002). This test facility includes representative sealing air supply geometry, rim seal geometry, interstage labyrinth seal geometry and blade profile geometry. Experimental methods through which the use of concentration measurements can be extended to attempt to quantify rim seal flows and re-ingestion flow are presented for a number of sealing flow supply geometries.

3 Test Facility Overview

3.1 Introduction

This chapter introduces the TSW test facility as well as the instrumentation and data acquisition system used to both control the rig and to record the required experimental data over the test matrix. The description of the system gives an overview of the experimental facility as well as detailed explanations of each subset of instrumentation.

The design and build of the test facility, as well as the instrumentation of the test section was completed in collaboration with, Dr. N. R. Atkins, Dr. D. D. Coren, J. R. Turner and S. Davies under the guidance of principal investigator Dr. C. A. Long and previously Professor. P. Childs.

The author did not join the program until after the initial planning, concept designs and preliminary build of the test facility had been completed. This work included the initial rig design layout, early modelling of rig flow requirements and selection of measurement locations. On joining the program the author was involved in the installation and commissioning of the test facility, including the development of the control systems and the manufacture and installation of the of instrumentation. The DAQ system development was led by J. R. Turner, the author assisted in the debugging and development of the system.

The design and commissioning of the test facility is described in Coren et al (2010), included in Appendix C.

3.2 Test Facility External Systems

The operation of the TSW rig requires close control of air supplies, cooling circuits and oil systems. In addition to controlling these parameters a dynamometer is required to control the rig speed and also to absorb the power produced by the turbine. Figure 3-1 shows an overview of the system required to control and supply these flows and parameters. Main annulus air is supplied by a modified DART engine and compressor, described by Turner et al (2000). This flow is passed through a settling chamber before entering the rig in order to reduce asymmetries in the main annulus flow in the test section. A CFD investigation, reported in Coren et al (2010) found the bulk mean velocity in the settling chamber to be $\leq 1 \text{ ms}^{-1}$. Using four total pressure rakes at different circumferential locations the total rig inlet pressure was found to be within $\pm 1.5\%$ of the dynamic head at 80 ms^{-1} . An ATLAS ZX250 compressor supplies the cooling air to the test section, which can be seeded with carbon dioxide for concentration experiments. A Hydrovane compressor supplies a number of blown seals within the rig; it is also used to cool the rotating frame temperature measurement telemetry unit. Outside of the rig the Hydrovane is also used to control a number of pneumatic valves as well as to pressurise the dynamometer lubrication system. The main water circuit is required to supply the dynamometer. The water supply determines the load capabilities of the dynamometer and also removes heat. A water circuit is also used to cool the ATLAS cooling air before it enters the rig. Two oil circuits are required for the gearbox/shaft output of the rig. The first circuit which supplies the gearbox has a small water system to cool the oil. This oil supply is pumped by the gearbox. A second oil circuit which supplies the rig output shaft is not water cooled, however, it does include an external pump to increase oil supply pressure.

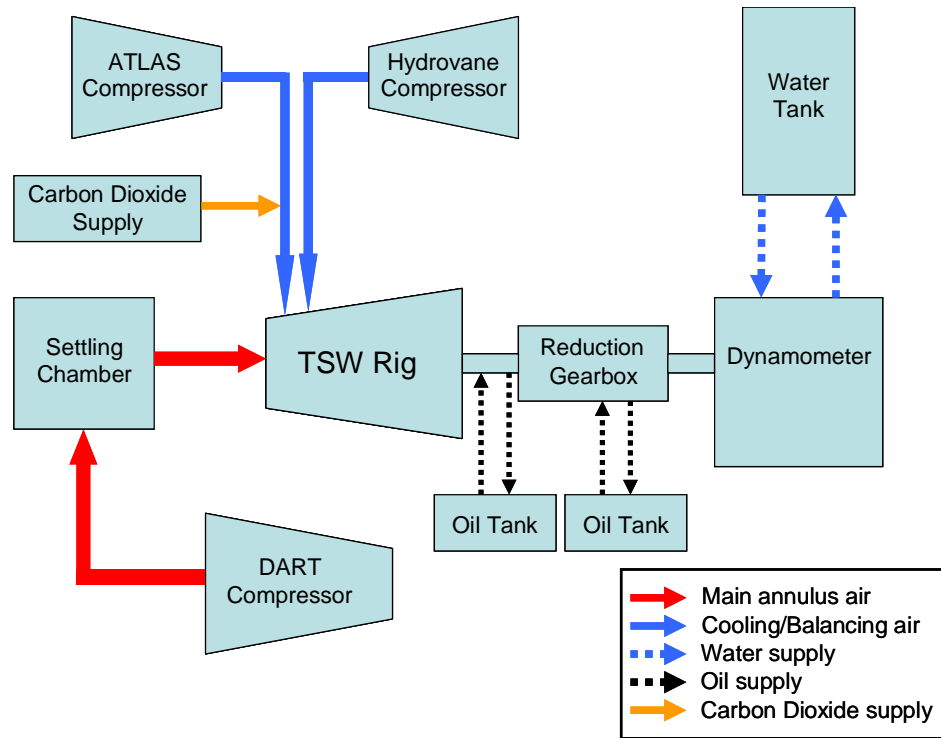


Figure 3-1: Test facility major component overview

3.3 Test Section Air Supply

The DART compressor consists of a Rolls-Royce two stage centrifugal compressor powered by a DART turboprop engine. When used to supply the TSW rig the compressor typically provides the rig with 4.8 kg/s of air at 2.9 bar abs, where the air temperature at the rig inlet ranges between 431 K and 438 K. The system is capable of supplying 10.5 kg/s of air at 3.3 bar abs. The supply line between the DART and rig inlet is heavily insulated, so small changes in the inlet temperature can be attributed to the atmospheric temperature seen during a test run.

The ATLAS ZX250 compressor, manufactured by Atlas Copco, consists of an oil free screw type compressor capable of supplying 0.8 kg/s of air at a maximum pressure of 7.5 bar abs. When used to supply cooling air to the TSW rig between 0.03 kg/s and 0.075 kg/s is required at a pressure of between 1.7 bar abs and 3.7 bar abs depending on

operating conditions. An additional flow of between 0.001 kg/s and 0.014 kg/s can be utilised from the ATLAS for the balancing and vent flows associated with controlling the passage of the cooling air within the rig.

The Hydrovane consists of an electrically driven sliding vane type compressor capable of supplying 0.1 m³/s of air at 8 bar abs. During operation of the TSW rig the Hydrovane is used to supply between 0.01 kg/s and 0.03 kg/s of air to cool the telemetry unit. The Hydrovane is also used to provide pressure to pneumatic valves, including two bypass valves, a control valve used to meter the ATLAS cooling air, and a DART emergency bypass valve which when cut vents the main annulus supply to the atmosphere rather than entering the test section.

3.4 Drive Train and Dynamometer

The power produced by the test rig is absorbed via a sluice gate type Heenan and Froude DPY590 dynamometer. A cross section of the dynamometer is shown in Figure 3-2. The dynamometer consists of a rotor and stator system submerged in water. The action of the rotor and stator churning the water absorbs the power by doing work on the fluid. The loading of the dynamometer is changed by opening and closing the sluice gates to cut the interaction of the rotor and stator reducing the work done on the fluid.

The dynamometer requires a constant water supply in order to operate. Work is done on the water as it passes through the dynamometer causing the water outlet temperature to increase. In order to avoid recirculation of water at the outlet temperature and also to avoid running at a total loss a large reservoir and cooling system is used. Figure 3-3 shows the water system. The water tank, located in the test cell, holds 2270 litres of

water. The tank can be supplied directly with mains water to replace any loss from the system.

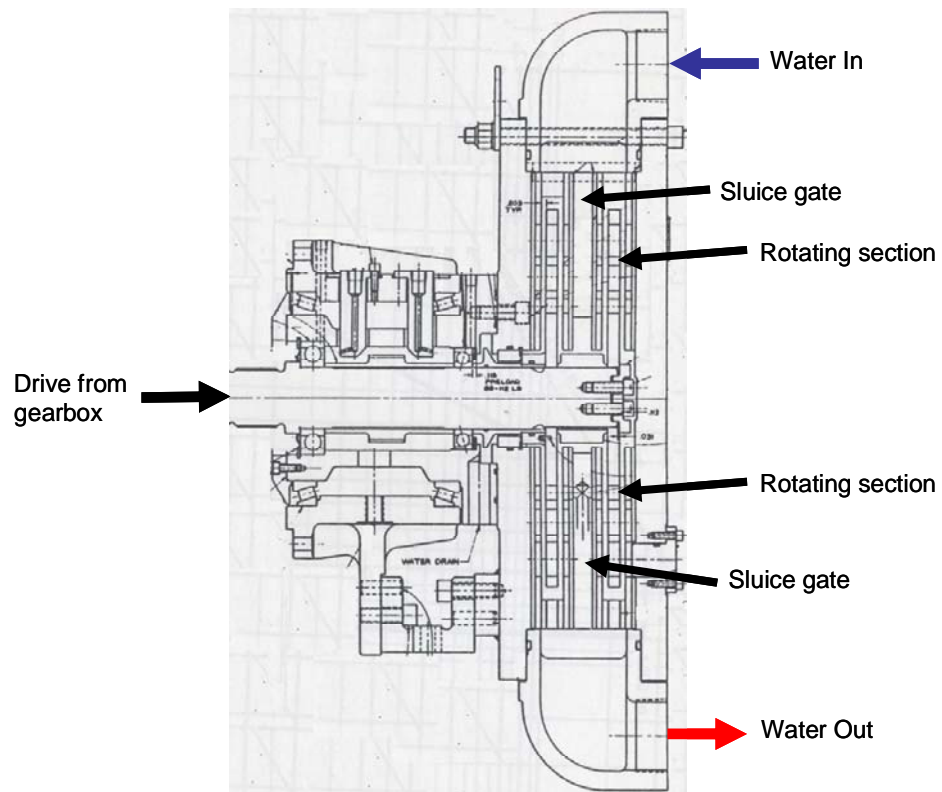


Figure 3-2: Heenan and Froude DPY590 dynamometer cross section

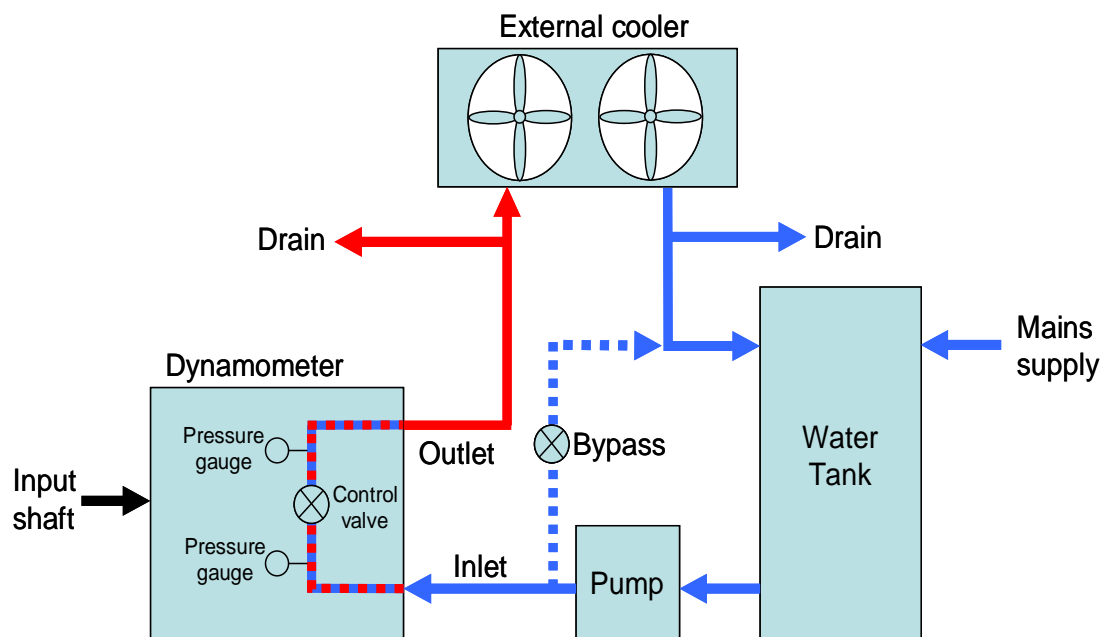


Figure 3-3: Dynamometer water circuit

The water is pumped to the dynamometer by an Ingersoll-Dresser pump, capable of supplying 200 litres per minute at 3.44 bar. A bypass valve located at the pump outlet allows pumped water to be directly fed back into the reservoir. This is used to control the water delivery pressure to the dynamometer. At the inlet to the dynamometer the water pressure is measured by a WIKA pressure gauge, visible to the operator.

Under normal operating conditions the inlet pressure is maintained at just below 1 bar gauge. The pressure drop across the dynamometer can be controlled by the operator via a valve located on the exterior of the dynamometer. Opening the valve reduces the inlet pressure and increases outlet pressure, whilst closing the valve restricts the flow causing the inlet pressure to rise and the outlet pressure to drop. The outlet pressure is also measured via a WIKA pressure gauge visible to the operator. On exiting the dynamometer the water is pumped to a Guntner cooler unit, located externally above the test cell roof. The cooled water is then returned to the water tank. Although the system greatly reduces the temperature of the water during periods of extended running, at design point conditions the water temperature in the reservoir can be seen to rise. When this occurs valves can be opened which cause a proportion of the water to be drained. This can be done before or after the cooler. The lost water is replaced automatically by mains water which fills the tank when a level switch is activated.

The rig drive train consists of a modified Gnome engine reduction gearbox with a modified oil feed system. The main features of the gearbox are shown in Figure 3-4. The power output shaft of TSW rig is connected to the gearbox via a polygon coupling. This directly turns a high speed shaft rotating at the test rig speed design speed of

10630 rpm. The high speed shaft is connected via helical gears to an intermediate speed shaft. This shaft includes the drive for the gearbox oil pump.

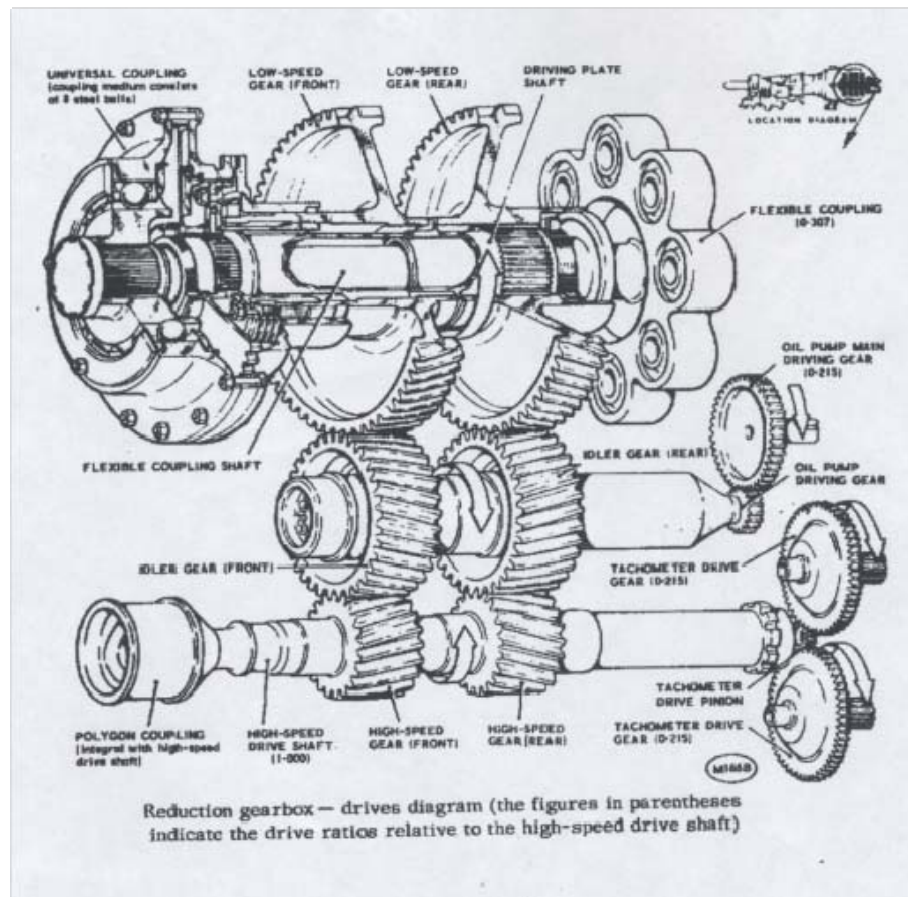


Figure 3-4: Gnome reduction gearbox internals, Stefanis (2007)

The intermediate shaft in turn is connected to the low speed shaft, the output of which is connected to the dynamometer via a flexible coupling. The gearbox gives a reduction ratio of 3.25:1, giving an output speed of approximately 3270 rpm when the TSW rig is at its design speed of 10630 rpm. The dynamometer is required to absorb approximately 400 kW of power from the TSW rig.

Figure 3-5 shows the external oil circuit used to feed the gearbox during operation. Oil is drawn from a external tank by the internal gearbox pump. Once the oil has passed through the internal cooling circuit of the gearbox the oil is pumped to an external oil to water heat exchanger. From here the oil is returned to the oil tank reservoir. The

reservoir includes a breather which vents through a vapour extractor to atmosphere. By metering the flow rate of mains water to the heat exchanger the rig operator can control the temperature of the gearbox oil feed, to keep it at an optimum of $\approx 50^{\circ}\text{C} - 70^{\circ}\text{C}$.

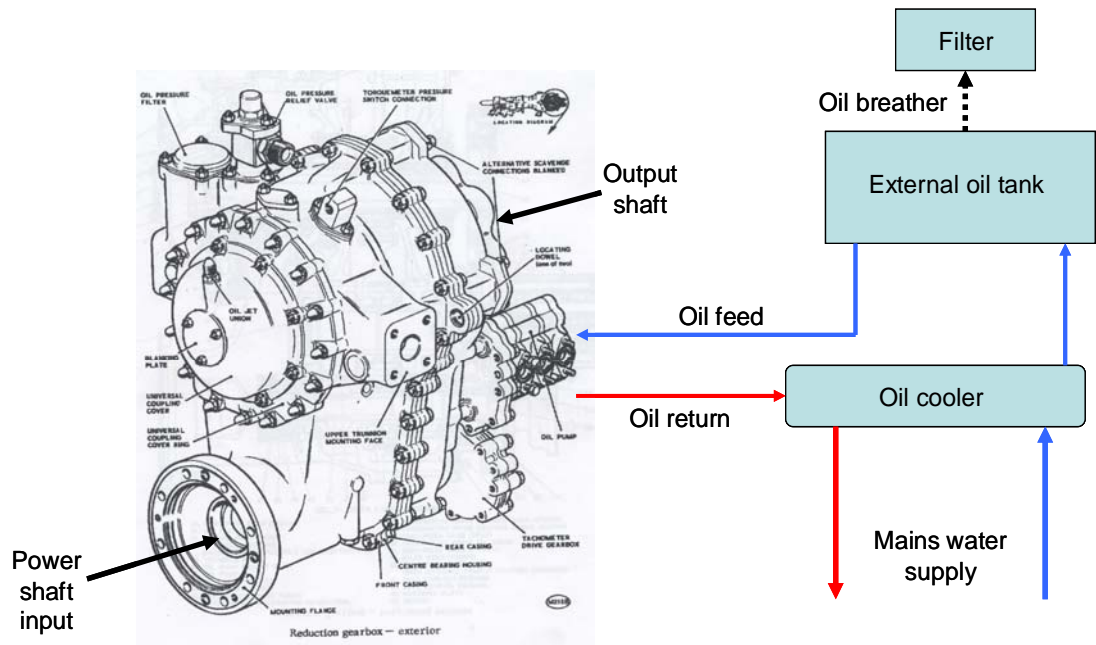


Figure 3-5: Gnome gearbox external oil circuit (Courtesy of Rolls-Royce plc)



Figure 3-6: TSW facility test cell arrangement

Figure 3-6 shows the test facility cell arrangement, where the features described in this section are highlighted.

3.5 Test Rig Internal Components and Systems

Figure 3-7 shows a cross section of the TSW rig. Although many features of the rig have not been labelled, an overview of the major components is given in order to provide descriptions of features which are shown in more detail later in this chapter. The inlet nose cone is located at the intake to the rig. The nose cone provides protection for the telemetry unit which is mounted on the front end of the main shaft and also directs the inlet flow to the main annulus. The telemetry unit which transmits the rotating frame temperatures to the data acquisition system is insulated from the main annulus air temperature by a section of Rohacell. The front end of the rig shaft is supported by a bearing, referred to as the upstream bearing. A blown seal located downstream of the telemetry unit provides cooling air to the unit and prevents the escape of test section air. The test section air supply enters the rig across the main annulus through a number of supply struts. The test section of the rig consists of a rotating assembly, which has two rotor blade rows, and a stationary section consisting of two NGV rows.

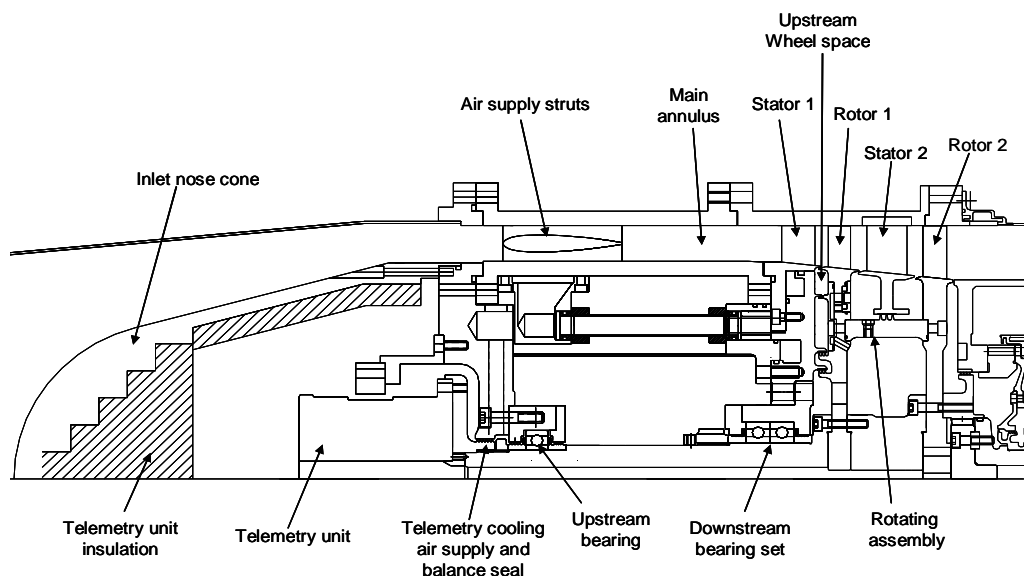


Figure 3-7: Cross section of TSW test facility

3.5.1 Test Section Air Supply Paths

Figure 3-8 shows the air supply paths to the test section of the rig. The main annulus flow is represented by a red arrow. The main annulus flow rate at design speed is between 4.6 kgs^{-1} and 4.8 kgs^{-1} . At the leading edge of stator 1 the inlet total air temperatures T_{INLET} varied over the range $155 \leq T_{\text{INLET}} \leq 167 \text{ }^{\circ}\text{C}$. The inlet total pressures P_{INLET} varied over the range $2.830 \leq P_{\text{INLET}} \leq 2.927 \text{ bar abs}$. This variation is the result of the atmospheric conditions seen over the test period and the effect on DART operating parameters from run to run. The cooling flow delivery to the test section is shown by a blue arrow. Cooling air flow is delivered to the test section at flow rates of between 29.8 gs^{-1} and 75.8 gs^{-1} corresponding to partial disc entrainment rates of $0.7 \leq C_{w,\text{ent}} \leq 1.44$. The cooling air entry temperature measured at mp013, a thermocouple measurement location defined in Table 3-4, varied over the range $41.8 \leq \text{mp013} \leq 65.6 \text{ }^{\circ}\text{C}$. The path through the test section is shown in greater detail in section 3.6.

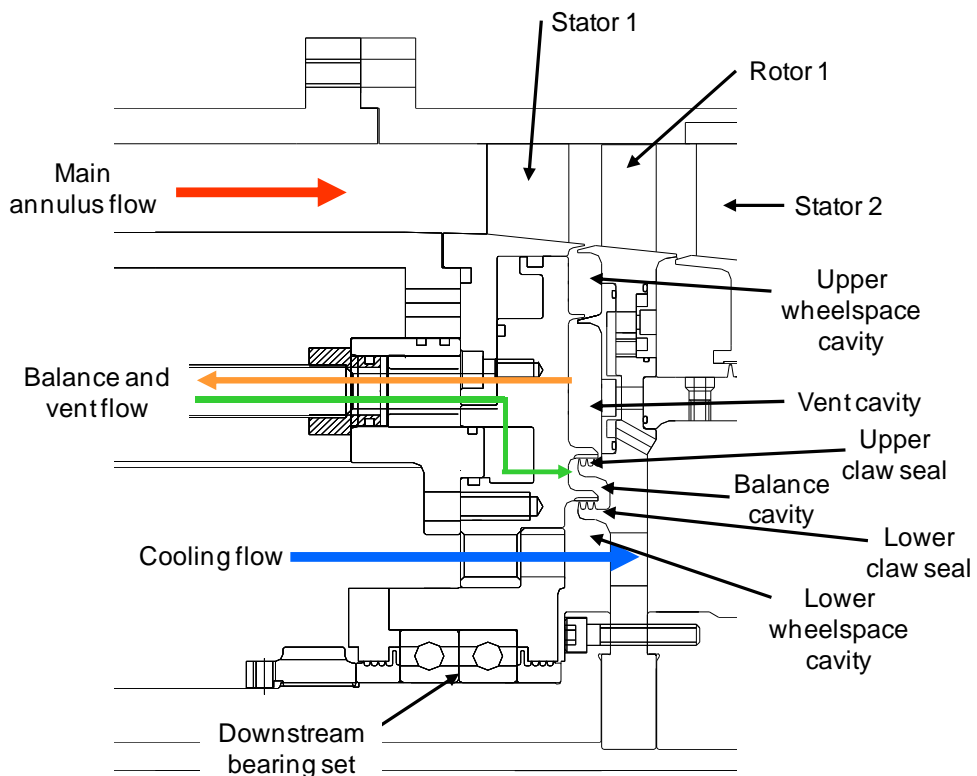


Figure 3-8: TSW facility test section air supply paths

Figure 3-8 shows the air systems within the upstream wheelspace used to ensure the cooling flow reaches the test section at the required flow rate. A pressure balance between the lower wheelspace cavity and balance cavity is required to achieve this. The balance cavity can be supplied with air whilst the vent cavity can have flow removed. These flow paths are shown by the orange and green arrows. By close control of these flow rates it is possible to balance the pressures in the wheelspace to control the pressure difference across the two claw seals. This often involves a trade off in terms of air being egressed from the upper wheelspace cavity into the main annulus or main annulus air being ingested into the upstream wheelspace. The control of these flows and the effects on the wheelspace conditions are discussed in greater detail in chapter 4.

3.6 Test Section Features

Figure 3-9 shows the main features of the TSW rig test section. This area of the rig contains the most highly instrumented features and the geometries of interest. Cooling flow enters the test section from the lower wheelspace cavity and passes through eight coolant passage holes in rotor one to the lower supply cavity. From here the cooling air is supplied to the upstream stator well by one of two methods. The cooling air can either be passed directly through the drive arm via drive arm holes, or the cooling air can be passed through simulated lock plates in the Rotor 1 disc. The upstream cavity consists of the boundary created by the forward face of the stator foot, the drive arm, the upstream entrance of the interstage labyrinth seal, the Rotor 1 disc and the upstream rim seal. The air contained within the upstream stator well will pass through the upstream rim seal and interstage labyrinth seal at a given rate determined by rig operating conditions, rig geometry and fluid properties. Air exchanged through the upstream rim seal will interact with the main annulus flow, whilst air passing through

the interstage labyrinth seal will enter the downstream wheelspace. The downstream wheelspace is defined by the boundaries of the rear face of the stator foot, the exit of the interstage labyrinth seal, the drive arm and the upstream face of the Rotor 2 disc. Air which enters the downstream stator well will tend to flow through the downstream rim seal into the main annulus. Figure 3-10 gives the major dimensions of the test section in terms of the main annulus outer radius h . Figure 3-11 gives the major stator well dimensions in terms of the rotor stator spacing s . Quantitative test facility geometry is given in Appendix A. The journal publication by Eastwood et al (2012) is included in Appendix C.

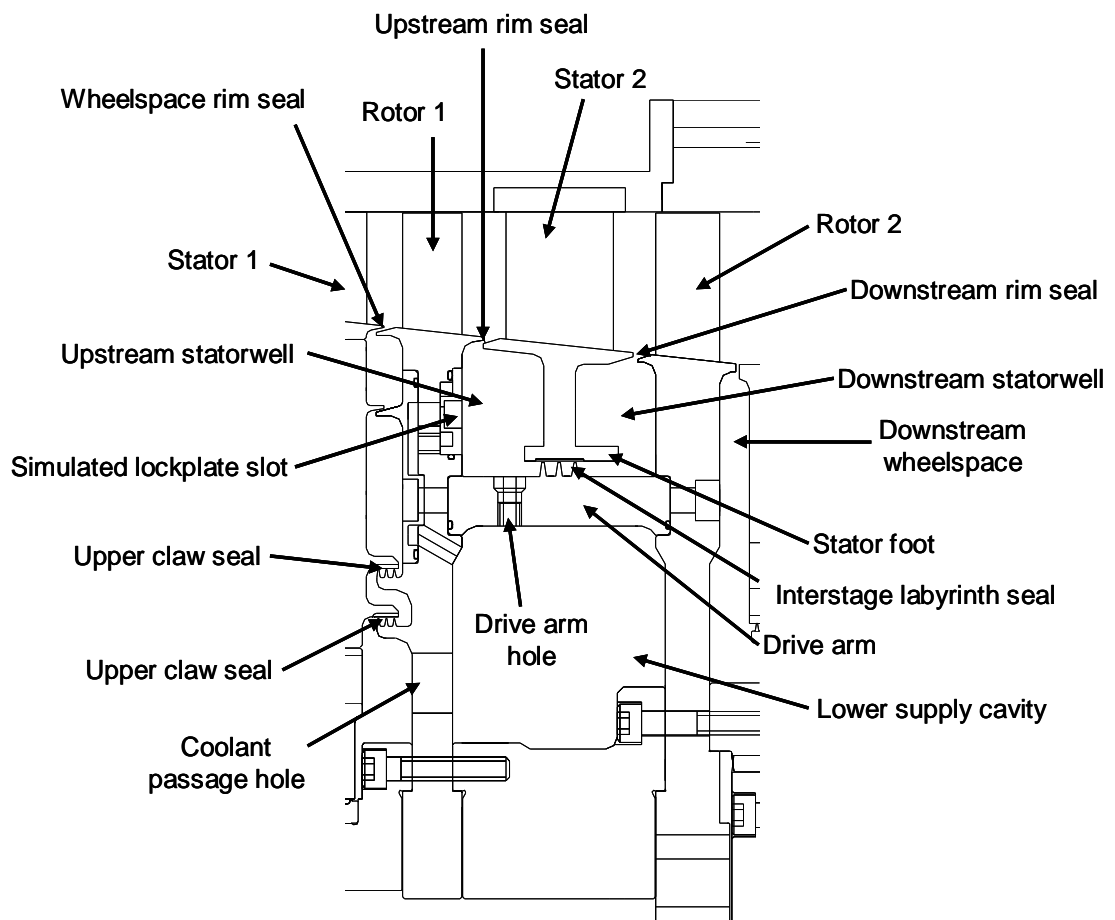


Figure 3-9: Test section main features

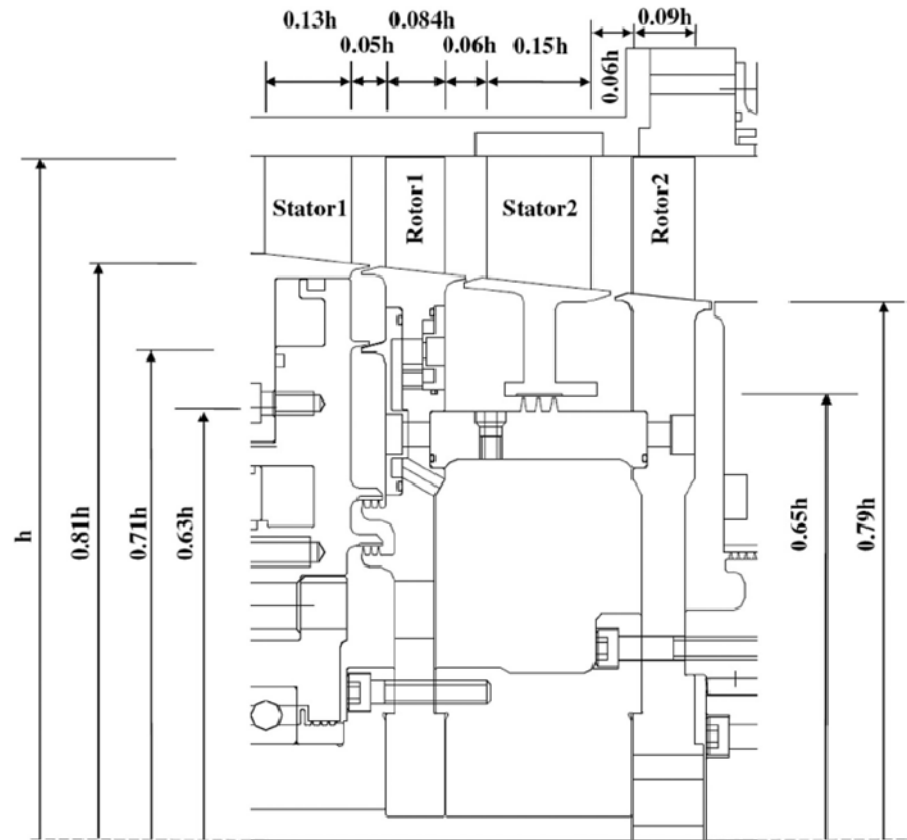


Figure 3-10: Major test section dimensions in terms of main annulus outer radius h , Eastwood (2012)

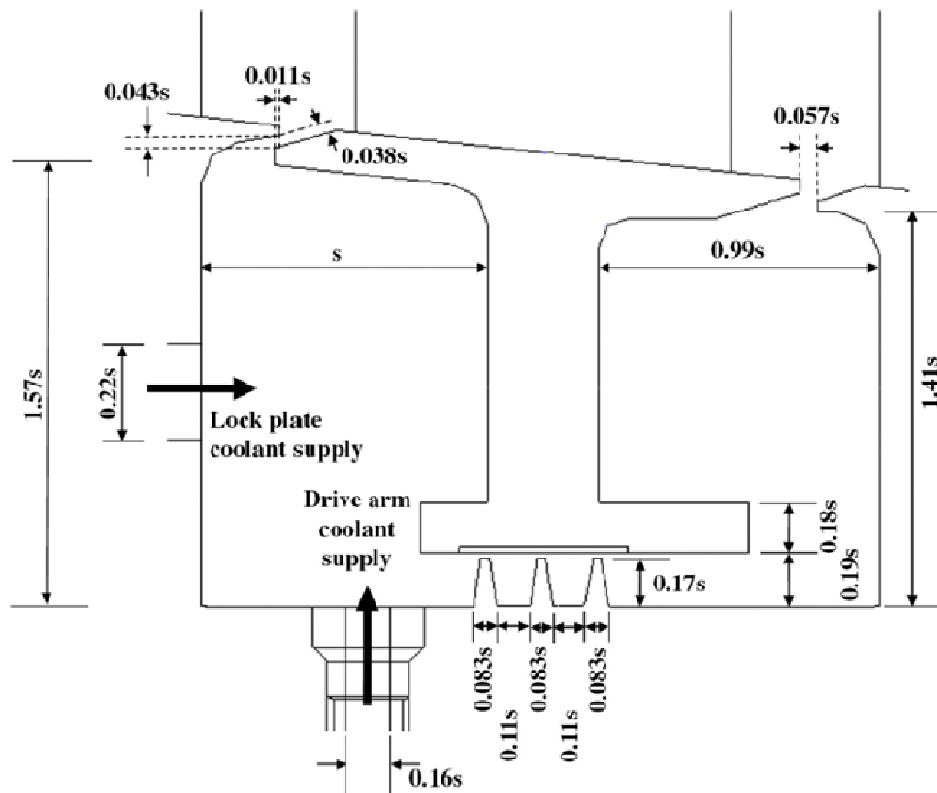


Figure 3-11: Stator well dimensions in terms of the rotor stator spacing s , Eastwood (2012)

3.7 Coolant Delivery Geometries

The design of the TSW rig allows the rapid re-configuration of the coolant supply paths to the upstream stator well. The coolant supply geometries fall into the two main categories of drive arm insert geometries and lock plate slot geometries. The test section supply path for drive arm geometries is shown in Figure 3-12. This represents the general coolant supply path. The supply path can be altered by varying the number and circumferential spacing between the drive arm inserts. The effect of these changes was studied as part of the Phase 1 test matrix. The exit angle of the coolant from the inserts can also be altered. The effect of the coolant supply angles was studied as part of the Phase 2 test matrix. The drive arm geometries studied are summarised in Table 3-1.

The general test section supply path for the lock plate slot geometries is shown in Figure 3-13. As with the drive arm geometries the coolant supply through the lock plate can be varied by altering the number and circumferential spacing between the lock plate slots. The lock plate supply geometries studied as part of the Phase 1 test matrix are shown in Table 3-2.

In addition to the drive arm and lock plate slot geometries a third geometry type was studied as part of phase 2 testing, shown in Figure 3-14. This consists of an annular ring within the upstream stator well, referred to as a "deflector plate". The plate is attached to the foot via spacers which allows flow to pass to the rear of the plate. The geometry was developed in order to try to encourage coolant to become entrained by the rear face of rotor 1 rather than directly feeding the interstage seal flow. The deflector plate was run with both the 39 and 26 drive arm inserts previously tested as

part of the Phase 1. This geometry arose as a result of the CFD studies carried out by industrial partners of the Phase 1 data which suggested that the feature could encourage entrainment of coolant on to the Rotor 1 surface.

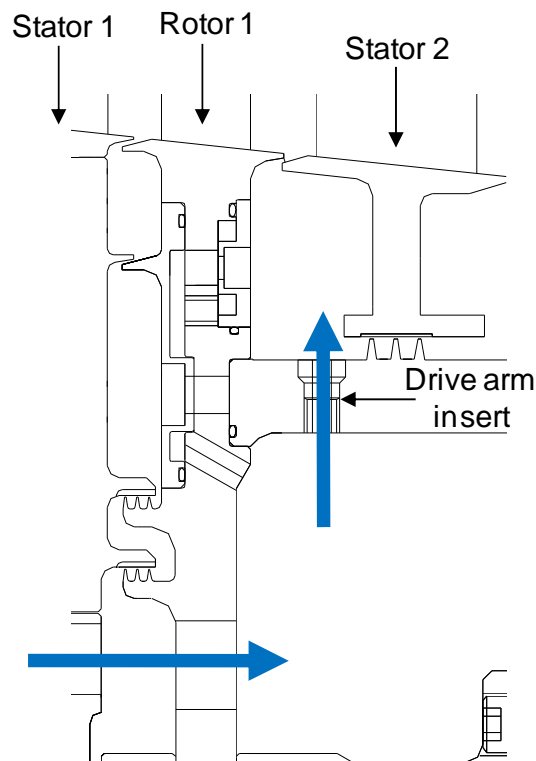


Figure 3-12: Drive arm coolant supply path

Test Phase	Geometry no.	Inserts	Flow area (mm ²)	Circumferential spacing (deg)	Insert design
1	1	39	314	9.23	
	2	26	209	13.85	
	3	13	104	27.70	
2	1	39	162	9.23 (Angled axially 25° towards rotor 1 downstream face)	
	2	39	162	9.23 (Angled circumferentially 25°)	

Table 3-1: Drive arm coolant delivery geometries

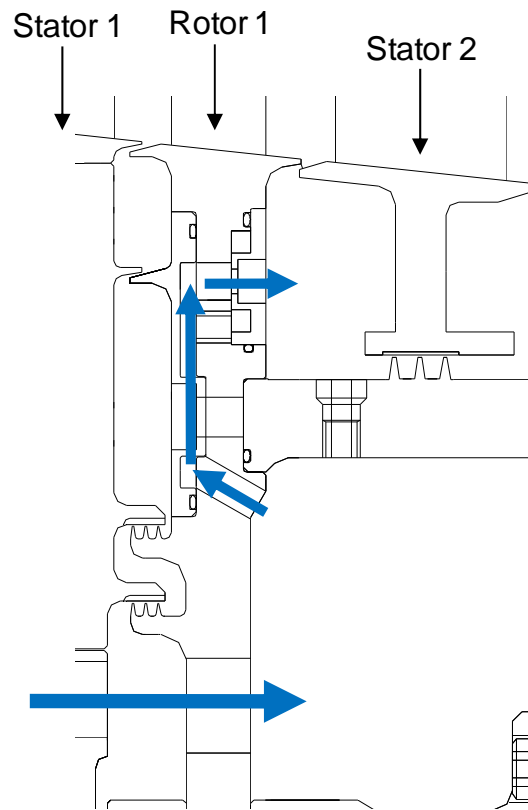


Figure 3-13: Lock plate slot delivery path




Test Phase	Geometry no.	Lock plate slots	Flow area (mm ²)	Circumferential spacing (deg)	Lock plate design
1	1	39	70.2	9.23	
	2	26	46.8	13.85	
	3	13	23.4	27.70	

Table 3-2: Lock plate slot geometries

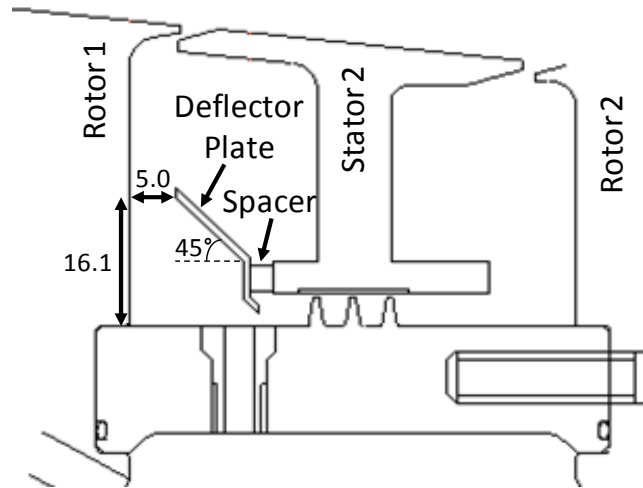


Figure 3-14: Deflector plate geometry

3.8 Rotor Blades and NGV Geometry

Table 3-3 gives a summary of the blades and NGVs shown in Figure 3-7. More detailed quantitative information for the main annulus geometry is given in Appendix A.

	Stator 1	Rotor 1	Stator 2	Rotor 2
Pitch/Chord	0.6806	0.7791	0.7301	0.7512
Height/Axial Chord	1.199	2.188	1.233	2.568
Inlet Mach number	0.1885	0.2763	0.2570	0.3014
Exit Mach number	0.6563	0.6001	0.6529	0.6143
Blade relative inlet flow angle (°)	0.00	36.68	19.02	23.32
Blade relative exit flow angle (°)	70.07	65.36	64.60	59.33

Table 3-3: Blade and NGV geometry, Stefanis (2007)

3.9 Test Facility Design Point Summary

Throughout this thesis reference will be made to "design point" or "test point" operation. This refers to the test facility reaching a steady state condition at which settled test data can be taken. A summary of the target operating conditions is given in Table 3-4. Control of the test facility to achieve these conditions is discussed in Chapter 5.

Parameter	Test Point Condition
Rotational Speed (rpm)	10630
Power Output (kW)	<400
Main Annulus Flow Rate (kg s^{-1})	4.8
Cooling Flow Rate (kg s^{-1})	0.03 - 0.075
Test Section Inlet Temperature (K)	430 - 440
Test Section Inlet Pressure (bar abs)	2.9
Test Section Pressure Ratio	2.7:1

Table 3-4: Facility Design Point Conditions Summary

3.10 Temperature Measurements

A total of 154 separate temperature measurements can be made in the TSW rig. This section will describe the measurements which are taken on the major rig components. These measurements relate directly to the research being undertaken. Other measurements are not included here. These relate to the monitoring of rig operational conditions such as bearing and telemetry unit temperatures as well as various points within the coolant delivery path. Although these are of high importance with regards to the rig operation and monitoring inlet conditions they do not offer direct measurements of test section temperatures and so are excluded from this section. The stationary components of the test section contain 73 K-type thermocouples at various locations including both metal and air temperature measurements. Figure 3-15 shows the measurements locations relating to Stator 1. Metal temperatures are shown as light blue, air temperatures as green.

Table 3-5 gives the measurement location co-ordinates, where the axial datum is taken from the leading edge of the first NGV row. Measurements taken at mp009 and mp013 give the coolant delivery temperature to the test section. The measurement locations which run up the face of Stator 1 give temperature measurements relating to each of the cavities of the upstream wheelspace. The measurement point mp008 gives the metal temperature at the foot of the first NGV row.

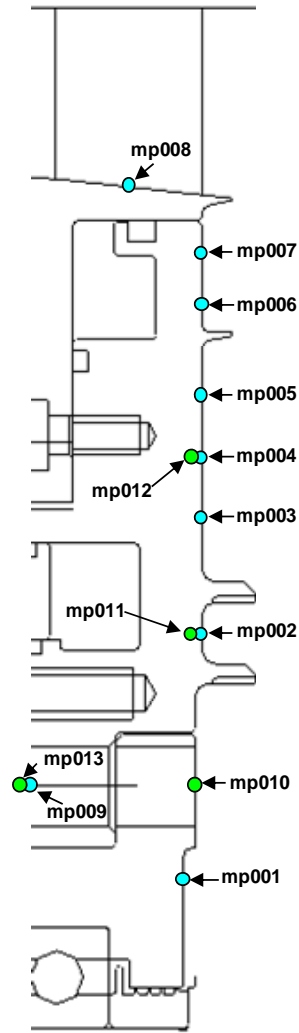


Figure 3-15: Stator 1 temperature measurements

Label	Measurement	Axial (mm)	Radial (mm)	Circumferential (deg)
mp001	Metal temp	19.32	47	130
mp002	Metal temp	22.32	84.14	250
mp003	Metal temp	22.32	101.59	255
mp004	Metal temp	22.32	110.25	313
mp005	Metal temp	22.32	118.91	325
mp006	Metal temp	22.32	133.59	340
mp007	Metal temp	22.32	142.59	338
mp008	Metal temp	11.18	151.11	114
mp009	Metal temp	-7.18	60	235
mp010	Air temp	21.32	60	135
mp011	Air temp	22.32	84.14	241
mp012	Air temp	22.32	110.25	305
mp013	Air temp	-7.18	60	230

Table 3-5: Stator 1 temperature measurement locations

Figure 3-16 shows the temperature measurements taken at Stator 2; coordinates are given in Table 3-6. The measurement locations are positioned to monitor the metal and air temperatures relating to both the upstream and downstream stator well cavities.

Measurements are taken of the metal temperatures in the main annulus above each of the stator well rim seals. The locations also provide information on the upstream and downstream interstage seal conditions.

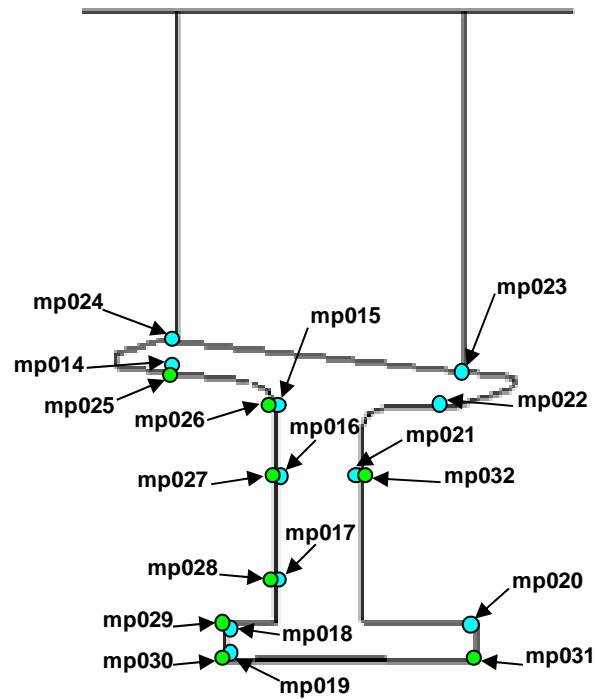


Figure 3-16: Stator 2 temperature measurements

Label	Measurement	Axial (mm)	Radial (mm)	Circumferential (deg)
mp014	Metal temp	56.97	143.13	110
mp015	Metal temp	66.43	139.41	115
mp016	Metal temp	66.43	132.11	116
mp017	Metal temp	66.43	120.8	117
mp018	Metal temp	62.02	119.3	230
mp019	Metal temp	62.02	115.3	234
mp020	Metal temp	84.85	119.3	252
mp021	Metal temp	74.43	132.11	118
mp022	Metal temp	82.68	139.88	112
mp023	Metal temp	83.9	143.23	232
mp024	Metal temp	56.97	146.15	227
mp025	Air temp	56.97	143.13	247
mp026	Air temp	66.43	139.41	113
mp027	Air temp	66.43	132.11	250
mp028	Air temp	66.43	122.53	250
mp029	Air temp	62.02	119.3	250
mp030	Air temp	62.02	115.55	115
mp031	Air temp	84.85	115.55	115
mp032	Air temp	74.43	132.11	249

Table 3-6: Stator 2 temperature measurement locations

The rotating assembly contains 81 K-type thermocouples. The measurement locations relating to Rotor 1 are shown in Figure 3-17. The co-ordinates of the measurement locations are given in Table 3-7. The locations chosen provide measurements of the coolant delivery temperature at the inlets to the coolant delivery geometries. The locations also provide measurements of the radial temperature gradient on the upstream face of the upstream stator well (the downstream face of Rotor 1). Due to the high rotational speed of the rotating assembly and the danger of damage to the thermocouples, each measurement location has three thermocouples in order to mitigate the danger of instrumentation losses.

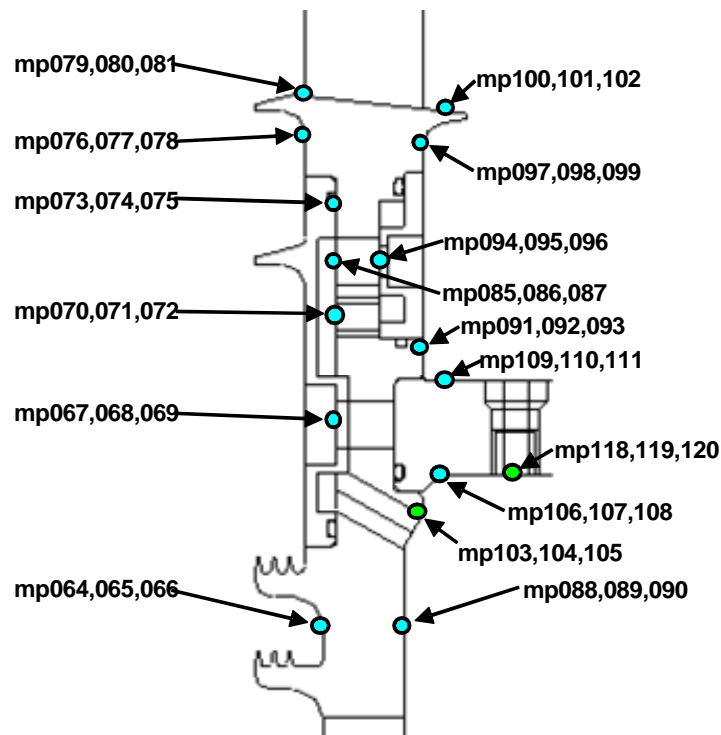


Figure 3-17: Rotor 1 temperature measurements

Figure 3-18 shows the measurement locations relating to Rotor 2. The co-ordinates of the Rotor 2 measurement locations are given in Table 3-8. The locations give the radial temperature gradient along the downstream face of the downstream stator well (the upstream face of Rotor 2). They also provide measurements of the radial temperature gradient along the downstream face of Rotor 2. As with the Rotor 1 measurement

locations, each location has three thermocouples in order to mitigate the risk of instrumentation losses.

Label	Measurement	Axial (mm)	Radial (mm)	Circumferential (deg)
mp064	Metal temp	33.711	79.45	252.25
mp065	Metal temp	33.711	79.45	258.85
mp066	Metal temp	33.711	79.45	261.475
mp067	Metal temp	35.32	106.29	90
mp068	Metal temp	35.32	106.29	90
mp069	Metal temp	35.32	106.29	90
mp070	Metal temp	35.32	118.79	5
mp071	Metal temp	35.32	118.79	5
mp072	Metal temp	35.32	118.79	5
mp073	Metal temp	35.32	134.26	13.846
mp074	Metal temp	35.32	134.26	13.846
mp075	Metal temp	35.32	134.26	13.846
mp076	Metal temp	31.32	143.98	65.192
mp077	Metal temp	31.32	143.98	68.05
mp078	Metal temp	31.32	143.98	69.583
mp079	Metal temp	31.32	148.93	292.55
mp080	Metal temp	31.32	148.93	290.433
mp081	Metal temp	31.32	148.93	287.158
mp082	Metal temp	35.32	118.79	250
mp083	Metal temp	35.32	118.79	250
mp084	Metal temp	35.32	118.79	250
mp085	Metal temp	35.32	127.5	225
mp086	Metal temp	35.32	127.5	225
mp087	Metal temp	35.32	127.5	225
mp088	Metal temp	43.92	79.45	100
mp089	Metal temp	43.92	79.45	100
mp090	Metal temp	43.92	79.45	100
mp091	Metal temp	46.2	115.79	154.858
mp092	Metal temp	46.2	115.79	151.6
mp093	Metal temp	46.2	115.79	137.992
mp094	Metal temp	40.82	127.5	160
mp095	Metal temp	40.82	127.5	160
mp096	Metal temp	40.82	127.5	160
mp097	Metal temp	46.2	142.39	69.992
mp098	Metal temp	46.2	142.39	68.517
mp099	Metal temp	46.2	142.39	65.425
mp100	Metal temp	49.03	147.01	293.542
mp101	Metal temp	49.03	147.01	290.208
mp102	Metal temp	49.03	147.01	284.55
mp103	Air temp	45.07	91.802	250
mp104	Air temp	45.07	91.802	250
mp105	Air temp	45.07	91.802	250
mp106	Metal temp	49.2	99.247	104
mp107	Metal temp	49.2	99.247	104
mp108	Metal temp	49.2	99.247	104
mp109	Metal temp	49.2	111.8	316.033
mp110	Metal temp	49.2	111.8	319.925
mp111	Metal temp	49.2	111.8	313.008
mp118	Air temp	58.05	99.286	335
mp119	Air temp	58.05	99.286	335
mp120	Air temp	58.05	99.286	335

Table 3-7: Rotor 1 temperature measurement locations

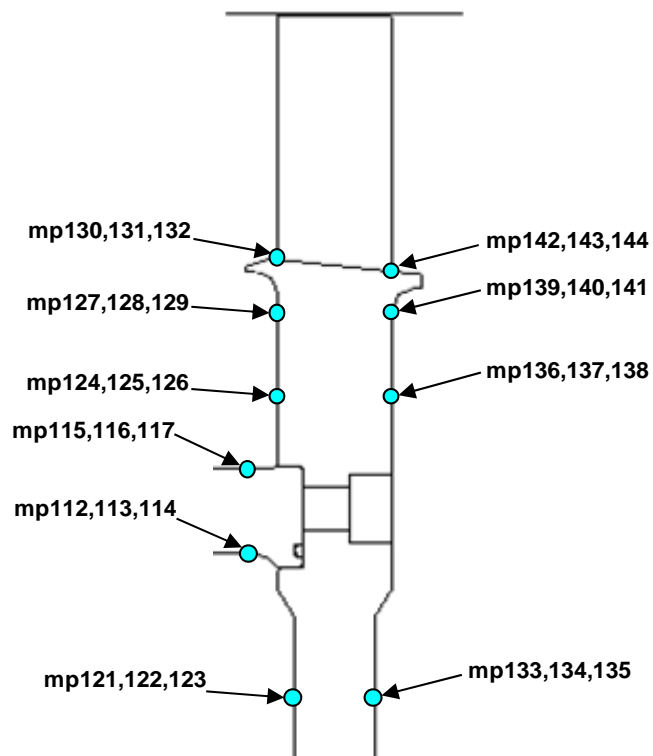


Figure 3-18: Rotor 2 temperature measurements

Label	Measurement	Axial (mm)	Radial (mm)	Circumferential (deg)
mp121	Metal temp	97.22	77.61	332
mp122	Metal temp	97.22	77.61	332
mp123	Metal temp	97.22	77.61	332
mp124	Metal temp	94.67	119.99	43.925
mp125	Metal temp	94.67	119.99	45.583
mp126	Metal temp	94.67	119.99	50.62
mp127	Metal temp	94.67	133.99	135.183
mp128	Metal temp	94.67	133.99	140.158
mp129	Metal temp	94.67	133.99	134.692
mp130	Metal temp	94.67	142.07	227.283
mp131	Metal temp	94.67	142.07	222.325
mp132	Metal temp	94.67	142.07	231.45
mp133	Metal temp	108.31	77.61	315
mp134	Metal temp	108.31	77.61	315
mp135	Metal temp	108.31	77.61	315
mp136	Metal temp	110.66	119.99	45
mp137	Metal temp	110.66	119.99	45
mp138	Metal temp	110.66	119.99	45
mp139	Metal temp	110.66	133.99	136.65
mp140	Metal temp	110.66	133.99	141.617
mp141	Metal temp	110.66	133.99	132.217
mp142	Metal temp	110.66	140.34	228.75
mp143	Metal temp	110.66	140.34	226.133
mp144	Metal temp	110.66	140.34	223.383

Table 3-8: Rotor 2 temperature measurement locations

Figure 3-19 shows the temperature measurement locations relating to the main annulus. The co-ordinates of the measurement locations are given in Table 3-9. Metal temperatures are taken at the inlet and exit of each NGV and blade row. Total air temperatures are taken at the inlet and exit of each NGV row and at the test section exit. The total air temperatures are shown as orange dots. The thermocouples used for the total air measurements taken in front of the NGVs are routed through the NGV so are given with both a circumferential co-ordinate and a relating NVG blade number. The installation of the instrumentation is shown in detail in chapter 4.

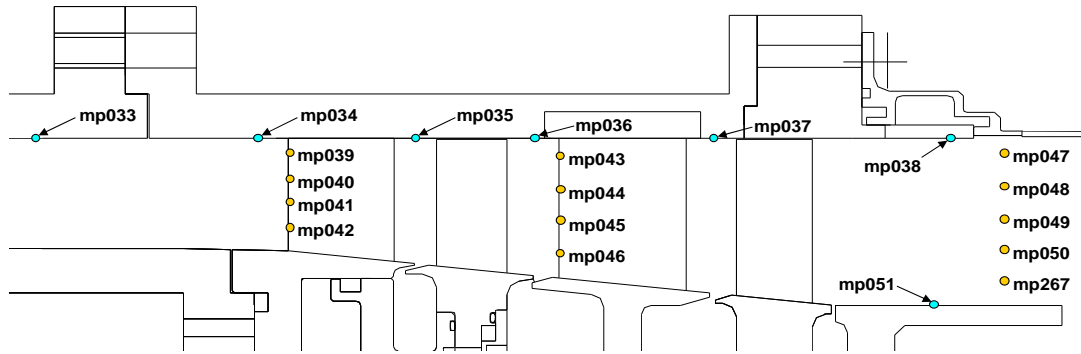


Figure 3-19: Main annulus temperature measurements

Label	Measurement	Axial (mm)	Radial (mm)	Circumferential (deg)
mp033	Metal temp	-52.18	178	210
mp034	Metal temp	-5	178	210
mp035	Metal temp	26.34	178	210
mp036	Metal temp	51.18	178	210
mp037	Metal temp	89.04	178	210
mp038	Metal temp	143.87	178.35	10
mp039	Total air temperature	0	173	144 (Blade 16)
mp040	Total air temperature	0	168	144 (Blade 16)
mp041	Total air temperature	0	163	144 (Blade 16)
mp042	Total air temperature	0	158	144 (Blade 16)
mp043	Total air temperature	56.97	172.5	227 (Blade 25)
mp044	Total air temperature	56.97	167	227 (Blade 25)
mp045	Total air temperature	56.97	161.5	227 (Blade 25)
mp046	Total air temperature	56.97	156	227 (Blade 25)
mp047	Total air temperature	150.66	172	47
mp048	Total air temperature	150.66	166	47
mp049	Total air temperature	150.66	160	47
mp050	Total air temperature	150.66	154	47
mp051	Metal temp	139.54	139.8	4
mp267	Total air temperature	150.66	145.7	47

Table 3-9: Main annulus temperature measurement locations

3.11 Test Section Pressures Measurements

Figure 3-20 shows the static pressure measurements taken along the face of Stator 1. The co-ordinates of the measurement locations are given in Table 3-10. The upstream wheelspace, of which Stator 1 makes up the upstream face, is balanced under operational conditions in order to ensure the coolant is delivered to the test section as required and to limit the ingress of hot main annulus gasses. The wheelspace includes a balancing flow inlet and a vent which exits through the face of Stator 1. The pressure measurements are critical to this task. This is discussed in detail in Chapter 4.

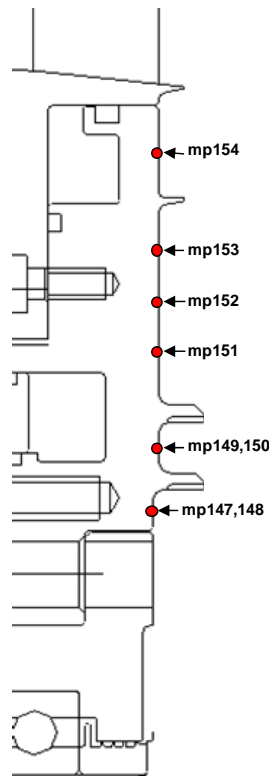


Figure 3-20: Stator 1 pressure measurements

Label	Measurement	Axial (mm)	Radial (mm)	Circumferential (deg)
mp147	Static pressure	21.32	72.83	271
mp148	Static pressure	21.32	72.83	90
mp149	Static pressure	22.32	84.14	280
mp150	Static pressure	22.32	84.14	105
mp151	Static pressure	22.32	101.59	60
mp152	Static pressure	22.32	110.25	80
mp153	Static pressure	22.32	118.91	73
mp154	Static pressure	22.32	138.09	286

Table 3-10: Stator 1 pressure measurement locations

Figure 3-21 shows the pressure measurement locations relating to Stator 2. The coordinates of the measurement locations are given in Table 3-11. The measurements give information relating to the upstream and downstream stator wells as well as the upstream and downstream conditions of the interstage seal. A number of the pressure measurement locations are also used during the gas concentration experiments in order to pipe gas out of the rig to the gas analyser equipment, indicated by an asterisk in Table 3-11. This operation is covered in detail in chapter 4.

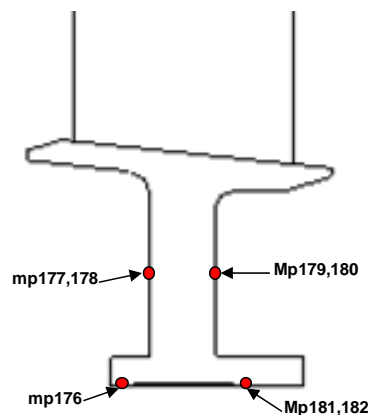


Figure 3-21: Stator 2 pressure measurements

Label	Measurement	Axial (mm)	Radial (mm)	Circumferential (deg)
mp176	Static pressure	63.06	115.55	264
mp177*	Static pressure	66.43	130.11	235
mp178*	Static pressure	66.43	130.11	131
mp179*	Static pressure	74.43	130.11	227
mp180*	Static pressure	74.43	130.11	126
mp181*	Static pressure	77.81	115.55	189
mp182*	Static pressure	77.81	115.55	96

Table 3-11: Stator 2 pressure measurement locations

Figure 3-22 shows the pressure measurements made in the main annulus. The coordinates of the measurement locations are given in Table 3-12. Static pressure measurements are made around the circumference of the rig between each NGV and blade row. Total pressure measurements are made at the leading edge of each NVG row and at the exit to the test section. The total pressure measurements are shown as purple dots. The locations of the total pressure measurements are given with both a circumferential location and a blade number relating to the blade through which the pressure tap is led out of the rig.

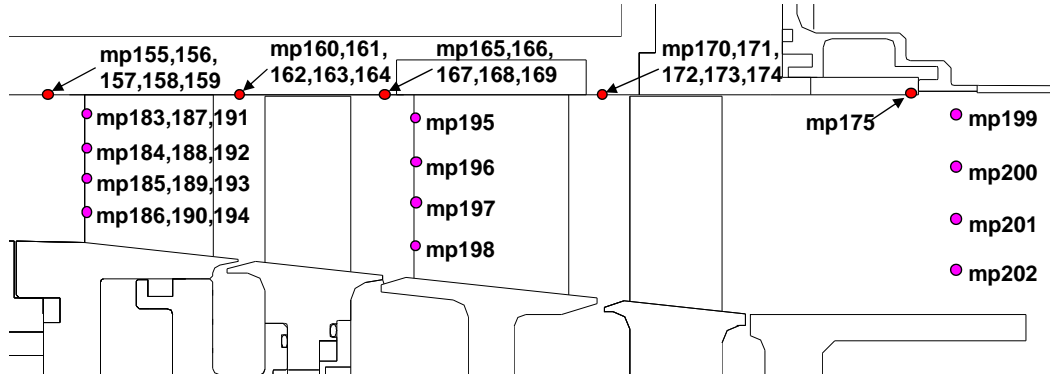


Figure 3-22: Main annulus pressure measurements

Label	Measurement	Axial (mm)	Radial (mm)	Circumferential (deg)
mp155	Static pressure	-5	178	3
mp156	Static pressure	-5	178	80
mp157	Static pressure	-5	178	152
mp158	Static pressure	-5	178	224
mp159	Static pressure	-5	178	296
mp160	Static pressure	26.34	178	8
mp161	Static pressure	26.34	178	80
mp162	Static pressure	26.34	178	152
mp163	Static pressure	26.34	178	224
mp164	Static pressure	26.34	178	296
mp165	Static pressure	51.18	178	8
mp166	Static pressure	51.18	178	80
mp167	Static pressure	51.18	178	152
mp168	Static pressure	51.18	178	224
mp169	Static pressure	51.18	178	296
mp170	Static pressure	89.04	178	8
mp171	Static pressure	89.04	178	80
mp172	Static pressure	89.04	178	152
mp173	Static pressure	89.04	178	224
mp174	Static pressure	89.04	178	296
mp175	Static pressure	143.87	178.35	0
mp183	Total pressure	0	173	10 (Blade 1)
mp184	Total pressure	0	168	10 (Blade 1)
mp185	Total pressure	0	163	10 (Blade 1)
mp186	Total pressure	0	158	10 (Blade 1)
mp187	Total pressure	0	173	134 (Blade 15)
mp188	Total pressure	0	168	134 (Blade 15)
mp189	Total pressure	0	163	134 (Blade 15)
mp190	Total pressure	0	158	134 (Blade 15)
mp191	Total pressure	0	173	276 (Blade 30)
mp192	Total pressure	0	168	276 (Blade 30)
mp193	Total pressure	0	163	276 (Blade 30)
mp194	Total pressure	0	158	276 (Blade 30)
mp195	Total pressure	56.97	172.5	240 (Blade 26)
mp196	Total pressure	56.97	167	240 (Blade 26)
mp197	Total pressure	56.97	161.5	240 (Blade 26)
mp198	Total pressure	56.97	156	240 (Blade 26)
mp199	Total pressure	150.66	172	228
mp200	Total pressure	150.66	166	228
mp201	Total pressure	150.66	160	228
mp202	Total pressure	150.66	154	228

Table 3-12: Main annulus pressure measurement locations

3.12 Control and Data Acquisition Overview

The test rig employs a range of instrumentation consisting of k-type thermocouples, various pressure sensors, platinum resistance thermometers, various flow meters, eddy current displacement sensors and gas analysers. Figure 3-23 shows a schematic of the system including the measurement source, acquisition device and the connection path to the DAQ PC for each measurement type. The left hand column of the schematic shows the measurement sources, including the stationary and rotating frame temperature measurements and pressure measurements. Other devices such as flow meters, PRTs, concentration meters and inductive rotational speed measurements are also shown. The central column of the schematic shows the data acquisition devices, which receive the signals from the measurement devices. The data acquisition (DAQ) system includes a number of devices including Serial, Ethernet and SCXI devices. The output signals from the DAQ devices are handled via a National Instruments PXI system, shown on the right in the grey column. This step in the instrumentation path amplifies and consolidates all the measurement channels to allow transmission to the data logging terminal. The 280 instrumentation channels are logged via Labview 8.5 Virtual Instrumentation, "VI" . The VI also allows real time monitoring of the rig during a test run and is discussed further in section 3.13.

The DAQ equipment is located in a test cell adjacent to the rig. This allows the devices to operate in a temperature controlled environment, whilst being sufficiently close to the rig to allow direct connection of instrumentation. The equipment is contained in two dedicated cabinets, shown in Figure 3-24, which are in turn located within a temperature controlled area containing a Challenge air conditioning unit with a heating

capacity of 3.2 kW and a cooling capacity of 3.5 kW. The full enclosure is shown in Figure 3-25.

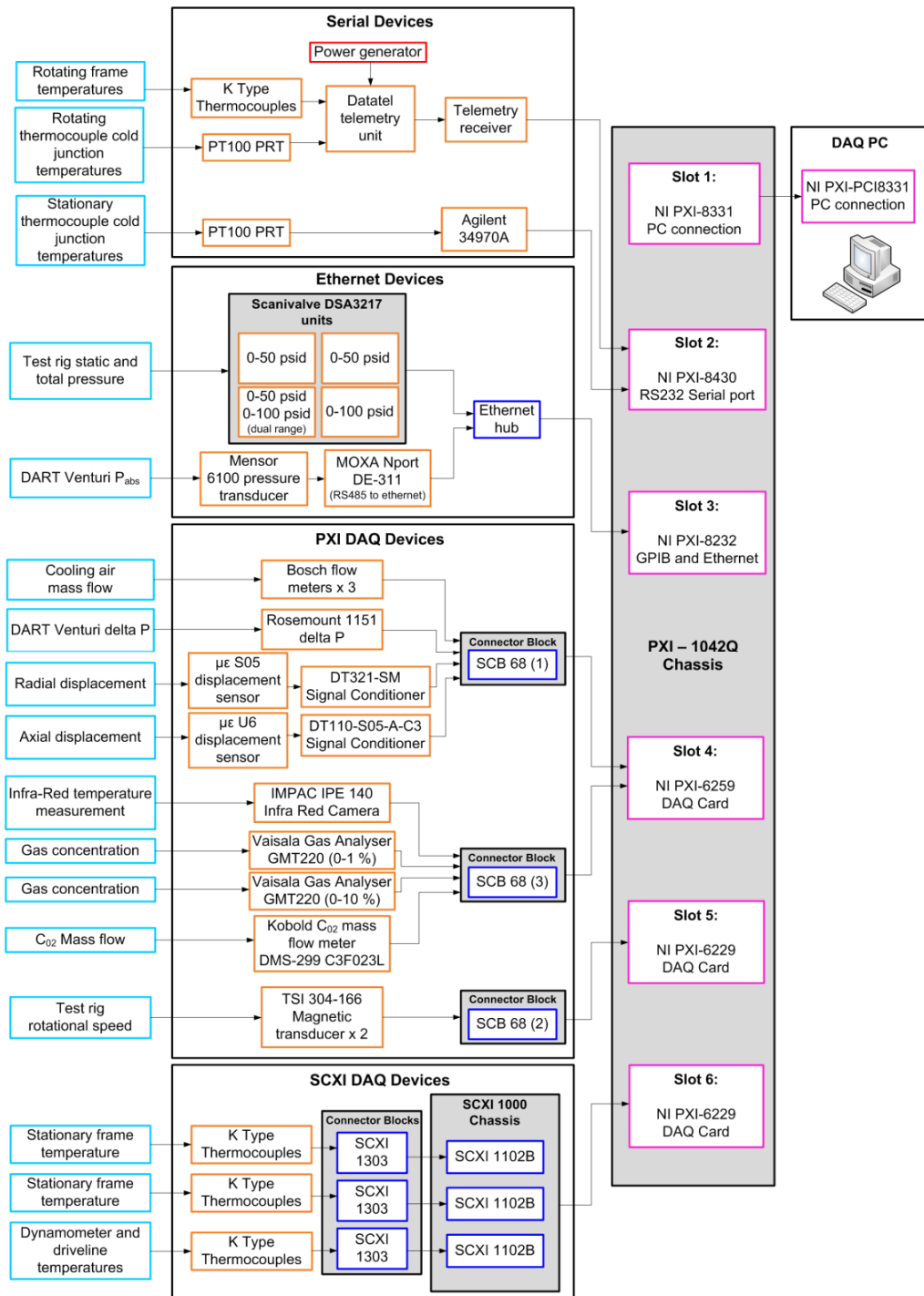


Figure 3-23: Data acquisition system, Coren et al (2010)



Figure 3-24: Temperature controlled instrumentation cabinets



Figure 3-25: Temperature controlled instrumentation enclosure

3.13 Labview VI

The primary function of the Labview VI is to provide a graphical user interface (GUI) for the operator. The design and implementation of the VI was primarily conducted by J. T. Turner and is described by Coren (2010). Figure 3-26 shows the terminal from which the operator controls the test rig and the front end of the Labview VI. This allows the operator to monitor all measurement channels and rig parameters.



Figure 3-26: Test Rig Operator Terminal

The data is logged at a frequency of 0.5 Hz allowing it to be viewed in near real time. This is of particular importance in terms of monitoring the rig bearing and lubrication systems. Figure 3-27 shows the screen arrangement of the VI; each box represents a user screen, where the screen number is given in brackets. Screen 1 allows the user to assign a test number to the data to be taken and then start the VI to initiate the logging of the test data. Once running, this screen allows the operator to monitor critical rig parameters including rotational speed, rig cooling and seal balancing flows, main annulus air supply conditions, dynamometer bearing and water temperatures, rig bearing and oil temperatures, and gearbox oil temperatures. This screen also provides the operator with instrumentation cold junction temperatures. This is particularly important for the rotating thermocouple telemetry unit. As this unit is mounted in the

inlet cone area of the rig the temperature must be closely monitored and the associated cooling flow controlled in order to keep the unit within its specified operating conditions. A summary of critical rig parameters monitored by the operator are given in Table 3-13.

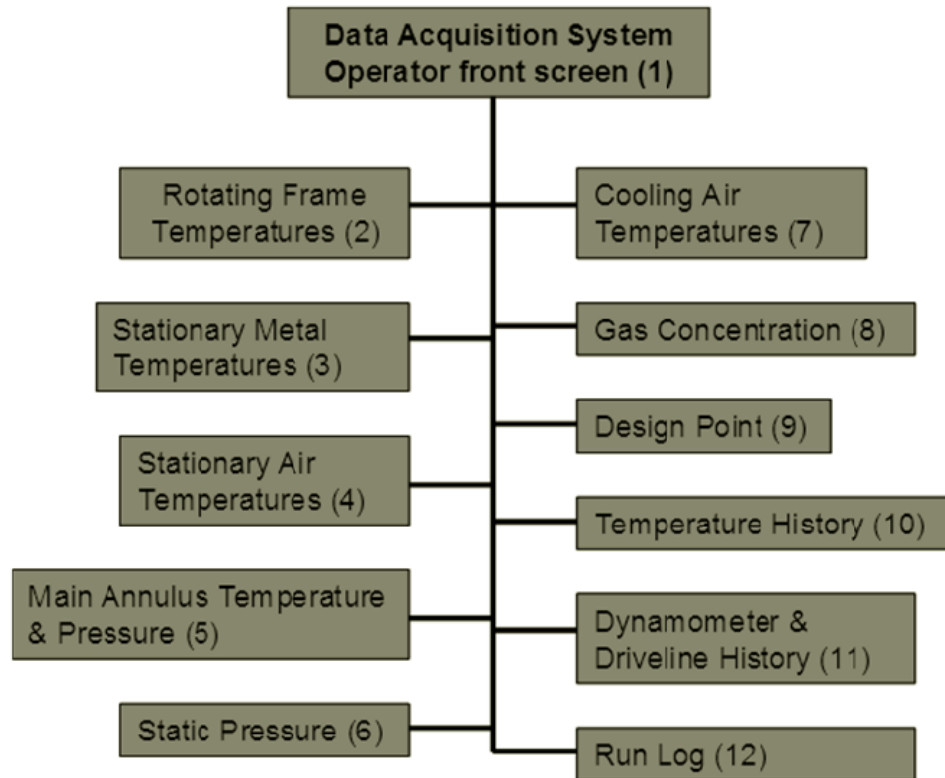


Figure 3-27: Labview VI rig operator system

Parameter	Critical Temperature (°C)
Upstream Bearing 1	≤ 110
Downstream Bearing 1	≤ 110
Downstream Bearing 2	≤ 110
Turbine Shaft Oil Supply	≤ 70
Gearbox Shaft Oil Supply	≤ 70
Dynamometer Water Supply	≤ 50

Table 3-13: Critical rig parameters

Due to the critical nature of the main parameters monitored through this screen an independent system is available to the operator. Located on this panel are the dynamometer controls which allow the rig speed to be closely controlled without the need to enter the test cell. Independent displays of rig speed and bearing temperatures

are located on the far right control panel, as seen in Figure 3-26. In the event of the Labview VI failing, these displays and controls could be used to safely shut down the rig. The front end screen is always visible to the rig operator due to the importance of the parameters which are monitored. However, the VI also has a second monitoring screen containing a number of tabs (screens 2-12 in Figure 3-27) which allows the operator to view data in more accuracy. Screen 2 shows all measured temperatures on the rotating assembly. The ability to view this data whilst running the test rig allows the operator to monitor temperatures on both faces of Rotors 1 and 2.

Screen 3 of the VI allows the operator to monitor the stationary metal temperatures in the upstream wheel space, the upstream and downstream stator well cavities and the main annulus casing. The lower radius metal temperatures in the area of the coolant entry point to the upstream wheel space are of particular interest whilst running the rig due to the influence of the surrounding metal temperature on the bearings.

Screen 4 of the VI allows the operator to monitor the stationary air temperatures within the rig. This includes temperatures in the three rotor-stator cavities as well as the coolant delivery temperature before entering the main test section of the rig. This measurement is of particular importance as it allows the heat pick up of the cooling air to be quantified before entering the main test section.

Screen 5 of the VI allows the main annulus conditions to be monitored, including both total pressure and total temperature. Each group of four measurements is taken at identical circumferential and axial positions. The four measurements are however, spread across the main annulus at four separate radial positions. This is achieved by the

measurement devices being located in the leading edge of NGV blades. The measurements are taken at both Stator 1 and 2. The total pressure measurements taken at the leading edge of Stator 1 are taken in sets of four across three blades of various circumferential locations. This allows the operator to check circumferential uniformity of the main annulus flow at the test section inlet.

Screen 6 on the VI allows the operator to monitor the static pressures within the upstream wheel space and the two stator well cavities. It also allows the operator to monitor the main annulus pressure at the outer annulus radius at each stage. The pressures in the upstream wheel space are of particular importance whilst the rig is running as these measurements indicate the sealing of the cooling air from main stream air ingress. This is a prominent part of the set up and operation of the rig, and is discussed in greater detail in Chapter 5. This screen also shows the static pressures across the front bearing/telemetry seal. These are monitored throughout the test to ensure the seal is balanced. If the telemetry unit cold junction temperatures are seen to increase to an unsatisfactory level the cooling flow to the unit can be increased.

Screen 7 of the VI allows the operator to monitor the temperature of the rig cooling air at various points on its way to the test section. Due to the rig geometry it is a feature of the rig that a substantial amount of heat pick up occurs along the cooling air system. Various heat exchangers and insulated sections of pipe are in place to reduce the effects of heat transfer to the cooling air before entry to the rig, however, the internal supply path cannot be altered. The measurements on this tab allow this to be estimated between various points along the supply path.

Screen 8 of the VI is specifically designed to allow the operator to view all instrumentation concerned with the gas concentration experiments as well as estimated cavity flow rates based on the measurements. The primary indicators based in the central panel show the measured carbon dioxide levels as percentage volume for both gas analysers, the high range instrument, GC1, having a range of 0-10%, and the low range instrument a range of 0-1%. The central panel also shows the indicated carbon dioxide flow rate and the cooling flow rate to the test section. The estimated cavity flows shown on the tab are based on simplified calculations based on the measured flow rates and measured gas concentrations. They are shown simply as indicators of flow levels whilst conducting the various gas concentration experimental procedures. The full gas concentration experimental results are post-processed and are discussed in detail in Chapter 9.

Screen 9 of the VI allows the operator to monitor the primary operating conditions of the rig in terms of non dimensional mass flow and the rig pressure ratio from inlet to exhaust. These values are plotted against the design point curve at regular intervals allowing the operator to make required changes to the main annulus supply flow until satisfactory values are reached.

Screen 10 of the VI serves two functions. The first is to provide the operator with a graphical trace of the rig temperature history during a test run. This allows the operator an overview of the rig conditions during the warm up of the rig and also indicates how settled the rig conditions are. The second function of the tab is to indicate to the operator when the data from the rig can be considered settled. When the settling conditions are met the indicators at the bottom of the tab will light up green. This

occurs when an average of the stationary and rotating temperatures changes by less than a user specified value over a given time.

Screen 11 of the VI is of particular importance to the operator during the rig warm up. The tab gives a temperature trace of the critical rig components, including bearing and lubrication fluid temperatures for the rig, gearbox and dynamometer. By viewing the temperature history of these components any unprecedented change can be far more apparent to the operator than looking at a single current value. The trace also allows the operator to make changes to the rig conditions before maximum temperatures are reached by examining temperature trends and acting before problems occur by, for example, increasing the cooling of gearbox oil, or reducing rig speed to bring down bearing temperatures. A sudden jump in temperatures on the trace could also be the first indicator that an operator would have of a component failure and allow a safe shut down of the rig.

Screen 12 of the VI can be used by the operator to enter information concerning the test run, which is then saved in the test log file.

3.14 Summary

This chapter introduced the Turbine Stator Well test facility at the University of Sussex. The test facility external infrastructure has been described, including the test section air supplies, lubrication systems and water circuits. The facility test section air flows, instrumentation locations and data logging systems have also been described. The high density of instrumentation within the test section and the interchange-ability of cooling flow supply geometries allows experimental data to be taken for a wide range of stator well sealing conditions.

4 Test Facility Instrumentation

4.1 Introduction

In this chapter the test facility instrumentation will be discussed in detail. This will include the off rig calibration and instrumentation installation techniques used in order to ensure measurement accuracy requirements were met. The work presented in this chapter was conducted in collaboration with the authors of Coren (2010).

4.2 Thermocouple Manufacturing Process

The K-Type thermocouple was selected as the most suitable for the test facility and was used exclusively in the rig. A K-Type thermocouple consists of a Chromal and Alumel leg. The thermocouples were manufactured within the TFMRC workshop using an inert gas arc welding technique. The bead formed when the two wires of the thermocouple were welded, were examined under a microscope in order to ensure proper formation of the joint, which is the hot junction of the finished thermocouple. Any thermocouples which did not meet the required standard were stripped back and re-welded. Figure 4-1 shows a variety of possible outcomes when welding thermocouples. Type 'A' shows a well formed example. The bead is the result of the two legs melting and forming a sphere. The bead is well formed and each leg of the thermocouple enters the bead at a similar angle. The legs are well spaced and unlikely to touch. Type 'B' shows an example where one leg of the thermocouple has not properly attached to the bead. This will not create the necessary circuit for the thermocouple to produce a voltage. This is often seen if the legs are not of equal length when welding. Type 'C' shows a case where

one leg of the thermocouple has broken out from the bead. Although this thermocouple would initially operate correctly the fact that one leg has not melted fully into the other suggests that the bead may be weak. This could lead to the thermocouple breaking easily. The extra lump of wire may also lead to measurement errors due to embedding issues. This is most often seen when the legs are of a slightly different length or are held too far apart when welding.

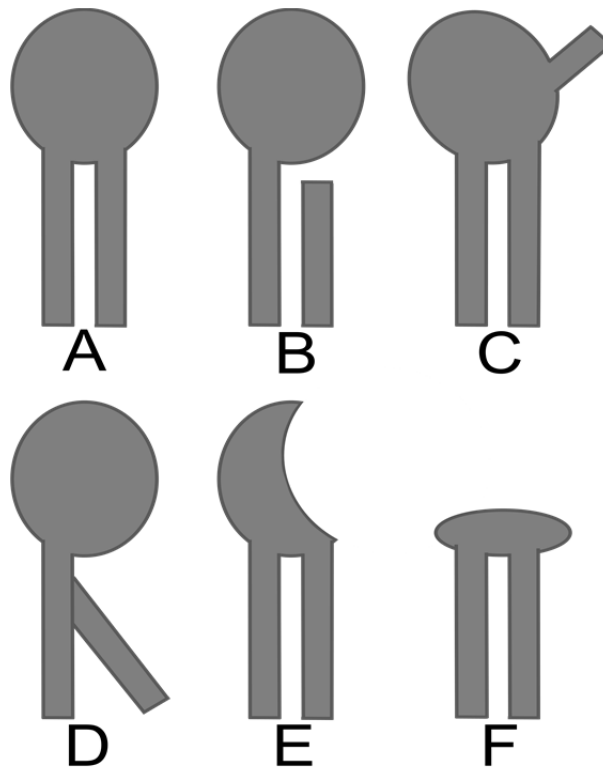


Figure 4-1: Thermocouple bead types

Type 'D' shows the case where although connected, one leg of the thermocouple is not part of the bead. This not only creates a weak joint but also creates a false junction. This would lead to any temperature data being taken using the thermocouple corresponding to the point where the legs meet, rather than the bead. Type 'E' shows the case where the bead is misshapen; this can manifest as surface bubbling, pitting or large sections of the bead missing. This can be caused by too high a power on the welder, the inert gas shield not being supplied around the weld properly or contamination of the leg material. Type

'F' shows the case of a small or misshapen bead. This is often the result of the power being set too low on the welder. Both types 'E' and 'F' will function correctly, however the beads are prone to failure and were not considered acceptable for the TSW rig. Only thermocouples which matched case 'A' were passed for use on the TSW rig.

4.3 Initial Thermocouple Calibration Investigation

Although standard calibration curves are available for K-Type thermocouples, material properties can vary between suppliers and batches. In order to reduce uncertainty due to this, the Chromal and Alumel wire used to manufacture the thermocouples was procured as a single batch. An initial batch of thermocouples was manufactured and a random sample taken for off rig calibration and testing. Figure 4-2 shows the layout used for the calibration. A single thermocouple was selected from the test. The 'hot junction', referring to the bead of the thermocouple was placed in a Jupiter 650B liquid bath. An Isotech, UKAS calibrated platinum resistance thermometer, 'PRT', was also placed into the liquid bath to give a reference temperature. Each leg of the thermocouple was connected to a digital volt meter (DVM) lead then submerged in a separate test tube containing calibration oil. Each of the test tubes was then placed in a triple point ice bath. A full description of the procedure can be found in "TFMRC Laboratory Thermocouple Calibration Procedure 2006 document 06/TFMRC/TR255". The procedure can be summarised as:

1. To create a triple point ice bath, an insulated container with a volume of approximately 1 litre is filled with crushed ice made from distilled water. Distilled water is then added to a level just below the top of the crushed ice. The PRT is then used to ensure the temperature of the ice bath is between 0 and 0.02 °C.

2. The thermocouple is then placed in its entirety into the ice bath and its voltage output measured. If the ice bath is prepared correctly the resulting EMF should fall within $\pm 4 \mu\text{V}$.
3. The bead of the thermocouple is then attached to the tip of the PRT using copper tape and the pair are placed in the liquid bath.
4. The temperature of the liquid bath is then increased in incremental steps over the calibration range, recording PRT reference temperatures and thermocouple voltage output.

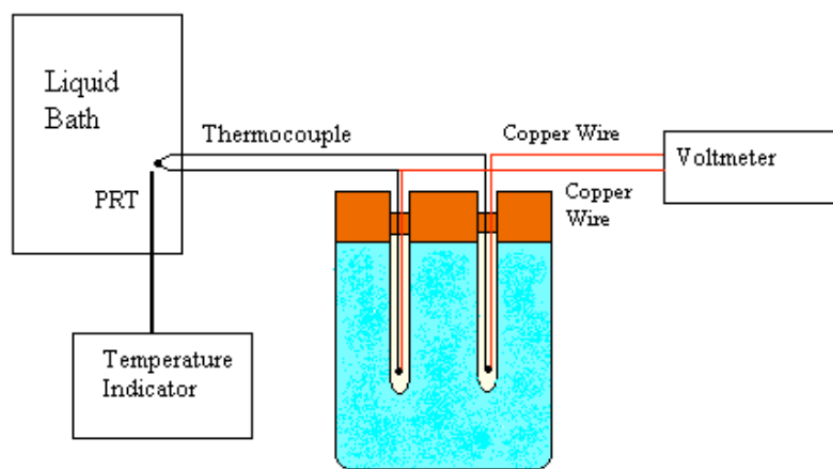


Figure 4-2: Traditional thermocouple calibration technique

Initial calibrations showed that when the thermocouple was placed in the triple point ice bath, where both junctions are at an equal temperature, an unwanted EMF of up to $20 \mu\text{V}$ (approximately 0.5°C for a K-Type thermocouple) was present rather than the acceptable range of $\pm 4 \mu\text{V}$. Further investigation showed that the calibration circuitry appeared sensitive to external temperature variation when the leads between the thermocouple and the DVM were heated. The operating temperature of the DVM was also shown to affect the measured EMF. In order to rectify this problem the original DVM leads were replaced with identical copper wires (i.e. taken from the same batch). The DVM was also allowed to reach operating temperature before beginning the calibration. With these changes in place the measured EMF, where both the hot and cold

junction were placed in the ice bath was found to be within the required $\pm 4 \mu\text{V}$. Using this configuration the initial batch of nine thermocouples were calibrated. Figure 4-3 shows the results obtained from a single thermocouple. The oil bath temperature is plotted against deviation from standard K-Type indicated temperature. The oil bath temperature was measured using the "laboratory PRT". This is a traceable platinum resistance thermometer which has been calibrated by a UKAS accredited third party and is used as the reference device at TRMRC. The indicated temperature is the temperature calculated using K-type thermocouple coefficients for the measured voltage output of the thermocouple; the deviation is the difference between this standard temperature and the measured PRT temperature. It was found that the temperature measured by the PRT varied by as much as 0.3°C from the standard indicated temperature obtained from standard k-Type tables.

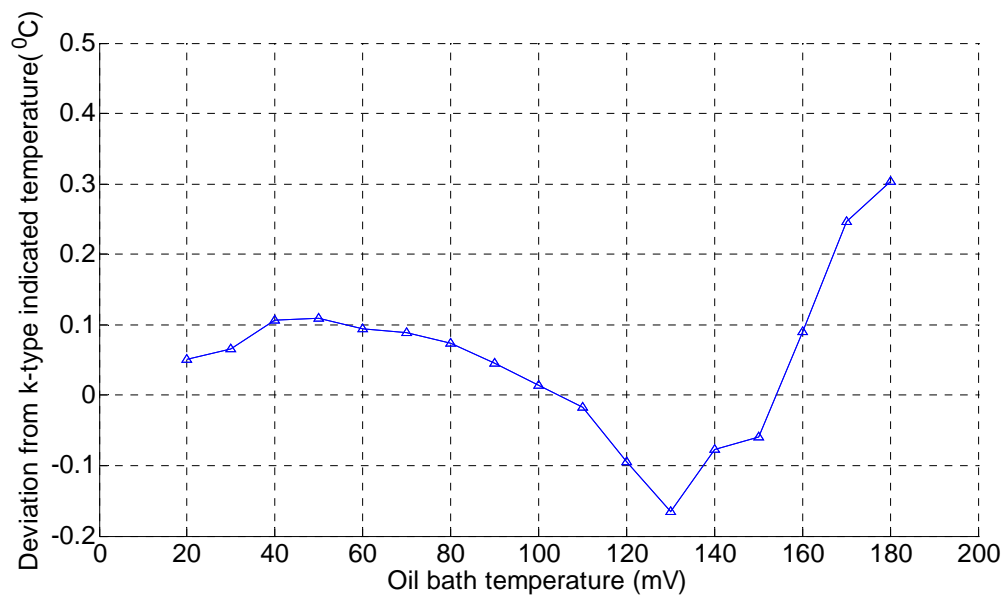


Figure 4-3: Initial thermocouple calibration

From the single calibration, it was unclear if the deviation from the standard indicated temperature was due to the calibration process or a feature of the materials and manufacturing process being used for the thermocouples. This result prompted further investigation of the thermocouple batch. Figure 4-4 shows the results of the calibration

procedure carried out on four thermocouples. The average of the four thermocouples is shown together with bars showing the maximum and minimum deviation from the average. Each thermocouple showed the same trend as the initial calibration, with a deviation from the standard K-Type indicated temperature of up to 0.3°C . However, the deviation of each thermocouple from the batch average was found to be within $\pm 0.1^{\circ}\text{C}$.

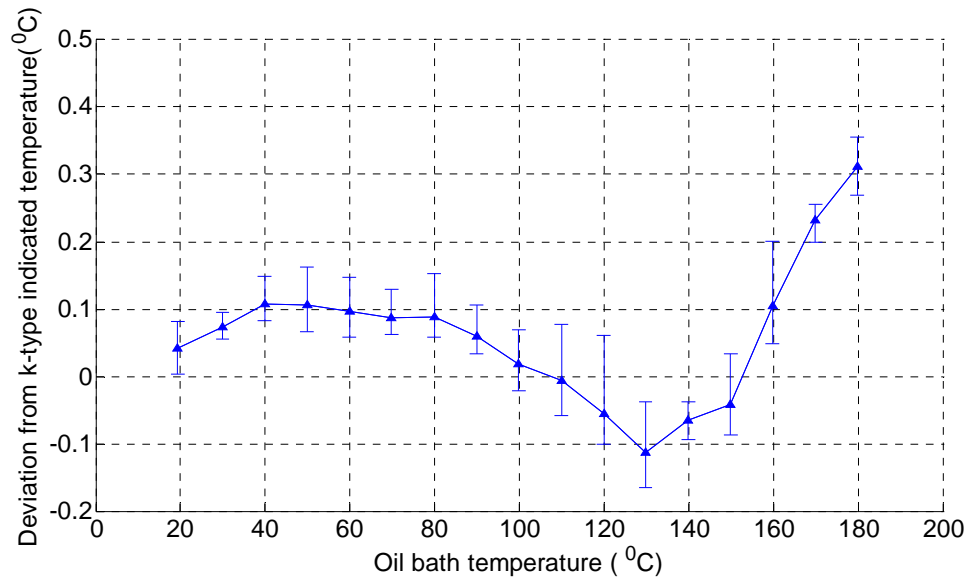


Figure 4-4: Initial thermocouple batch calibration

These results obtained from this initial investigation suggested (given the accuracy of temperature measurement required) that it would be necessary to complete a calibration of each individual thermocouple to be used on the rig. In order to meet this objective a "through calibration" procedure was devised. "Through calibration" is a term used in this thesis to describe a method where all thermocouples to be used on the rig are connected to the data logging equipment via the exact path and channel number to be used during rig operation. This process is described in greater detail in section 4.6. In order to carry out the through calibration it was necessary to complete the installation of the data logging equipment, manufacture each thermocouple to be used on the test rig and to install and calibrate the cold junction temperature measurement instrumentation.

4.4 Stationary Thermocouple Cold Junction

The stationary thermocouples for the TSW rig are connected via two National Instrument cards to the data acquisition system as shown in Chapter 3, Figure 3-23. In standard form the two NI-SCXI-1303 cards include both the input terminals to which the thermocouple legs are connected and also the cold junction reference temperature measurement. This is made via a thermistor bedded into a small aluminium plate on the rear face of the internal card. The original configuration is shown in Figure 4-5.

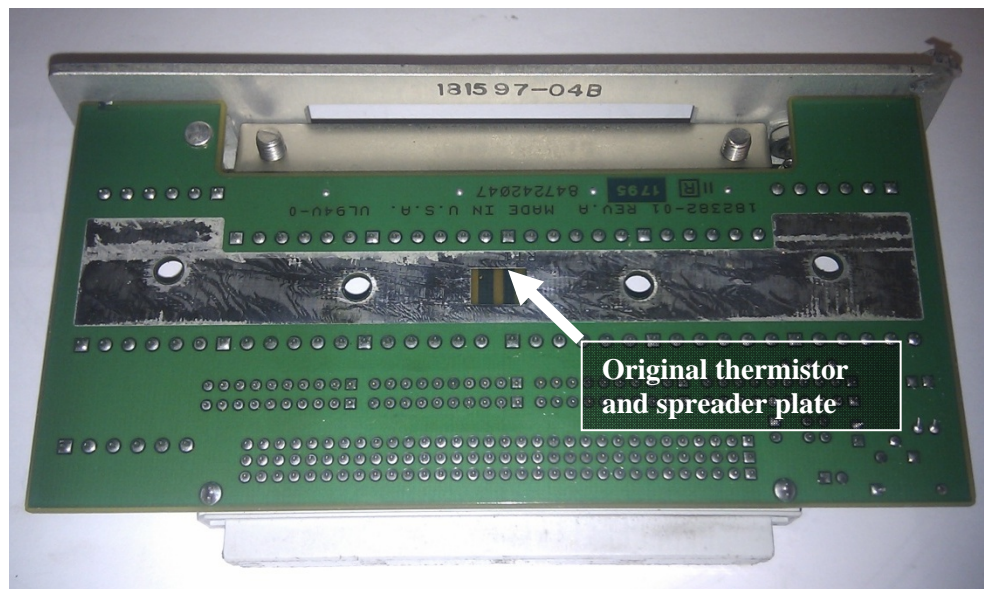


Figure 4-5: Standard NI card cold junction measurement

This configuration was considered to be inadequate to provide the necessary accuracy for the cold junction reference temperature. In order to improve this measurement the casing of the NI cards was modified in order to accept a larger spreader plate which could house three platinum resistance thermometers. Figure 4-6 shows the casing of a NI card after being machined and prior to fitting of the larger spreader plate. Unlike the original thermistor which uses an internal channel to output the temperature of the card unit, the outputs of the three PRTs embedded in the larger spreader plate are measured independently by the Agilent 34970A DVM.



Figure 4-6: NI-SCXI-1303 machined ready for new spreader plate

Figure 4-7 shows the new spreader plate, with the three locations for embedding the PRTs. The Plate is attached firmly to the thermocouple terminal board via four cap head screws, the threaded holes for which are shown. The other various tracks and cut outs are to allow clearance between the copper plate and the terminals of the card.

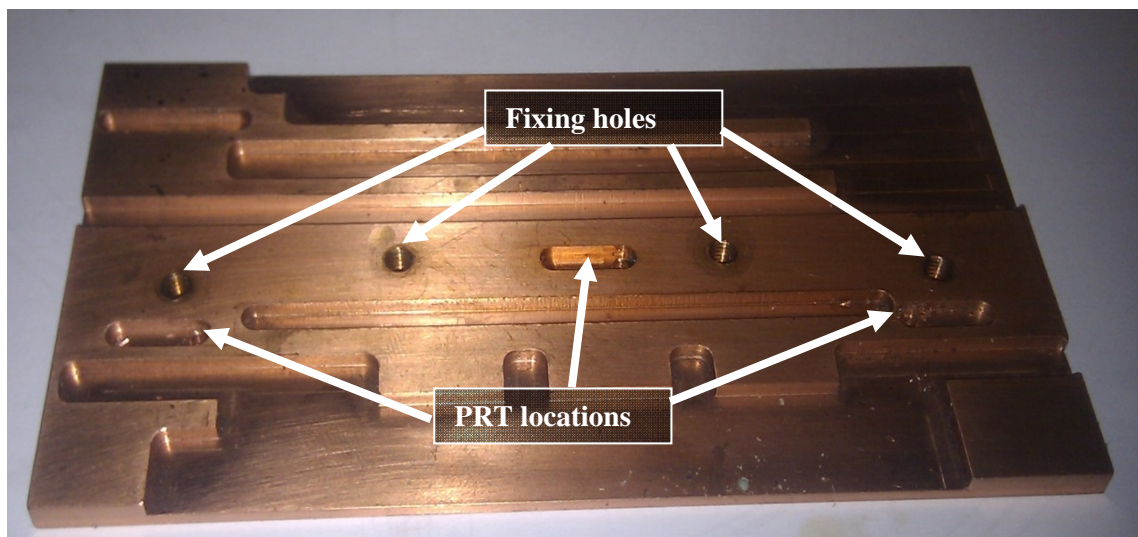


Figure 4-7: Copper spreader plate prior to installation

Figure 4-8 shows two views of an open SCXI-1303 module with the large copper spreader plate attached. The three PRTs are bonded to the underside of the plate, as close to the junctions of the thermocouples as possible, with epoxy resin. The lead outs from the three PRTs can be seen taped to the plate. The right hand view shows how the spreader plate is flush with the thermocouple terminal card.



Figure 4-8: Open NI SCXI-1303 with spreader plate and PRTs attached

Before final installation of the PRTs in the copper spreader plates the PRTs were calibrated. This process is described in the next section.

4.5 Cold Junction PRT Calibration

Figure 4-9 shows the equipment used for the stationary thermocouple cold junction temperature measurement PRTs calibration. Six PRTs were lowered into a Isotech 915 parallel tube oil bath. These were connected via a terminal block to the Agilent DVM which directly measures the resistance across the PRTs, in turn connected via a NI PCI

to the data logging system. All reference temperature measurements made during the calibration process. The laboratory reference PRT was submerged alongside the PRTs to be calibrated in the oil bath in order to give a reference temperature.

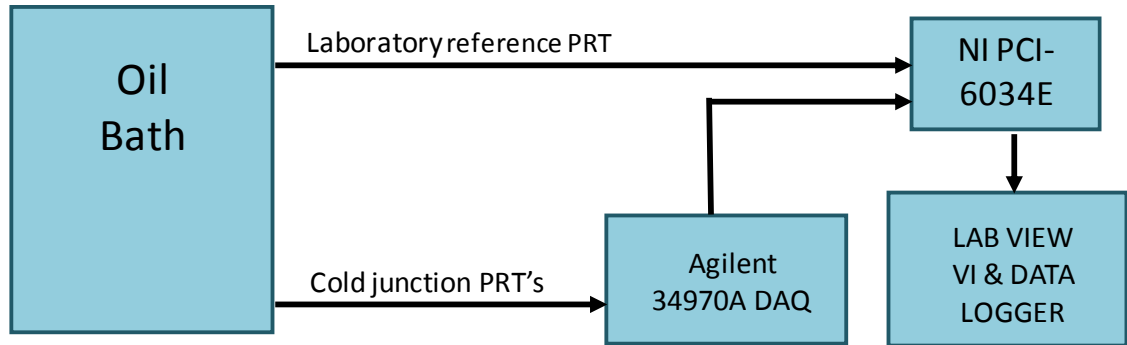


Figure 4-9: Stationary thermocouple cold junction PRT calibration

The oil bath was set at a number of temperatures, covering the expected operating range of the PRTs. Although not shown by this diagram, the PRTs were also submerged in a triple point ice bath, prepared as described in section 4.3, in order to produce calibration points at 0 °C. Figure 4-10 shows the calibration results for the six PRTs, where change in resistance of each PRT is plotted against PRT temperature. The PRTs were seen to produce resistances of between +/- 0.05 Ohms of the batch average. If an average of the batch was used to produce a general coefficient for the PRTs this would result in an uncertainty of +/- 0.1 °C. However, due to the high level of accuracy required for the test rig, coefficients for each individual PRT were produced by applying a fit to each set of data.

Once the PRTs had been installed in the new copper spreader plates and attached to the NI SCXI-1303 card, a single card was plugged into an SCXI 1102B amplifier in the SCXI 1000 chassis. This is the instrumentation route for the stationary thermocouples as shown in Chapter 3, Figure 3.23.

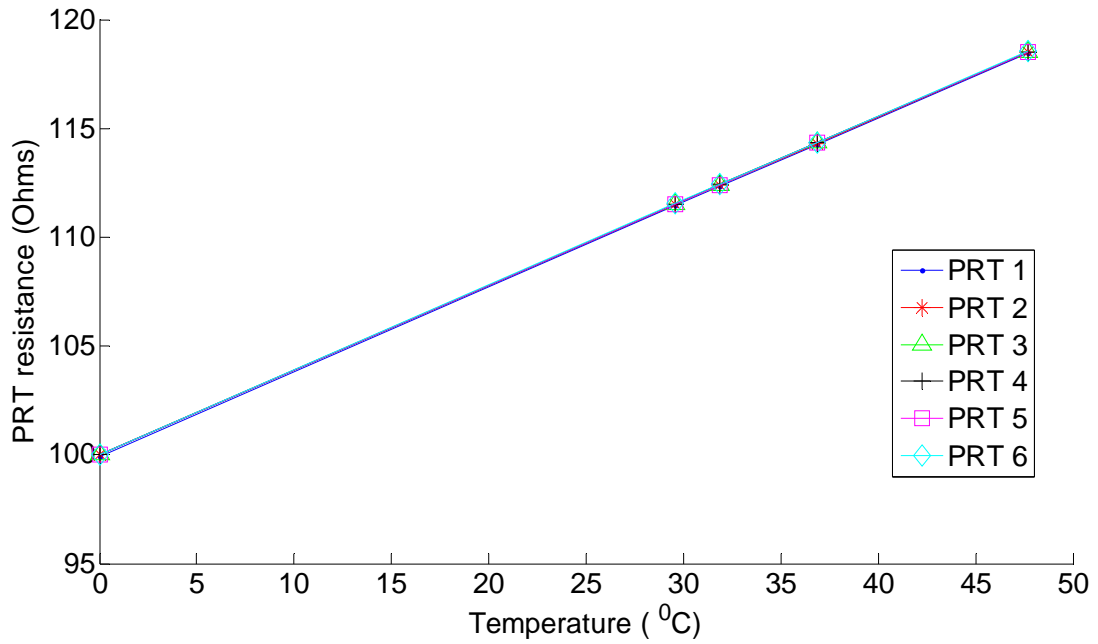


Figure 4-10: Cold junction PRT calibration, Turner et al (2008)



Figure 4-11: SXCI-1303 card connected to SXCI-1000 chassis

Figure 4-11 shows the card plugged into the SCXI 1000 chassis. The blue PRT leads can be seen exiting the front of the card. The card casing had been removed and no thermocouples were attached to the card. The SCXI 1000 chassis was then powered up, making the NI SCXI-1303 card live. The PRT temperature readings were then taken,

using the Agilent 34970A. Despite the addition of the copper plate, upon reviewing the calibration data, a temperature gradient of $0.4\text{ }^{\circ}\text{C}$ was measured between the three PRTs on the single card. This gradient was examined further in order to rule out the possibility of a calibration error for the PRTs. Two methods were used in order to confirm the gradient. A spot check of the card temperatures was made by attaching a thermocouple to the PRT locations with conductive copper adhesive tape. These measurements showed a temperature gradient of similar magnitude across the PRT locations. Further locations across the card were then tested using the same method. The higher temperatures on the plate were located in the area of the card closest to the NI-SCXI-1000 amplifiers. It was concluded from this test that heat from the amplifiers was the cause of the gradient. In order to verify this an infrared camera system was used.

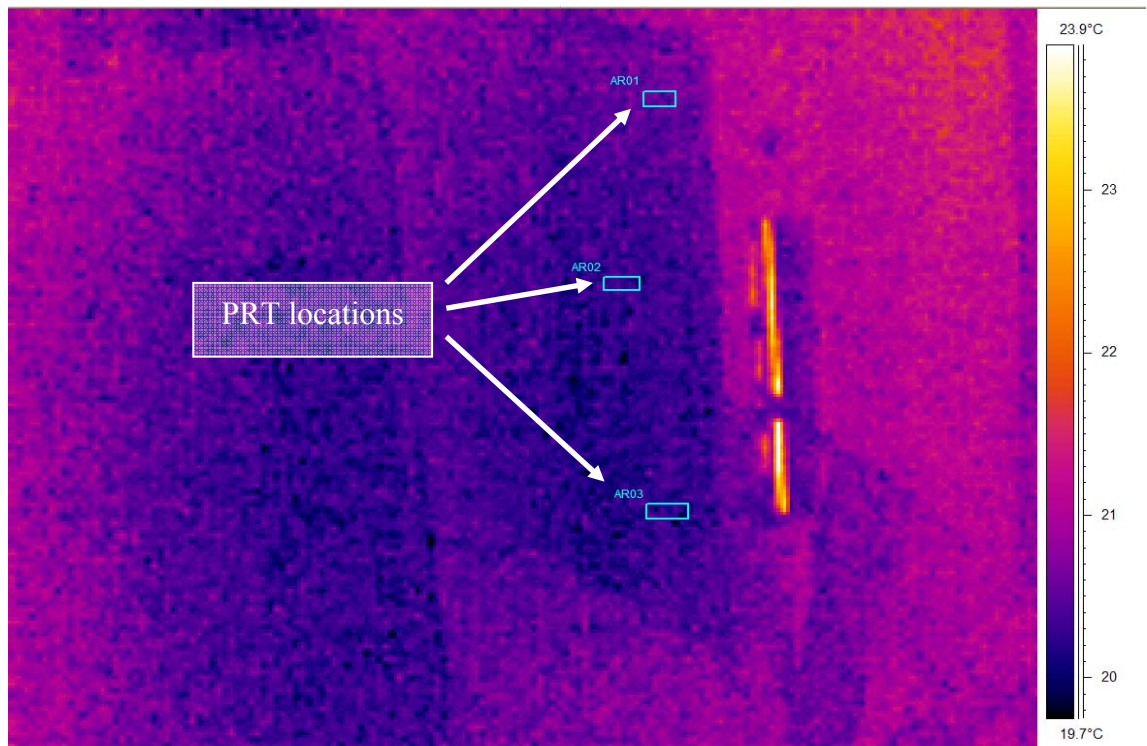


Figure 4-12: Infrared image of NI-SCXI-1303 card

Figure 4-12 shows an infrared image of the SCXI module whilst powered up. The results from the infrared camera showed a similar gradient across the PRT locations, of

around 0.5°C, as the thermocouple spot checks and the PRT measurements. The infrared images also showed that some locations on the card reached temperatures of over a degree more than the card average. This area is shown as yellow in Figure 4-12.

It was concluded from these investigations that the gradient across the SCXI card was unacceptable given the accuracy required for the stationary thermocouple measurements. A method was required to move the SCXI cards away from the SCXI 1000 chassis and amplifiers. In order to achieve this, break out leads were required between the SCXI-1303 cards and SCXI-1102B units. However an "off the shelf" solution was not available for the given hardware. Although extension leads were available from National Instruments which had the correct number of pins, these items were designed for alternative NI hardware and inverted the instrumentation channel paths. A number of these units were purchased and re-wired correcting the channel paths. The modified leads were extensively continuity tested to ensure correct channel transmission. It was also necessary to modify the SCXI-1303 card casing in order to mechanically connect the lead to the module rather than rely on a push fit. Figure 4-13 shows the casing of a SCXI-1303 module with the terminal card removed. The modified lead can be seen attached to the casing, together with the machined connector blocks used to connect the two. Figure 4-14 shows the terminal card inserted into the casing and screwed into position, providing the mechanical fixing of the lead to the card terminals. The top half of the casing has been removed in order to show the connection. A number of thermocouples can be seen leading from the terminals, out through the opposite side of the card. Under normal operation the top casing is sandwiched between the front and back side of the casing before the final assembly of the unit.

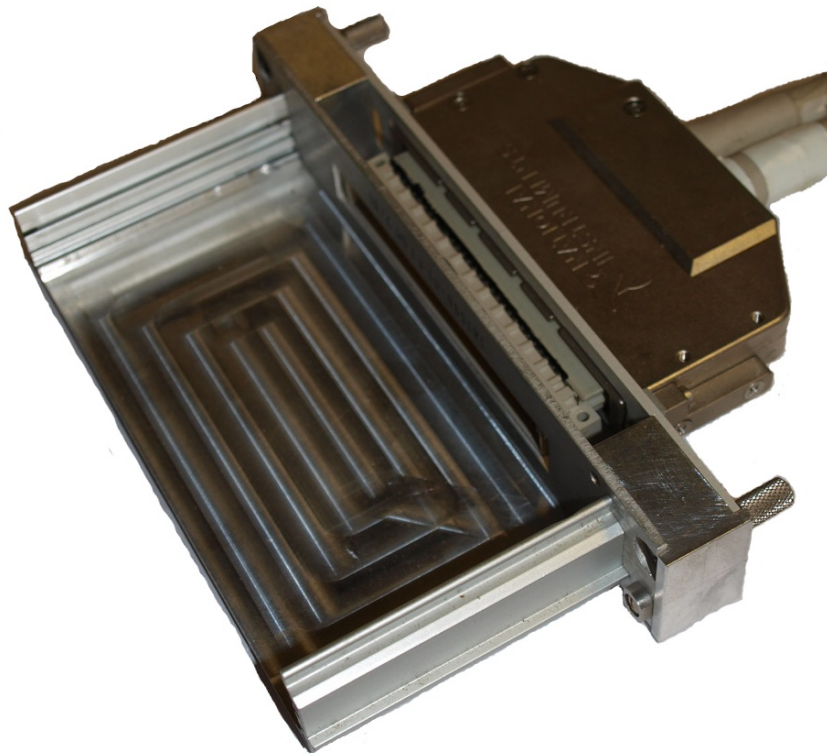


Figure 4-13: SXCI-1303 card casing attached to modified NI lead



Figure 4-14: Modified SCXI 1303 with top casing removed

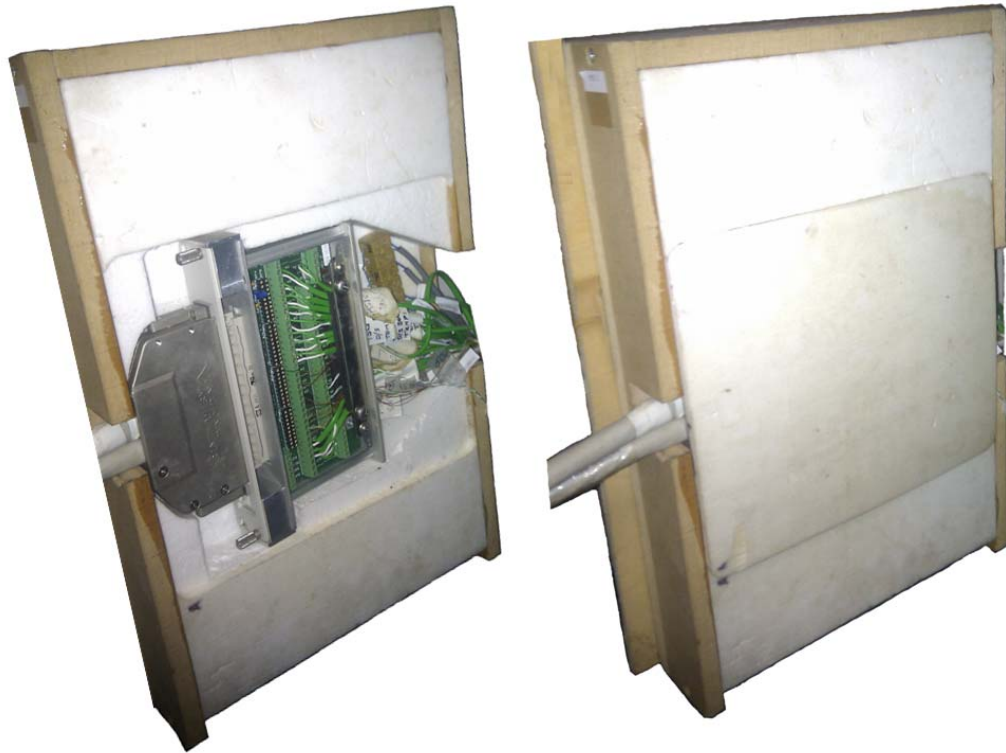


Figure 4-15: SCXI-1303 card in isothermal box

The extension lead reduces thermal gradients across the card by moving the thermocouple terminals away from possible internal heat sources. The copper spreader plate reduces thermal gradients across the card due to its high thermal conductivity. However by increasing the internal thermal conductivity of the card it becomes more susceptible to changes in external temperatures. In order to reduce this the SCXI cards were placed in individual isothermal boxes. Figure 4-15 shows the modified SCXI-1303 card with the modified extension cable placed within an isothermal box. The isothermal boxes were manufactured using a casing of MDF. Rohacell insulation was then milled to shape to hold the SCXI cards and cables. This was glued into the MDF casings. The image on the left of Figure 4-15 shows the arrangement with both the top half of the Rohacell and the MDF removed. The casing of the SCXI card has also been removed. The image on the right shows the arrangement with the top half of the Rohacell insulation in place.

Figure 4-16 shows cold junction temperatures as measured by three reference temperature PRT's in a single SCXI-1303 module, with the stated modifications, across a typical test run cycle. The deviation between all PRT's from the single module average are less than ± 0.065 K. The total deviation across all modules was less than ± 0.25 K, with a total drift in module average temperature over a 3 hour run of less than 0.6 K.

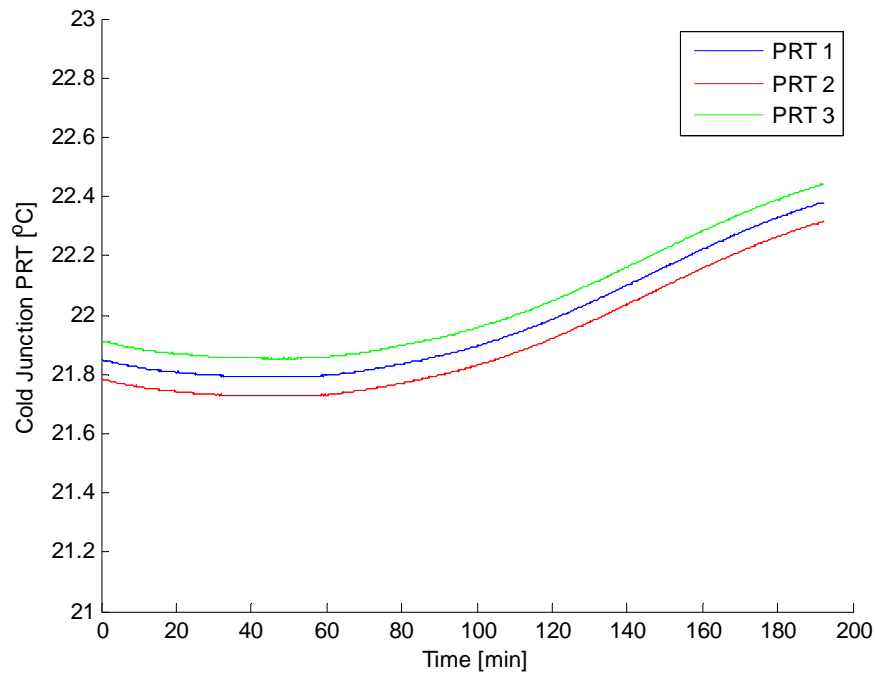


Figure 4-16: SCXI-1303 cold junction temperature variation

4.6 Stationary Thermocouple Calibration

Following the initial thermocouple investigations and the resulting improvements made to the data acquisition system it was decided that off rig batch calibration of the test rig thermocouples would not be sufficient. A through calibration technique was selected as the most efficient and accurate method of calibration. This involves calibrating each thermocouple individually for its given channel, using the exact measurement instrumentation to be used in the final instrumentation system. Figure 4-17 shows the instrumentation path used for the calibration. Rather than being in their measurement

positions on the rig, the thermocouples were placed into a Isotech liquid bath. The laboratory reference PRT was also placed within the liquid bath. Other than these two additions the thermocouple outputs were measured and logged via the exact path as used during rig operation.

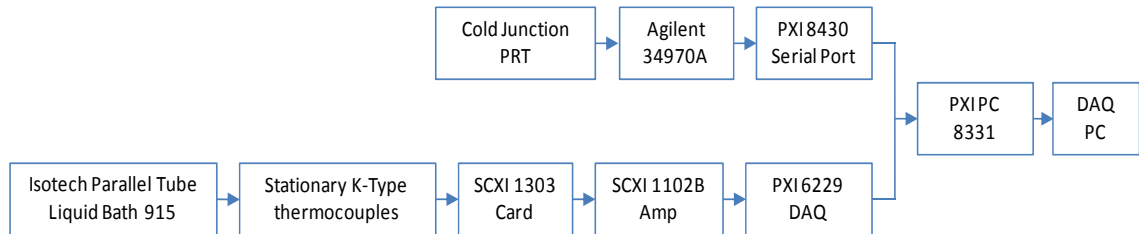


Figure 4-17: Stationary thermocouple calibration instrumentation path

Figure 4-18 shows a diagram of the calibration equipment within the Isotech bath. The bath consists of a large bath of oil, in the centre of which is a large aluminium block, into which instruments can be lowered. The bath then pumps oil, heated to a required temperature, over the block. Due to the installation method for the stationary thermocouples it was necessary to prevent any calibration oil coming into contact with the thermocouple leg insulation material as it would prevent proper bonding of the thermocouples to the measurement surfaces of the test rig. In order to achieve this a calibration "bomb" was manufactured. This consists of a large bomb shaped copper block into which glass tubing is bonded. The glass tubing extends above the bath oil level allowing thermocouples to be fed down to the required depth within the bath without making contact with the oil. The bomb also has a hole of the same depth as the thermocouple glass tube holes into which the reference PRT can be placed.

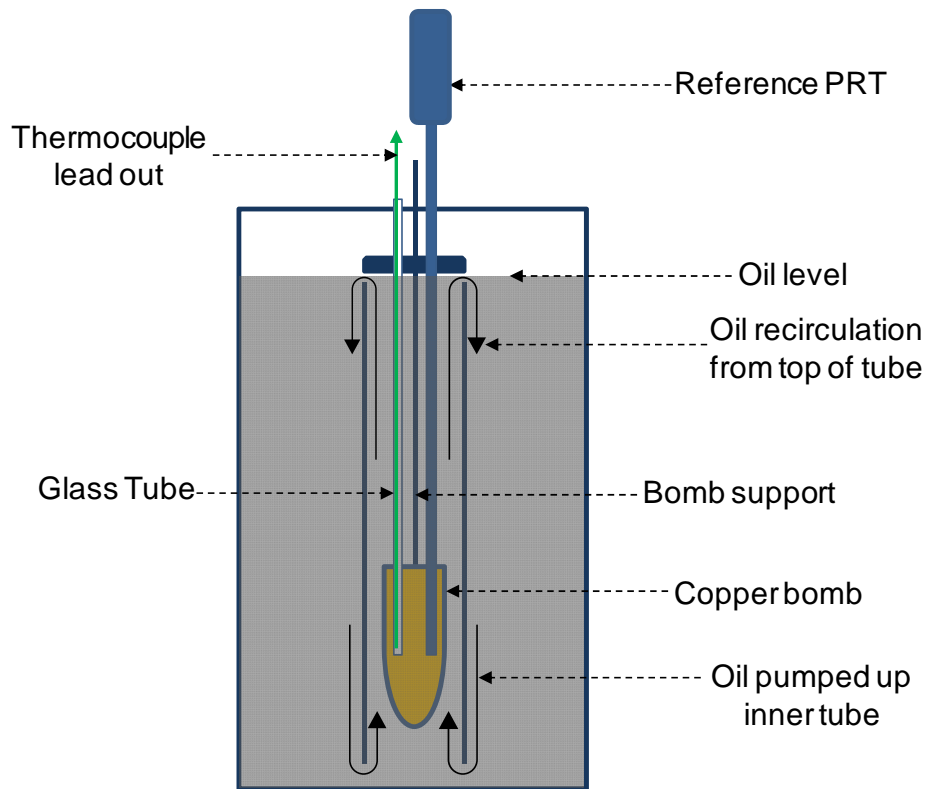


Figure 4-18: Isotech bath layout

Figure 4-19 shows the liquid bath set points for the stationary thermocouple calibration. The Isotech bath has its own internal heater and thermostat to maintain the oil temperature. The cycle shown was completed over a 14 hour period allowing 30 minutes for each calibration point to be reached. Data was then taken from the last minute of each point, from which the calibration co-efficient of each thermocouple and channel combination were calculated.

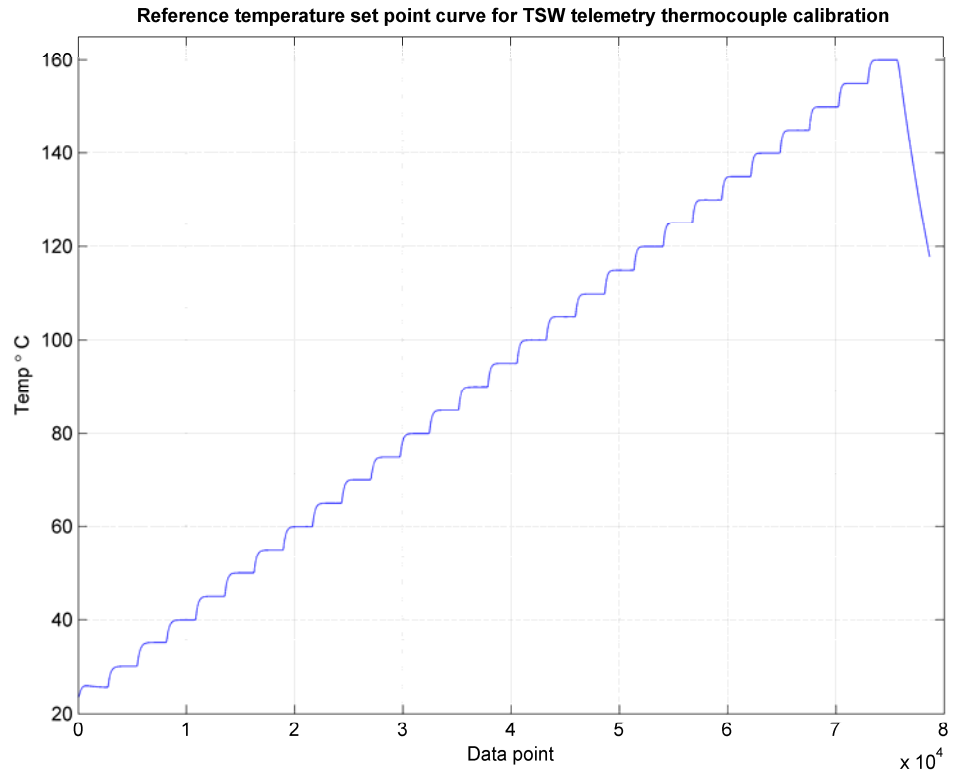


Figure 4-19: Isotech liquid bath temperature set points, Turner et al (2008)

Figure 4-20 shows the results of the stationary thermocouple calibration, where the voltage output of the thermocouples is plotted against the reference temperature PRT for each set point.

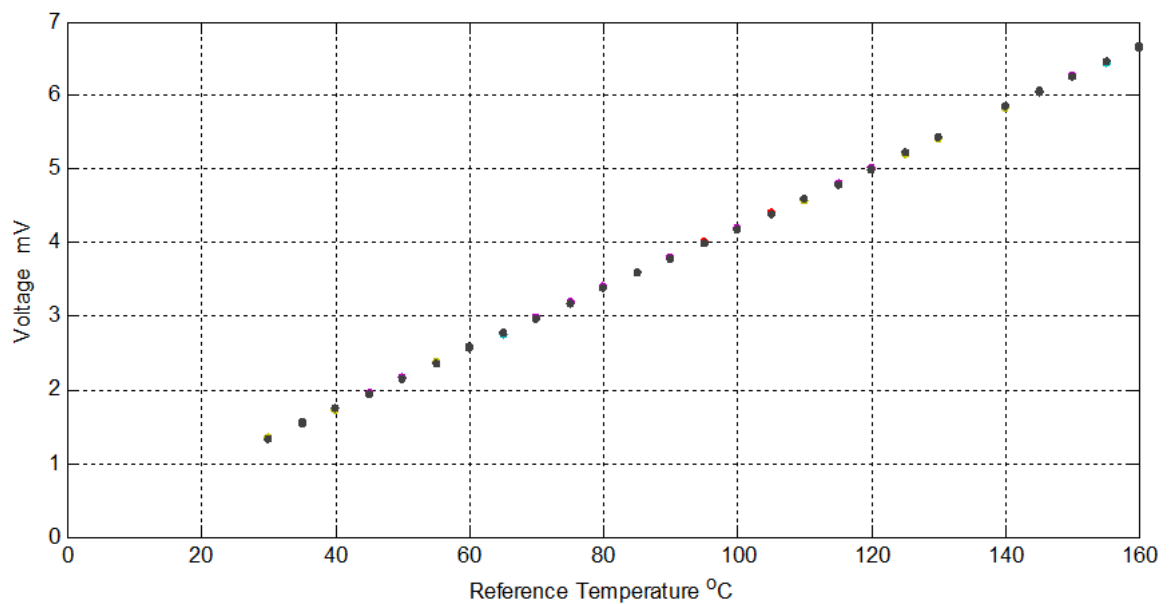


Figure 4-20: Stationary thermocouple voltage output, Turner et al (2008)

The calibration data was used to create fits for each individual channel from which coefficients for each thermocouple were obtained. These coefficients were then re-applied to the voltage data recorded during the calibration. Figure 4-21 shows the deviation of the resultant temperature measurement made by each thermocouple against the PRT reference temperature. The deviation was found to be less than ± 0.1 K by Turner et al (2008).

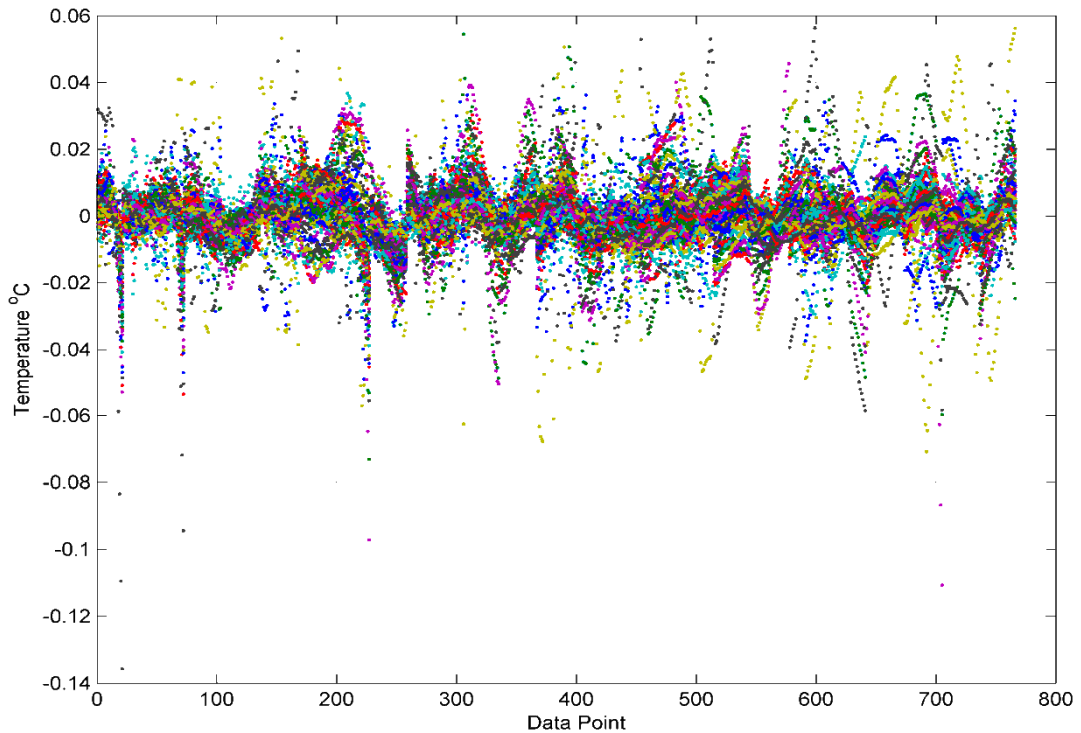


Figure 4-21: Deviation of post processed thermocouple temperature data from reference temperature, Turner et al (2008)

4.7 Stationary Thermocouple Installation

In this section examples will be given of the techniques used throughout the rig to install the stationary thermocouples. Although not subject to the loads associated with the high rotational speeds of the thermocouples installed on the rotating components of the rig, the stationary thermocouples require mounting methods which both protect the thermocouples from accidental damage over prolonged test periods but also avoid embedding errors. Figure 4-22 shows an example of stationary thermocouples installed on the stationary face of the upstream wheelspace. The thermocouples are identifiable

by the small dark tracks on the face of the disc. These tracks are machined to allow the last part of the thermocouples legs before the bead to be laid flat against the disc. For metal temperature measurements the bead is also bonded to the disc face, in contact with the metal. For air thermocouple measurements the thermocouple bead is left between 0.5mm and 1mm proud of the component surface. The tracks, with the thermocouple laid inside, are then smoothed over with a resin to restore the flat face of the disc. The remaining length of the thermocouple passes through the face of the disc, from where it is led out from the rig through the aerodynamic struts in the main annulus and then to the data logger.

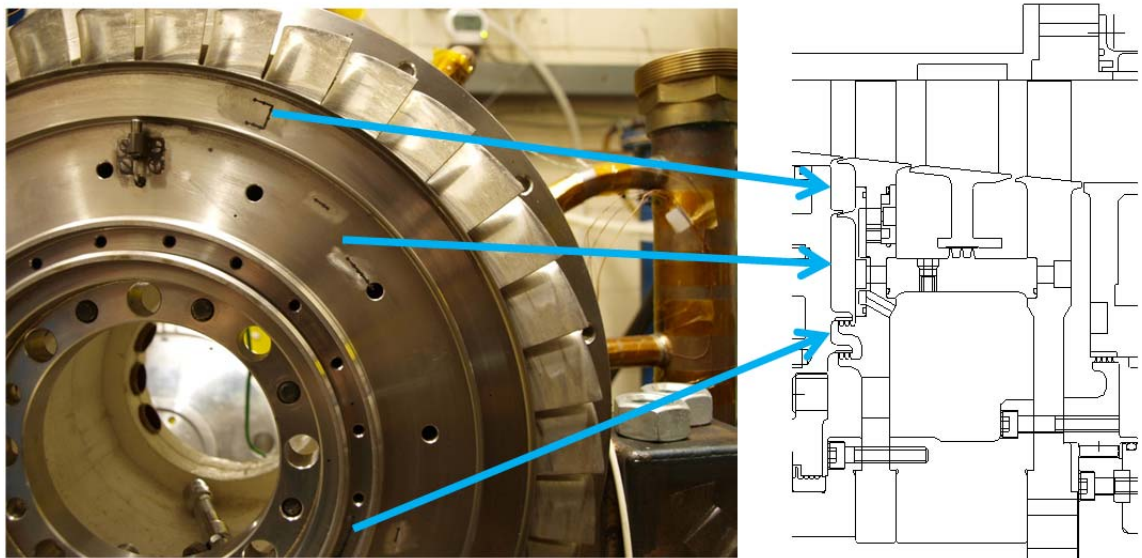


Figure 4-22: Stator 1 thermocouple installation

Figure 4-23 shows an image of air thermocouples installed on the stator 1 nozzle guide vane row. The thermocouple beads can be seen standing proud of the leading edge of the guide vane. The resin used to set the thermocouples into the vane can be seen as small black circles on the surface. The thermocouples are fed to the vane by means of a slot running from the outer to inner radius of the vane on the suction side. From here four small holes are drilled through from the leading edge into the slot. The thermocouples are fed through the four holes, into the main slot, then radially

downwards to join the forward thermocouple route out of the rig used by the thermocouples shown in Figure 4-22. Figure 4-24 shows air thermocouples being installed in the second nozzle guide vane row on stator 2. This image shows the suction side of the vane before being filled with Duralco 4525-IP epoxy resin. The thermocouple wires can be seen laid within the milled slot in the vane. In this case, unlike the NGV 1 vane, the thermocouple leads can be seen leaving the blade radially outwards.

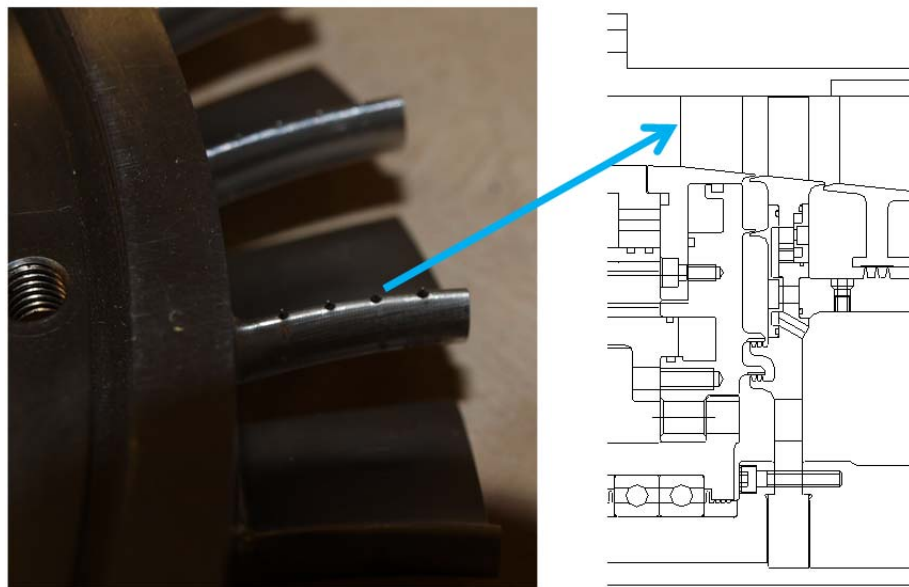


Figure 4-23: NGV 1 air thermocouples

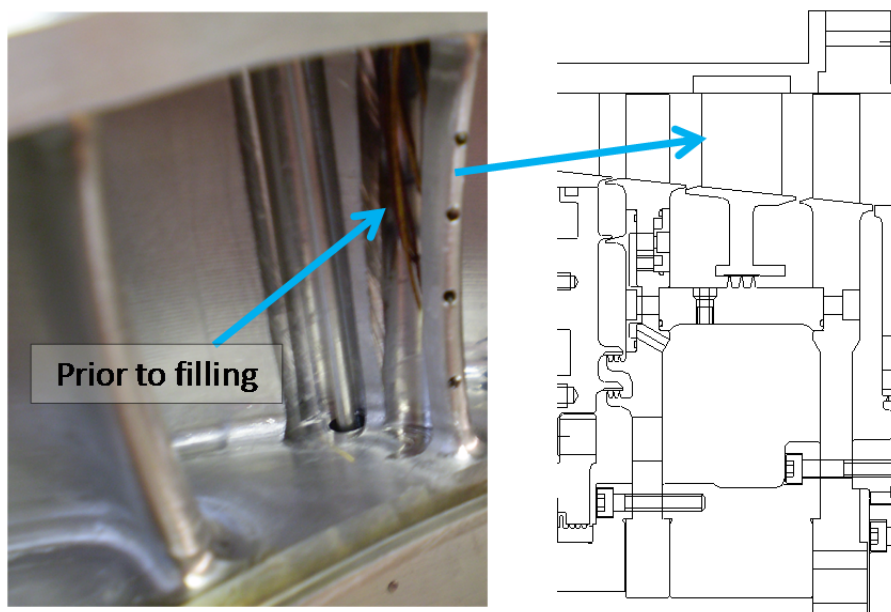


Figure 4-24: NGV 2 air thermocouple installation

Where thermocouples were installed within vane rows, as shown in Figure 4-23 and Figure 4-24, prior to the vane tracks being machined, castings were made of the profile in order to provide a mould for the underside of the vane.



Figure 4-25: Female vane mould and clamp system

Figure 4-25 shows the mould along with an image of the mould being used to set resin in NGV 1 vane. An outer clamping piece can be seen laid across the outer radius of the vane row and held in place by a number of g-clamps.

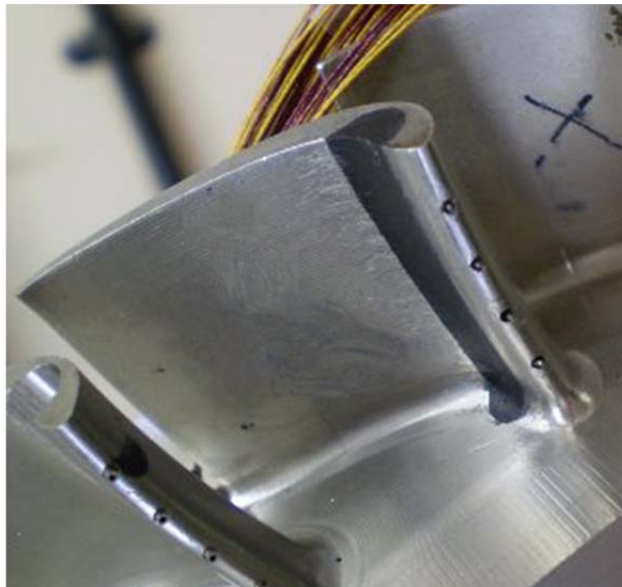


Figure 4-26: Re-profiled NGV 1 vane

Figure 4-26 shows the vane with the mould removed. The re-profiled section made from black resin can be seen to follow the original profile of the vane. Figure 4-27 shows the complete assembly of Stator 2 of the test section. Both halves of the casing can be seen bolted together, forming the annulus ring of the stator well foot. Red overbraid is used to protect the thermocouples from abrasion and damage resulting from coiling and bending and is used for the full length of the thermocouples up until it reaches the data logging equipment.

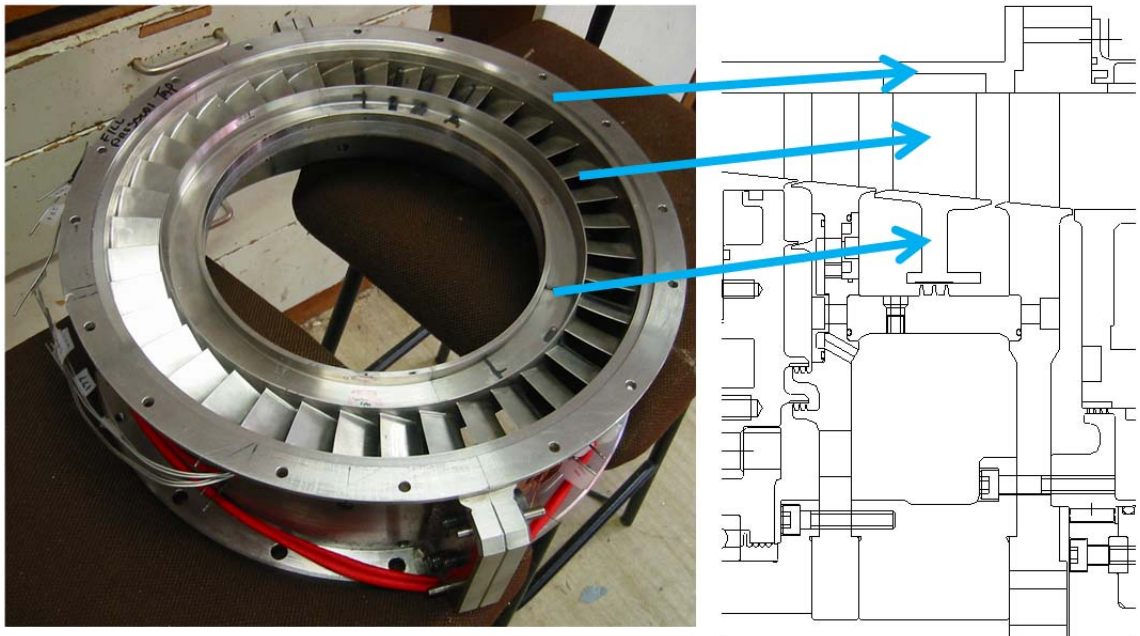


Figure 4-27: NGV2 in stator 2 assembly

4.8 Rotating Thermocouple Calibration

As with the stationary thermocouple measurements, the rotating thermocouples require accurate cold junction temperature measurements in order to provide the resolution required for the program. The PRTs selected to make this measurement for the stationary temperature measurements were considered to be suitable for the rotating frame instrumentation. However, unlike the stationary thermocouple location where the PRTs could be located within the data acquisition card, it was necessary to locate the PRTs within the telemetry unit, mounted at the front of the rotating section of the rig. The rotating thermocouple cold junctions are soldered to gold pins which are mounted

within a cap which plugs into the telemetry unit. Figure 4-28 shows one of the telemetry caps with a PRT bonded into the unit. The four wires from the PRT have been soldered to the four pins shown (the thermocouple pins have not been located), allowing the signal to be transmitted via the telemetry unit. Prior to installation of the PRTs in the telemetry caps the PRTs were calibrated using the procedure outlined in section 4.4.

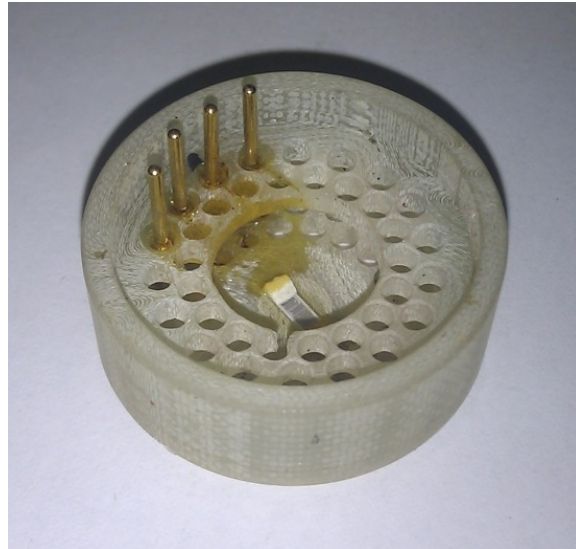


Figure 4-28: PRT installed in telemetry unit cap

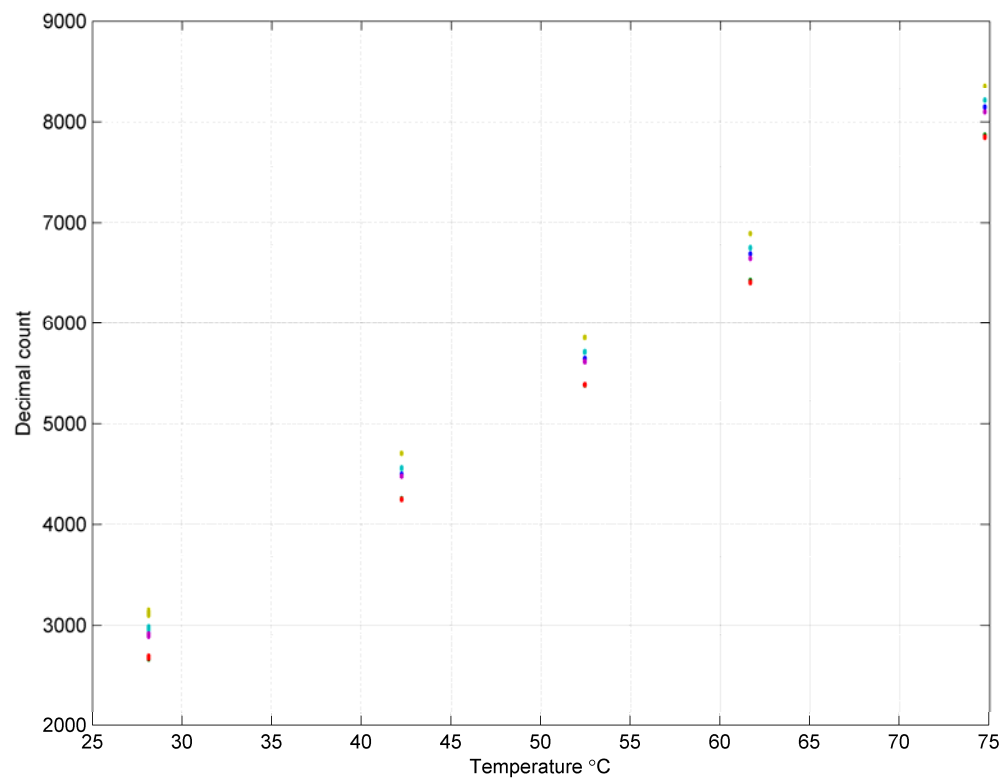


Figure 4-29: Rotating PRT calibration points, Turner et al (2008)

Unlike the stationary measurement, PRTs where the resistance can be measured directly by the data logging system, the rotating PRT measurements are transmitted by the telemetry unit. This means that the data received from the telemetry unit is logged as a decimal count, where the value of the measurement channel is inferred from the magnitude of the decimal count. Figure 4-29 shows the decimal count returned by the telemetry unit for the rotating PRTs against the five set point temperatures measured by the reference PRT. A fit of the magnitude of the decimal count against the reference PRT temperature recorded for each PRT channel was then used in order to produce coefficients for each individual unit and channel. These coefficients were then used along with the original decimal count to obtain rotating PRT temperatures for each calibration point. Figure 4-30 shows the deviation of the PRT derived temperatures from the reference temperature. The deviation was found by Turner et al (2008) to be less than ± 0.15 K.

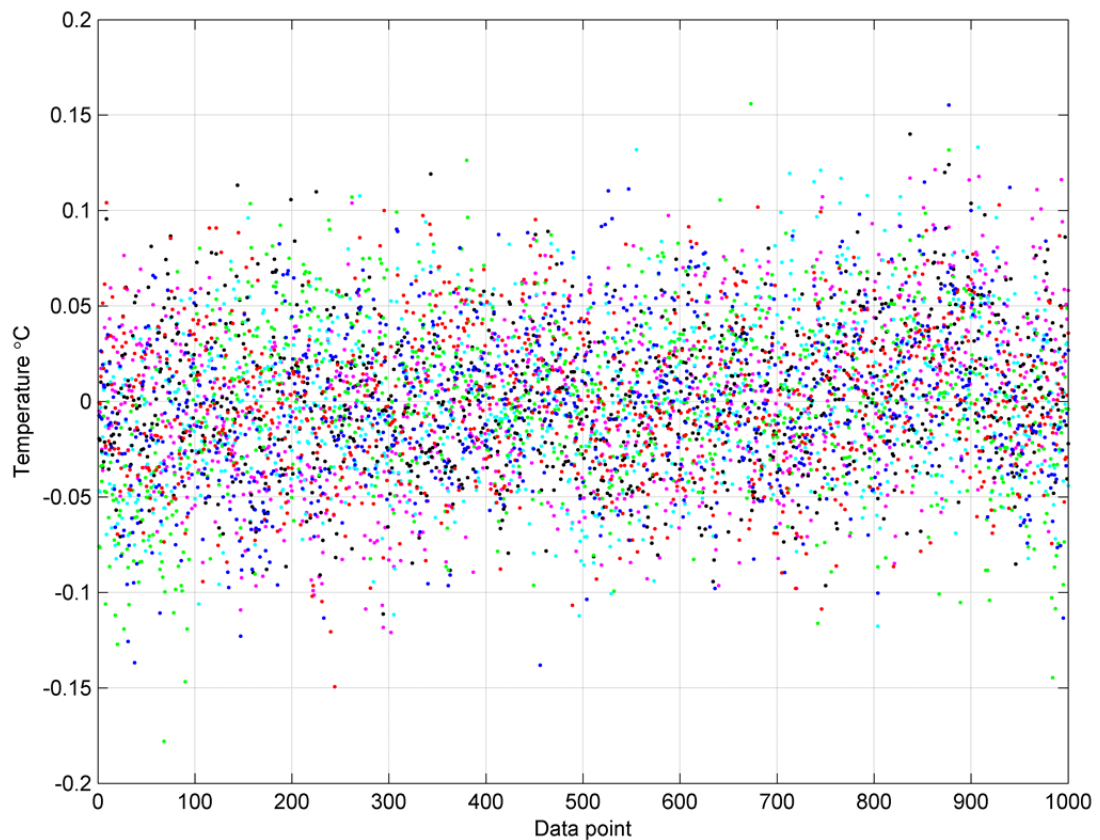


Figure 4-30: Rotating frame PRTs deviation from reference PRT, Turner et al (2008)

Figure 4-31 shows the instrumentation path used for the calibration. As with the stationary thermocouple calibration, rather than being installed in the rig the thermocouples were placed within an oil bath. The thermocouples and cold junction

PRTs were plugged into the telemetry unit and the outputs were measured and logged via the exact path as used during rig operation.

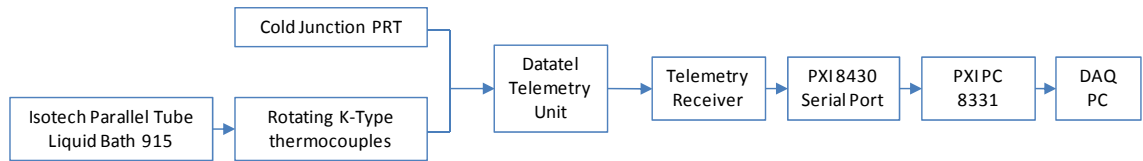


Figure 4-31: Rotating thermocouple calibration instrumentation path

The calibration was conducted over a temperature range of 30 °C to 160 °C in increments of 5 °C. The magnitude of the decimal count transmitted for each thermocouple channel along with the reference temperature was then used to produce coefficients for each of the rotating thermocouples. Figure 4-32 shows the deviation of the temperatures produced by using the coefficients to obtain temperatures for 27 of the rotating thermocouples. The representative uncertainty was given by Turner et al (2008) to be ± 0.25 °C.

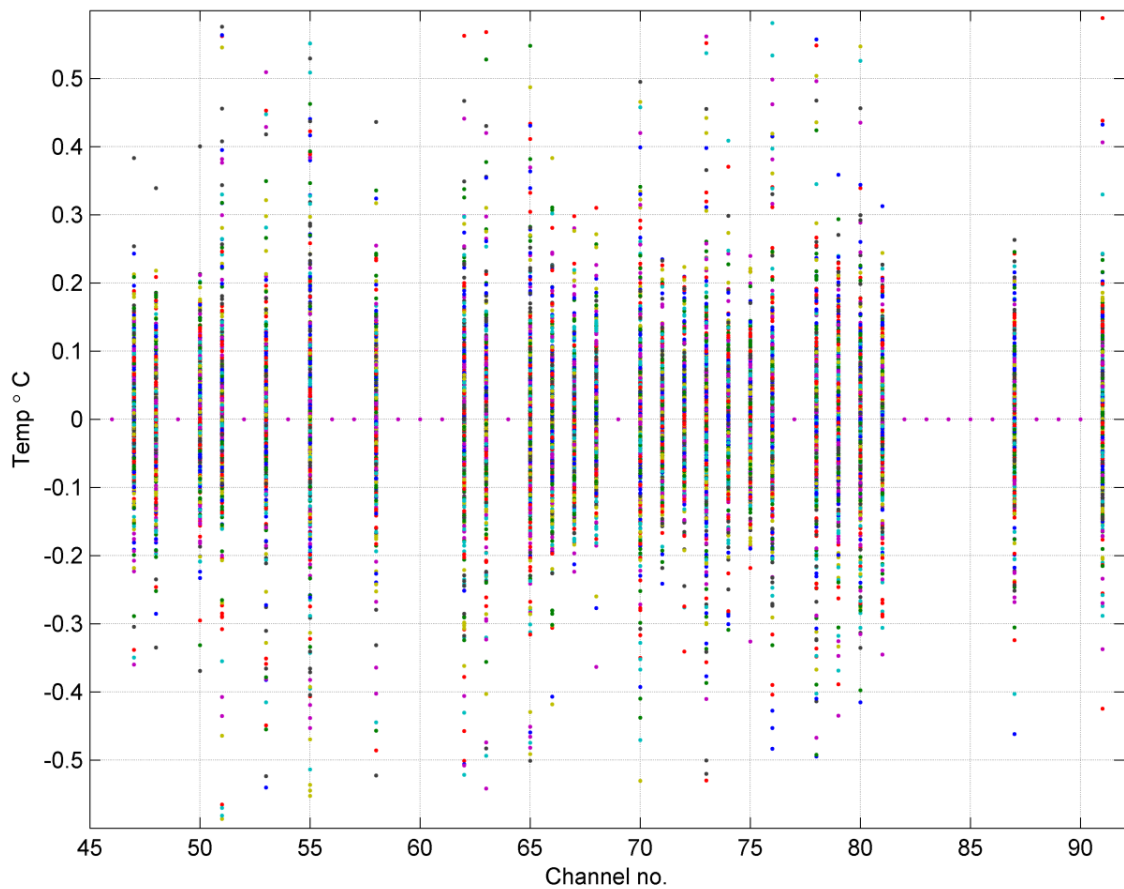


Figure 4-32: Deviation of post processed thermocouple temperature data from reference temperature, Turner et al (2008)

4.9 Rotating Thermocouple Installation

Although of low mass, the thermocouples installed on the rotating section of the test rig are subject to centrifugal loads due to the high speed of rotation. If improperly installed this can cause thermocouples to become detached, possibly damaging the rig. The Duralco epoxy resin used in the stationary installation was not considered sufficient for the rotating thermocouples in this respect. Figure 4-33 shows an example of the installation of the beads of rotating thermocouples within the rig. It can be seen that the final run of the thermocouples legs, where still covered by insulation, are glued into the surface using the Duralco resin. The thermocouple bead has then been peened to the measurement surface.

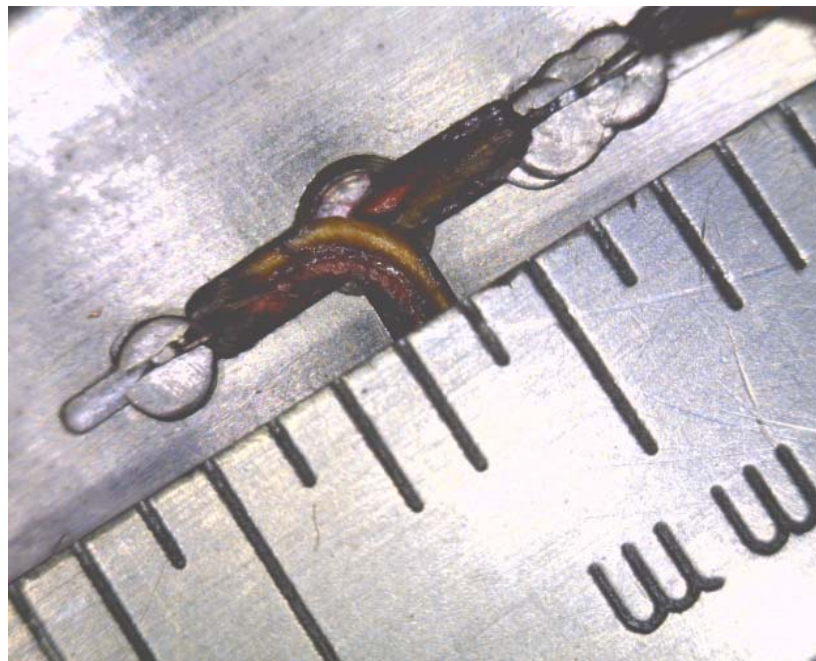


Figure 4-33: Rotating thermocouple embedding

Figure 4-34 shows the route of the rotating thermocouples out of the rig. From the measurement locations on each disc the thermocouples pass through the centre of the discs (1). Once the cover plates are bolted down this section of the thermocouples is not exposed to the stator wells. The thermocouples then pass through a transfer hole to the

lower cavity of the rotating section (2). From here to the lower radius of the section the thermocouples are embedded in machined slots and secured using epoxy resin (3). From here the thermocouples pass through the centre of the rotor shaft to the telemetry unit bolted to the front of the shaft (4).

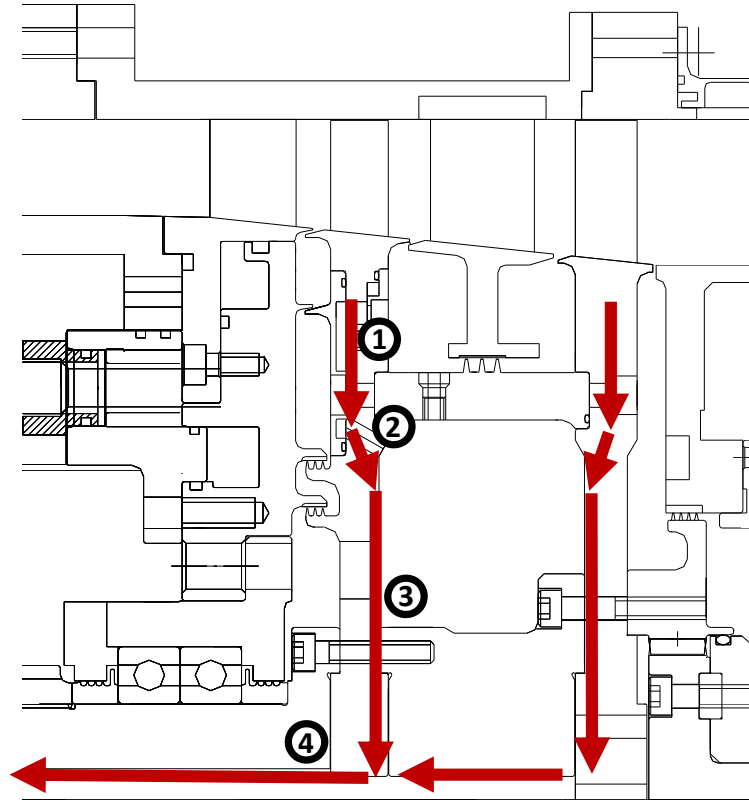


Figure 4-34: Rotating thermocouple rig routing

Figure 4-35 shows the thermocouples on the inner faces of the rotating section. As this section of lead out is not lying along a measurement surface it is not necessary to machine the face and resin in the thermocouples flush. This is also the area of greatest concern with regards to securing the thermocouples sufficiently for high speed test points. The figure shows how the thermocouples have been bunched and held down with spot welded covers. The bunch can be seen entering the transfer hole to the lower radius of the rotating section. Where the thermocouples are led to the individual measurement locations the thermocouples can be seen disappearing into the surface, where they pass through drilled holes to the measurement surface.

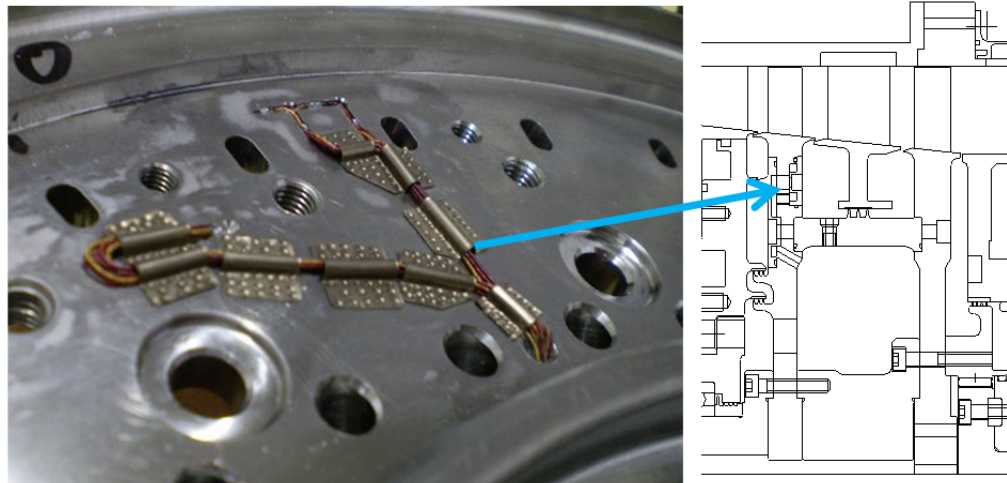


Figure 4-35: Upstream internal face, rotor 1 thermocouple routing

Figure 4-36 shows the downstream face of rotor 1 prior to thermocouple installation. The machined tracks into which the thermocouples are embedded are shown. These allow the thermocouples to run from the transfer holes from the higher radius disc locations to the rotor shaft. The exit of the transfer hole from the higher radius section is seen at the end of the machined tracks. The hole through which the thermocouples pass to the central rotor shaft can be seen in the centre of the disc at the opposite end of the machined tracks.

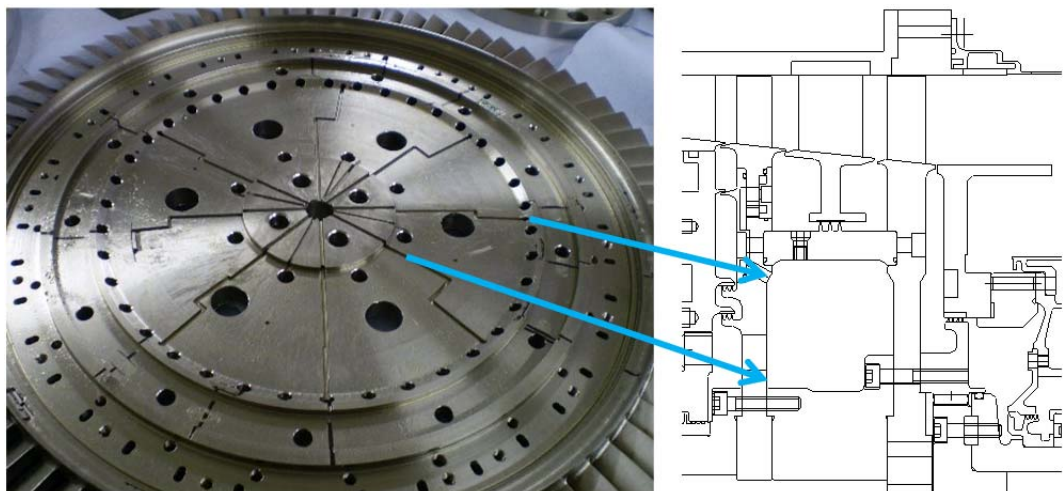


Figure 4-36: Rear face tracks, rotor 1

Figure 4-37 shows the assembled rotating section of the test rig. The image shows the complete assembly comprising two rotor discs and the rotor shaft. The upstream and downstream bearing carriers can also be seen. The rotating frame thermocouples can be seen leaving the end of the rotor shaft forward of the upstream bearing carrier.

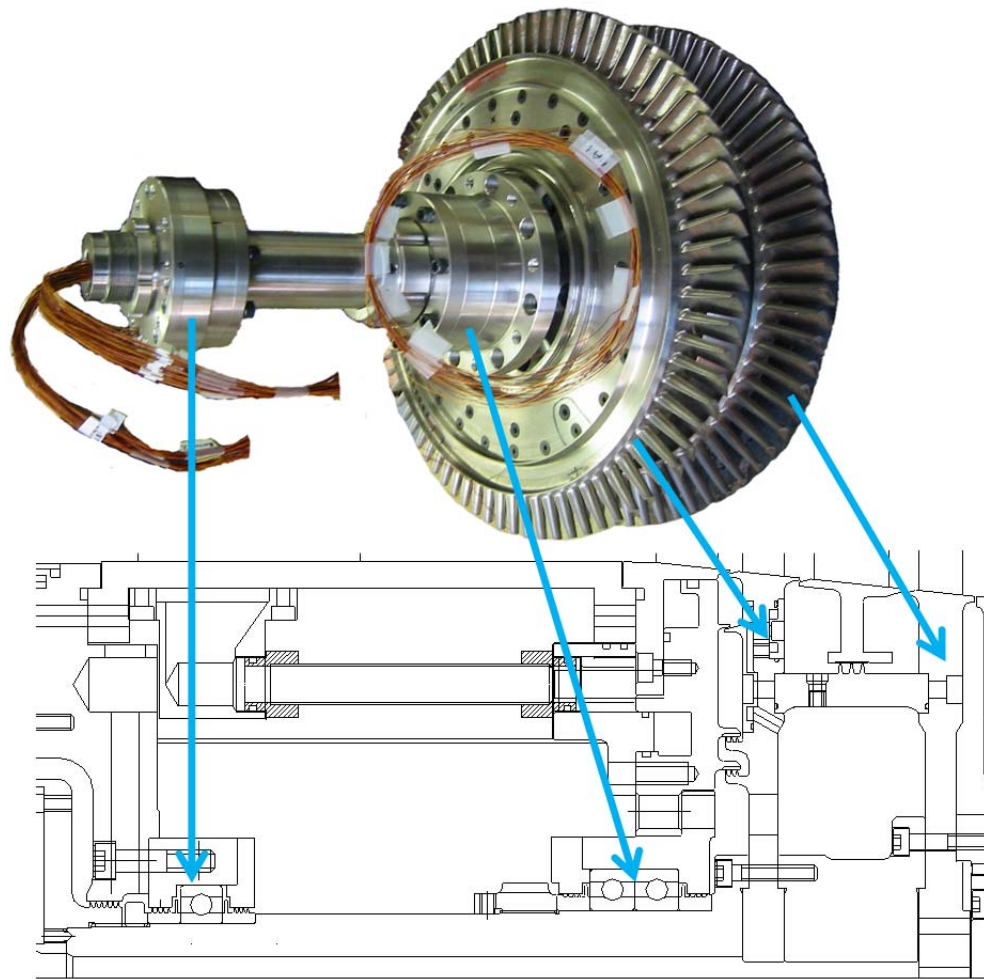


Figure 4-37: Assembled rotating section

Figure 4-38 shows the telemetry unit module attached to the end of the rotor shaft. The thermocouples can be seen gathered and laid within the unit before installation of the telemetry unit cover plate. Although not visible in this image, the telemetry unit cold junction modules are positioned directly below the plate on which the thermocouples are laid.

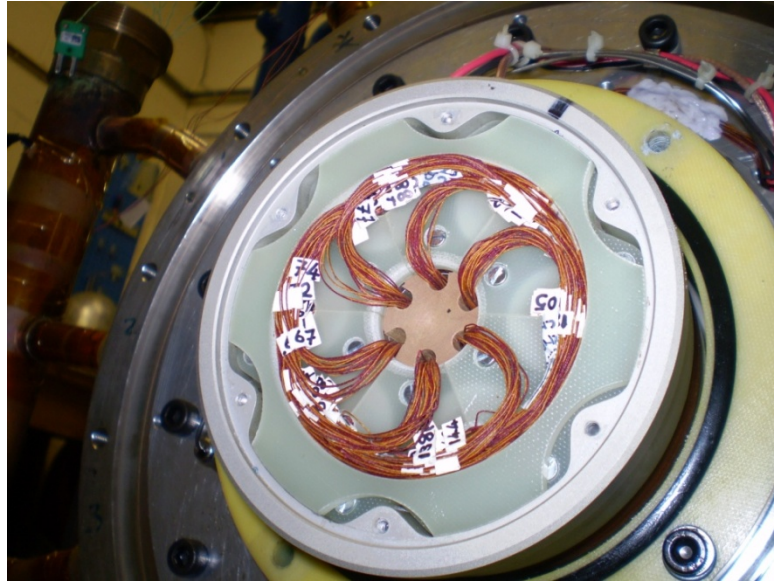


Figure 4-38: Telemetry unit to rotating thermocouple installation

4.10 Temperature Measurement Uncertainty

Due to the importance of the thermocouple measurements to the MAGPI test program conducted on the TSW test rig, great care was taken in the calibration process as described in the previous sections of this chapter. Childs et al (2011) conducted a review of the temperature measurements toward the end of the test program. The representative uncertainty for all temperature measurements was found to be ± 0.3 K. The contributions to uncertainty identified by Childs et al (2011) are summarized in Table 4-1.

Source of Uncertainty	Mitigation Technique	Uncertainty
Wire Non-Homogeneity	Thermocouples manufactured from common material batch	-
Calibration	Through calibration technique of all DAQ temperature channels	± 0.1 K
Measurement Junction	Calibrated PRTs used for cold junction measurements of both stationary and rotating temperature measurements	± 0.1 K
Thermocouple Extension Wires	Extension wires removed by locating DAQ (in temperature controlled environment) near test facility	-
DAQ resolution	PXI DAQ specified with resolution an order of magnitude smaller than required temperature resolution	-
Installation of Thermocouples	Thermocouples peened into rig surface to reduce embedding errors	± 0.1 K

Table 4-1: Sources of Temperature Measurement Uncertainty

In Chapter 8 rig metal temperatures T_H are presented in normalised form ϕ , given in Equation 4-1. This allows the comparison of temperature measurement results between test runs where the temperature of the supplied coolant T_C and the main annulus gas temperature T_H may vary.

$$\phi = \frac{T_M - T_C}{T_H - T_C} \quad \text{Equation 4-1}$$

The uncertainty in the normalised parameter ϕ can be evaluated by:

$$U_\phi = \left[\left(\frac{\partial \phi}{\partial T_M} U_{T_M} \right)^2 + \left(\frac{\partial \phi}{\partial T_C} U_{T_C} \right)^2 + \left(\frac{\partial \phi}{\partial T_H} U_{T_H} \right)^2 \right]^{\frac{1}{2}} \quad \text{Equation 4-2}$$

The uncertainties in the temperature measurements, U_{T_M} , U_{T_C} and U_{T_H} are given the value obtained by Childs et al (2011) resulting in the equation for the normalised uncertainty of ϕ :

$$U_\phi = \left[\left(\frac{1}{(T_H - T_C)} U_{T_M} \right)^2 + \left(\frac{(T_M - T_H)}{(T_H - T_C)^2} U_{T_C} \right)^2 + \left(\frac{(T_C - T_M)}{(T_H - T_C)^2} U_{T_H} \right)^2 \right]^{\frac{1}{2}} \quad \text{Equation 4-3}$$

4.11 Pressure Transducer Calibration

The Scanivalve pressure transducer units, used for all internal test section pressure measurements, were calibrated by a UKAS accredited third party. Three unit types were used for these measurements including a 0-50 psi unit, a 0-100 psi unit and a dual range unit consisting of channels capable of both of these ranges. The uncertainty obtained after calibration was 0.017 % for the 0-50 psi units and 0.023 % for the 0-100 psi unit. This is reported in Turner et al (2008).

A study was conducted in order to assess the angle sensitivity of the main annulus total pressure measurements. This was carried out in order to ensure representative measurements could be made, even with some misalignments between annulus flows and the probes in the leading edges of the NGV rows.

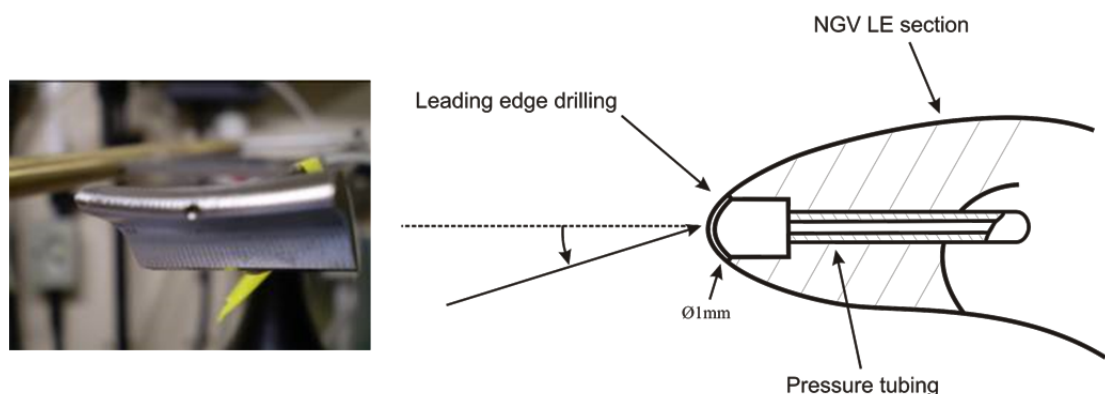


Figure 4-39: Angle sensitivity test, Turner et al (2008)

Figure 4-39 shows the dummy NGV used for the study as well as a diagram of the pressure tubing installation and swept angle used in the study. The opening of the pressure drilling was lightly countersunk in an attempt to reduce the angle sensitivity. In order to assess the sensitivity a jet was then directed onto the NGV. The NGV was rotated on an axis parallel to the leading edge and passing through the centre of the pressure inlet. Figure 4-40 shows the results of the study where the NGV has been

turned ± 10 deg from the flow. The study was conducted for two jet velocities, where the data is presented in terms of the leading edge Reynolds number. The percentage error in total pressure is calculated from the measured deviation from the maximum total pressure recorded where the NGV pressure tap is incident to the jet. The dynamic head is calculated at the maximum total pressure, where dynamic head $= u^2/2g$. The variation in dynamic head with angle is then calculated by the variation in velocity u , where u is found from the variation in total pressure. The error in dynamic head at a given angle is then the deviation from the maximum. Up to an angle of ± 5 deg the angle deviation from the flow stream shows little effect on the measured pressure.

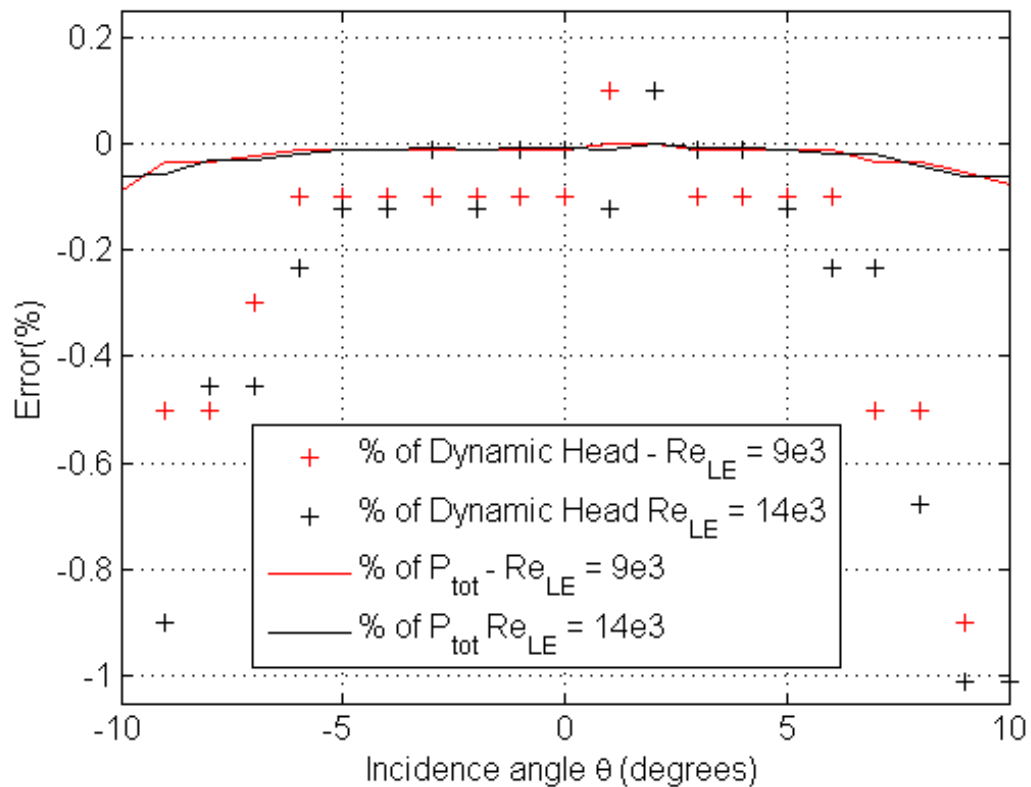


Figure 4-40: Angle sensitivity study results, Turner et al (2008)

4.12 Pressure Tap Installation

Figure 4-41 shows examples of pressure taps installed within the test section. The locations shown are total pressure measurements from the leading edge of a NGV on row 1. As with the thermocouples installed in similar locations, the profile was milled out. The instrumentation was then installed, and the NGV re-profiled using a female mould and Duralco resin. Total pressure measurements were made via bell mouthed tapping's with an internal diameter of 0.5 mm. Static pressure measurements were made via flush straight drilled tapping's with an internal diameter of 1.0 mm.



Figure 4-41: NGV 1 total pressure taps

Figure 4-42 shows the pressure tap lead out method during installation of the instrumentation. On the left a section of an NGV can be seen part assembled with a number of pressure tubes exiting the part. At this stage the tubing has been soldered into place on the back of a pressure tapping at a measurement location on the NGV part. As the test section is assembled the piping is routed through the rig, in this case through one of the aerodynamic struts passing through the main annulus, to the outer radius of the rig. The image on the right shows the piping exiting the rig where it is soldered to an intermediate manifold. From these manifolds, mounted on the outer rig casing,

connections to the Scanivalve pressure transducer units are made via flexible Scanivalve tubing which is easily routed and disconnected when necessary to gain access the the rig.



Figure 4-42: Pressure tap lead out

4.13 Pressure Tube Manufacturing Faults

During the analysis of the phase one test data by Smith et al (2012), incompatibilities between pressure measurements and sealing flow rates in the upstream wheelspace were observed. Upon investigation by the research group at TFMRC, small manufacturing defects were discovered in the pressure tubing lead outs. Figure 4-43 shows the imperfections found in the tubing, and how once bent these imperfections can cause a rupture in the tubing wall.

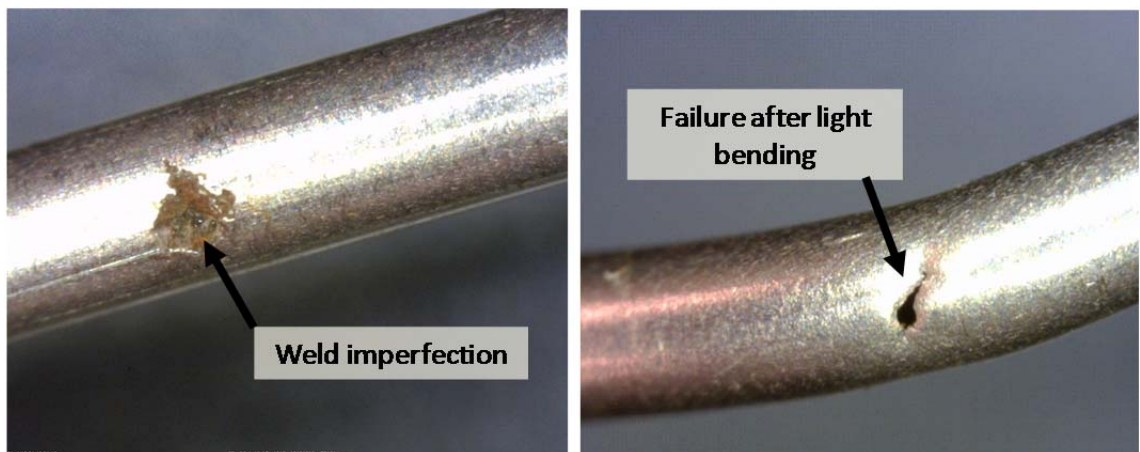


Figure 4-43: Manufacturer defect in pressure lead out tubing

Although the imperfections should not have been present, upon consultation with suppliers it was concluded that the initial imperfections were a result of the tubing being of re-drawn and welded type manufacture. The imperfections were a result of oxidation of the chromium content. The pressure taps used in the wheelspace measurements required tight turns to exit the rig, leading to the failure at these measurement points. The faulty lines and those considered at risk, but not showing any evidence of failure, were replaced for phase two testing with seamless drawn tubing. For the early test points where the test section supply rates were affected by the erroneous measurements, augmented flow rates were used. The method through which this study was conducted and the flow rates corrected is discussed in Chapter 8.

4.14 Flow Meters Calibration

The main annulus mass flow measurement is made via a venturi section in the supply pipe work between the DART air supply and the pre-rig inlet settling chamber. The venturi parameters, designed to BS1042, are given in Table 4-2. The measurement equipment consists of a standard venturi test section, an upstream static pressure measurement, the inlet total temperature and the pressure drop across the section. The differential pressure measurement was made by a Mensor unit, calibrated by an accredited UKAS third party, giving an uncertainty of 0.015 % of span.

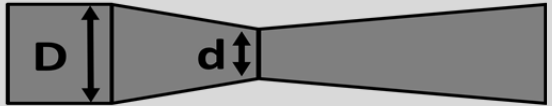
Main Annulus (DART) Venturi Parameters		
D(mm)	250	
d(mm)	129.95	
β	0.52	

Table 4-2: Main annulus supply venturi parameters

The cooling flow and balancing flow supplied to the test section as well as the upstream wheelspace air vented from the rig are measured via hot film flow meters. Figure 4-44 shows one of the instruments installed in the cooling flow air line prior to the rig. The sensor consists of the black section joined to the copper pipe by silicon connectors. The signal lead out can be seen plugged into the sensor. Within the sensor is a heated wire. As air flow passes over the wire it is cooled, reducing the resistance. The mass flow through the sensor is therefore proportional to the resistance. The meters were calibrated by a UKAS accredited third party to an uncertainty of $\pm 1.3\%$ of the measurement point. The flow meter calibrations were reported in Turner et al (2008).



Figure 4-44: Hot Film Flow Meter installed in cooling air line

4.15 Summary

The calibration and installation of the TSW measurement instrumentation has been described in detail. Particular care has been taken with the preparation and calibration of thermocouples, which has resulted in a temperature measurement uncertainty of ± 0.3 K.

5 Rig Operation Procedure

5.1 Introduction

In this chapter the start up, operation and shut down of the TSW rig will be discussed. This will highlight the necessary steps needed to ensure the required settled test points were reached at the required experimental parameters. However this section does not discuss operation of the DART air supply, other than monitoring of supply parameters to the TSW rig. A detailed description of the DART engine and its operation can be found in Turner et al (2000). Due to the long time scales of the TSW test program, close adherence to the operating procedure was vital in order to obtain repeatable, valid data. This section does not identify specific valves by location but rather gives an overview of the methodology of the rig operation. Rig data will be presented in order to highlight the critical operating parameters. A full start up check list for the TFMRC air system can be found in Appendix B.

5.2 Rig Pre-Start Up Procedure

Before the rig is supplied with any airflow a number of initial checks are made. These are intended to allow monitoring of the rig during the rest of the start-up procedure and of the atmospheric operating conditions.

- The atmospheric pressure is measured and recorded using a laboratory barometer.

- The data logging equipment is switched on. In order for the DAQ system to be identified on the data system network this must be done before the data logger PC is booted.
- The instrumentation leads are checked for any disconnected channels. This is done at both the rig and DAQ ends of the connection. This step is of particular importance after a geometry change, where it is necessary to disconnect a number of pressure taps to aid removal of the top half of the rig casing.
- The air conditioning unit in the DAQ room is set to 20°C. The unit is located within the DAQ cabinet. After the unit has been switched on the DAQ cabinet is closed for the duration of the test.
- The large extractor fan in the roof of the TSW test cell is switched on. This is required in order to keep temperatures down in the test cell once the rig is operational.
- The rig monitoring console is switched on. This provides the vital rig parameters in the event of a DAQ PC failure.
- Finally the rig is turned by hand. This is done by turning the coupling between the TSW rig gearbox and dynamometer. This ensures the rig is free to rotate before any load is applied.

After the initial checks the Hydrovane air supply is prepared. The Hydrovane supply is required for a number of pneumatic control valves as well as the telemetry module cooling air. It is also used to pressurise the dynamometer lubrication circuit.

- All outlet valves from the Hydrovane are initially closed. The oil and water separators located on the Hydrovane line are emptied.

- The three phase isolator for the Hydrovane power supply is then switched on and the Hydrovane started.
- Once the Hydrovane compressor has initially pressurised (identified by a change in compressor pitch) the outlet valve is opened. A large air storage tank is located immediately downstream of the Hydrovane. In the event of a Hydrovane failure the tank provides a limited amount of air supply to allow a shutdown of the rig before loss of control of the pneumatic valves.
- The telemetry cooling flow rotameter is then opened allowing cooling flow to enter the rig. The path of the telemetry cooling flow through the rig is shown in Figure 5-1. The flow crosses the main annulus through aerodynamic struts before moving radially inwards toward the telemetry unit.

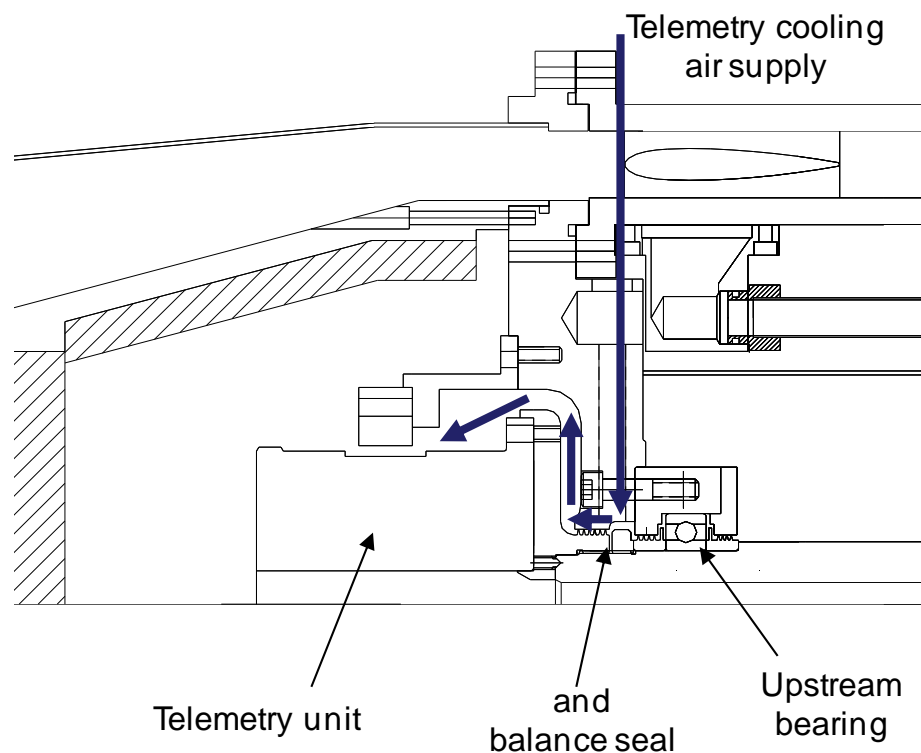


Figure 5-1: Telemetry cooling supply path

- A drain valve is then opened between the Hydrovane and dynamometer. This allows excess water to be bled from the line. When no more moisture is seen to exit the valve, it is closed.
- An air regulator is then opened on the DART line which pressurises the dynamometer oil mist lubrication system. The regulator for the lubrication system is set to 1bar gauge.
- The safety blow off valve for the DART air supply is then checked. This valve is activated when the Hydrovane is pressurised and closes the blow off valve on the DART line. If the Hydrovane fails or the emergency stop button is depressed the valve opens, venting the DART air to atmosphere and cutting off the main annulus flow to the TSW rig. The emergency stop button is pressed as part of the start up procedure. It must be manually re-set before the blow off valve can be re-closed. The test is done before the DART air supply is started.

Once the pneumatic valves, which are controlled via Hydrovane air, are online the ATLAS Copco compressor can be started. The ATLAS compressor supplies both the main cooling flow and the upstream wheelspace balance flow as discussed in chapter 3.

- Water valves are opened for the inlet air cooler. This is a water to air type cooler located just upstream of where the cooling air supply enters the test rig.
- All ATLAS lines to the test rig and neighbouring test cells are closed.
- The TSW main annulus inlet and exhaust valves are opened. In operation the DART provides mass flow through these valves. Although not active at this point in the rig preparations, the valves are opened to prevent over pressurisation of the rig when the DART is started, which could lead to damage of internal rig seals and instrumentation.

- A number of ATLAS line valves are then opened so that when switched on the ATLAS air exits the line via a bypass valve which is open to atmosphere.
- The compressor room extractor fan is then switched on. Without this in operating it is possible for the compressor room temperature to reach a level high enough to trip cut outs on both the ATLAS and Hydrovane compressors.
- The ATLAS compressor is then started, with the output exiting via the bypass valve.
- With the majority of the ATLAS output exiting via the bypass valve the ATLAS line valves are opened to allow some ATLAS air to path through an inline air drier.
- Once through the drier, this proportion of air then exits to atmosphere via a second bypass valve. The first bypass valve is then slowly closed until the total mass flow from the ATLAS compressor is passing through the drier unit and then through the second bypass valve.
- The rotameter supply for the cooling flow to the rig is then opened. With the second bypass valve fully open the flow rate into the rig is less than 10 gs^{-1} . The bypass valve is then slowly closed and the rotameter opened until a cooling flow of the order required for the commencing test is reached and the ATLAS outlet pressure is approximately 3.2 bar.

Once the Hydrovane and ATLAS air supplies have been set, the dynamometer is prepared to take load. This includes both the oil lubrication system and the water pressure across the load cell.

- Initially, the three phase power supply is switched on. The automated load and unload buttons are checked. These allow the rig operator to change the

dynamometer setting from outside the test cell. During the set up procedure one operator is required in the test cell to confirm the required movement of the sluice gate lead screws while a second operator operates the controls. The lead screw is then set to a position to give a load equivalent to approximately half that required at full rig speed.

- The dynamometer oil supply is then switched on. A visual check is made to confirm the lubrication circuit is working via a sight glass. The oil vapour extractor is turned on.
- The dynamometer water supply and cooling system is then prepared. Supply valves for the water reservoir, pump system and cooler are opened. The pump is then switched on as well as the cooler fans.
- The pump bypass valve and the dynamometer flow valves are then adjusted to give a dynamometer inlet pressure of approximately 20 psi and an exit pressure of approximately 10 psi.
- Finally the rig to dynamometer gearbox lubrication system is opened. This system works from a passive pump so will not operate until the rig begins to turn over.

5.3 Rig Start Up Procedure

Once the steps outlined in section 5.2 have been completed the DART engine is started. This pressurises the main annulus supply line and almost immediately begins to turn the rig. Figure 5-2 shows an example of the speed increments of the rig, from stationary up to the design speed of 10630 rpm. The speed can be controlled by both altering the rotational speed of the DART engine, and therefore the mass flow through the rig, and also by altering the dynamometer load.

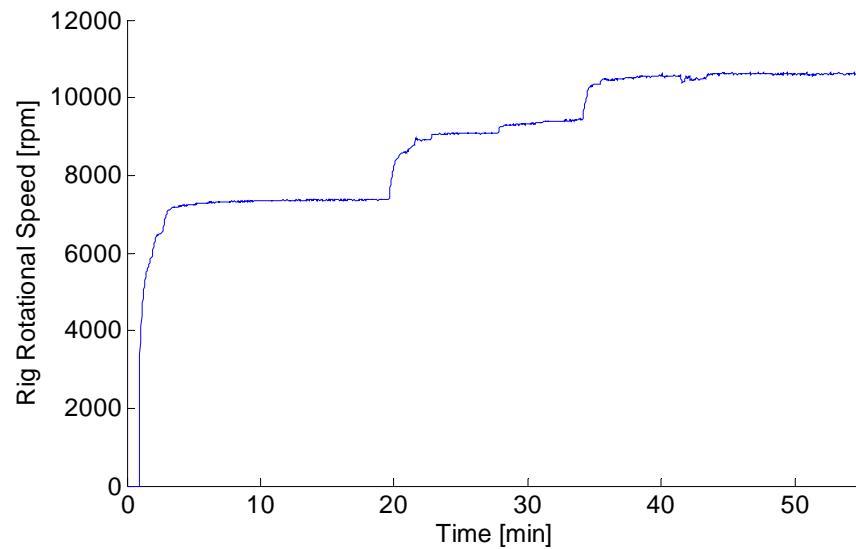


Figure 5-2: Rig speed steps during standard start up process

The speed increments are necessary in order to preserve the life of the rig bearings. The bearings are sensitive to temperature in terms of both the working temperature of the grease and changes in loads due to the expansion and contraction of the surrounding material and bearing carriers. Thermal shock can also limit the useful life of the bearings.

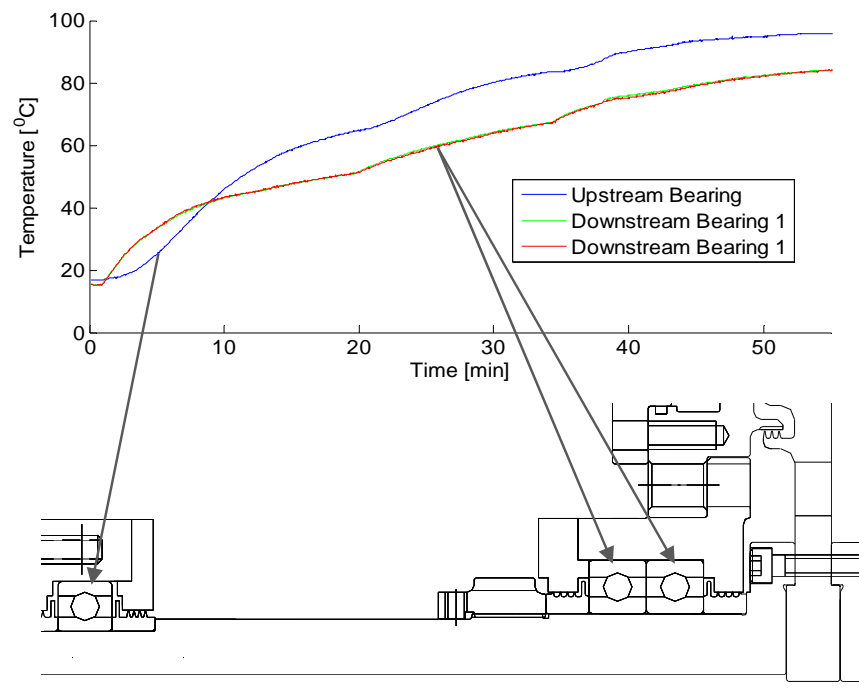


Figure 5-3: Rotating section bearing operating temperature history

Figure 5-3 shows the temperatures of the three rig bearings during the start up procedure. The bearing temperature is a function of the rotational speed, the surrounding metal temperature and the axial load placed on the bearings. The axial load is taken by the two downstream bearings. As the speed of the test rig is initially increased it can be seen that these two bearing see the steepest temperature gradient as the axial load on them increases. The downstream bearing temperature rises less quickly due to the lack of axial load; the main mode of bearing heating comes from the frictional heating due to the rotational speed. However, the temperatures of the upstream bearing and downstream bearings are seen to cross at a run time of around 9 minutes. At this point the rig temperatures have increased with the increased mass flow and temperature of the main annulus supply. However, the housing in which the two downstream bearings run also forms part of the coolant supply path, whereas the upstream bearing has no direct coolant supply. The coolant reduces the temperature of the material surrounding the downstream bearings, dropping the temperature below that of the upstream bearing.

Over the course of the MAGPI program the rig bearing arrangement was updated. Initially the two downstream bearings were arranged back to back, however during early phase 1 testing high bearing temperatures were seen, exceeding the recommended bearing grease temperature. The downstream bearings were replaced with identical 15° tapered units, however the rearmost bearing was flipped axially so that both bearing tapers faced the same direction. This arrangement was used until the end of the phase one tests. For phase two testing the bearing arrangement was again examined and improvements made by increasing the taper angle of the two downstream bearings to 25°.

Figure 5-4 shows the ISO bearing life predictions of Coren et al (2010) for the three bearing arrangements used in the test facility, where bearing life in hours is plotted against axial load. It can be seen that each increment in bearing arrangement substantially increases bearing life. The increase in bearing life is due to the increased ability of the arrangement to manage axial load, which in turn lowers bearing temperatures.

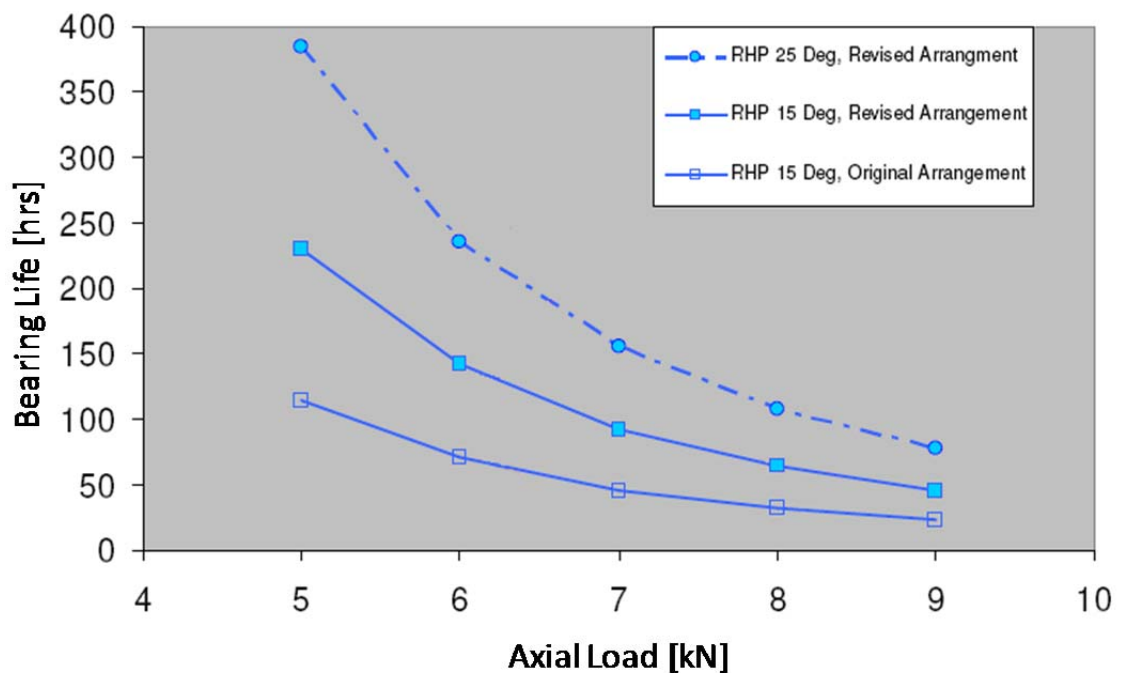


Figure 5-4: Bearing life prediction for three bearing arrangements, Coren et al (2010)

Figure 5-5 shows the five static pressure measurements taken at axial locations along the outer radius of the main annulus. The magnitude of the pressure and the pressure differential across each stage can be seen to increase with each increase in rig speed, where both the pressure and speed are a result of increased mass flow through the test section as the main annulus supply is increased. Close examination of Figure 5-2 shows a small step change in the rig rotational speed at 27 minutes which is not reflected in the main annulus pressures shown in Figure 5-5. This represents a point where the

dynamometer load has been reduced to increase rotational speed, without an increase in the main annulus mass flow.

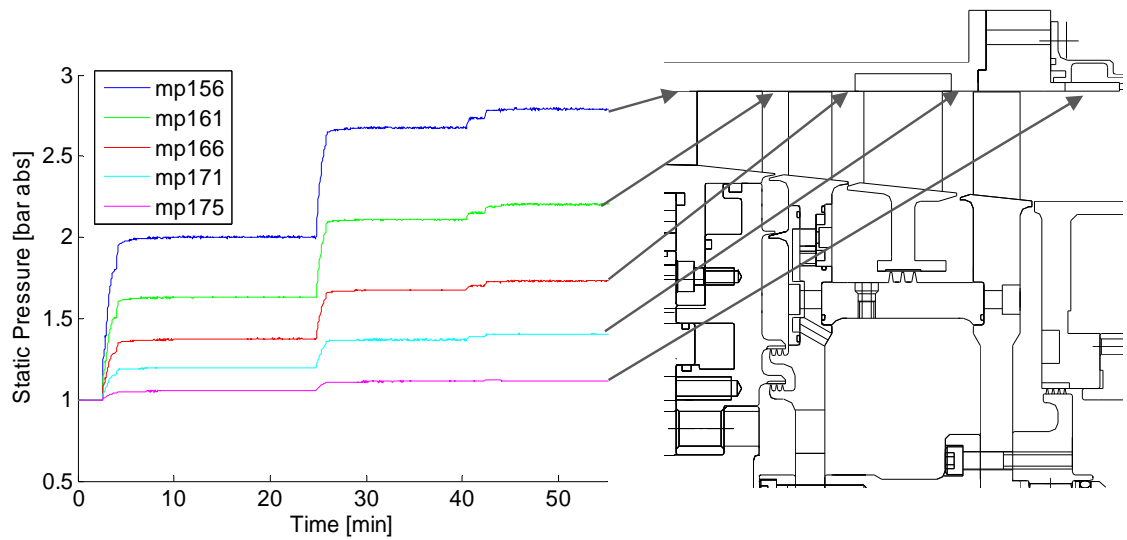


Figure 5-5: Main annulus static pressure

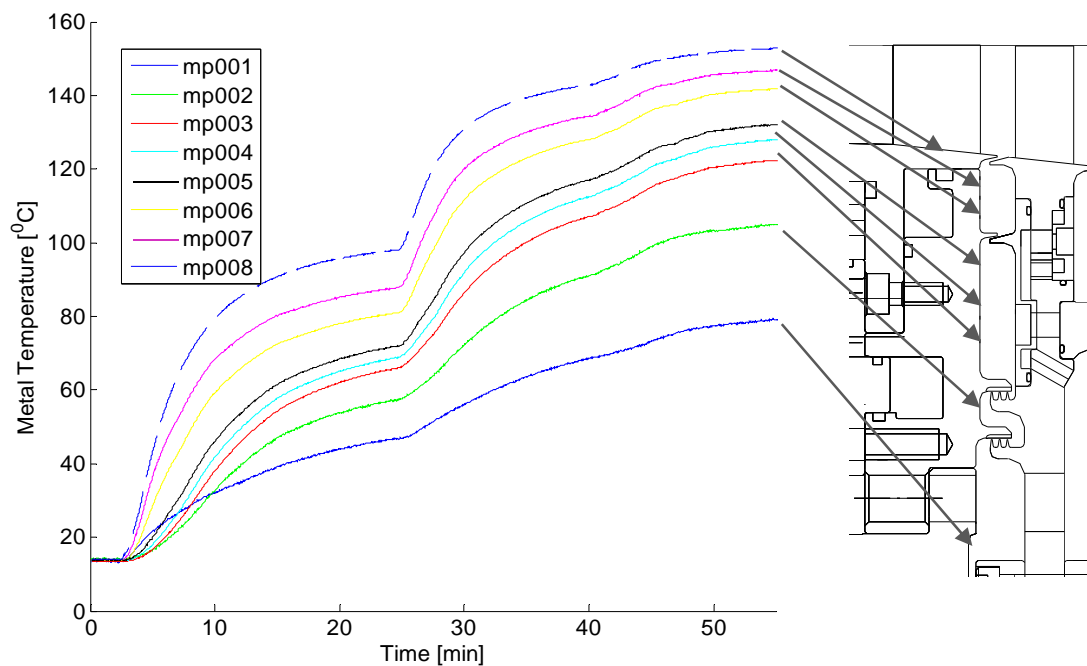


Figure 5-6: Upstream wheelspace stationary metal temperatures

Figure 5-6 shows the corresponding stationary metal temperatures in the upstream wheelspace. The temperatures can be seen to increase with each increase in rotational speed, where the resulting temperature rise is driven by the increase in the main annulus air supply temperature. The radial temperature gradient at any given point is a result of

the high radius main annulus temperature, conduction down the stator face and the lower radius temperatures which are largely controlled by the cooling flow rate. At the outer radius of the face at MP008 where the metal surface forms part of the main annulus the metal temperature is near the gas temperature. The temperature at MP008 can be seen to respond quickly to increases in the main annulus temperature. As the radius of the measurement locations decreases the temperature drops towards the coolant temperature and the response to the changes in main annulus temperature reduces.

5.4 Operating conditions

Once the test rig has reached design speed, the cooling air supply rate is set to the desired level. Although cooling flow is supplied during the start up procedure, the flow rate can change as the pressure within the test section rises. The balance and vent supply must also be adjusted in order to ensure the cooling flow enters the test section rather than passing through the upstream wheelspace into the main annulus. This is achieved by equalising the pressure across the lower claw seal. When this is achieved the mass flow through the seal is a minimum and it can be assumed that the cooling flow passes through the lower radius chamber of the upstream wheelspace, through the rotor 1 transfer holes and into the lower stator well cavity. Figure 5-7 shows an example of how these flow rates can be set. The main cooling flow of 40 gs^{-1} is shown as a blue arrow entering at the lower radius of the test section. In this instance the vent flow is higher than the balance flow, allowing the mid cavity pressure to be dropped.

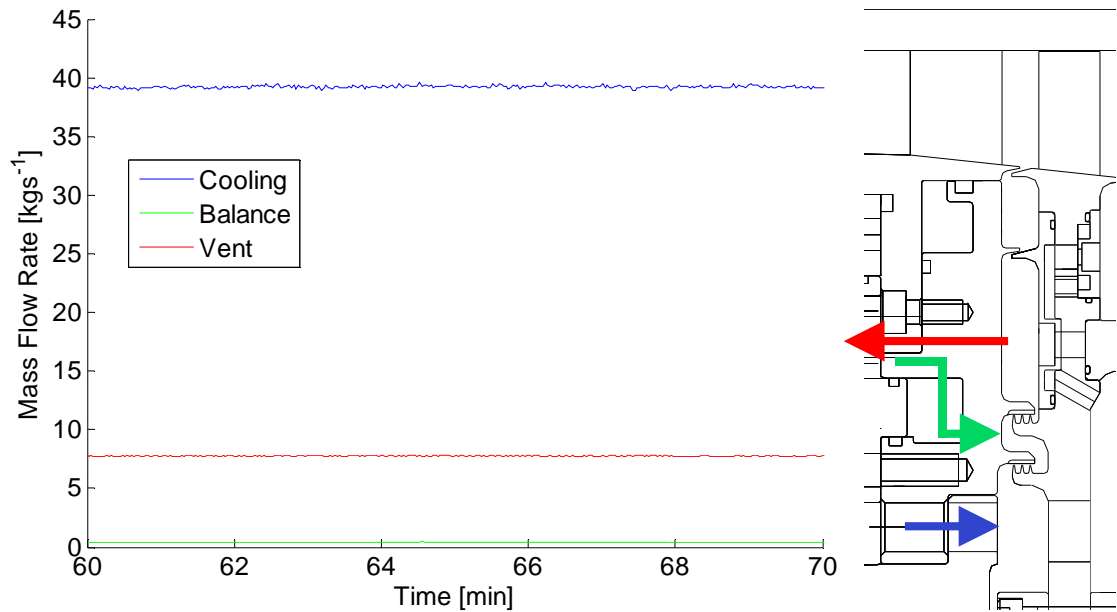


Figure 5-7: Test section air mass flows

Figure 5-8 shows the resulting pressures in the upstream wheelspace. The pressure within the wheelspace can be seen to reduce with radius in the cavities above the two claw seals. The two lower cavities, which lie either side of the lower cavity seal, can be seen to be at equal pressure.

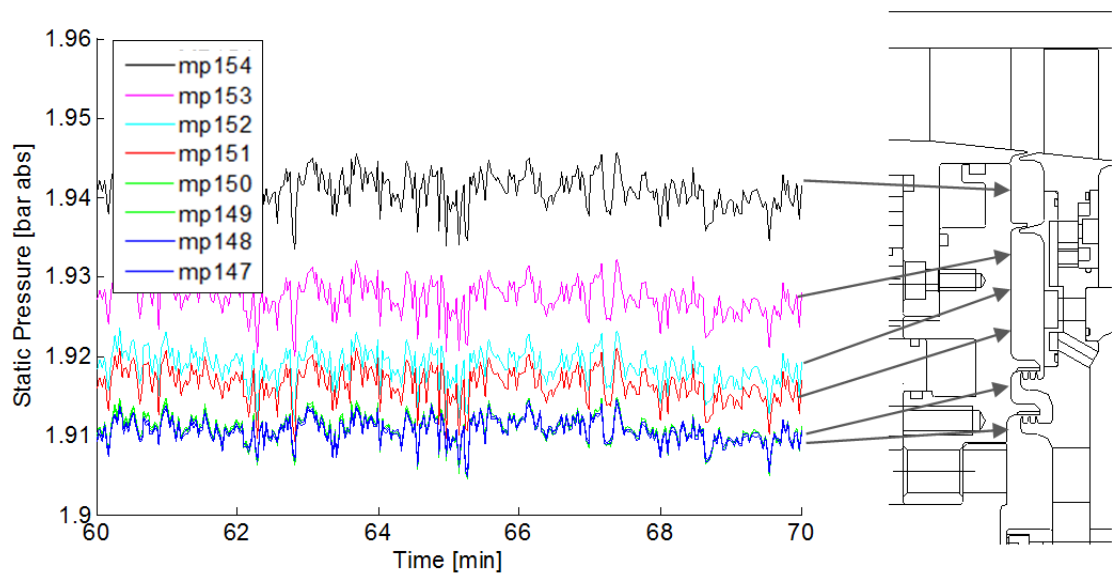


Figure 5-8: Upstream wheelspace static pressure

5.5 Data Settling

Once the rig is up to design speed, the main annulus is at the required mass flow rate and the wheel-space flows have been set, the rig temperatures are allowed to settle before test point data is taken in. This ensures consistent seal gaps within the test section and stable flow rates. Depending on operating conditions this can take up to 45 minutes, during which time all of the test rig parameters must be monitored and small adjustments made to mass flows and the dynamometer load to maintain the rig at the required operating conditions. In order for the test rig to be considered "settled" two temperature variation parameters must be met. These parameters were applied across the test matrix to ensure consistency. The two parameters consist of a limit to a moving average variation of rig metal temperatures. One parameter consists of a moving average of a selection of stationary temperatures and the other from a group of rotating temperatures. These temperatures were selected to cover both high and low radial positions, various axial locations and also the separate components which the test section consists of. The measurement locations were considered settled when the moving average of the temperatures was less than 0.2 K over a period of three minutes. Figure 5-9 shows near settled temperature data for the stationary face of the upstream stator well. The temperature can be seen to reduce with radius. Figure 5-9 shows near settled data for the rotating face.

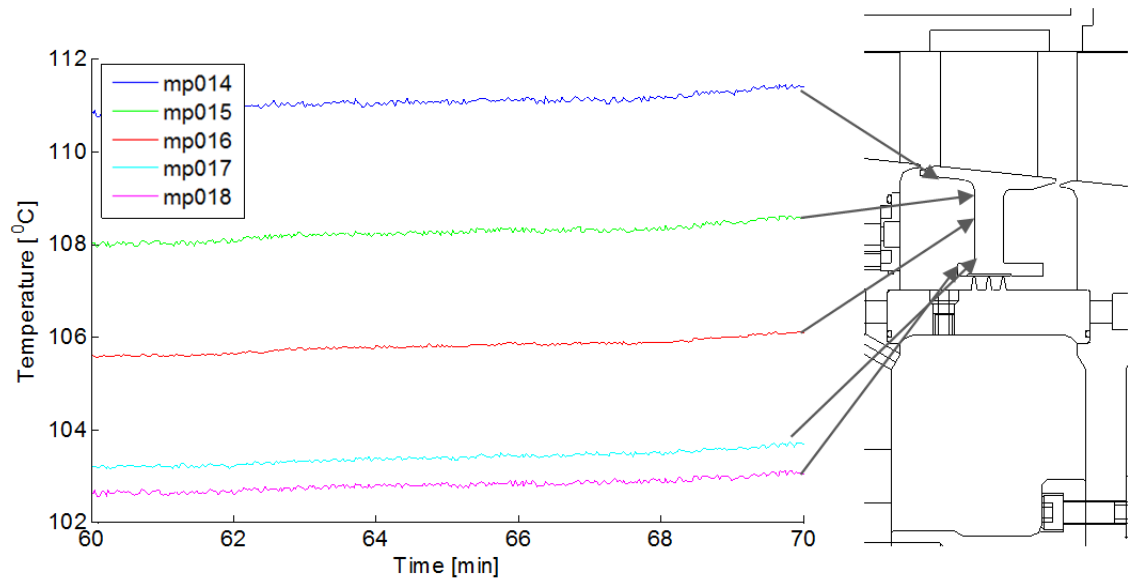


Figure 5-9: Stationary stator well temperatures at a near settled condition

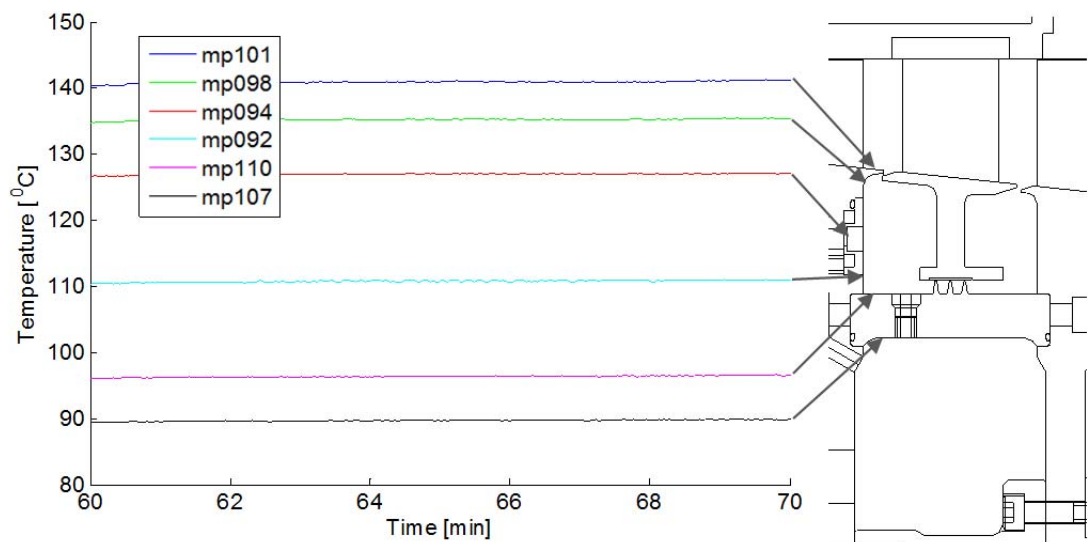


Figure 5-10: Rotating stator well temperatures at near settled condition

5.6 Changing of Flow Rates

For a given geometry a number of test points were required. These could often be obtained in the same test run. Once settled data was taken for a given point, the test section supplied was changed to the next required level. Figure 5-11 shows the upstream wheelspace supply between the end of a test point at a cooling flow of 30 gs^{-1} to a settled point at a 55 gs^{-1} . The balance and vent rates can be seen to be varied to match the new operating conditions. As the cooling supply rate increases the pressure in the lower radius cavity increases. This requires an increase in the balance supply to the inter-claw seal cavity in order to maintain the pressure balance across the lower claw seal.

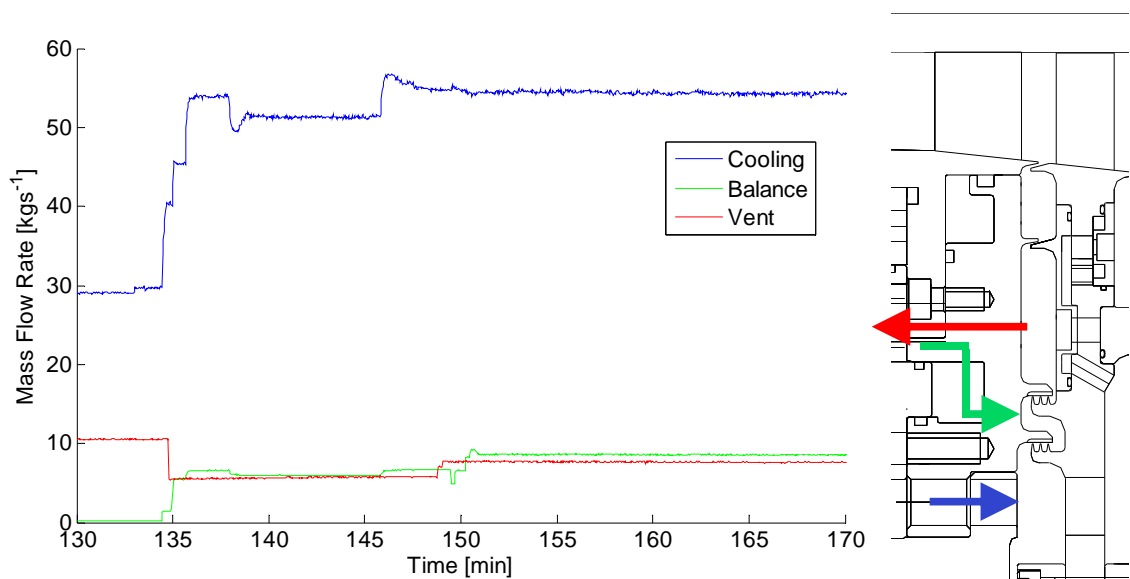


Figure 5-11: Test section air mass flows

Figure 5-12 shows the corresponding wheelspace temperatures across the same period. The temperatures can be seen to drop sharply at 135 minutes as the cooling flow rate is increased, with the effect being larger at the lower radius points near the cooling flow inlet. The rate of change in the rig temperature then drops as the temperatures approach the settled conditions between 155 - 170 minutes.

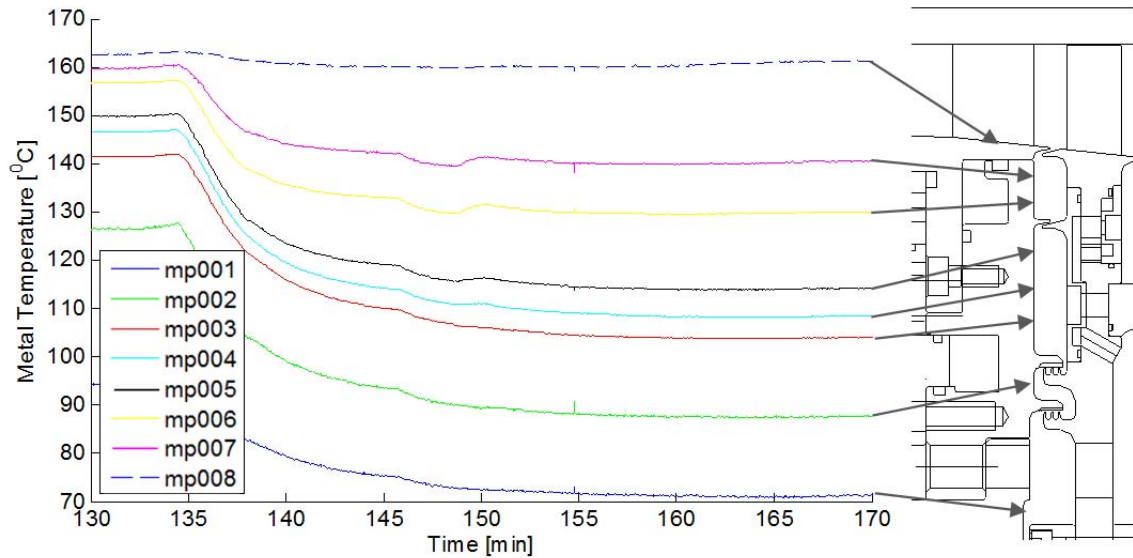


Figure 5-12: Upstream wheelspace stationary metal temperatures

5.7 Rig Shut Down Procedure

Once all settled data has been taken for a given test run, the rig is shut down in such a way as to prevent any damage to the rig in terms of thermal shock loads, or overheating due to the termination of cooling flows. The air, water and oil supplies are also returned to a safe state so as to be in the proper positions to start the next test and prevent damage to systems in the interval.

- Initially, the DART air supply is gradually reduced to zero flow, resulting in a quick reduction in speed.
- Cooling air supplies to the rig are maintained in order to prevent heat soak back from the hot outer radius of the rig to the low radius bearings.
- The dynamometer water circuit pump is switched off to prevent damage to the dynamometer seals. During rig operation the dynamometer setting may be adjusted to a point which is acceptable whilst rotating but results in a high inlet pressure when returned to stationary.

- The rig is then left in this state until all the rig metal temperatures are below 50°C. This is a nominal value well below that which could cause damage to rig components.
- The dynamometer and gearbox oil supplies are then shut off.
- The cooling air flow is then reduced by opening the ATLAS line bypass valves. Once fully open the ATLAS supply to the rig is closed off. The ATLAS compressor is then shut down
- The Hydrovane telemetry cooling and pneumatic valve lines are then closed.
- The dynamometer water circuit is closed to isolate the dynamometer and reservoir tank from the cooler circuit. The Hydrovane line air is then used to purge the cooler circuit. This is done to avoid freezing of coolant in the cooler which could lead to damage and a reduction in cooler efficiency.
- Finally the Hydrovane compressor is shut down and all valves returned to pre-test positions.

5.8 Data Processing

Once a run has been completed and the test rig shut down the data is processed into engineering units, saved and backed up. Figure 5-13 show the storage structure of the TSW rig data. The top level of storage contains directories for instrumentation reference data, calibration coefficients, commissioning data and test phase data. Both the instrumentation and calibration data files are referenced when converting test data to engineering units. Within the test phase folders are the run data files for each geometry run as part of a test phase. This level also contains an analysis folder for work pertaining to comparisons between geometries in the test phase. Within the geometry folder are the

test data folder and an analysis folder for comparison of different runs for a given geometry. The test run folder contains the individual test runs for a given geometry together with a run analysis folder and run plots folder.

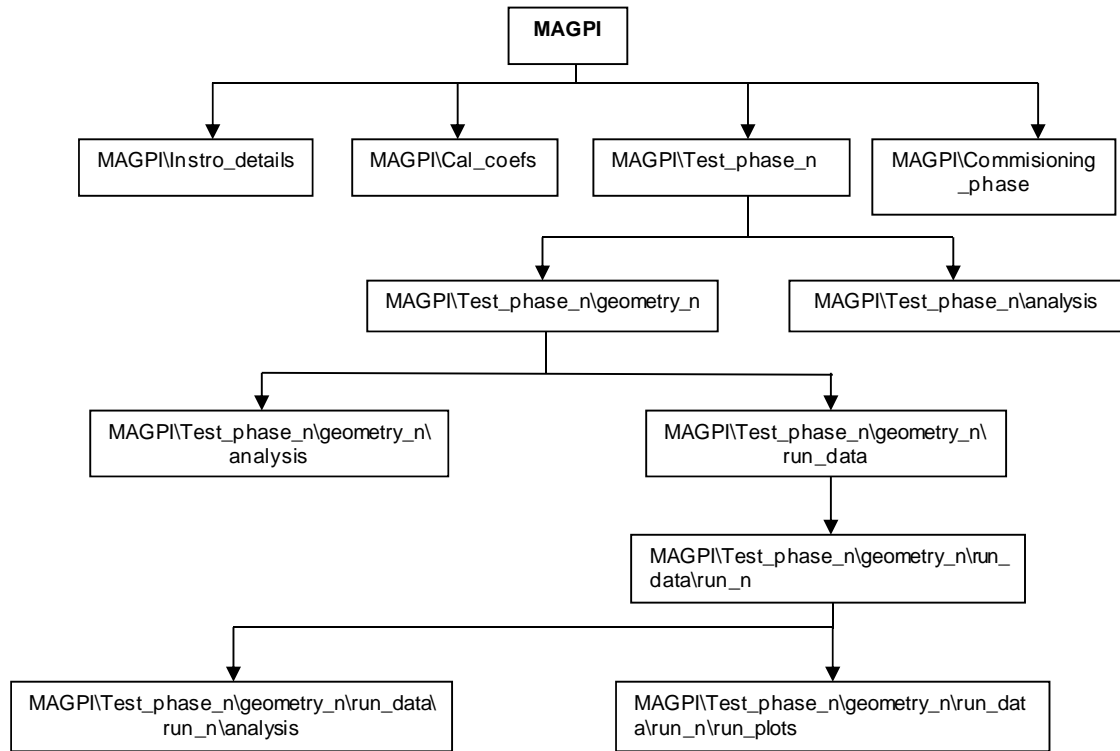


Figure 5-13: Test data storage structure

5.9 Summary

The operation of the TSW experimental facility has been described in order to highlight the complexities of operating such a test facility. The careful calibration and installation of instrumentation described in Chapter 4 together with closely controlled experimental procedures described in this chapter, ensured valid, high quality data was obtained across all experimental tests presented later in this thesis.

6 Gas Concentration Experiments

6.1 Introduction

In this chapter the instrumentation and experiments devised to satisfy the three distinct measurement objectives are discussed.

- Provide data to quantify interstage seal flows for a range of rig conditions
- Provide data to determine rim seal exchange flows for both bulk ingress and egress conditions
- Provide data to quantify re-ingestion into the test cavity

In order to meet these objectives three distinct experiments were devised. The experimental procedure for each is described in detail. The calculation method and equations used to estimate the flows for each experiment are also presented, including the derivation of uncertainty. In the second half of the chapter the measurement systems used to meet the objectives are introduced, together with information on the associated instrumentation. The carbon dioxide delivery and sampling system is discussed along with commissioning and proof of concept experiments.

6.2 Interstage Seal Flow Experiment

The Interstage labyrinth seal demand as discussed in Chapter 2 is one of the primary flows which affect the flow structure within the upstream stator well cavity. The displacement technique used to calculate this flow will be discussed in Chapter 7. In

order to support this technique an experimental method of measuring the seal flow was devised. Figure 6-1 shows the interstage seal flow experiment graphically. The ingress of main annulus gas into the cavity is shown as red, while the cooling flow (in this case being introduced through drive arm hole inserts) is shown by a blue arrow. A mixture of these two flows then passes through the interstage seal, shown as a green arrow. The carbon dioxide tracer gas, shown as orange, is injected directly upstream of the seal. A sample of the flow is then taken downstream of the seal. This is shown as a green and orange flow. As the carbon dioxide is injected at 100% concentration, the change in concentration, as measured at the downstream location, is a result of mixed stator well gas. This is calculated using Equation 6-1, where the mass flow through the interstage labyrinth seal \dot{m}_l , is a function of the mass flow of seeding gas \dot{m}_g and the measured concentration c_m downstream of the seal.

$$\dot{m}_l = \left[\frac{\dot{m}_g}{c_m} \right] \quad \text{Equation 6-1}$$

A simple case is shown in Figure 6-2. As before the stator well gas is shown as a green arrow and the seeding gas flow as an orange arrow. Carbon dioxide is shown as being injected at 2 gs⁻¹. The downstream concentration, shown as the mixed orange and green arrow, is measured at 5 %. Using Equation 6-1 this would indicate a seal flow of 40 gs⁻¹. This is a simplified case and ignores the ambient carbon dioxide content which will be present in the stator well gas, this is however accounted for when post processing results. Once an initial flow value has been measured the amount of ambient carbon dioxide can be estimated and the flow results adjusted accordingly.

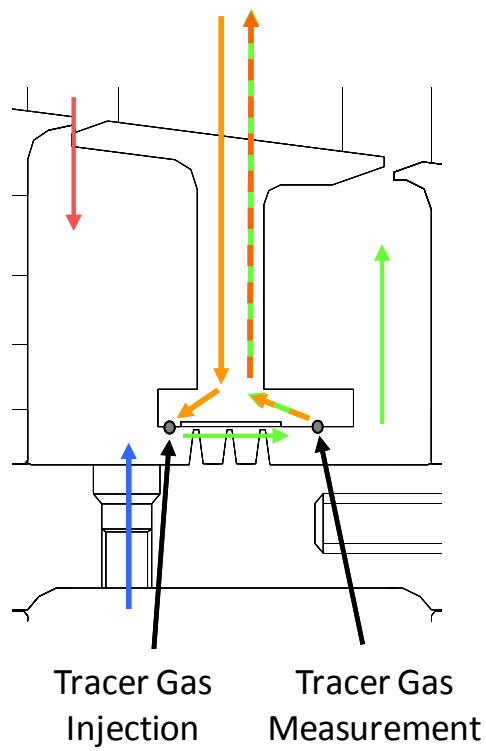


Figure 6-1: Interstage seal experimental flows

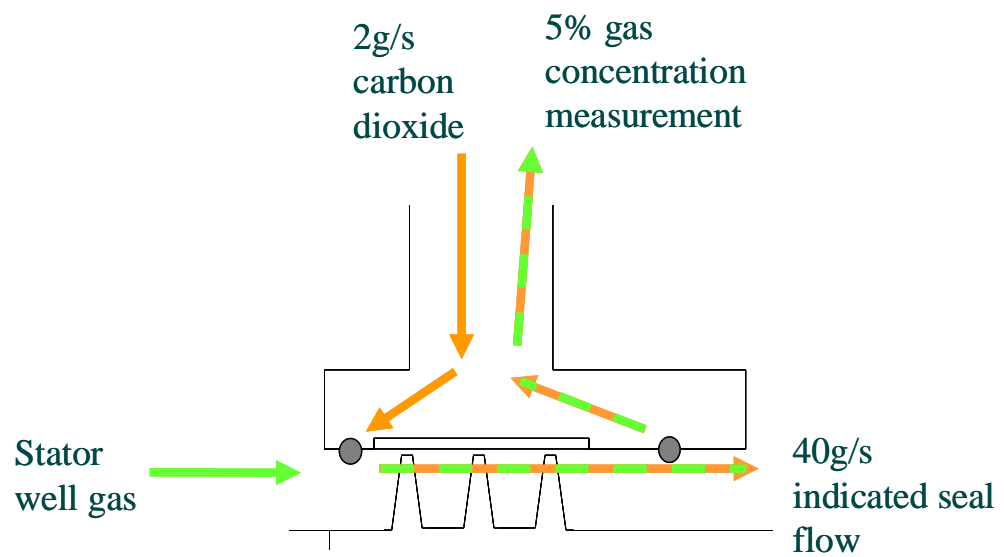


Figure 6-2: Simple seal flow case

6.3 Rim Seal Exchange Experiment

The rim seal exchange experiment was designed to study the interaction of the stator well flows with the main annulus flow. It allows the estimation of rim seal exchange flows by using a summation approach to provide values of ingress and egress. The experimental results can also give an indication of flow structures and bulk ingestion or egress. Figure 6-3 shows the primary flows involved. The coolant flow is shown in blue, being introduced through either the simulated lock plate slots or the drive armholes. At the stator well rim seal both main annulus gas, shown in red, and coolant flow is present. For conditions where rim seal flow is bi-directional main annulus gas will ingress into the cavity, whilst mixed main annulus gas and coolant will egress back out of the rim seal. Depending on the stator well conditions a proportion of the main annulus and coolant will pass through the interstage seal to satisfy the seal demand. The concentration measurement locations are shown located on the stator in the upstream and downstream cavity.

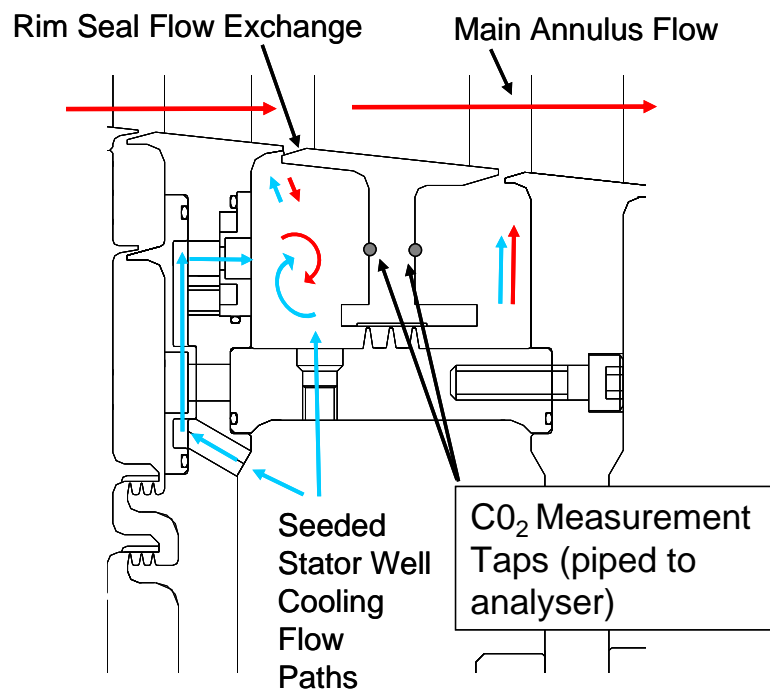


Figure 6-3: Rim seal experimental flows

In order to quantify these flow interactions the cooling flow is seeded with carbon dioxide tracer gas. Both the coolant and tracer gas are metered giving a known concentration before the mixture enters the test section. The tracer gas is injected into the coolant before it enters the rig, ensuring a homogeneous mixture. A concentration measurement is then taken within the stator well. The change in concentration together with a known interstage seal flow allows the rim seal exchange to be quantified. This method has the advantage of allowing the quantification of simultaneous ingress and egress through the rim seal flow. Figure 6-4 shows a comparison of a simple summation approach to the concentration measurement approach. For case A, a known cooling flow rate of 40 gs^{-1} has been used in conjunction with a known seal flow of 58 gs^{-1} to estimate the net ingestion of 18 gs^{-1} . This approach is limited by the assumption that the rim seal flow is unidirectional. For case B, where the cooling flow and seal flow are of the same magnitude, but supported by a concentration measurement in the cavity, rim seal exchange can be quantified. If the GC measured was in the region of 66% of the supplied coolant concentration, giving a dilution ratio of 0.66, this would suggest around 20 gs^{-1} ingress. A summation of the flows would then show that 2 gs^{-1} is egressing through the rim seal back into the main annulus.

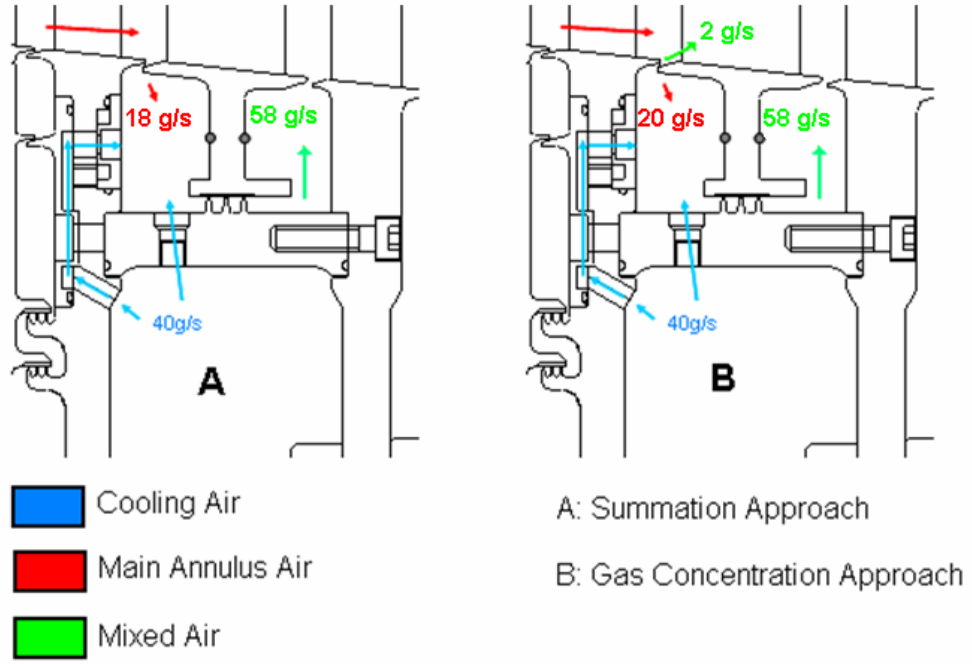


Figure 6-4: Comparison of summation and concentration approach

The carbon dioxide flow \dot{m}_g is mixed with the superposed cooling air flow \dot{m}_o before entering the test section. The total mass flow rate of the seeded cooling flow \dot{m}_s , is then calculated.

$$\dot{m}_s = \dot{m}_o + \dot{m}_g \quad \text{Equation 6-2}$$

From the known mass flows of carbon dioxide \dot{m}_g and cooling air \dot{m}_o , the concentration c_s of the supplied seeded coolant flow \dot{m}_s is calculated, taking into account the ambient carbon dioxide level.

$$c_s = \left[\frac{100}{\dot{m}_s} \right] \times \left\{ \dot{m}_g + \left[\left[\frac{\dot{m}_o}{100} \right] \times \text{Ambient } CO_2 \right] \right\} \quad \text{Equation 6-3}$$

From the calculated delivery concentration c_s and the concentration measured in the stator well c_m , a dilution ratio η is calculated. For this experiment the dilution ratio η can be used to indicated sealing effectiveness ε_c , where a value of 1 indicates no

ingestion into the cavity and a value of 0 indicates no coolant at the measurement location.

$$\eta = \frac{c_m}{c_s} \quad \text{Equation 6-4}$$

The dilution ratio/sealing effectiveness ε_c is then used to calculate the total flow into the cavity \dot{m}_c , which includes the imposed seeded coolant \dot{m}_s , and the ingested main annulus gas.

$$\dot{m}_c = \left[\frac{\dot{m}_s}{\eta} \right] \quad \text{Equation 6-5}$$

The rim seal exchange values for seal ingress \dot{m}_i and egress \dot{m}_e , can then be calculated.

$$\dot{m}_i = \dot{m}_c - \dot{m}_s \quad \text{Equation 6-6}$$

$$\dot{m}_e = \dot{m}_c - \dot{m}_l \quad \text{Equation 6-7}$$

6.4 Re-Ingestion Experiment

The re-ingestion test was devised to measure the amount of cooling air re-ingested into the stator well, where the cooling air had been egressed upstream of the stator well rim seal. Quantifying the re-ingestion of coolant gas is often difficult or impossible with temperature and pressure measurements alone. The main obstacle to this measurement is differentiating between re-ingested and normally supplied cooling air to a cavity. In order to address this an experiment was devised where the coolant supply paths to the stator well were blocked. Figure 6-5 shows the geometry and main flows for the experiment. It can be seen that both the drive arm holes and the simulated lock plates are blocked. The pressure balance and vent flow paths are also blocked. This ensures

that the coolant, shown as blue arrows must exit via the wheelspace rim seal into the main annulus. As the only path for the coolant to enter the stator well is through the stator well rim seal any, coolant detected in the stator well can be attributed to re-ingestion. This ingestion will be a mixture of coolant and main stream gas, shown in red.

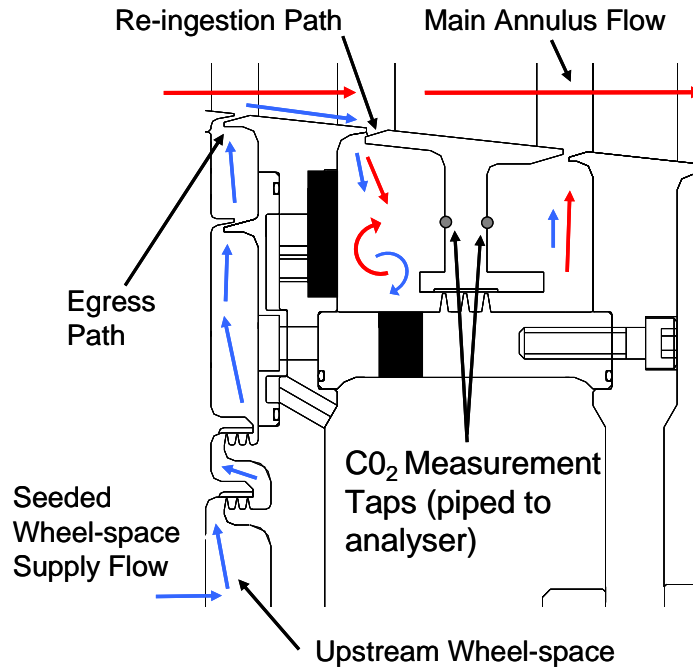


Figure 6-5: Re-ingestion experimental flows

Imposed sealing air \dot{m}_o , seeded with a known quantity of carbon dioxide \dot{m}_g , is supplied to the upstream wheelspace. The total supply of seeded air to the wheelspace \dot{m}_w , is calculated from these measured values.

$$\dot{m}_w = \dot{m}_o + \dot{m}_g \quad \text{Equation 6-8}$$

The concentration of the coolant supplied to the wheelspace can then be calculated.

$$c_s = \left[\frac{100}{\dot{m}_w} \right] \times \left\{ \dot{m}_g + \left[\left[\frac{\dot{m}_o}{100} \right] \times \text{Ambient } CO_2 \right] \right\} \quad \text{Equation 6-9}$$

Concentration measurements are then taken in the upstream and downstream stator wells. The dilution ratio η of the supplied wheelspace coolant flow concentration c_s , and the measured stator-well concentration c_m , can then be calculated. Unlike the rim seal experiment η cannot be used as an indicator of sealing effectiveness ε_c as there is no superposed flow to the stator well.

$$\eta = \frac{c_m}{c_s} \quad \text{Equation 6-10}$$

As the coolant delivery paths to the stator well are blocked the mass flow into the upstream stator well \dot{m}_c must come from rim seal ingress and be equal to the interstage seal flow \dot{m}_l . For re-ingestion experimental results discussed later in the thesis the interstage seal flow is calculated from the displacement technique discussed in Chapter 7.

$$\dot{m}_c = \dot{m}_l \quad \text{Equation 6-11}$$

The wheelspace flow which has been re-ingested into the stator-well \dot{m}_r can now be calculated.

$$\dot{m}_r = \dot{m}_c \times \eta \quad \text{Equation 6-12}$$

6.5 Gas Concentration Instrumentation

The system installed on the TSW rig in order to acquire the data required to satisfy the experimental objectives is shown in Figure 6-6. Carbon dioxide is stored in a high pressure reservoir, shown in the bottom left of the figure. As the carbon dioxide leaves the reservoir and expands through the valve, the gas temperature reduces. In order to correct this, the carbon dioxide flows through an inline heater bringing the gas temperature back up to the required levels. This is discussed further later in this section. After exiting the heater the carbon dioxide passes through a Kobold flow meter. From

here the carbon dioxide can either be introduced into the coolant flow or directly into the rig through solenoid 7. When introduced into the coolant flow the carbon dioxide is injected upstream of the rig ensuring a homogenous mixture before the coolant enters the test section. The carbon dioxide is introduced after the cooling flow has been metered so that the ratio of each can be easily calculated. The lines connecting the solenoids to the rig are pressure lines during normal rig operation. The solenoids allow these lines to be broken when conducting the gas concentration experiments. Solenoid 7 is unique in that this line is used to supply carbon dioxide to the rig rather than take gas samples. Solenoids 1-6 are connected to 6 distinct measurement locations within the rig. When solenoids 1-6 are being used to take gas samples the line is diverted from the Scanivalve units to the manifold shown at the top of the figure. From the manifold the gas is passed to the analyser. The analyser consists of two Nondispersive Infrared "NDIR" sensors. This is discussed further in section 6.9.

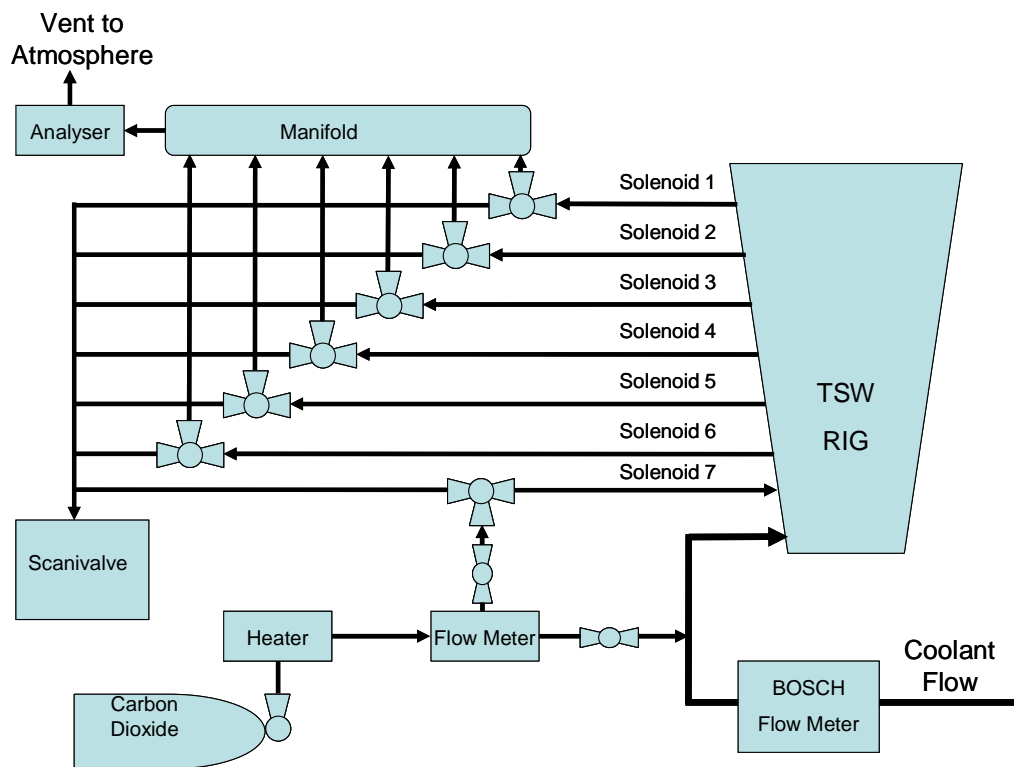


Figure 6-6: Gas concentration supply and measurement system

6.6 Carbon Dioxide Supply

Carbon dioxide was selected as the tracer gas for the experiments. Carbon dioxide was seen to be used successfully by both Gentilhomme et al (2003) and Dunn et al (2010). It is also easy to handle, is non corrosive and has a unique absorbance, making it suitable for use with the chosen gas analyser type, discussed in section 6.9. Nitrous oxide, as used by Phadke and Owen (1988a) and Dadkhah (1992) was discounted. Nitrous oxide can be more complex to handle and is also a strong oxidiser so can become unstable if contaminated. The carbon dioxide gas bottles are shown in Figure 6-7. Each bottle contains 25 kg of carbon dioxide. A maximum test time of 15 minutes at 10 gs^{-1} per gas concentration test point requires 9 kg of carbon dioxide.



Figure 6-7: Carbon dioxide supply

Carbon dioxide can pose an asphyxiation risk, to mitigate against this risk both the test cell and facility control station were equipped with Carbon Dioxide alarms.

6.7 Carbon Dioxide Flow Meter

The flow meter used to measure the carbon dioxide mass flow into the rig or cooling air is shown in Figure 6-8. Carbon dioxide enters the meter from the left hand side from the inline heater via a 3/8" compression fitting. The carbon dioxide exits via a similar fitting on the right hand side. The output is connected to the valves controlling the flow to either the rig cooling flow or solenoid 7. The signal output is connected via a RS-232 interface seen on the left hand side of the unit.



Figure 6-8: Carbon dioxide mass flow meter

The meter is a bypass capillary type system calibrated for carbon dioxide, the range of the meter being 0 - 5 gs^{-1} for an output of 0 – 10 Volts. The meter was calibrated at a gas temperature of 20 °C, with a measurement uncertainty of 0.05 % of full scale per °C variation.

6.8 In-Line Heater

The uncertainty in seeding gas mass flow measurements due to gas temperature variation was identified during early commissioning runs of the seeding system. Due to the pressure drop from the carbon dioxide reservoir to the mass flow meter, the gas temperature was found to reduce by more than 10 °C from the ideal delivery temperature. An inline heater was installed to limit the gas temperature variation. Figure 6-9 shows the gas delivery temperature to the mass flow meter for a number of heater configurations. Where data is presented for low pressure cases the carbon dioxide bottle regulator has been set to reduce the pressure drop between the bottle and flow meter. With no heating, the gas temperature was seen to drop below 15 °C for the low pressure case and 10 °C for the high pressure case. With the heater at full capacity the gas delivery temperature was seen to increase to over 30 °C for the high pressure case.

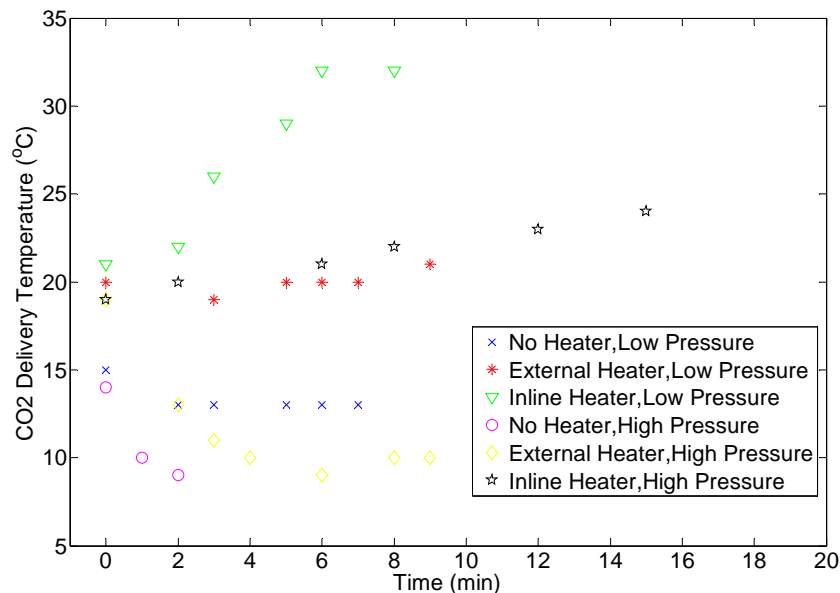


Figure 6-9: Seeding gas temperature variation

This test confirmed that the inline heater had the required capacity to heat the carbon dioxide to a delivery temperature greater than that required. In order to control the gas temperature a variable transformer was added to the power supply for the heater.

6.9 Gas Analyser

Non-dispersive infrared (NDIR) sensors were chosen for the gas concentration experiments. A NDIR sensor operates on the principle that molecules absorb light at specific wavelengths. The Lambert-Beer law states that the absorbance of a gas is directly proportional to its concentration. Carbon dioxide has strong absorbance at 4.26 μm . The absorbance band is unique when compared to other gases so is easily detected. Figure 6-10 shows the basic layout of a NDIR sensor. Light is shone through the sample gas. The light which is not absorbed by the gas then passes through a filter to the detector.

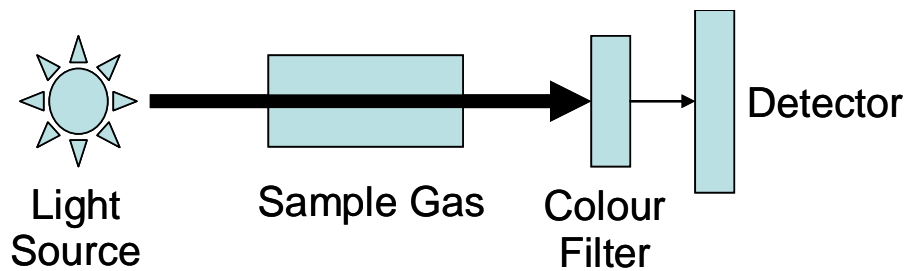


Figure 6-10: Basic NDIR sensor fundamental operation

A bespoke analyser unit was constructed for the TSW rig gas concentration experiments. The unit is shown in Figure 6-11. Gas samples from the rig are split between two NDIR sensors, one sensor having a range of 0-1 % volumetric concentration of carbon dioxide, the second having a range of 0-10 % volumetric concentration. Once passed through the analysers the gas is vented to atmosphere. The voltage output of the sensors is connected through the TSW rig DAQ system. The NDIR sensors were calibrated using reference grade carbon dioxide mixed with reference grade nitrogen. The 0-1 % sensor was found to measure the reference gas

within $\pm 0.003\%$. The 0-10 % sensor was found to measure within $\pm 0.005\%$ of the reference gas.

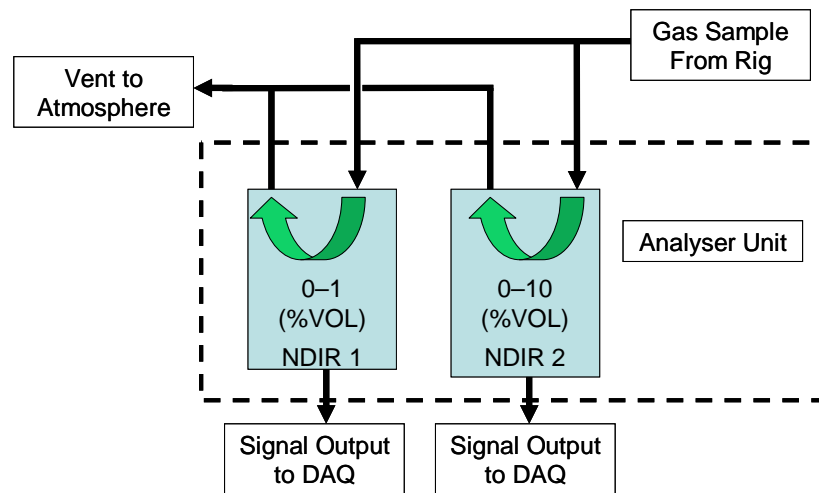


Figure 6-11: TSW gas analyser unit

6.10 Solenoid Measurement Locations

The measurement locations corresponding to the solenoids are shown in Figure 6-12. Solenoid 7 is located directly upstream of the interstage seal and allows pure carbon dioxide to be injected at this point. Solenoids 1 and 2 are located directly downstream of the seal. Samples taken here give the carbon dioxide concentration of gas passing through the seal. Solenoids 3 and 4 are located in the downstream cavity around the mid height of the stator face and allow samples of the gas in the cavity to be taken. Solenoids 5 and 6 are located in the upstream cavity at the mid height of the stator face.

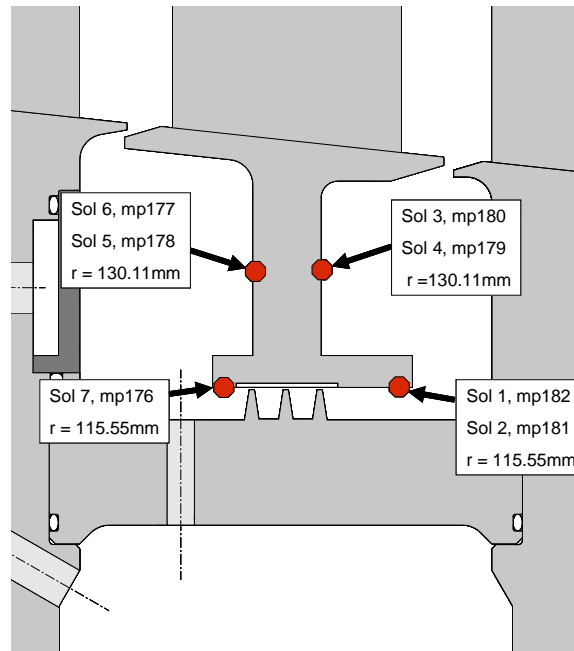


Figure 6-12: Gas concentration seeding and measurement radial and axial locations

The gas concentration measurement locations are shown in their circumferential position in Figure 6-13. Solenoids 5 and 6, located in the upstream cavity, are spaced by 104° . This allows measurements in the cavity to be compared for circumferential variation. Similarly, solenoids 3 and 4 in the downstream cavity are spaced by 101° . Solenoids 2 and 1 are located 75° and 168° from solenoid 7 respectively.

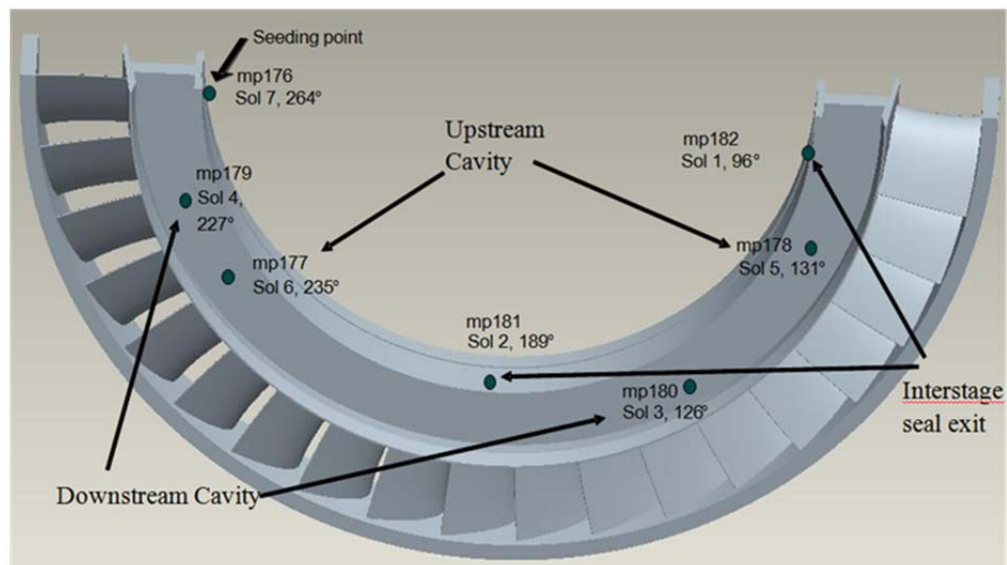


Figure 6-13: Gas concentration seeding and measurement circumferential locations

6.11 Gas Concentration System Commissioning

Before installation of the gas concentration system on the TSW rig, an off rig test was conducted. The test was devised to both test the seeding and measurement system as well as to test the data acquisition and processing techniques. Figure 6-14 shows the layout of the experimental apparatus. The main cooling air supply was attached to a length of steel pipe with a 75mm diameter. Cooling air was supplied to the pipe at a rate of 50 g/s. Carbon dioxide was then injected into the pipe. A sample of the air and carbon dioxide mixture was then taken from a tapping downstream of the injection point. The tapping was made 100 diameters downstream of the carbon dioxide injection point to ensure homogenous mixing of the seeding gas with the main flow. The gas sample was piped to the analyser and a concentration measurement taken before being vented to atmosphere.

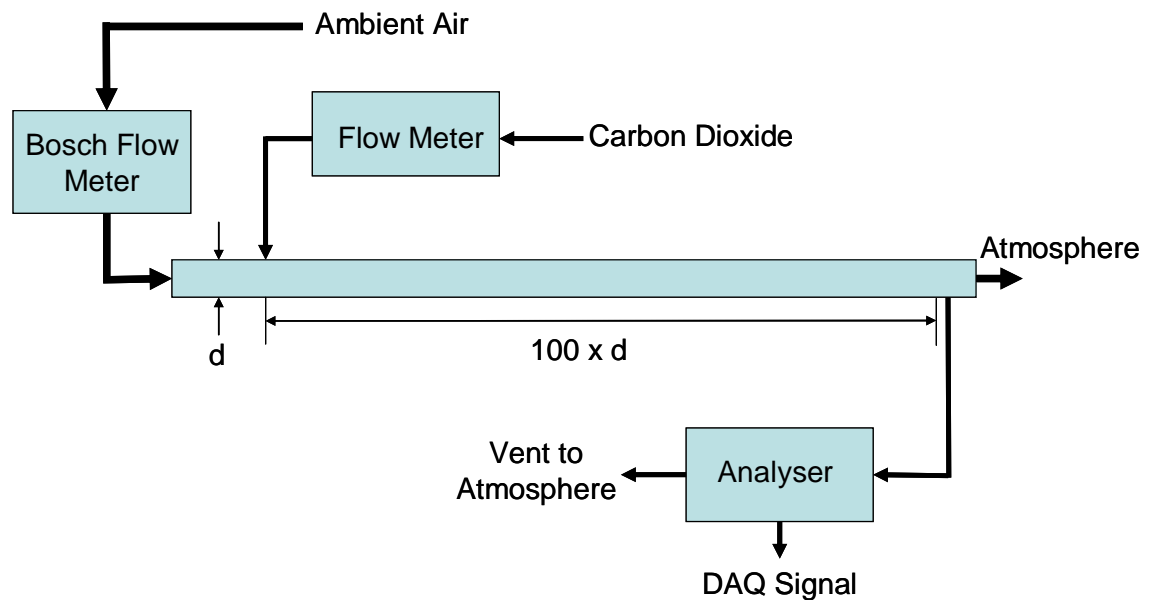


Figure 6-14: Pipe test gas seeding experiment

Both the carbon dioxide and air entering the pipe were metered. The concentration was then calculated from these two values, corrected to allow for the ambient carbon dioxide

content in air. Figure 6-15 shows the carbon dioxide seeding rate supplied to the pipe against the calculated carbon dioxide concentration and the measured carbon dioxide concentration. The concentration calculated from the known air and carbon dioxide supply rates are shown as red markers. The blue markers represent the concentration measured by the analyser. For the flow rates tested it was found that the measured concentration value was within 0.1 % of the calculated supplied concentration.

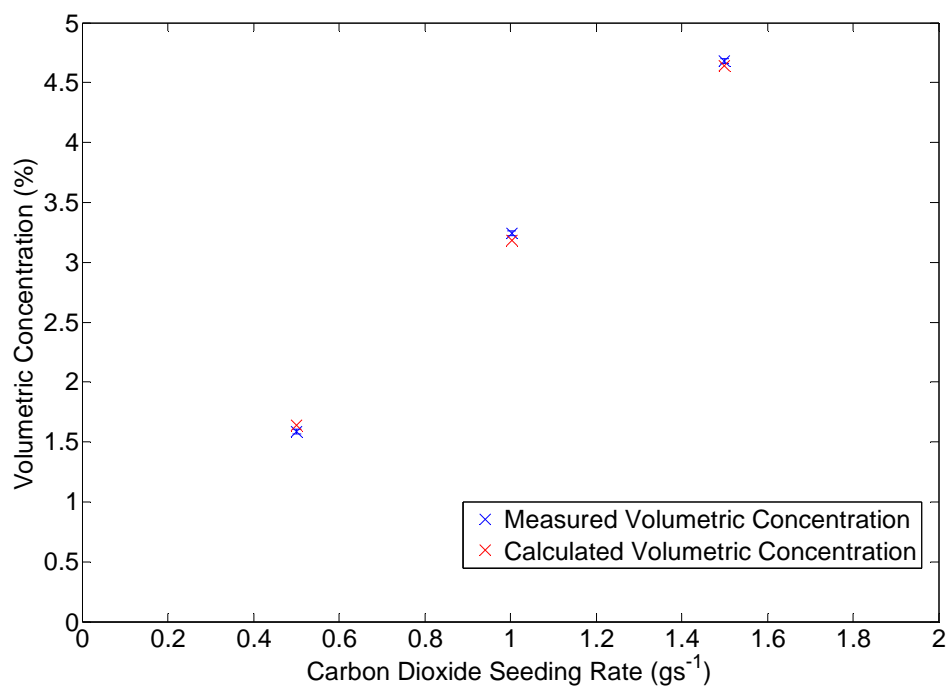


Figure 6-15: Pipe seeding test experiment results

Once the analyser system had been installed on the TSW rig a second commissioning test was conducted. Both the rig inlet and outlet were closed. The rig was then supplied with cooling air which raised the rig pressure ensuring the pressure drop and mass flow through the gas analysers was representative of real gas concentration test conditions. A metered amount of carbon dioxide was then injected into the cooling air being supplied to the rig. Concentration measurements were then made at each of the six measurement locations in the test section individually. Figure 6-16 shows the measured concentration

for all six locations obtained for three carbon dioxide seeding flow rates. For each flow rate, the concentration measured at the six measurement locations were found to be within 0.1 %.

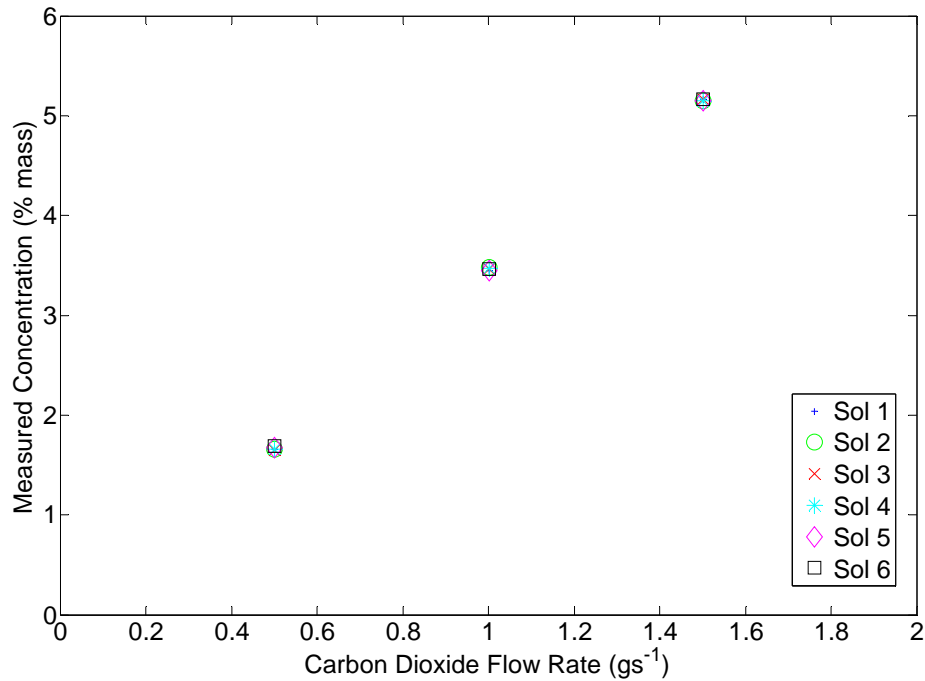


Figure 6-16: Seeded coolant rig flood test

The gas analyser does not have an auxiliary pump but relies on the pressure gradient between the sampling point and the drop to atmospheric pressure after the analysers to drive the flow. For an NDIR analyser the measurement is independent of the gas velocity, which was shown by Phadke (1988), as discussed in Chapter 2. The transport time of a gas sample to the analyser however is dependent on the velocity. During the second commissioning test the response time of the analysers from the opening of each solenoid was recorded and found to be less than 20 seconds. All test points taken during the gas concentration experiments were taken after 60 seconds of a solenoid opening.

6.12 Uncertainty of Gas Concentration Experiments

The main sources of measurement uncertainty in the gas concentration experiments come from the cooling air supply \dot{m}_o , the carbon dioxide seeding flow rate \dot{m}_g and the measured concentration c_m . These uncertainties are summarised in Table 6-1.

Measurement	Source of Uncertainty	Uncertainty
\dot{m}_o	Bosche Hot Film Flow Meter	$\pm 1.3 \%$
\dot{m}_g	Kobald Capillary Flow Meter	$\pm 0.005 \%$ per deg from calibration gas temperature
c_m	VAISALA Flow Meter	$\pm 0.1 \%$

Table 6-1: Contributions to gas concentration measurement uncertainties

The three experiments presented in Section 6.2, 6.3 and 6.4 are all based on these three measurements, where flows within the test section are calculated following the steps described. The uncertainty in each step of the three calculations can be determined from the general equation, where $z = f(x, y, w, \dots)$:

$$z_\phi = \left[\left(\frac{\partial z}{\partial x} U_x \right)^2 + \left(\frac{\partial z}{\partial y} U_y \right)^2 + \left(\frac{\partial z}{\partial w} U_w \right)^2 + \dots \right]^{\frac{1}{2}} \quad \text{Equation 6-13}$$

The equations required for the gas concentration experimental analysis fall into three forms. For gas concentration equations of the form $z = x \pm y$:

$$U_z = \left[U_x^2 + U_y^2 \right]^{\frac{1}{2}} \quad \text{Equation 6-14}$$

For equations of the form $z = x/y$:

$$U_z = \left[\left(\frac{1}{y} U_x \right)^2 + \left(\frac{x}{y^2} U_y \right)^2 \right]^{\frac{1}{2}} \quad \text{Equation 6-15}$$

For equations of the form $z = xy$:

$$U_z = \left[(yU_x)^2 + (xU_y)^2 \right]^{\frac{1}{2}} \quad \text{Equation 6-16}$$

For equations of the form $z = \frac{100}{x} \left(y + \left(\frac{w}{100} \right) C \right)$:

$$U_z = \left[\left(\frac{100}{x^2} (y + w \times C \times 10^{-2}) U_x \right)^2 + \left(\frac{100}{x} U_y \right)^2 + \left(\frac{C}{x} U_w \right)^2 \right]^{\frac{1}{2}} \quad \text{Equation 6-17}$$

The gas concentration experiments rely on the assumption of complete mixing at the measurement locations. This assumption and the impact of incomplete mixing are discussed in Chapter 9.

6.13 Gas Concentration Experimental Procedure

The gas concentration experiments are conducted in conjunction with the main test matrix runs, apart from the re-ingestion experiment which requires its own specific geometry, as discussed in section 6.4. Where conducted in conjunction with a main test matrix run the procedure for taking the gas concentration data is started once settled cooling flow data has been taken. The necessary requirements for settled data have been discussed in Chapter 4. The process of taking gas concentration data for each of the three experiments is discussed in this section.

6.13.1 Interstage Seal Flow Experimental Procedure

The experimental procedure for obtaining the interstage seal flow experimental data is as follows:

- The carbon dioxide regulator is connected to the carbon dioxide bottle designated for the test (seen in Figure 6-7)
- The gas bottle valve is fully opened until the gauge reads 50-60 bar
- The regulator is set to an outlet pressure of 10 bar (this can require adjustment once the carbon dioxide begins to flow)
- Solenoid 7 is then opened. Under normal rig operation the scanivalve piping connected to model point MP176 is routed to the scanivalve pressure transducers. Once solenoid 7 is opened MP176 becomes the carbon dioxide seeding point. MP176 is no longer usable as a pressure measurement line until the solenoid is closed
- The valve which allows the carbon dioxide to solenoid 7 is then opened and gas begins to flow into the rig. The valve is adjusted until a flow rate of between 3 – 4 gs^{-1} is seen on the data acquisition VI
- Solenoid 1 is then opened. Under normal rig operation the scanivalve piping connected to model point MP182 is routed to the scanivalve pressure transducers. Once solenoid 1 is opened MP182 is routed to the gas analyser and becomes a concentration measurement location. MP182 is no longer usable as a pressure measurement line until the solenoid is closed
- The outlet to the gas analyser can be piped through a liquid in order to confirm a flow through the analyser
- The concentration is logged for ten times the transportation time of the gas from the rig to the analyser
- Solenoid 1 is then closed, returning MP182 to a pressure measurement model point
- Solenoid 2 is then opened and a concentration measurement made from MP181
- This is then repeated for solenoids 3 and 4, giving concentration measurements at MP180 and MP179
- Once the required measurements have been taken the gas bottle regulator is closed. Solenoid 7 is left open at this point in order to de-pressurise the line
- Solenoid 7 is then closed. Solenoids 1, 2, 3 and 4 are then opened to purge the gas analyser, returning the carbon dioxide levels to ambient
- Solenoids 1, 2, 3 and 4 are then closed returning the rig to normal operating conditions

6.13.2 Rim Seal Exchange Experimental Procedure

The experimental procedure for obtaining the rim seal exchange experimental data is as follows:

- The carbon dioxide regulator is connected to the carbon dioxide bottle designated for the test (seen in Figure 6-7)
- The gas bottle valve is fully opened until the gauge reads 50-60 bar
- The regulator is set to an outlet pressure of 10 bar (this can require adjustment once the carbon dioxide begins to flow)
- The valve which allows the carbon dioxide to enter the rig cooling air is then opened. The valve is adjusted until a carbon dioxide flow rate of 3 gs^{-1} is seen
- Solenoid 3 is then opened. Under normal rig operation the scanivalve piping connected to model point MP180 is routed to the scanivalve pressure transducers. Once solenoid 3 is opened MP180 is routed to the gas analyser and becomes a concentration measurement location. MP180 is no longer usable as a pressure measurement line until the solenoid is closed
- The concentration is logged for ten times the transportation time of the gas from the rig to the analyser
- Solenoid 3 is then closed, returning MP180 to a pressure measurement model point
- This is then repeated for solenoids 4, 5 and 6, giving concentration measurements at MP179, MP178 and MP177
- Once the required measurements have been taken the gas bottle regulator is closed.
- Solenoids 3, 4, 5 and 6 are then opened to purge the gas analyser, returning the carbon dioxide levels to ambient
- Solenoids 3, 4, 5 and 6 are then closed returning the rig to normal operating conditions

6.13.3 Re-Ingestion Experimental Procedure

The re-ingestion experiment is conducted using the same procedure as the rim seal exchange experiment. The same measurement locations are used and similarly the

carbon dioxide is seeded into the cooling flow in the same way. However, as previously discussed, the geometry used is unique to the experiment so is not conducted after a main test matrix cooling flow rate. With the normal cooling flow supply routes blocked, with sealed blanking plates, the pressure in the upstream wheelspace cavity is greatly increased for a given flow rate. This ensures the seeded coolant exits via the upstream wheelspace rim seal only, as required for the experiment. This arrangement ensures that the only path for seeded coolant to reach the upstream stator well sampling point is through re-ingestion from the main annulus. This arrangement does however reduce the certainty to which ingestion into the downstream stator well cavity can be discounted, therefore during the design of the experiment it was noted that it was possible for air which had passed from the upstream cavity, through the interstage seal and into the downstream cavity to mix with main annulus air ingested through the downstream cavity rim seal. This would result in higher concentration measurements in the upstream stator well than the downstream, however it will be seen in Chapter 9 that re-ingestion rates calculated from both the upstream and downstream sampling locations agree within the bounds of uncertainty of the measurement. It would be highly unlikely for this to happen unless the assumptions made for the re-ingestion test to succeed were valid. These include good mixing of the re-ingested flow as it is ingested through the upstream stator well rim seal, homogeneous mixture of air and carbon dioxide at the upstream measurement location, the re-ingested flow passing through the interstage seal and no or limited ingress of additional main annulus gas in the downstream stator well cavity.

The increased upstream wheelspace pressure required for the re-ingestion experiment increases the axial load on the rotating assembly, increasing the axial load on the shaft

bearings which produces high bearing temperatures. In order to preserve the rig bearing it was necessary to run with a much reduced cooling flow rate compared to the interstage seal and rim seal exchange. Gas concentration results are given in Chapter 9.

6.14 Summary

The gas concentration experimental procedures devised to meet the three experimental objectives of the authors research have been described. The system through which the tracer gas is supplied to the test facility and the gas samples taken has been shown. The calibration of the instrumentation has been presented along with the derivation of the uncertainties of the gas concentration experiment equations from which the required flow rates are calculated.

7 Hot Geometry and Seal Flow Study

7.1 Introduction

The gas concentration experiments described in Chapter 6 are highly dependent on the ability to quantify internal seal flow rates, in particular the interstage seal flow. Although one of the gas concentration experiments was devised to directly take measurements of this seal flow, a second method of obtaining the interstage seal flow was also implemented. In this section a method of direct seal measurement is described, including measured rig hot geometry data, finite element modelling and numerical seal flow calculations. This Chapter expands on the work reported in Eastwood et al (2012), which can be found in Appendix C.

7.2 Mechanics of Seal Movement

The cross sectional area of the interstage labyrinth seal is the area defined in Figure 7-1. The lower radius edge of the seal passage is shown to be bounded by the surface of the rotating drive arm. The higher radius edge of the seal is shown to be bounded by the stationary stator foot. The seal inlet and outlet are defined by the respective ends of the stator foot.

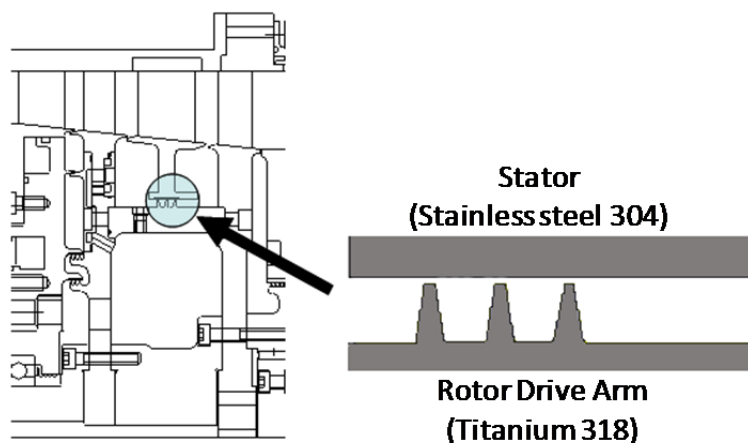


Figure 7-1: Interstage seal area

The relative axial and radial movement of the rig from its stationary position is a result of inertial rotating forces, pressure loading on turbine blades and discs, and thermal loading. At any given condition a combination of these parameters determines the expansion or contraction of the rig, directly affecting the overall area of the interstage seal. The major components of the rig are manufactured from titanium 318 and stainless steel 304, where the rotating assembly including the drive arm is titanium 318 and the stator foot stainless steel. Properties of particular importance include the co-efficient of thermal expansion and the thermal conductivity of the materials. In order to take direct interstage seal dimension measurements during test rig operation, two displacement sensors were installed in the TSW rig.

7.3 Displacement Sensor Selection

Displacement sensors were used in the rig to obtain accurate measurement of geometry changes in the vicinity of the stator well area, the results of which were used to determine the clearances of the interstage labyrinth seal and ring seals, both of which are fundamental in understanding the cooling flows and their interaction with the main annulus flow. Figure 7-2 shows the sensor locations.

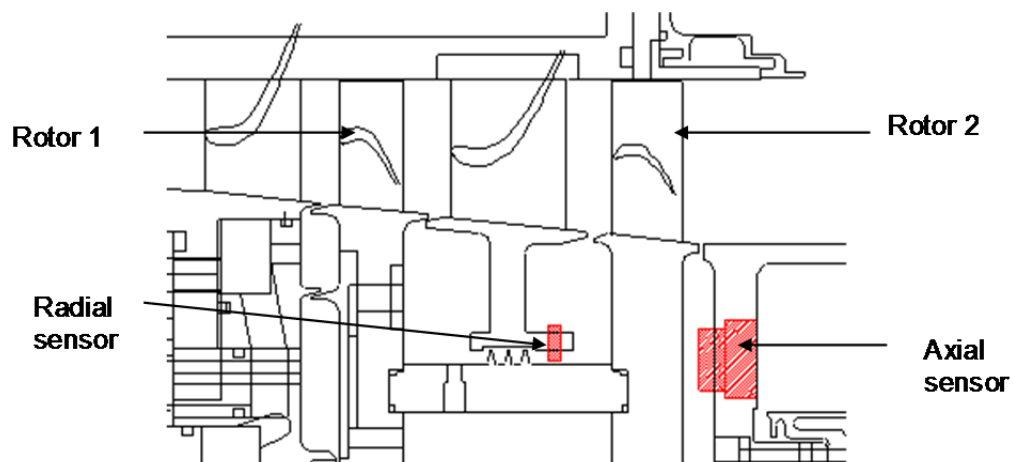


Figure 7-2: Cross section of test rig sensor locations

The large sensor located downstream of Rotor 2 is positioned in order to measure axial displacement, while the smaller sensor located on the stator well foot is positioned to measure radial displacement from the drive arm. In order to devise a practical and successful means of making these measurements the general requirements of possible sensors were considered. The system was required to operate at temperatures up to 400 K and to be able to target a surface with an angular velocity of over 1100 rad/s, whilst measuring displacements of the magnitude of 1×10^{-5} m. Micro-Epsilon Eddy current sensors were selected over similar systems, including optical and direct contact systems, due to their high precision and resolution of $\pm 6 \mu\text{m}$ together with their suitability for the operating environment.

It was noted during the assessment of the feasibility of using displacement sensors that a single radial sensor would not give a true measurement of seal clearance if the stator well foot and drive arm ran eccentrically. During the installation of the sensor both the drive arm and stator well foot were measured using a coordinate measuring machine (CMM) and found to be within tolerance. The rig rotating assembly, which includes the drive arm, was dynamically balanced before installation and runs on tapered bearings ensuring the centralisation of the assembly when subjected to axial load. The CMM measurements gave confidence in the variation of seal gap circumferentially of $\pm 15 \mu\text{m}$. On consideration of this and also the desire to limit any disruption of flow through the seal it was concluded one sensor would be sufficient. This decision was supported by the correlation of modelled and measured seal displacements discussed in section 7.5.

The systems selected to meet the requirements of the axial and tangential displacement measurements were the Micro-Epsilon U6 and SO5 sensors, with appropriate

supporting signal conditioning electronics. The conditioning electronics have two functions, the first of which is the oscillator electronics. This circuit provides an AC voltage to the sensor with a highly stable frequency and amplitude. The second function of the units is to output the measurement signal which is amplified and linearised. This circuit is known as the demodulator electronics.

7.4 Calibration and Installation

The calibration procedure for the sensors is best conducted using the actual measuring environment as this reduces uncertainties due to changes in operating environment and target geometry. However, due to constraints within the rig, the sensors could not be tested over their full measurement range, hence calibration of the sensors in their operational positions was not possible. It was necessary to complete the sensor calibration before rig assembly, which meant that the sensors could not be calibrated whilst subject to operating temperature and pressure. Figure 7-3 shows the instrumentation setup used to quantify the possible uncertainty of calibrating at ambient temperature. Each sensor was mounted on a traverse with a suitable target material at the midpoint of the sensor range. The traverse was then placed in an isothermal box and the voltage output recorded at ambient temperature. The box was then heated to rig representative temperatures. The change in sensor voltage was monitored. For each sensor the resultant measurement uncertainty due to temperature change from ambient to operating temperature was less than the dynamic resolution of the sensor ($\pm 6 \mu\text{m}$ and $\pm 5 \mu\text{m}$).

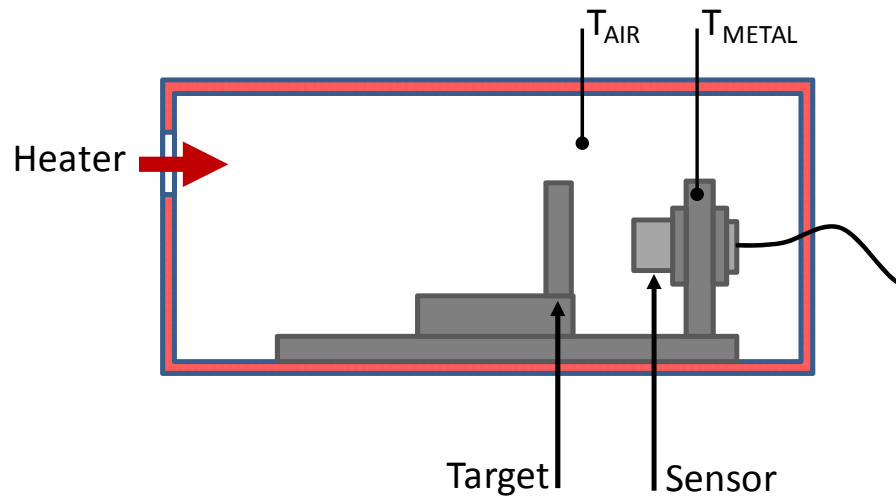


Figure 7-3: Thermal calibration drift check

Figure 7-4 shows the mounted U6 sensor in its calibration position; the blades of the Rotor can be seen protruding from under the stator. The offset distance was set by placing a feeler gauge of 0.6 mm between the sensor and rotor. Slip gauges were then placed around the circumference of the stator/rotor increasing the distance of the sensor from the rotor to 3.6 and 6.6 mm. The calibration process was then repeated, until the conditioning electronics produced the required output voltage at each range within the desired resolution.



Figure 7-4: U6 axial sensor calibration process

Figure 7-5 shows the iterations of the calibration at each target range. Each of the final calibration iterations showed the sensor output to be repeatable to within ± 0.015 V corresponding to a measurement uncertainty of ± 0.009 mm.

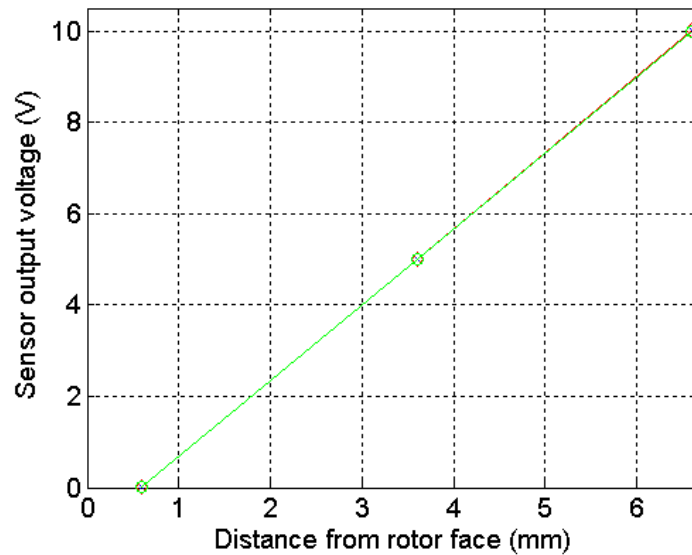


Figure 7-5: U6 axial sensor calibration results

The radial sensor was calibrated using a similar method. The sensor was located in its operational position within the statorfoot. A target of the same geometry and material as the drive arm was then used to give sensor readings for three displacement values; this setup can be seen in Figure 7-6.

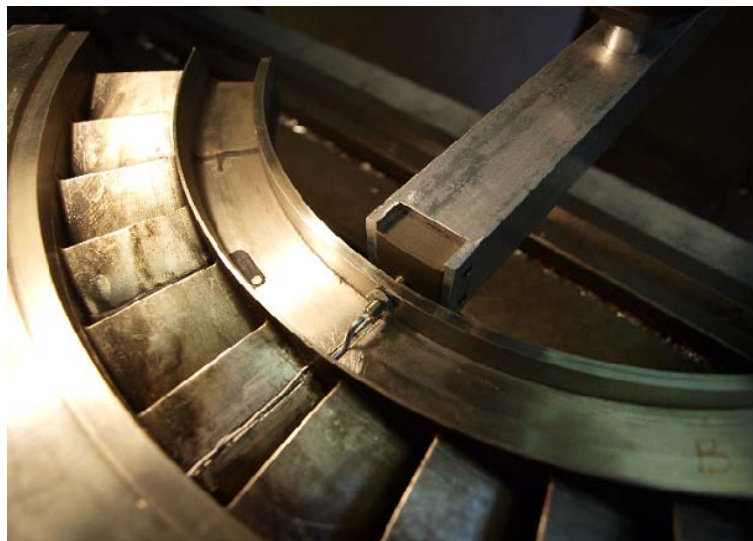


Figure 7-6: SO5 radial sensor and target

As with the U6 axial sensor the calibration was repeated three times, with the sensor outputs being repeatable to within ± 0.02 V, corresponding to a measurement uncertainty of ± 0.001 mm. The resultant voltages from the three calibration iterations can be seen in Figure 7-7.

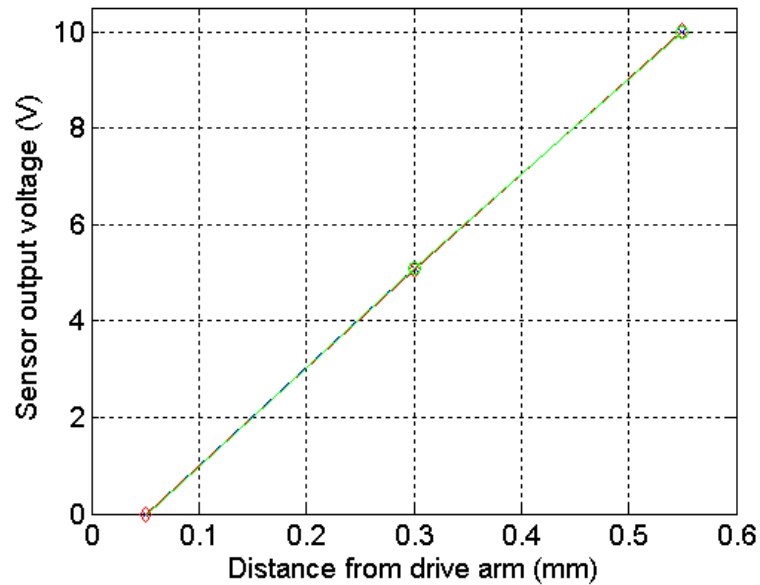


Figure 7-7: SO5 radial sensor calibration results

7.5 Thermo-Mechanical Modelling of Seal Movement

The S05 sensor selected for the radial measurement provided the range and resolution required for the radial movement of the seal, however with increased accuracy, the measurement range of eddy current sensors reduces, the S05 sensor having a useful range of 0.5 mm. In order to ensure valid measurements from the sensor, the sensor must be placed in a position which ensures seal movement is within the useful range. At its minimum range the sensor is within 0.05 mm of the target surface, this must not be exceeded or the sensor can make contact with the target surface, resulting in damage to the sensor head. Prior to installation of the sensor within the test section a basic thermo-mechanical model was run, using SC03, an in-house finite element modelling package

used by Rolls Royce plc. Figure 7-8 shows the basic geometry model used to assess possible seal movement. The geometry includes a 2D axisymmetric rotor and mock stator foot. The hub region connecting each rotor at the lower radius has been removed. Each rotor has been simplified to single thickness below and above the drive arm. The outer radius of both simplified rotors is set at the radius of rotor 1. The stator foot has been simplified to have a flat top of the same radius. The model is constrained at the bottom of each rotor for both axis of movement. The thermal expansion coefficient α for both the rotor and stator sections are given in Table 7-1. The stator is manufactured from Stainless Steel 304 and the rotor from Titanium 318.

Titanium 318		Stainless Steel 304	
Temperature (K)	α	Temperature (K)	α
293	8.5	293	14.7
400	9.1	400	16.3
500	9.6	500	17.5
600	10	600	18.6
700	10.3	700	19.5
800	10.6	800	20.2

Table 7-1: Material properties for SC03 model, Touloukian (1975)

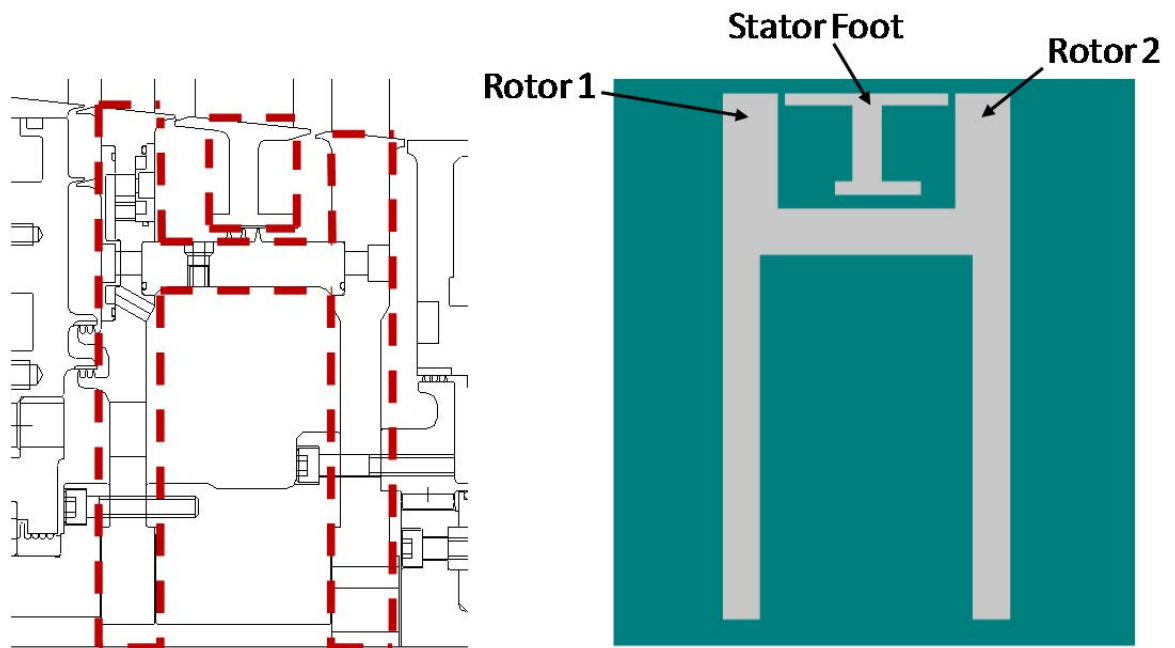


Figure 7-8: Basic geometry model of test section

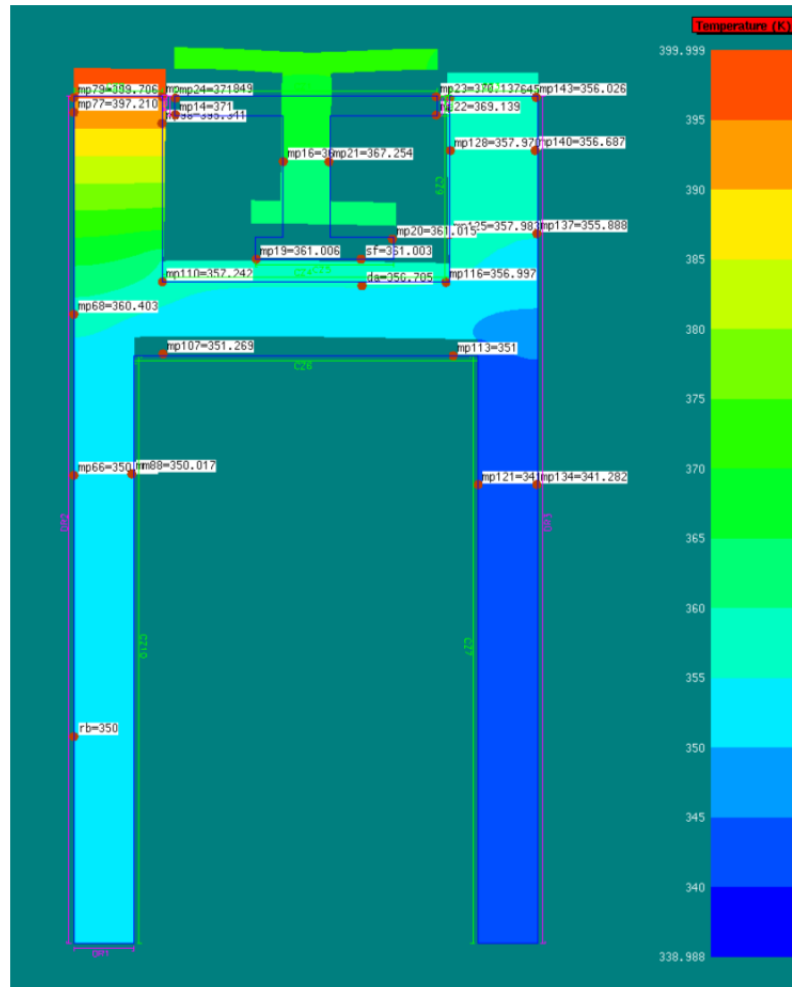


Figure 7-9: Contours of temperature on displaced model

Figure 7-9 shows displacement results obtained from the model. The model is shown with contours of temperature. Temperatures were imposed on the model by creating boundary convection zones on the geometry. Normally these would be used to represent fluid boundaries, however by using artificially high heat transfer coefficients the convection zones can be used to impose surface temperatures to the model. The labelled red dots seen on the model represent model points from the test rig. The temperatures at these points, obtained from the model, were matched to temperature data taken from the rig in a run prior to installation of the radial sensor by altering the boundary convection zone temperatures.

The model was run at two conditions to evaluate the effects of both temperature and centrifugal growth. Figure 7-10 shows results obtained at 9589 rpm, where temperature data is based on commissioning data from the experimental facility at 90% design speed. The results correspond to two nodes, one placed at a position representing the mounting point of the displacement sensor in the stator foot, the other representing the target area on the rotating drive arm. The top plot shows the displacement of each node. It can be seen that the node on the rotating section, shown as a red trace, moved radially outwards by 0.095 mm while the stationary node, shown as a green trace, has moved out radially by 0.16 mm. Despite the centrifugal growth of the rotating component and the similar radius of each node the stationary component shows significantly higher radial movement. This is due to the higher coefficient of thermal growth of the stainless steel. The second plot shows the change in relative position of the stationary node from the rotating node. It can be seen for this case that the seal gap has increased by 0.065 mm.

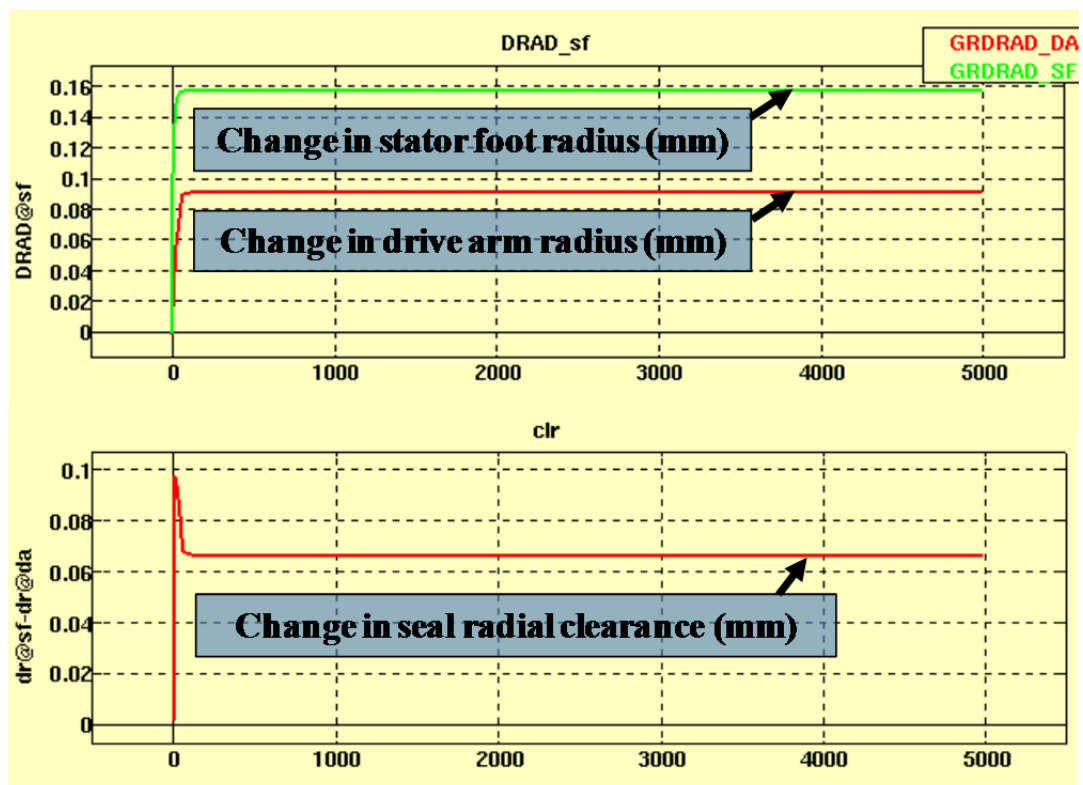


Figure 7-10: Component displacement and seal movement at 9589 rpm

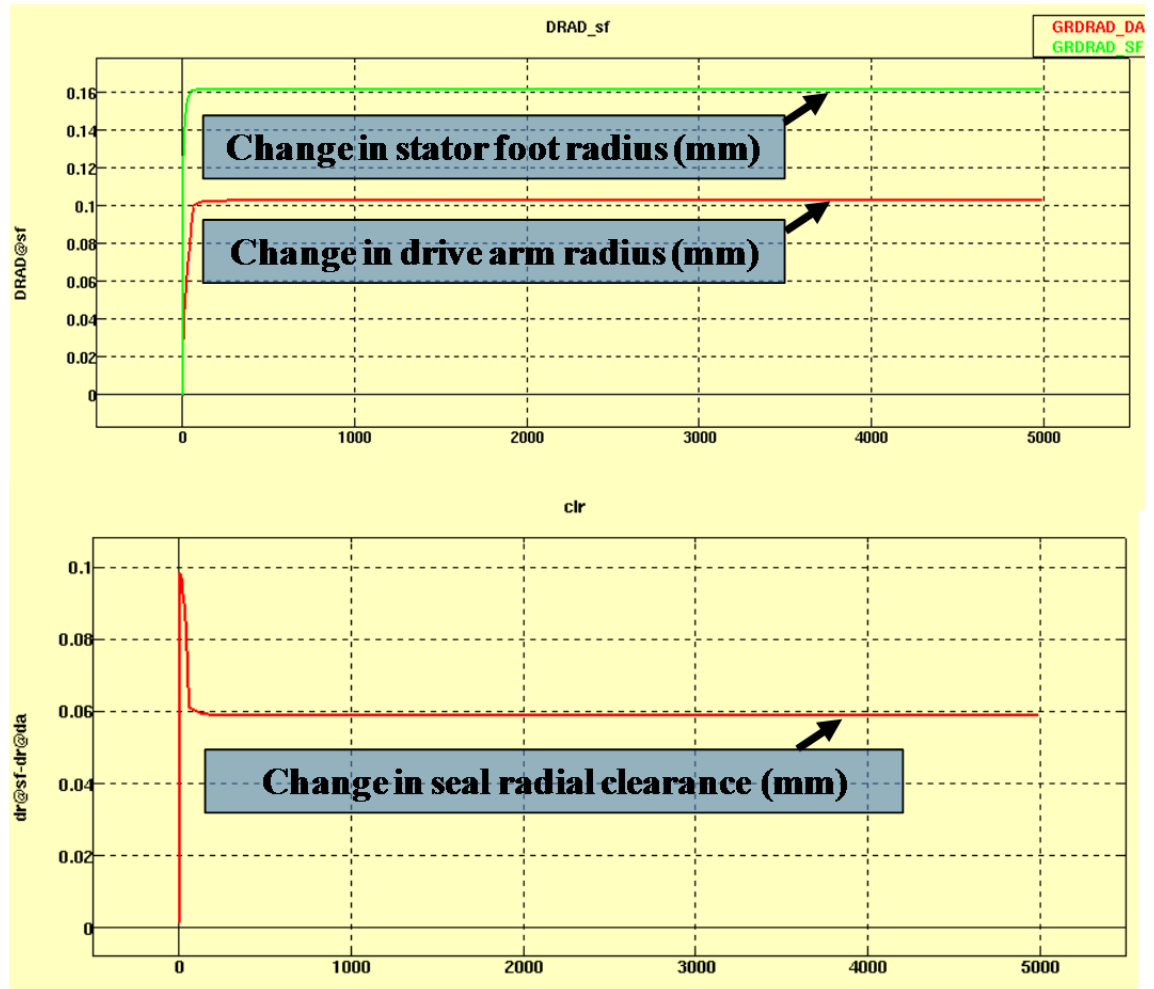


Figure 7-11: Component displacement and seal movement at 10630 rpm

Figure 7-11 shows the model run at a 10630 rpm condition. With increased rotational speed the displacement of the rotating node can be seen to increase to over 0.1 mm, decreasing the relative seal growth to below 0.6 mm. Although these models gave a good indication of the seal movement within the rig, it was only taken as a guide for installation of the sensor. Limitations of the model include the simplified geometry and the lack of gas pressure on the components. The exclusion of the blade rows being the most likely contribution to inaccuracy due to the underestimation of disc inertia, and the associated centrifugal growth of the discs.

7.6 Installation of Radial Sensor

Once the movement of the seal was understood the sensor was installed in the test section. Figure 7-12 shows the sensor mounted in the top half of the NGV 2 casing component prior to the build up of the rig. The sensor output wire can be seen exiting the back of the sensor. In this image it has not yet been bonded to the component. However, the lead out track is visible, behind the sensor, through the rim seal and up the face of the NGV. From here the wire exits the rig via a drilled hole in the outer casing. Prior to using the sensor the lead out was set into the track using epoxy resin, smoothed back to the NGV profile. For the section of wire from the sensor exit to the component face a shaped metal tube was used to contain the lead, this can be seen in Figure 7-6. Although not ideal in terms of possible flow disruption in the downstream stator well cavity, the two lock nuts on the rear of the sensor are necessary to prevent movement of the sensor during rig operation.



Figure 7-12: Radial sensor installed in stator foot

7.7 Full Structural Model for Seal Movement Calibration

The radial displacement sensor data was not available for a number of the test matrix runs, due to development of the measurement technique. Because of the limitations of the basic model, presented in section 7.5, a full test section model was developed, again using SC03. The geometry used for the full model is shown in Figure 7-13, with contours of metal temperature. The model can be seen to include the full test section geometry. This includes the main annulus geometry and casing. Bolted and pressed joint faces between component faces are accounted for in terms of both thermal conductivity between components and mechanical movement. Where sections represent blades, NGV's or coolant passages within the rig and the section cannot be said to be axisymmetric, the section properties are set accordingly. Areas of the rig where an air gap is present for the entire circumference of the rig are treated as voids.

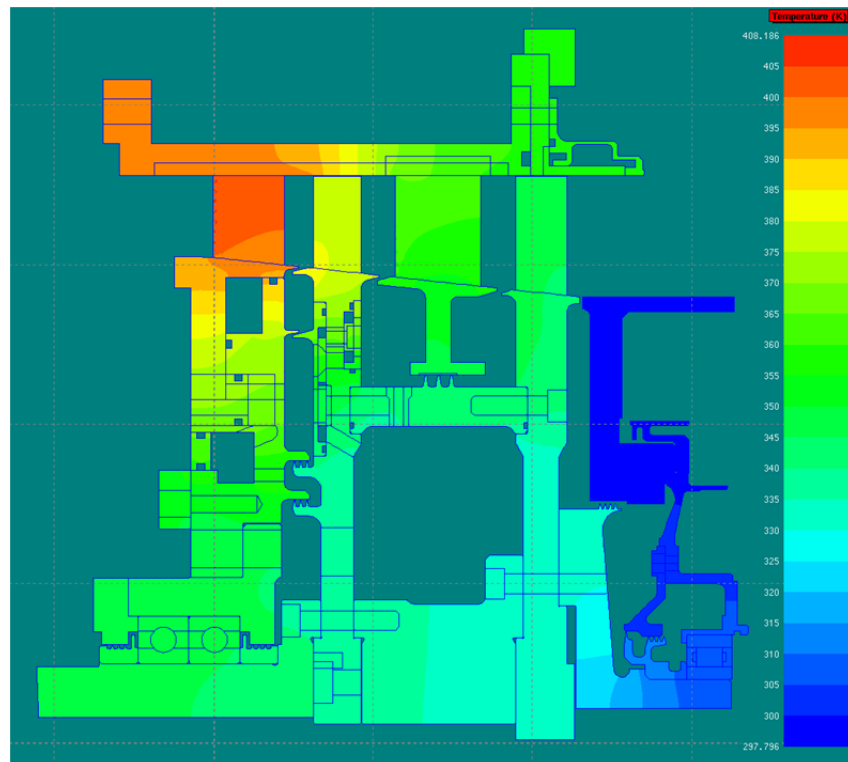


Figure 7-13: Full radial displacement calibration model

As with the basic geometry model, the metal temperatures are imposed by using convection streams at the component surfaces, with artificially high heat transfer coefficients. It was necessary to validate the model before it was used with test conditions where the radial sensor was not installed to provide a seal clearance value. This was achieved by comparison of modeled seal clearances and rig results for runs where the sensor was installed. The metal temperatures at all model points within the test section were matched to test rig measurements, where the maximum allowable deviation was 3 °K and the average deviation was less than 1 °K. Figure 7-14 shows a comparison of the modeled seal clearance change against measured seal change. The measured seal change is shown as a blue trace and the six red crosses represent the values obtained from the thermo-mechanical model, where the test section and rig speed have been matched. The model was found to match the measured rig values to an uncertainty of 0.009mm, corresponding to an uncertainty of 10% of seal clearance change and 2.5% of total seal clearance.

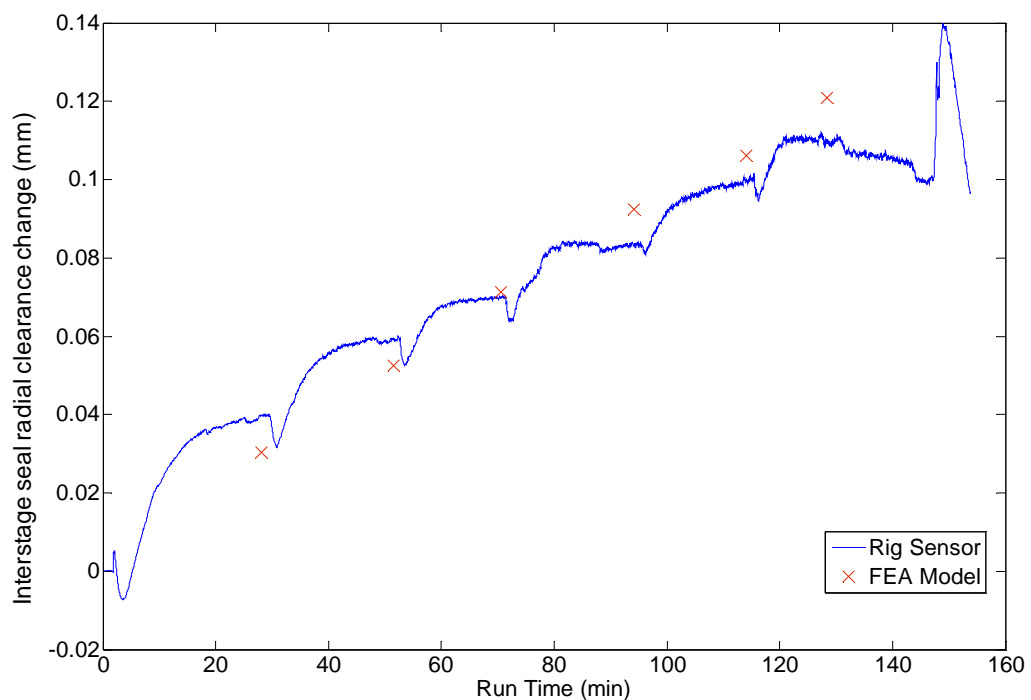


Figure 7-14: Comparison of predicted thermo-mechanical model and measured interstage seal radial clearance change

7.8 Test Matrix Seal Movement Calculations

In this section results obtained for seal displacement and resulting seal flow rates will be presented for both modelled and measured geometries. Figure 7-15 shows an example of the modelled seal displacement, in this case for 55 gs^{-1} and 39 drive arm hole inserts. The deflection magnitude is shown at a 1:24 scale, with contours of metal temperature.

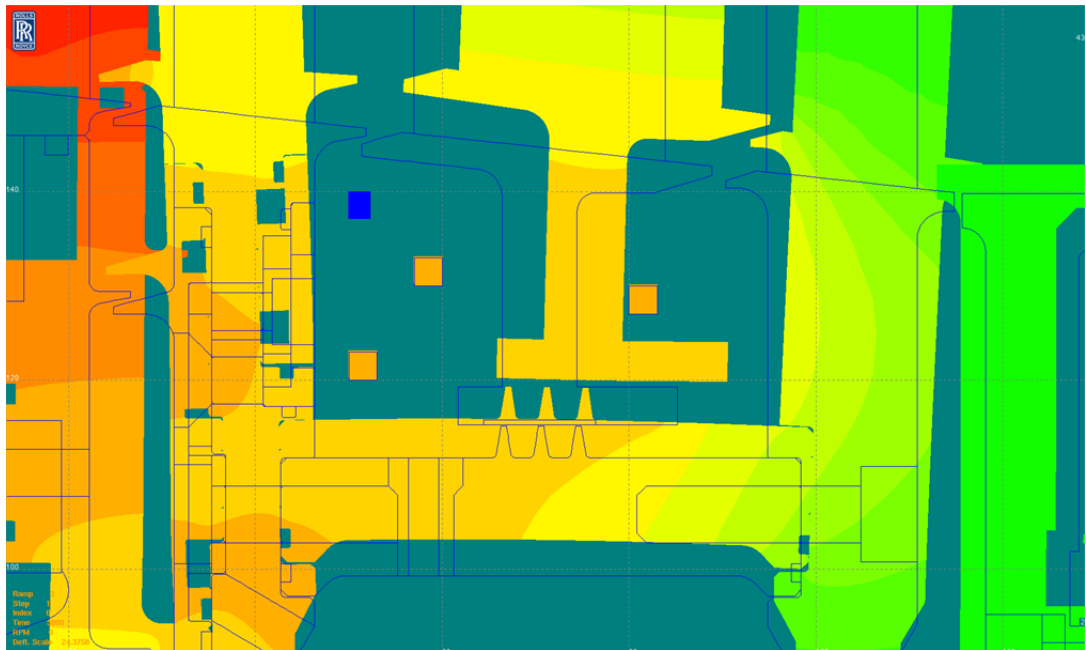


Figure 7-15: Deformed seal shape

Figure 7-16 shows the output of the thermo-mechanical model for a cooling flow rate of 55 gs^{-1} for the 39 lock plate slot geometry. The radial movement of the rotating drive arm is shown in green, the radial movement of the stator foot is shown in blue and the resultant change in seal gap is shown in red. This method of seal movement calculation was used throughout for the first four test geometries.

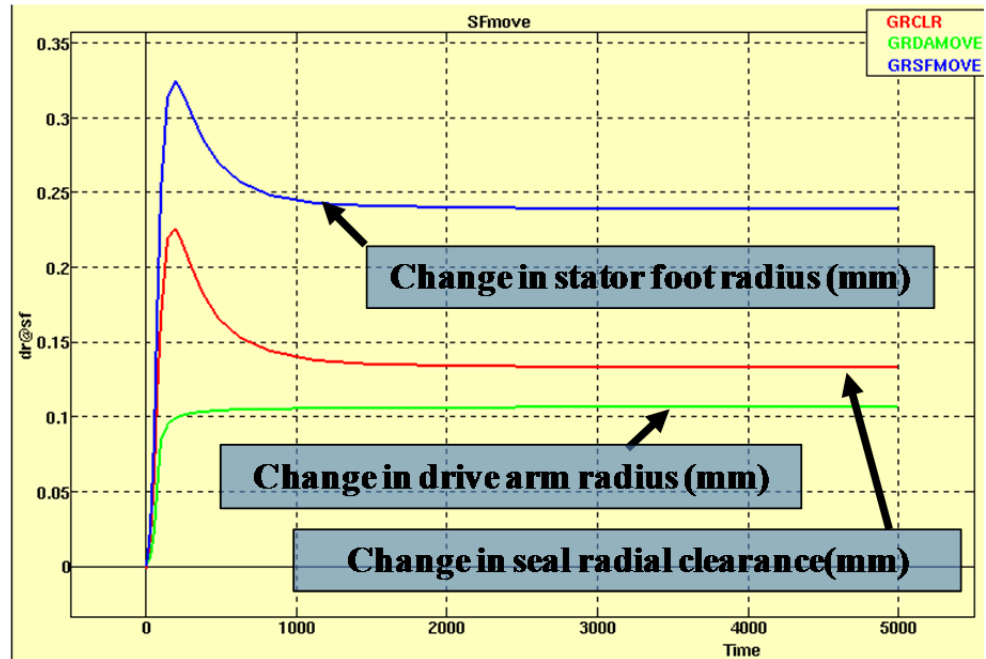


Figure 7-16: Displacement results for 39 lock plate slot geometry with a cooling flow rate of 55 gs^{-1}

Figure 7-17 shows an example of radial seal movement from the nominal cold clearance as measured by the S05 sensor, for a test run from which data was taken at the three specified cooling flow rates with 26 drive arm inserts and the deflector plate in place. Point 'A' on the trace shows the measured movement as main annulus air is initially passed through the test section. At this point the blade rows become loaded and an axial load is applied to the rotating section centralising the rotating section bearings. The internal seals of the rig also begin to pressurise directing more coolant to the stator foot, causing a slight contraction in the seal gap. As the rig metal temperatures begin to increase due to heat transfer from the main annulus air, thermal expansion of both the stator foot and drive arm cause the seal gap to open as indicated at point 'B'. Centrifugal growth of the seal is also seen to correspond to changes in rig speed. At point 'C' a feature can be seen where the rig speed has been dropped slightly then suddenly increased. At point 'D' the seal movement begins to stabilise as rig temperature variations begin to reduce, the fluctuations at this point being due to adjustments in rig speed, cooling flows and balancing flows in order to satisfy the conditions for the first

test point. Point 'E' indicates the seal movement at the first test point, for this example a cooling flow rate of 55 gs^{-1} . Points 'F' and 'G' represent the change in seal gap for the cooling flow rates of 40 gs^{-1} and 30 gs^{-1} . For all geometries where the displacement sensor was installed the seal gap was seen to increase with increased cooling flow rates. This is due to the increased cooling flow rates causing a higher temperature gradient from the lower radius of the rotating section to the main annulus. The cooler lower radius reduces the thermal expansion of the drive arm, increasing the gap to the stator foot. Point 'H' shows a sudden increase in the seal gap due to the rig being slowed after the final test point data has been taken, the increase resulting from the loss of centrifugal growth in the drive arm. Point 'I' indicated the closing of the seal gap as the test section begins to cool at the end of the test run.

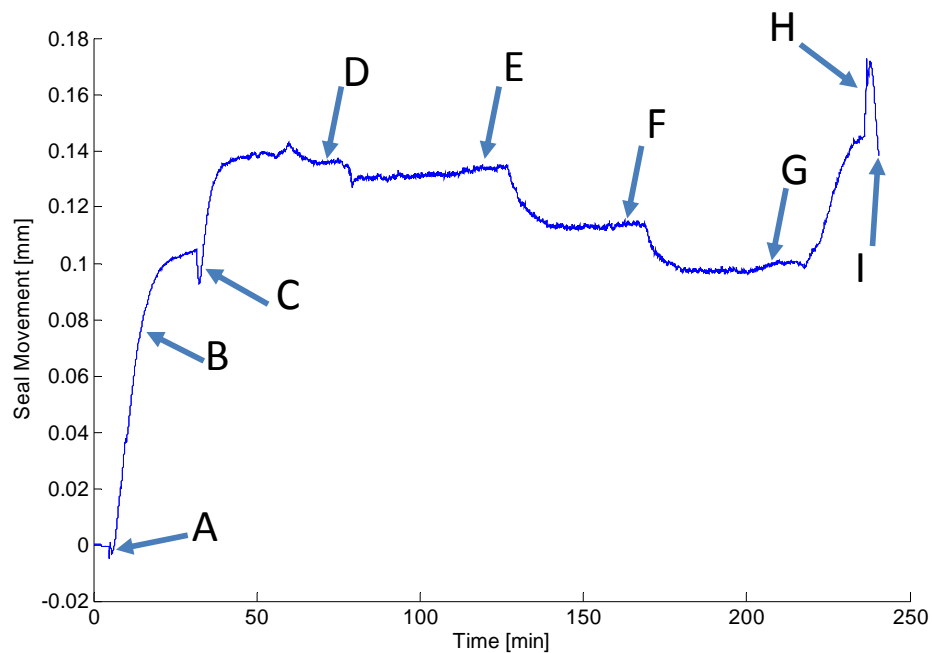


Figure 7-17: Radial seal displacement measurement for 26 drive arm holes with deflector plate

Table 7-2 shows the change in nominal seal clearance for all test matrix geometries and flow rates, for which gas concentration data is presented in Chapter 8. Values obtained from the thermo-mechanical modelling method are indicated with an asterisk. All other values were obtained from direct seal movement measurement.

	30 g/s	40 g/s	55 g/s
39 Drive Arm Holes	-	0.1167*	0.1223*
26 Drive Arm Holes	-	0.1286*	0.1331*
39 Lock Plate Slots	-	0.1250*	0.1301*
26 Lock Plate Slots	-	0.1218*	0.1275*
39 Axial Drive Arm Holes	0.0469	0.0786	0.0945
39 Circumferential Drive Arm Holes	0.0510	0.0739	0.1057
39 Drive Arm Hole + Deflector Plate	0.1174	0.1299	0.1397
26 Drive Arm Hole + Deflector Plate	0.1007	0.1143	0.1338

Table 7-2: Change in interstage seal radial clearance [mm] (* calculated from SC03 model)

7.9 Test Matrix Seal Flow Calculation

The St. Venant-Wantzell equation, discussed in Chapter 2, was used for all test geometries to calculate the interstage seal flow. For the purpose of this work, the 2D, non-rotating data of Wittig et al (1987) was used to estimate a C_D . The tightest clearance tested, 0.5 mm, (together with 2.5, 1.5 and 1.0 mm) is close to the TSW seal and the geometry is similar. Specifically, the estimation of the C_D value has been derived from an extrapolation of the 6 and 1 fin data, to a 0.3 mm clearance. An estimate for the 3 fin C_D was derived from the numerical modelling of the Wittig et al (1987) data by Kim and Cha (2009). Based on their results, the 3 fin C_D was estimated to be approximately 0.48. Figure 7-18 shows the measurement location used with Equation 2-14 to calculate the interstage seal flows. Model point mp030 was used to obtain a suitable upstream total temperature value T_θ . Model points mp176 and mp181 provided the required upstream and downstream static pressure measurements from which to calculate the pressure ratio P_2/P_1 . The seal area A was calculated from the nominal cold seal geometry and the seal displacement measurements shown in Table 7-2. The resulting interstage seal flows are given in Table 7-3.

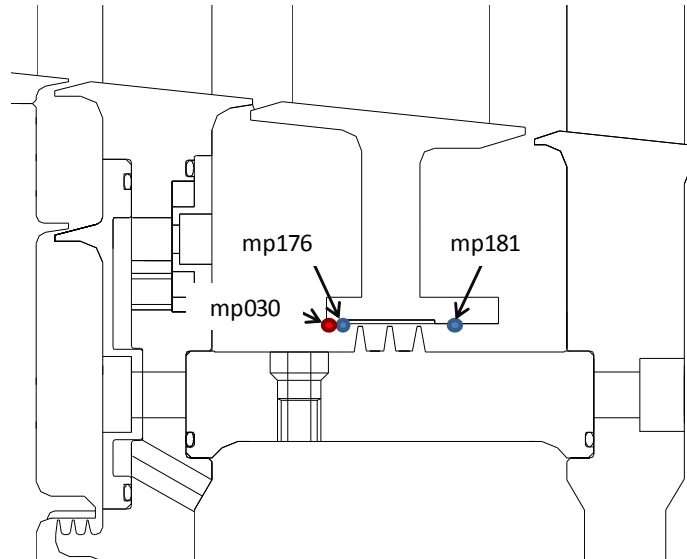


Figure 7-18: Seal flow parameter measurement locations

	30 g/s	40 g/s	50 g/s
39 Drive Arm Holes	-	45.4742	47.2672
26 Drive Arm Holes	-	47.3314	48.6634
39 Lock Plate Slots	-	45.0755	46.0342
26 Lock Plate Slots	-	44.6678	46.1789
39 Axial Drive Arm Holes	36.2607	40.1748	42.0589
39 Circumferential Drive Arm Holes	35.0499	37.2101	40.3266
39 Drive Arm Hole + Deflector Plate	43.7778	46.0456	48.6921
26 Drive Arm Hole + Deflector Plate	42.8879	45.0635	48.2871

Table 7-3: Interstage seal flow rates for all cooling flow supply geometries

Figure 7-19 shows a comparison of seal flows calculated using a C_D of 0.48 with the St. Venant-Wantzell equation, with seal flow results from CFD. The pressure ratio is the upstream to downstream seal pressure. The normalized seal flow is $\dot{m}_l/C_{w,ent}$. The CFD results were found to be within 2% of the calculated values. The effect of rotation has been shown to reduce the discharge coefficient, Waschka et al (1992). The TSW seal is at the borderline between the axial and rotationally affected regimes, so the effect is not expected to be significant.

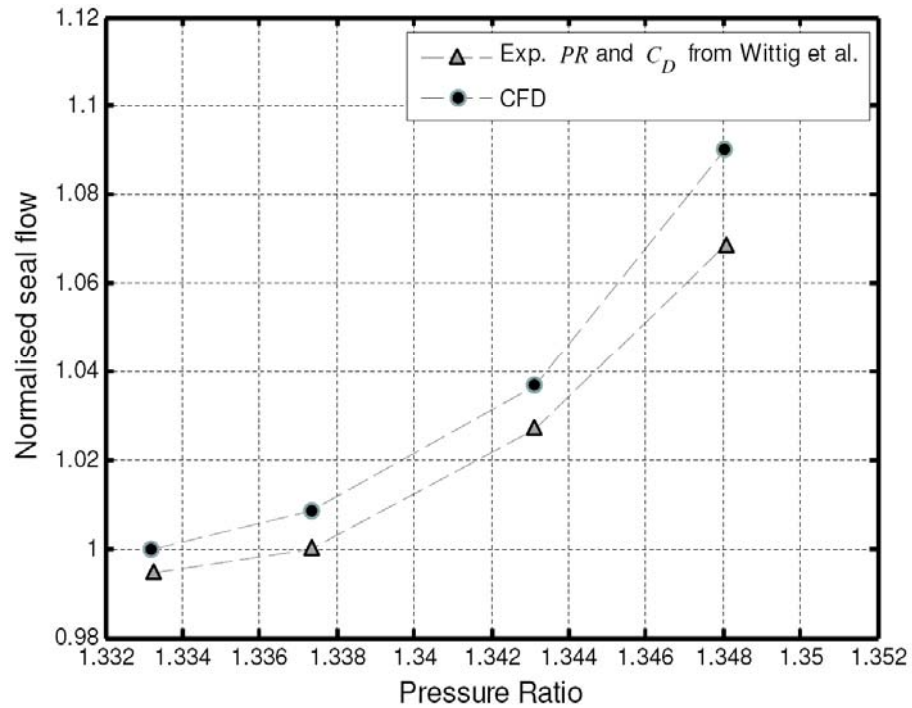


Figure 7-19: Comparison of CFD and calculated seal flows using a $C_D = 0.48$, Eastwood et al (2012)

7.10 Summary

In this chapter an alternative method for the calculation of the interstage seal flow has been described. This technique, which includes both displacement measurements and thermo-mechanical models of the interstage seal gap to inform seal equation inputs, was devised to mitigate the possibility of the interstage seal gas concentration experiment providing unsuitable answers. The possibility of this situation occurring was considered high due to the exploratory nature of the interstage seal gas concentration experiment. However, the use of the technique described in this chapter can introduces large uncertainties when used for the rim seal exchange and re-ingestion gas concentration mass flow calculations. This is discussed in Chapter 9.

8 Results - Stator Well Temperature

8.1 Introduction

In this chapter experimental temperature data will be presented. Pressure data is also given to quantify pressure asymmetry in the main annulus. The temperature data is shown in normalised form for each geometry and cooling flow supply rate, across both test phases. The variation in normalised temperatures across test cases is used to indicate the flow regimes within the stator well, which will be used to inform conclusions made from gas concentration experimental results presented in Chapter 9. The results presented in this chapter extend the work of Coren et al (2011).

8.2 Main Annulus Pressure

The study of the interactions of the main annulus gas with the stator well cooling flow is highly dependent on the ability to limit pressure asymmetry. As discussed in Chapter 2, previous studies have shown the effect of local pressure variation on the flow structure of a rotor stator cavity where the outer seal is subject to an external flow. Figure 8-1 shows the measurement locations of the total pressure probes installed on the leading edge of the Stator 1 NGV row, at the inlet to the test section. The taps are placed in sets of four, spanning the main annulus, where each set of four is installed in a single NGV. The NGVs used being numbers 1, 15 and 30. The circumferential position of each set is given as $\alpha = 10$ deg, 134 deg and 276 deg. The circumferential position is taken from the top centre of the rig, and then increases in a clockwise direction when viewed from the upstream position, looking in the direction of flow through the rig.

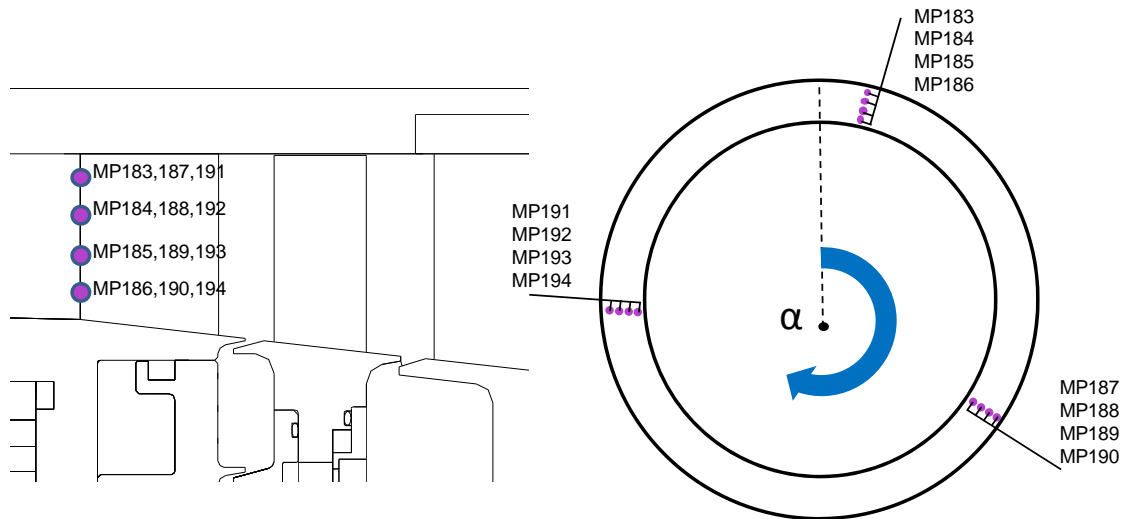


Figure 8-1: Test section inlet total pressure measurement locations

Figure 8-2 shows the total pressure measurements at each of the measurement locations for each test point taken over the two test phases, where the pressures are presented in terms of percentage deviation from the mean inlet pressure. The results show that for each test point the total pressure deviation was less than $\pm 0.5\%$ of the mean main annulus pressure.

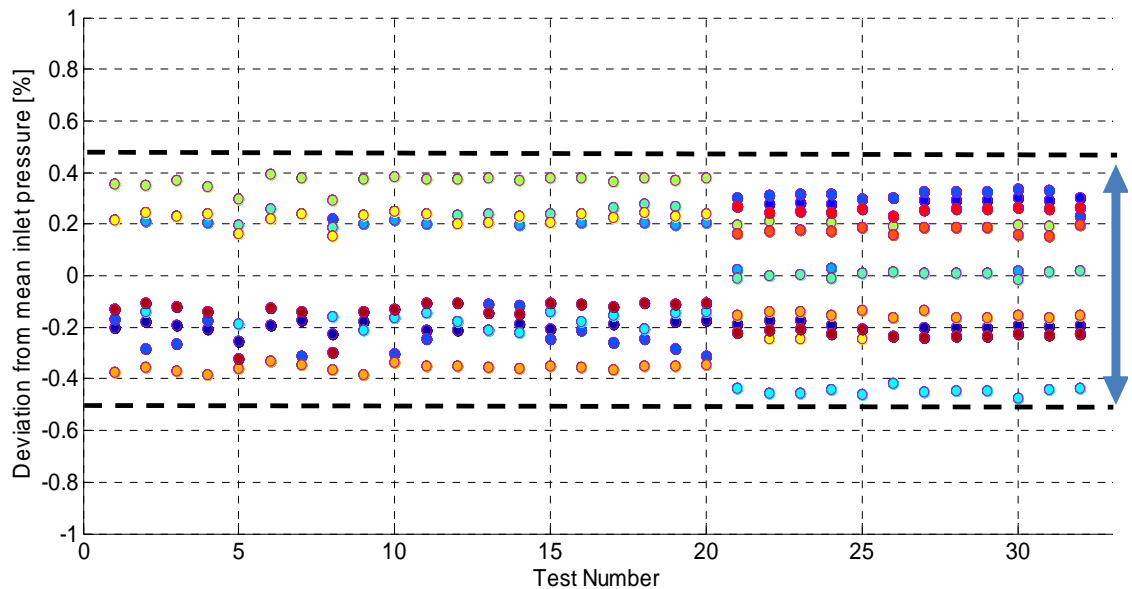


Figure 8-2: Total pressure asymmetry at test section inlet

8.3 Cooling Flow Rates

The measurement of cooling flow delivery was discussed in Chapter 4 and shown to be made using hot film flow meters, with an uncertainty of $\pm 1.3\%$ of the measurement point. The control of this flow through balancing of the wheelspace cavities, using the vent and balance flows was discussed in Chapter 5. A manufacturing fault found in the pressure lead out tubes of some of the wheelspace pressure measurements was also discussed in Chapter 4. This led to the lower claw seal being incorrectly balanced and additional air entering the coolant supply path from the balance flow during phase one testing. The pressure lines for mp148, mp150 and mp 154 were found to be undamaged giving correct measurements in the lower wheelspace cavity, the balance cavity and the upper wheelspace cavity. Model point mp151 was found to have a minimal leak, so was the focus of providing a corrected pressure in the vent cavity. This was achieved by considering inter cavity pressure gradients. These were estimated after consideration of rotational pressure recovery effects, superposed internal cavity flows and CFD results provided by industrial partners. All other pressure measurements in the wheelspace were discounted. Once mp151 had been corrected the cavity pressures were used with seal flow correlations, including allowances for hot running claw seal clearances, to estimate the additional balancing air entering the coolant flow. The hot running claw seal clearances were taken from the SC03 model described in Chapter 7. This study was conducted and documented by Coren (2010), and was reported by Dixon et al (2012) and Smith et al (2012).

The average balance flow leakage into the cooling flow was found to be an additional 6.5% of the total cooling flow. The uncertainty of the additional balance

flow calculated was considered to be $\pm 10\%$. Considering the worst case additional cooling flow case, 13 lock plate slots, and using equation 6.14 the uncertainty of the augmented flows, which are a summation on the measured cooling flow and the additional balance flow can be considered $\pm 2\%$.

Throughout this chapter comparisons are made between normalised temperature results for multiple geometries. In order to simplify these comparisons cooling flow rates are referred to at the nominal targeted flow rate for a given test point. The actual coolant flow rate however is presented where conclusions are drawn from these comparisons. Table 8-1 shows the achieved coolant flow rates for each phase one geometry. These are the augmented values previously discussed. Table 8-2 gives the measured flow rates for the phase 2 geometries, where the faulty pressure taps had been replaced and the lower claw seal was considered balanced.

Geometry	No. of flow features	Target Flow 30 gs^{-1}	Target Flow 40 gs^{-1}	Target Flow 55 gs^{-1}	Target Flow 75 gs^{-1}
Drive Arm Inserts	39	34.31	43.18	57.41	76.98
	26	33.58	43.36	56.81	73.91
	13	32.38	41.45	NA	NA
Lock Plate Slot	39	33.92	43.92	58.60	76.36
	26	32.83	41.59	57.43	73.44
	13	36.09	45.92	NA	NA

Table 8-1: Phase 1 augmented cooling flow rates ($\pm 2\%$ uncertainty)

Geometry	Target Flow 30 gs^{-1}	Target Flow 40 gs^{-1}	Target Flow 55 gs^{-1}	Target Flow 75 gs^{-1}
39 Drive Arm Inserts (Axial 25°)	30.39	39.95	54.53	NA
39 Drive Arm Inserts (Circumferential 25°)	29.64	39.28	54.31	NA
39 Drive Arm Inserts (Straight Inserts + Deflector)	29.67	39.86	53.72	NA
26 Drive Arm Inserts (Straight Inserts + Deflector)	29.82	39.97	53.42	NA

Table 8-2: Phase 2 measured cooling flow rates ($\pm 1.3\%$ uncertainty)

8.4 Normalised Temperature Methodology

Due to the extended period over which test runs were conducted, variations in the main annulus air temperature, the supplied cooling flow temperature and the ambient pressures were seen for each test run. Temperature data in this section is presented in normalised form in order to aid comparison of the different geometries tested, where the normalised temperature is a ratio of the temperature difference between different model points. Equation 8-1 shows the form of the ratio, where the normalised temperature ϕ is a ratio of the temperature difference between the model point temperature to be normalised T_M , and the coolant temperature at the test section inlet T_C , and the temperature difference between the main annulus gas temperature T_H and the coolant temperature T_C . The uncertainty of this parameter due to the thermocouple measurements was derived in Chapter 4. All temperature data presented in normalised form includes error bars, where the uncertainty is of a similar magnitude to the data markers.

$$\phi = \frac{T_M - T_C}{T_H - T_C}$$

Equation 8-1

Figure 8-3 shows the selected hot and cold reference temperatures. The selected cold reference point is the air temperature thermocouple at mp010, where the supplied cooling air enters the upstream wheelspace, and the hot temperature is the air temperature thermocouple at mp040, at the leading edge of NGV 1 in the main annulus flow. With no cooling flow being supplied to the rig the test section would approach the main annulus gas temperature. The normalised temperature for a given model point therefore represents the extent to which the cooling flow has reduced the metal temperature. It can be considered as a measure of normalised temperature. A

normalised temperature of 1 would correspond to a metal temperature equal to the main annulus gas temperature at model point mp040. A normalised temperature of 0 would correspond to a metal temperature equal to the coolant temperature at mp010.

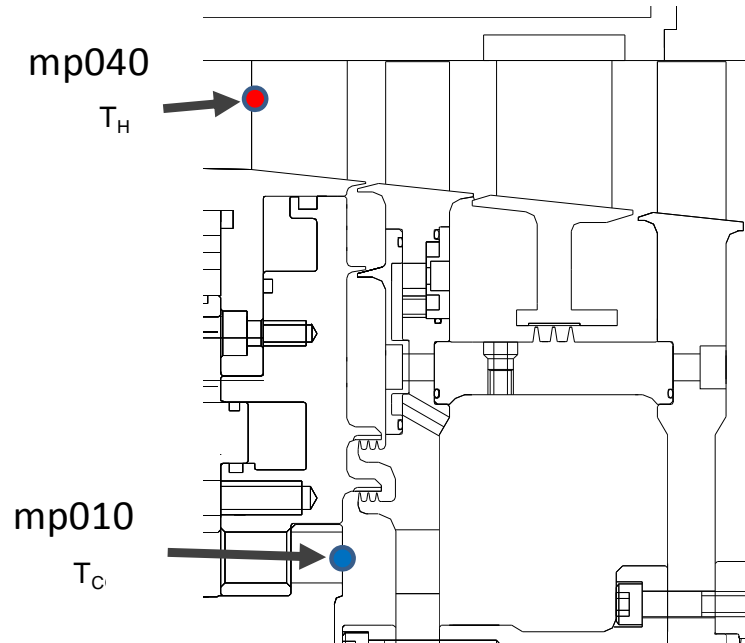


Figure 8-3: Normalised temperature reference model points

8.5 Upstream Wheelspace Temperatures

Figure 8-4 shows the model points for which measurements of metal temperatures are made on both the stationary and rotating face of the upstream wheelspace. The model points are positioned from low to high radius, where the low radius points are near the cooling flow inlet and the high radius points near the main annulus flow.

Figure 8-5 shows the normalised temperatures of the stationary face of the upstream wheelspace against the measurement radial location r/b . The results shown are for the 26 straight through drive arm hole geometry, with the deflector plate in place, for nominal cooling flows of 30 gs^{-1} , 40 gs^{-1} and 55 gs^{-1} . The lowest radius model point

mp001 is seen to have a normalised temperature of $\phi \approx 0.3$ at a nominal cooling flow rate of 30 gs^{-1} , reducing to a value of $\phi \approx 0.2$ at a nominal flow rate of 55 gs^{-1} .

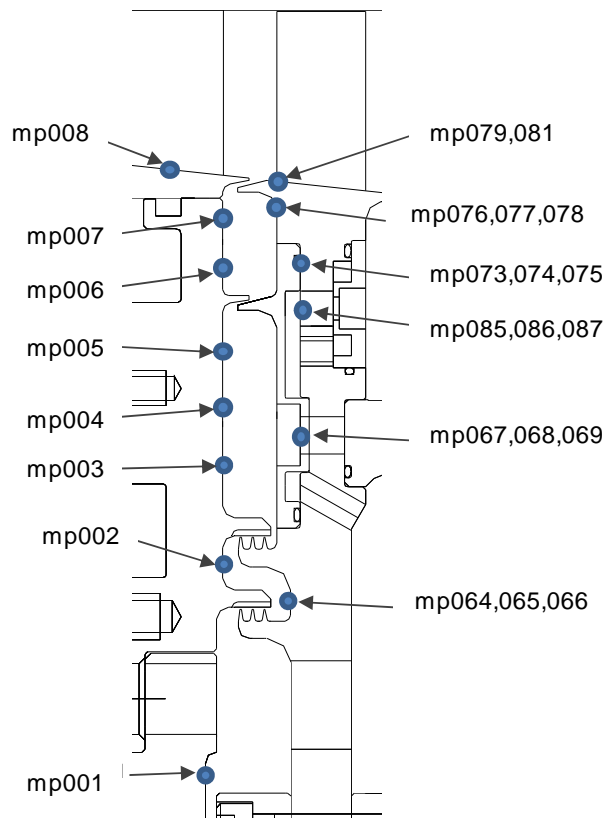


Figure 8-4: Upstream wheelspace normalised model point locations

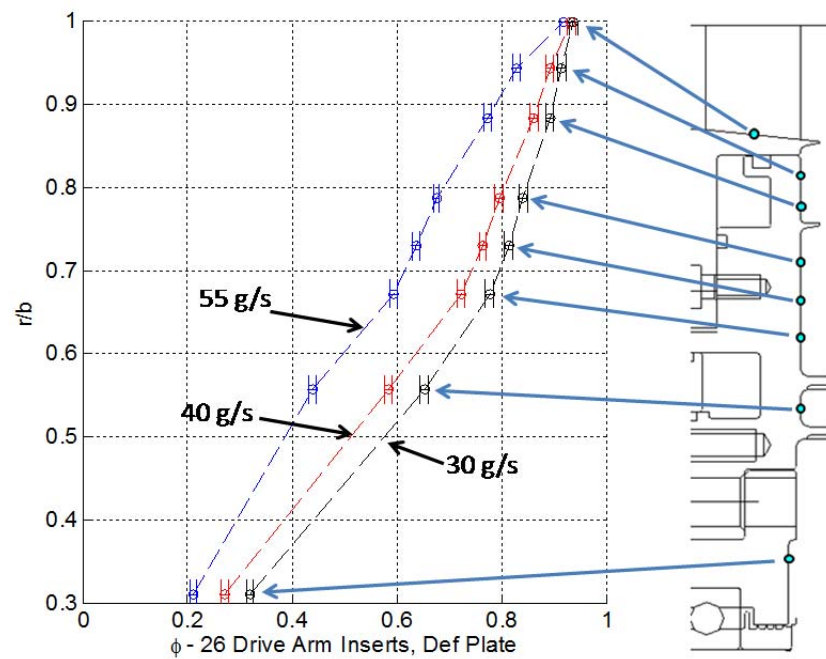


Figure 8-5: Normalised temperatures for 26 straight drive arm inserts and deflector plate

The location of mp001 is at a lower radius than the cooling flow inlet and below the wheelspace balance cavity, across which no main annulus gas can flow. The decrease in normalised temperature is driven by the increase in flow rate of the coolant and the corresponding drop in local metal temperature. Model point mp002 shows the same trend, where the normalised temperature decreases with increased coolant flow supply. However, the normalised temperature is higher than the value obtained at mp001 due to the higher radius location. Model points mp003, mp004 and mp005, again show the same trend, where ϕ decreases with increased coolant flow. These three model points correspond to the positions on the stator above the balance cavity. The gradient of ϕ is seen to become steeper between these three model points, where the metal temperature increases less with increased radius. This is attributed to the model points being effectively sealed off from the cooling air and dominated by conduction. Model point's mp006 and mp007 in the highest radius chamber show a very similar trend to the three model points in the chamber below. The normalised temperature at mp008 is seen to stay almost constant, this model point being adjacent to the hot main annulus gas flow. The slight improvement with increased cooling flow rate is due to the reduction in lower radius metal temperature and a change in the temperature gradient through the component.

Figure 8-6 shows the normalised temperature for the rotating model points of the upstream wheelspace for the same geometry and cooling flow rates. For each group of thermocouples, where the thermocouple hot junctions are at similar radial locations, a mean temperature has been used to calculate the normalised metal temperature. As with the stationary points, the lowest radius model points have the lowest normalised temperature, which increases with decreased cooling flow.

However, the change in ϕ with r/b for the lower two model points is greatly reduced when compared to the stationary points. This may be due to the fact that the cooling air reaches a higher radius up the back of rotor 1 before entering the stator well cavity. The higher radius points near to the main annulus flow show little or no improvement with increased cooling flow as seen with the stationary measurement positions. The top two radial positions lie within the uncertainty of the normalised parameter for all three cooling flow rates, where the temperature is dominated by the main annulus gas temperature and additional cooling flow has no effect. The change in ϕ with r/b for both the rotating and stationary measurement locations above $r/b = 0.8$ is similar, where the temperature profile is dominated by conduction down the disc face. The normalised temperature at the high radius position of the rotating surface is lower than the high radius position of the stationary surface of the wheelspace. This is due to the lower metal temperatures at the higher radius of Rotor 1 as compared to the higher radius temperatures of Stator 1 as the main annulus gas temperature reduces as it passes through each stage of the test section main annulus.

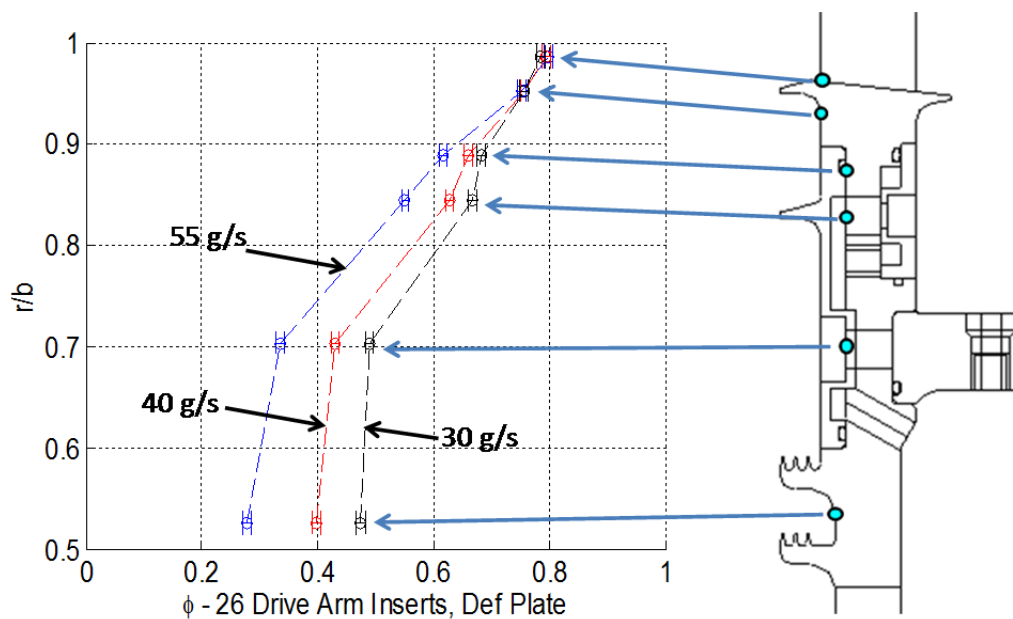


Figure 8-6: Normalised Temperature on front face of Rotor 1 for 26 drive arm inserts and deflector plate

As the wheelspace is balanced to seal the lower cavity and ensure the cooling flow reaches the test section, and the geometry of the wheelspace is unchanged over the test phases, the trends shown for this geometry are representative of all the geometries tested.

8.5.1 Normalised Rotating Upstream Stator Well Temperatures

Figure 8-7 shows the thermocouple locations used to assess the normalised temperature on the rotating face of the upstream stator well cavity (rear face of Rotor 1). The model points extend radially from the drive arm to the rim seal behind the blade row in the main annulus. T_H and T_C are taken from the locations shown in Figure 8-3.

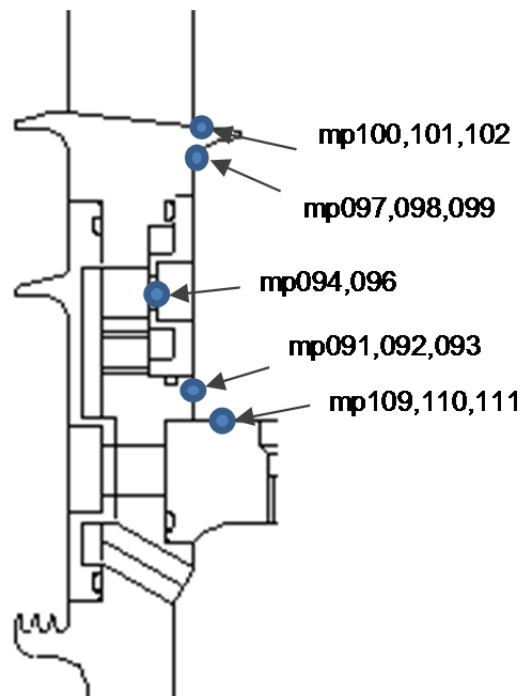


Figure 8-7: Rotor 1 rear face normalised temperature locations

Model Point	r/b
mp109, mp110, mp111	0.7605
mp091, mp092, mp093	0.7876
mp094, mp096	0.8673
mp097, mp098, mp099	0.9686
mp100, mp101, mp102	1.0000

Table 8-3: Rotor 1 rear face measurement location

Figure 8-8 shows the normalised temperature results for the rear face of Rotor 1, corresponding to the model points shown in Figure 8-7. Results are shown for all geometries and flow rates tested. Normalised temperature ϕ is plotted against the radial location given in Table 8-3 as a ratio of cavity height b . The geometry is not shown next to the plots, as it was for Figure 8-5 and Figure 8-6, in order to avoid obscuring the data. Flow rates are labelled for the first instance of each nominal cooling flow set. However for all axis, nominal cooling flow rates of 30 gs^{-1} are shown in black, 40 gs^{-1} nominal flow rates are shown in red, 55 gs^{-1} nominal rates are shown in blue and 75 gs^{-1} nominal flow rates are shown in green. The normalised temperature for thermocouples in the same radial position have been grouped and averaged. Error bars are included, where they are of a similar magnitude to the markers. For all geometries the normalised temperature at each radial location (except for those at $r/b = 1$) are shown to reduce with increased cooling flow.

Examination of the gradient between locations $0.97 \leq r/b \leq 1.00$ can provide indication of the extent to which the cavity is sealed. Where $d(r/b)/d\phi$ is large the temperature at $r/b = 0.97$ is approaching the main gas temperature, indicating ingress. As $d(r/b)/d\phi$ decreases the temperature difference between $r/b = 0.97$ and the main gas temperature increases, with cooling air reaching the higher radius positions of the cavity. The cooling air reduces the metal temperatures by both heat transfer from the metal surface and also by preventing the ingestion of hot gas. For all geometries shown the gradient between $0.97 \leq r/b \leq 1.00$ decreases with increased cooling flow, showing improved sealing. The lock plate geometries tend to show better sealing, particularly at lower cooling flow rates. It should be noted that the lock plate geometries at low flow rates had the highest deviations from nominal flow rates,

however even with this taken into consideration the results show at certain radii the nominal 30 gs^{-1} lock plate geometries resulted in lower normalised temperature than the nominal 40 gs^{-1} drive arm geometries. For example the data at the radial location $r/b = 0.8673$ for 13 lock plates slots at 36.09 gs^{-1} (30 gs^{-1} nominal) shows a normalised temperature $\phi \approx 0.35$, while the 13 drive arm hole geometry at 41.45 gs^{-1} (40 gs^{-1} nominal) shows a normalised temperature $\phi \approx 0.5$.

Comparison of the drive arm insert geometries to the lock plate slot geometries show a clear distinction between the temperature profile of the rotor. For the lock plate slot geometries where the coolant enters at a radius $r/b \approx 0.87$, the locations $0.76 \leq r/b \leq 0.87$ show a lower variation in normalised temperature than those seen for the drive arm geometries. For $0.87 \leq r/b \leq 1.00$ the reverse is true; the increase in ϕ with r/b is higher for the lock plate geometries than for the drive arm geometries, suggesting better sealing of the cavity. This can be attributed to both the internal cooling of the rotor as the cooling flow passes through it, and also to the higher radius of the coolant entry into the cavity. This is discussed further in section 8.5.4. The cooler normalised temperatures at the higher radius of the rotor, resulting from the lock plate geometry, could be employed as the starting point for the design of coolant delivery geometries in production engines, focusing on reducing temperatures at blade root fixing points.

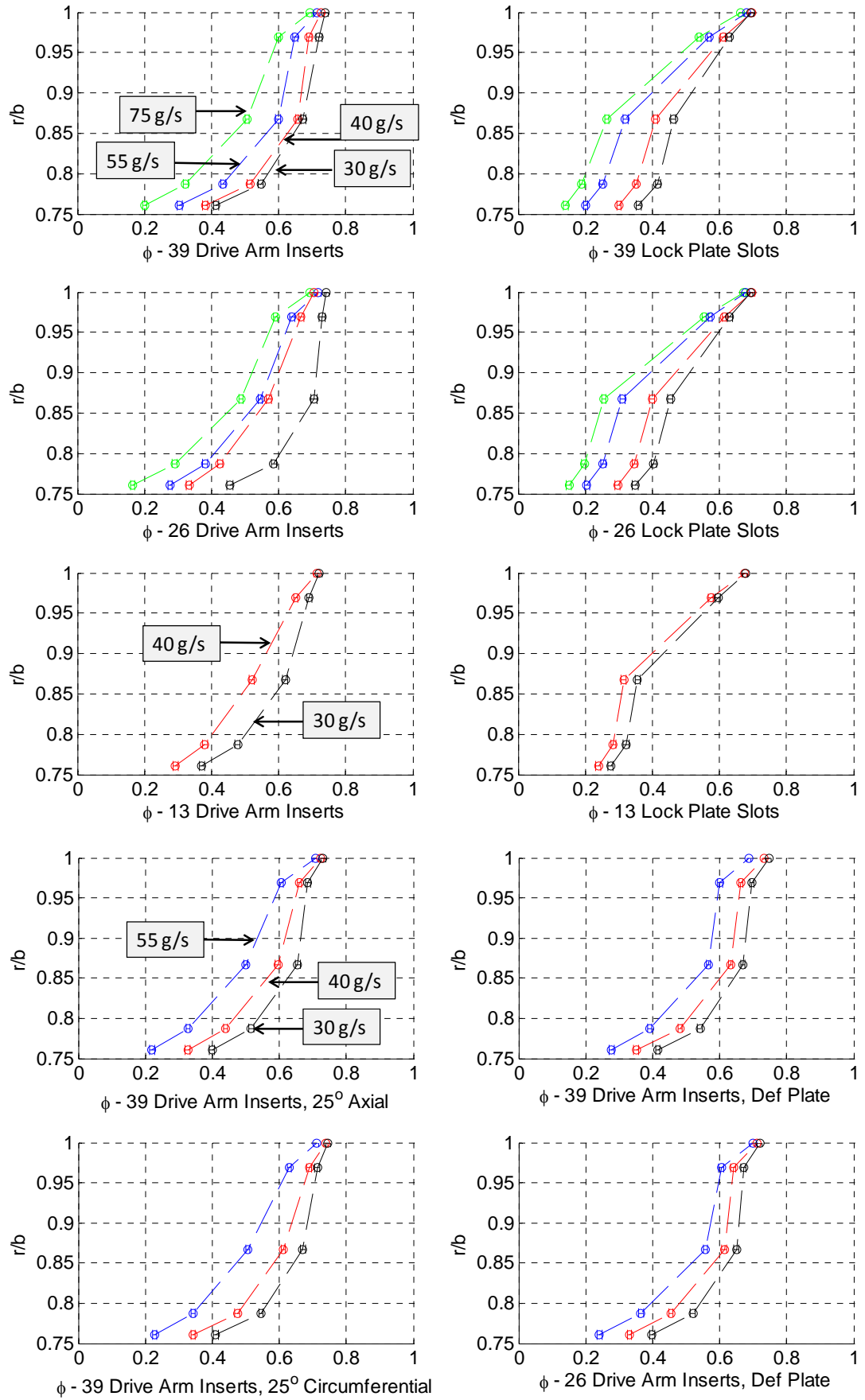


Figure 8-8: Rotor 1 rear face normalised metal temperature for all tested geometries and cooling flow rates

8.5.2 Normalised Stationary Upstream Stator Well Temperatures

Figure 8-9 shows locations of the metal surface temperature model points on the front face of Stator 2, making up the stationary face of the upstream stator well, the model points being positioned radially outwards from the inner radius of the stator foot, up to the stationary section of the stator well rim seal in the main annulus path. T_H and T_C are taken from the locations shown in Figure 8-3. The radial location of the measurement points are given as a ratio of the cavity height r/b in Table 8-4.

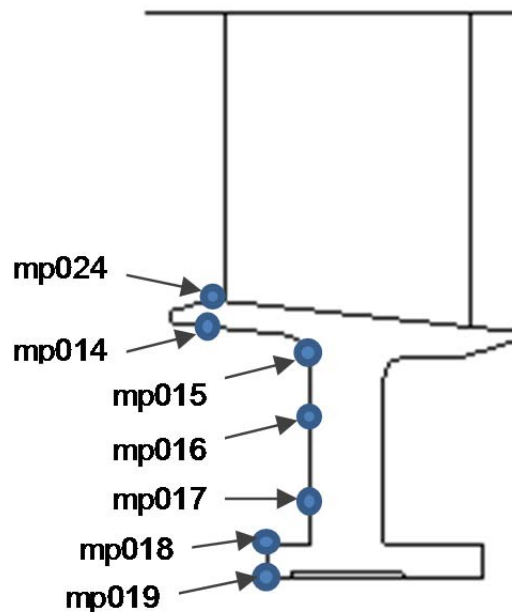


Figure 8-9: Normalised temperature locations on front face of Stator 2

Model Point	r/b
mp019	0.7843
mp018	0.8115
mp017	0.8217
mp016	0.8986
mp015	0.9483
mp014	0.9736
mp024	1.0000

Table 8-4: Stator 2 upstream face measurement location

Figure 8-10 shows the normalised temperature results for the front face of Stator 2 corresponding to the model points shown in Figure 8-9. As for the rotating normalised temperatures shown in Figure 8-8 all geometries and flow rates are shown. Normalised temperature ϕ is plotted against the radial location given in Table 8-4 as a ratio of cavity height r/b . Cooling flow rates are indicated in the same manner as Figure 8-8. Error bars are of a similar magnitude to the data markers.

As was shown for the rotating profiles, the gradient between the two top radial locations offer an indication of the cooling and sealing performance for a given geometry and flow rate, for the stator this is between the radial locations $0.97 \leq r/b \leq 1.00$. When compared to the results for the rotor the gradients between the points are generally much larger, particularly for lower cooling flow rates. This is due to the entrainment of ingested main annulus gas on the underside of the stationary section of the cavity rim seal. The gradient is seen to reduce with increased cooling flow indicating improved cavity sealing.

A similarly large gradient is seen at the low radius $0.78 \leq r/b \leq 0.81$, which shows little variation with changes in cooling supply. This is the leading edge of the stator foot which sees the majority of the cooling flow even at low flow rates.

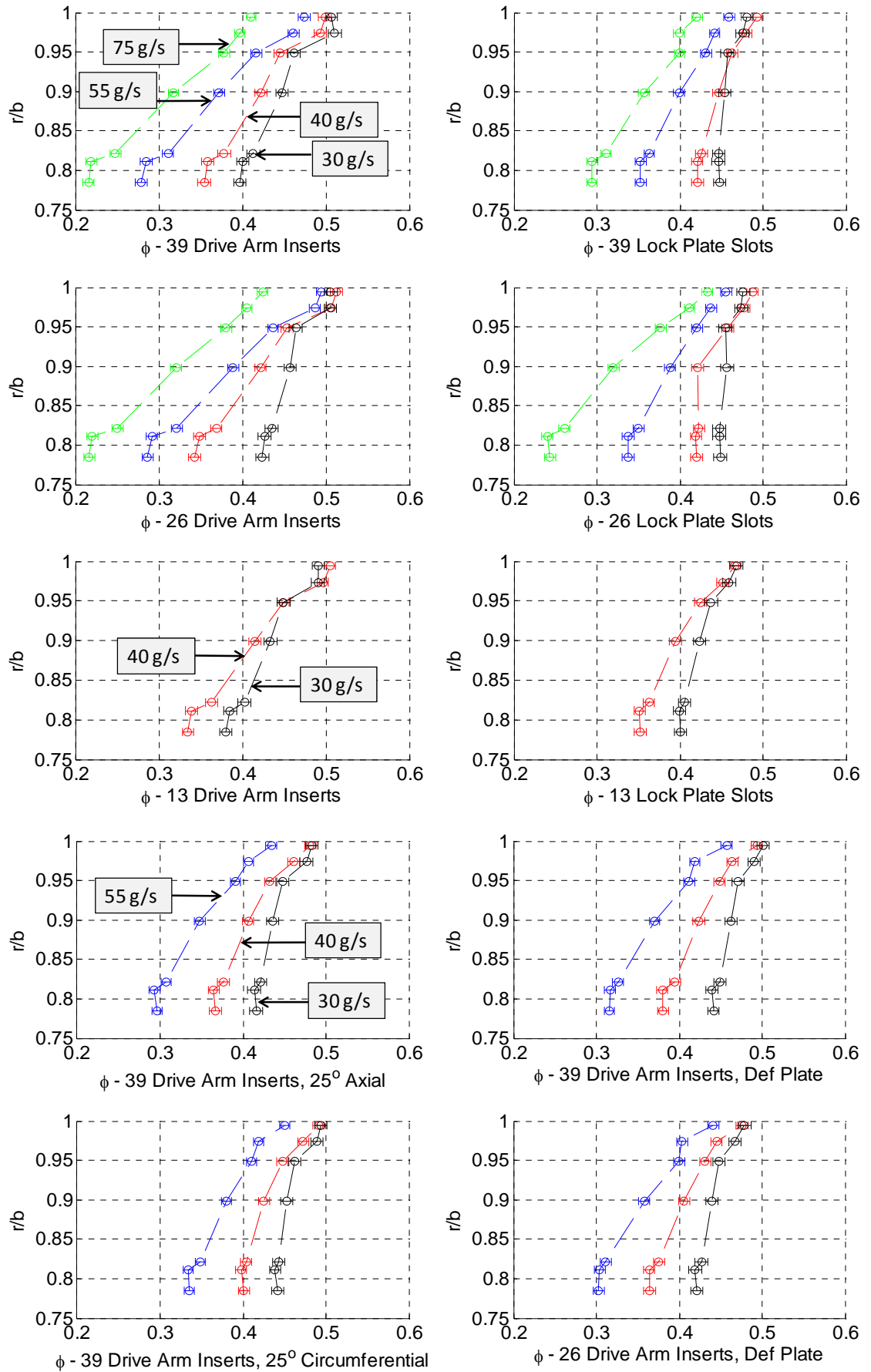


Figure 8-10: Stator 2 front face normalised metal temperature for all tested geometries and cooling flow rates

8.5.3 Comparison of Phase 1 Drive Arm Configurations

In this section the three drive arm insert configurations tested as part of the phase 1 test set are compared at each cooling flow rate. Figure 8-11 shows the normalised temperatures on the rear face of Rotor 1 with respect to radial position r/b , as described in Table 8-3. For 39, 26 and 13 drive arm inserts, nominal cooling flows of 30 gs^{-1} , 40 gs^{-1} , 55 gs^{-1} and 75 gs^{-1} are shown (55 gs^{-1} and 75 gs^{-1} not tested for 13 inserts). For the three higher cooling flows, a reduction in normalised temperature at each radius is seen on the rotor face as the number of inserts is reduced, except for the highest radius position $r/b = 1$ which is dominated by the main annulus gas temperature. At the lowest nominal cooling flow rate of 30 gs^{-1} this is not the case between 39 and 26 drive arm inserts, although again the 13 insert temperatures are lowest.

Examination of the exact supplied cooling flows in Table 8-1 shows that for all drive arm configurations the cooling flow dropped slightly with reduced number of flow features, except for the case of nominal 40 gs^{-1} , where the 26 drive arm configuration had a cooling supply rate of 43.36 gs^{-1} compared to 43.18 gs^{-1} for the 39 drive arm configuration. This further supports the observation that the normalised temperature reduced with reduced number of inserts. The improvement seen on the rotating face at low radius with reduced number of inserts suggests the cooling air is better entrained into the rotor boundary layer, suggesting a change in flow structure in the cavity. This is attributed to the higher radial momentum of the coolant from the drive arm holes when the number of flow features is reduced.

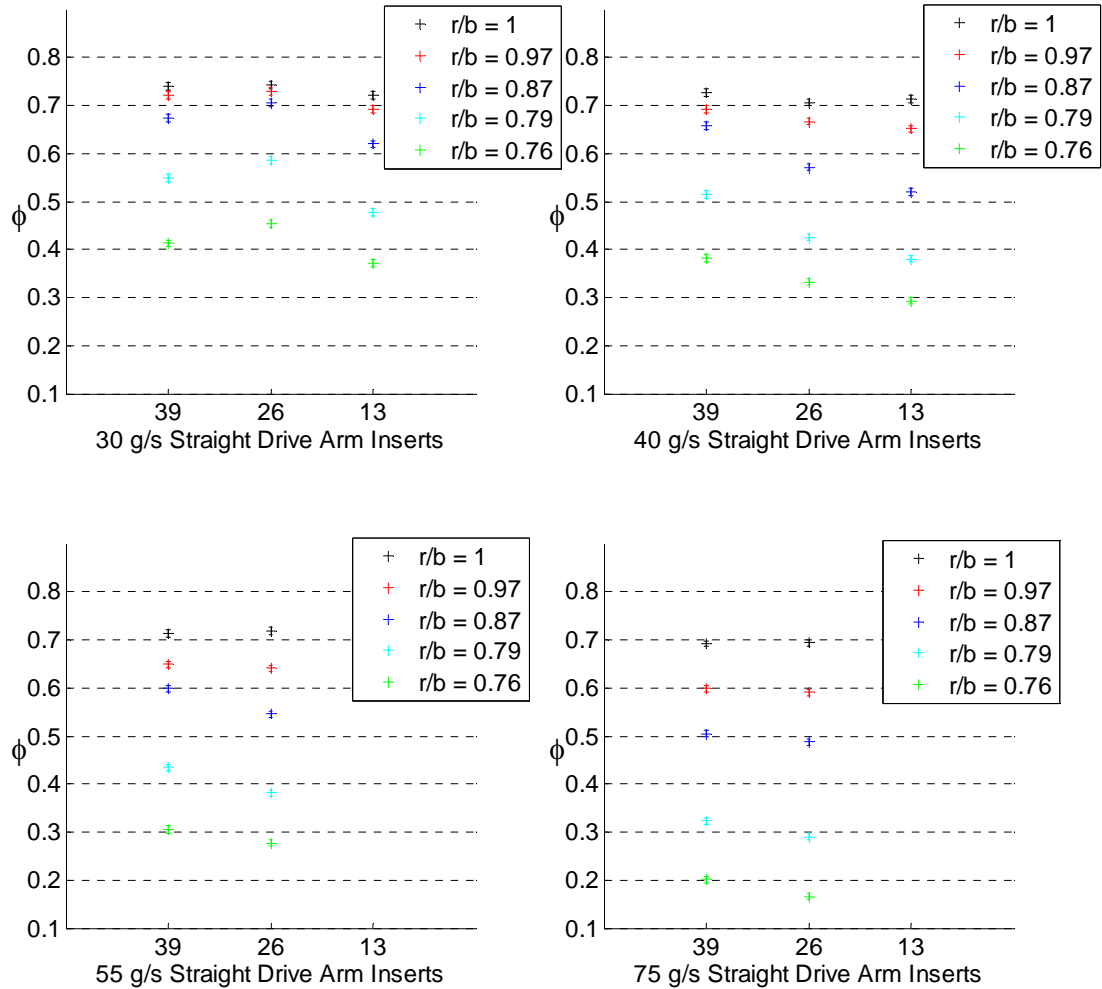


Figure 8-11: Rotor 1 rear face normalised metal temperature for all Phase 1 straight drive arm geometries and cooling flows

Figure 8-12 shows this effect in the upstream stator well graphically, where Coren et al (2011) used coolant streamlines to demonstrate that the coolant impingement into the cavity increases significantly as the number of delivery holes reduces, increasing the amount available for entrainment onto the rotor face. It can be seen that with 39 drive arm inserts the coolant directly feeds the interstage seal demand, whereas for the 13 drive arm hole case the coolant penetrates further into the cavity and is entrained onto the rotor disc.

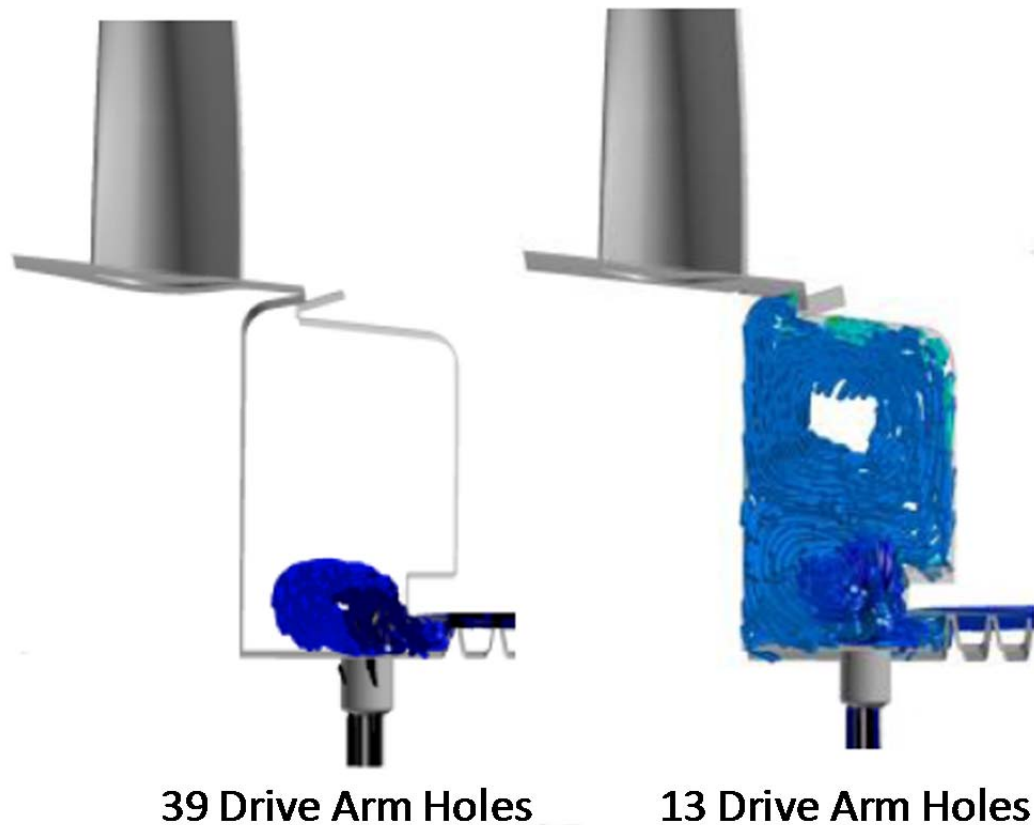


Figure 8-12: Adiabatic flow visualisation of coolant delivery through 39 and 13 drive arm holes at $0.63 \text{ Cw}_{\text{ent}}$ (Coren et al 2011)

Figure 8-13 shows normalised temperatures on the front face of Stator 2, for the radial positions given in Table 8-4, corresponding to the same geometries and cooling flows shown in Figure 8-11. As was seen on the rotor, for the nominal 30 gs^{-1} case the difference in normalised temperature between geometries does not show a strong trend. At nominal 40 gs^{-1} the lower radius temperatures are seen to reduce with reduced number of drive arm inserts. However this trend is not repeated at nominal 55 gs^{-1} and 75 gs^{-1} . For the three higher cooling flow rates and 26 drive arm inserts, the high radius location is seen to increase in temperature when compared to the 39 insert cases.

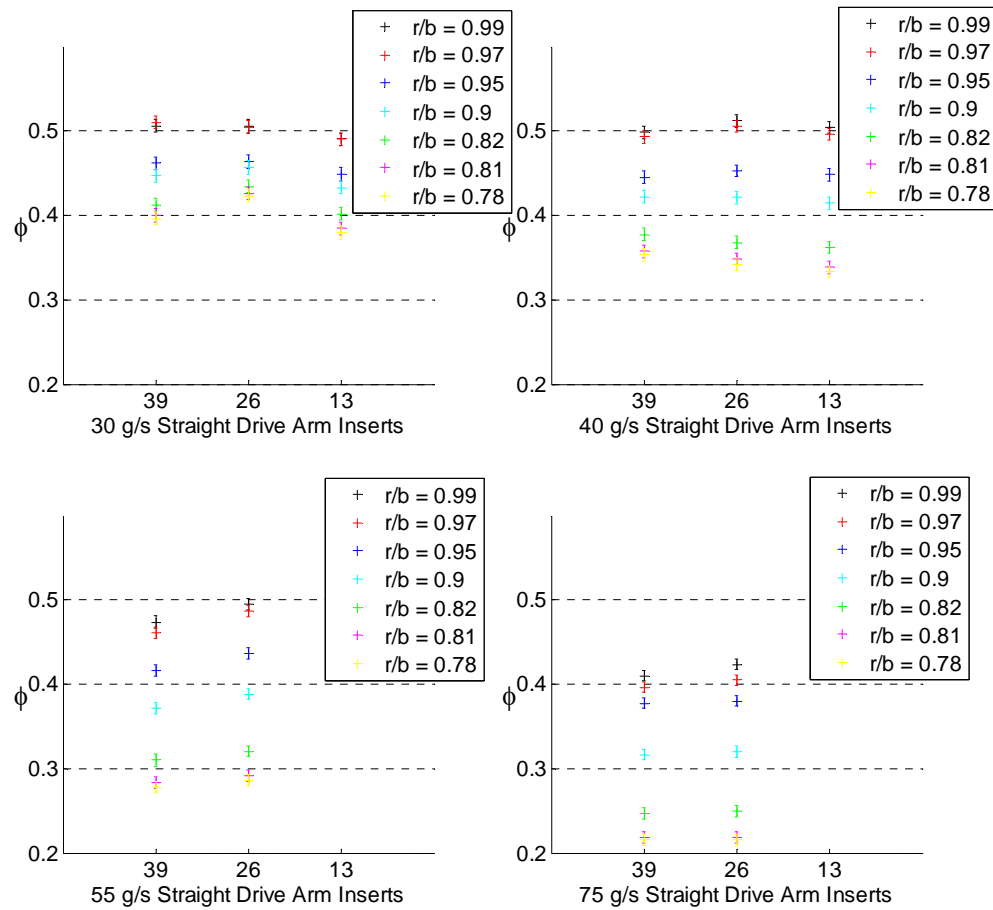


Figure 8-13: Stator 2 front face normalised metal temperature for all Phase 1 straight drive arm geometries and cooling flows

8.5.4 Comparison of Phase 1 Lock Plate Configurations

In this section the three lock plate slot configurations tested as part of the phase 1 test set are compared at each nominal cooling flow rate tested. Figure 8-14 shows the normalised temperatures on the rear face of Rotor 1 with respect to radial position r/b . For 39, 26 and 13 drive arm inserts, nominal cooling flows of 30 gs^{-1} , 40 gs^{-1} , 55 gs^{-1} and 75 gs^{-1} are shown (55 gs^{-1} and 75 gs^{-1} not tested for 13 inserts). As for the drive arm insert configurations, little change is seen in the high radius location between geometries for a given cooling flow rate. The trend of lower temperatures in the lower radius positions is again evident with a reduction in the number of flow features for the lower two nominal coolant flow rates. However this must be more

closely examined with respect to the exact flow rates given in Table 8-1. As mentioned in Section 8.5.1 the cooling flow rates for the 13 lock plate slot geometries at the nominal 30 gs^{-1} showed the largest deviation in achieved cooling flow. However Figure 8-14 shows that the 30 gs^{-1} 13 lock plate geometry, which had a flow rate of 36.09 gs^{-1} still has low normalised temperatures at the lower radius, even when compared to the nominal 40 gs^{-1} results for the 39 and 26 lock plate geometries, which had flow rates of 43.92 gs^{-1} and 41.59 gs^{-1} respectively.

The lower radius rotor metal temperatures are all seen to be cooler than for the drive arm geometries. For both the drive arm and lock plate geometries the coolant supply path is identical up to the lower supply cavity, as was shown in Chapter 3. At this point the coolant either enters the upstream stator well cavity through the drive arm inserts, or for the lock plate geometries passes through rotor 1. The cooler rotor temperatures seen for the lock plate geometries can be attributed to a number of effects. The coolant is being injected into the upstream stator well at a higher radius than the drive arm geometries, where it is directly feeding the disc entrainment. It also has axial momentum which effects the way in which the coolant interacts with the cavity flows and boundary layer. Streamlines showing this were presented by Dixon et al (2012). The third mechanism by which the lock plates increase rotor cooling is through the internal cooling of the disc before the coolant is injected into the cavity. It is a complex task to separate the internal cooling effects from the coolant injection location and momentum effects and was not conducted as part of the MAGPI program. In order to fully decouple these effects it would be necessary to complete a conjugate analysis of conduction and convection within the rotor.

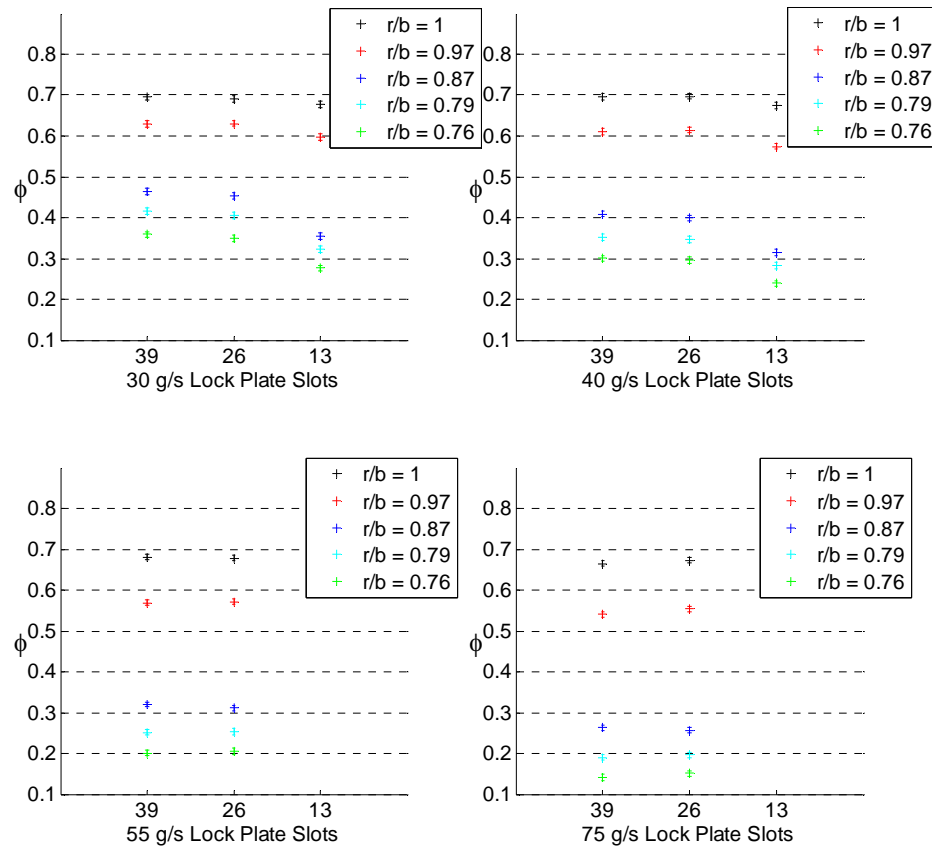


Figure 8-14: Rotor 1 rear face normalised metal temperature for all Phase 1 lock plate geometries and cooling flows

Figure 8-15 shows normalised temperatures on the front face of Stator 2, for the radial positions given in Table 8-4, corresponding to the same geometries and cooling flows shown in Figure 8-14. Contrary to the result for the drive arm insert geometries, where little or no reduction was seen in the normalised stator temperature with reduced flow features or increased cooling flow, a large improvement is seen for 13 lock plate slots, even at lower cooling flow rates and for 26 lock plate slots at the high cooling flow rate. This is attributed to a high axial momentum of the coolant at the exit of the lock plate slots increasing the coolant delivery to the stator.

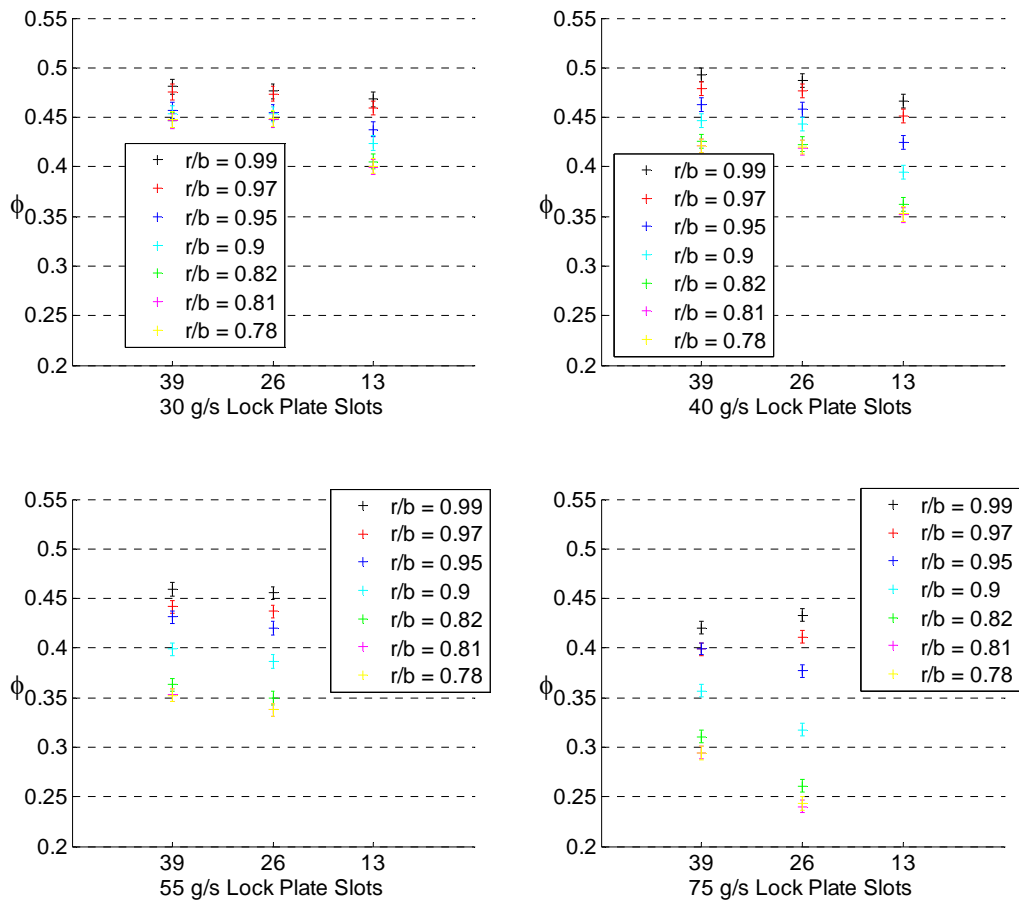


Figure 8-15: Stator 2 front face normalised metal temperature for all Phase 1 lock plate geometries and cooling flows

8.5.5 Comparison of 39 Drive Arm Holes with Angled Inserts

In this section the straight "STR", 25° axial angled "AXL", and 25° circumferentially angled "CIR", drive arm inserts are compared at each cooling flow rate tested. Figure 8-16 shows the normalised temperatures on the rear face of Rotor 1 with respect to radial position r/b , for nominal cooling flows of 30 gs^{-1} , 40 gs^{-1} , 55 gs^{-1} . At the low nominal cooling flow rate of 30 gs^{-1} there is no significant variation between the rotor temperatures for the three configurations. However when the exact flow rates presented in Table 8-1 and Table 8-2 are considered, where the straight drive arm configuration had an extra 4 gs^{-1} when compared to the axial and circumferentially angled configurations, it could be concluded that both angled inserts in fact more

effectively cool the rotor as they maintain the normalised temperatures seen with the straight insert even with the slightly reduced cooling flow. At 40 gs^{-1} nominal flow it can be seen that the axially angled inserts result in lower normalised temperature at all radial position, the circumferentially angled inserts also show lower temperatures than the straight inserts however, not to the same extent as the axial inserts. Again consideration of Table 8-1 and Table 8-2 show the straight drive arm geometry had the highest flow rate, further supporting the improvement seen with the angled inserts. This trend is increasingly prominent at nominal 50 gs^{-1} . For the axially angled inserts the improvement is a result of improved entrainment of coolant into the rotor boundary layer. The mechanism of improvement with the circumferentially angled insert is less clear, but is most likely to be a result of the effect on core rotation.

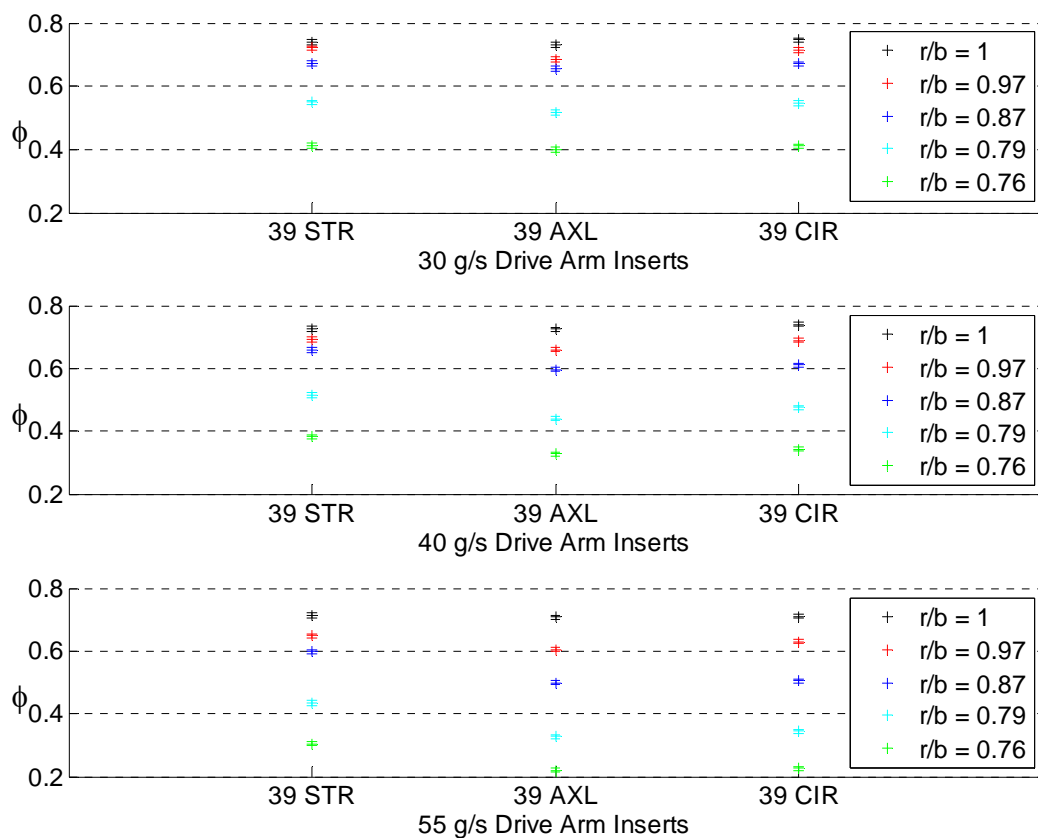


Figure 8-16: Rotor 1 rear face normalised metal temperature for all angled 39 drive arm insert geometries and cooling flows

Figure 8-17 shows normalised temperatures on the front face of Stator 2 for the angled insert geometries. The results show that for both the angled insert cases the lower radius of the stator face had higher normalised temperatures when compared to the straight insert geometry, while the outer radius normalised temperatures are lower, resulting in a lower temperature gradient across the stator.

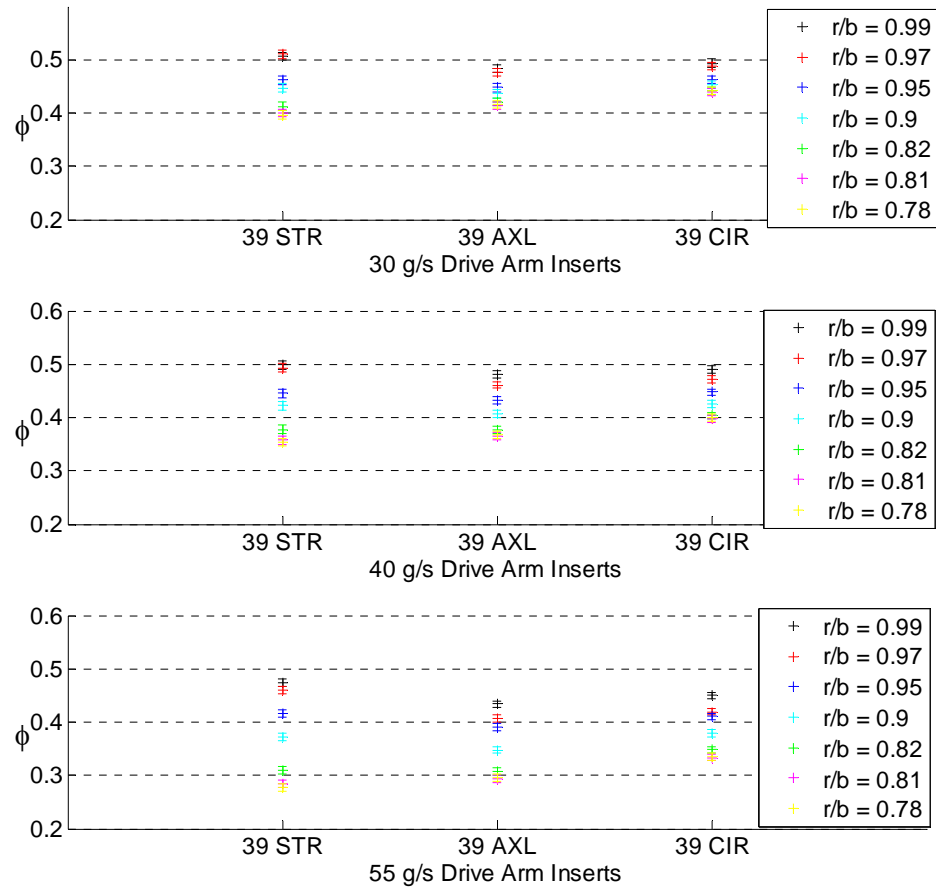


Figure 8-17: Stator 2 front face normalised metal temperature for all angled 39 drive arm insert geometries and cooling flows

Figure 8-18 shows coolant path lines based on contours of cooling effectiveness shown by Dixon et al (2012) for the axially angled drive arm geometry at 30 gs^{-1} . It shows how the coolant is directed towards the face of rotor 1 and entrained in the boundary layer. It is then pumped towards the higher radius area of rotor 1, before being drawn across the cavity to the higher radius of the stator. The lower normalised temperatures at the higher radius of the stator can be attributed to this effect. It can

also be seen that when compared to the 39 straight drive arm configuration shown in Figure 8-12 the amount of coolant impinging directly onto the lower radius of the stator foot is greatly reduced.

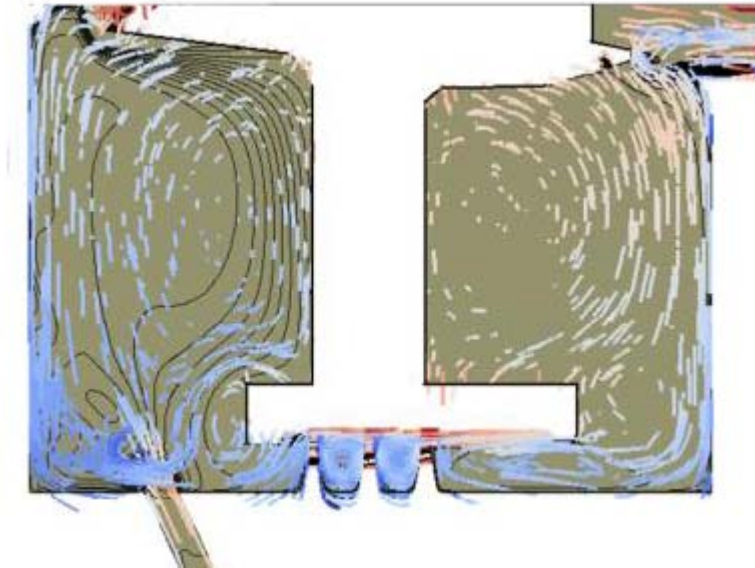


Figure 8-18: Pathlines of cooling effectiveness, Axial insert geometry, 30 g/s⁻¹, Dixon et al (2012)

This results in the higher normalised stator temperature at the lower radial positions, where there is a reduction in the previously un-entrained cooling air in the vicinity of the stator. For the rotor it was seen that the axial angled inserts best cooled the rotor face, which might suggest that the stator with the axial inserts should then be the least well cooled. However, this does not seem to be the case as the stator temperatures at the lower radius for the circumferentially angled inserts are shown to be slightly higher.

8.5.6 Comparison of Drive Arm and Deflector Plate Geometries

In this section the 39 and 26 straight drive arm insert geometries from Phase 1 are compared to tests running the same inserts but with the stator well deflector plate in place. Figure 8-19 shows each geometry at nominal cooling flow rates of 30 gs⁻¹, 40 gs⁻¹ and 55 gs⁻¹. The Phase 1 geometries without the deflector are denoted "STR"

and the geometries with the deflector in place are denoted "DEF". At the lower nominal cooling flow rate of 30 gs^{-1} little difference is seen with the inclusion of the deflector for the 39 drive arm insert geometry, however it should be noted that the case with no deflector plate has an additional 4 gs^{-1} . The 26 drive arm insert case with deflector plate shows a reduction in rotor temperatures at all radial locations, despite an additional 3 gs^{-1} of cooling flow for the 26 inserts without the deflector plate. The converse is true at nominal 40 gs^{-1} where the reduction in rotor temperatures, with the inclusion of the deflector, is more pronounced for the 39 insert case. At nominal 55 gs^{-1} the inclusion of the deflector shows reduced rotor temperatures for both 39 and 26 drive arm insert cases, despite lower cooling flow rates of 3 gs^{-1} when compared to the cases without the deflector in place.

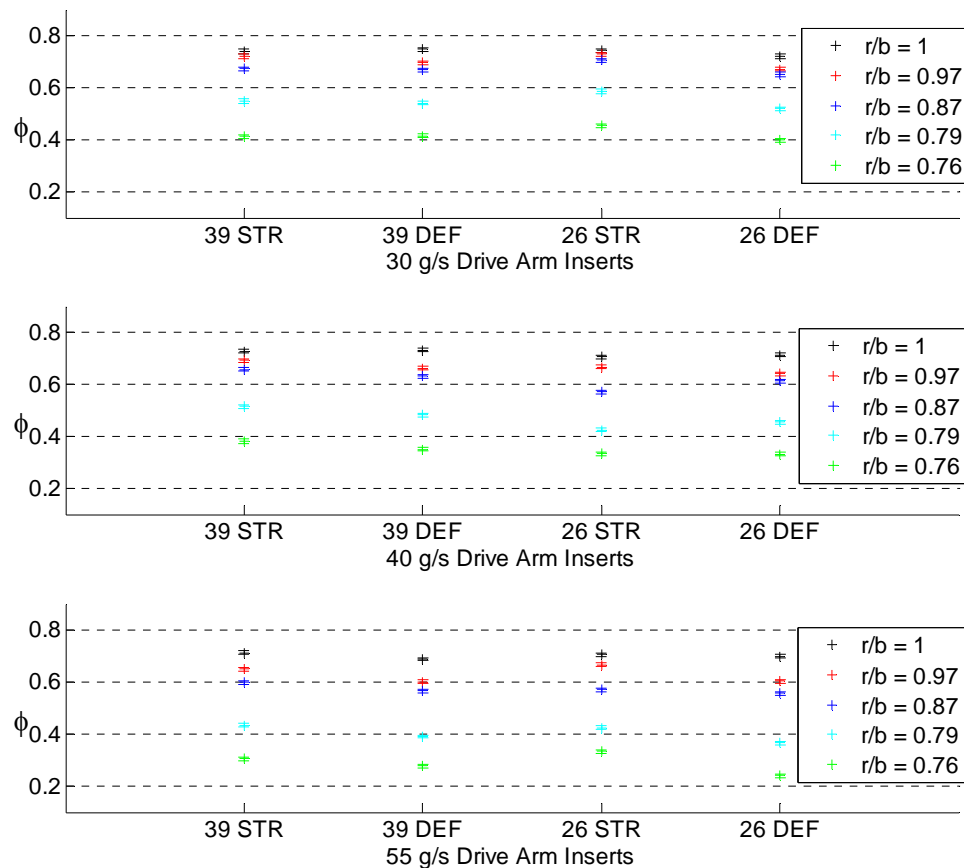


Figure 8-19: Rotor 1 rear face normalised metal temperature for 39 and 26 drive arm insert geometries, with and without deflector

Figure 8-20 shows normalised temperatures on the front face of Stator 2, for the drive arm insert geometries with and without the deflector. For all cooling flows the inclusion of the deflector plate is seen to both reduce high radius temperature whilst increasing low radius temperatures. The increase in lower radius temperatures is most likely the effect of the deflector plate preventing cooling flow from impinging onto the stator foot. The cause of the decrease in high radius temperature however, is less clear. It may be due to coolant attaching to the rotor and reaching the higher radius of the cavity or to the effect of the deflector on the core flow.

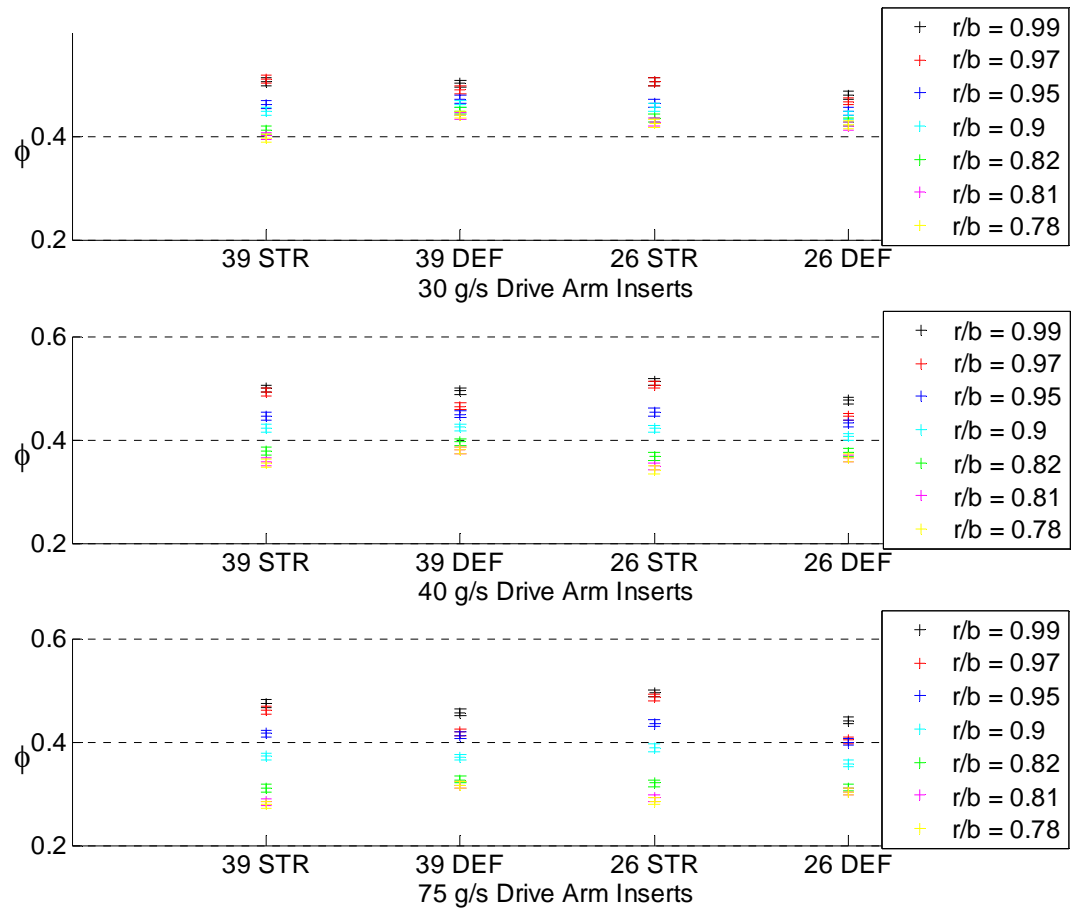


Figure 8-20: Stator 2 front face normalised metal temperature for 39 and 26 drive arm insert geometries, with and without deflector

8.6 Summary

In this chapter stator well temperatures have been presented for a range of cooling flow rates and supply geometry. The temperature data has been presented in normalised form in order to aid comparison between test runs and to highlight trends.

It was shown that for all geometries tested the normalised temperature reduced with increased superposed flow, except for model points at $r/b \approx 1$, dominated by hot gas temperatures. Lock plate slot geometries cooled Rotor 1 more effectively than the drive arm inserts, where the coolant both cooled the disc internally and directly fed the rotor boundary layer. This was particularly evident at low cooling flow rates. The normalised temperature profiles of the stator were more comparable between lock plate and drive arm geometries.

At cooling flow rates $\geq 40 \text{ gs}^{-1}$ the normalised temperatures were seen to reduce with reduced number of flow features for the straight drive arm inserts, suggesting improved entrainment of coolant on the rotor surface. Where the number of drive arm holes is reduced the increased radial momentum of the coolant is thought to increase the radius to which the coolant penetrates into the upstream stator well for a given flow rate. Contrary to this, for the lock plate slot geometries normalised rotor temperatures were seen to drop at the low cooling flow rates with a reduction in flow feature numbers. No improvement was seen between geometries in rotor temperature at high cooling flow rates. However, at high cooling flow rates the lock plate slot geometries showed much improved cooling of the stator as the number of flow features was reduced.

The Angled drive arm inserts showed only marginal improvement in rotor cooling, except for the higher cooling flow rate of 55 gs^{-1} , where the axial angled inserts gave the lowest rotor temperatures, followed by the circumferential inserts. Both the axial and circumferentially angled inserts caused an increase in the stator temperature when compared to the straight drive arm inserts.

For both the back to back tests of 39 drive arm inserts and 26 drive arm insert, with and without the deflector plate in place, the deflector plate was seen to improve cooling of the rotor. Interestingly the deflector plate had the effect of reducing the temperature gradient across the stator by both increasing low radius temperatures and reducing high radius temperatures.

The geometry trends identified in this chapter are discussed further in Chapter 9 where they are compared to gas concentration results.

9 Results - Concentration Measurements

9.1 Introduction

In this chapter results are presented from the gas concentration experiments, described in Chapter 6. The findings from the experiments are compared and contrasted with the results obtained from the temperature measurements shown in Chapter 8. The numerical modelling methods employed by fellow researchers are also compared to the results of the author.

In this chapter the superposed cooling flow \dot{m}_0 has been given quantitatively, where nominal flow rates of 30 gs^{-1} , 40 gs^{-1} , and 55 gs^{-1} have been tested for multiple geometries. In order to compare these flow rates it is often useful to express them in terms of a nondimensional flow rate. For the case of a rotor stator cavity with an inner hub, such as the TSW facility, the cooling flow rate can be expressed in terms of the partial disc entrainment $C_{w,ent}$, which was defined in Chapter 2 Equation 2-6. The cooling flow rates $30 \text{ gs}^{-1} \leq \dot{m}_0 \leq 55 \text{ gs}^{-1}$ can then be expressed as $0.71 \leq C_{w,ent} \leq 1.04$. These flow rates correspond to in cavity rotational Reynolds numbers of $1.71 \times 10^6 \leq Re_\phi \leq 1.86 \times 10^6$. The corresponding external axial Reynolds number for the region above the upstream stator well rim seal is $Re_w = 1.75 \times 10^5$ where $Re_w = uzr/\nu$.

9.2 Interstage Seal Flow Experimental Results

Figure 9-1 show the measurement locations used during the interstage seal flow experiment described in Chapter 6, section 6.2. During normal rig operation these model points measure static pressure. When conducting gas concentration experiments the pressure tap lines are re-directed to the carbon dioxide gas analysers via the instrumentation path, described in Chapter 6.2. Model point mp176 is used as the carbon dioxide injection point, upstream of the interstage seal. Gas concentration measurements are taken at two model points downstream of the seal, mp181 and mp182, and at two model points in the downstream stator well cavity, mp179 and mp180. The gas concentration measurements are taken following the procedure described in 6.13.1.

Figure 9-2 shows volumetric concentration measurements of carbon dioxide made at a cooling flow supply rate of 40 g/s for the phase 1 drive arm geometries. The concentration is plotted against the angular position from the seeding location. The measurements show a variation of over 1% volume between measurement locations. This was seen for each of the three geometries tested. In order to calculate the interstage seal flow rate using the method described in section 6.2 the assumption is made that the carbon dioxide injected upstream of the seal is fully mixed with the interstage seal flow. However, the concentration measurements suggest that full mixing has not occurred at the measurement locations.

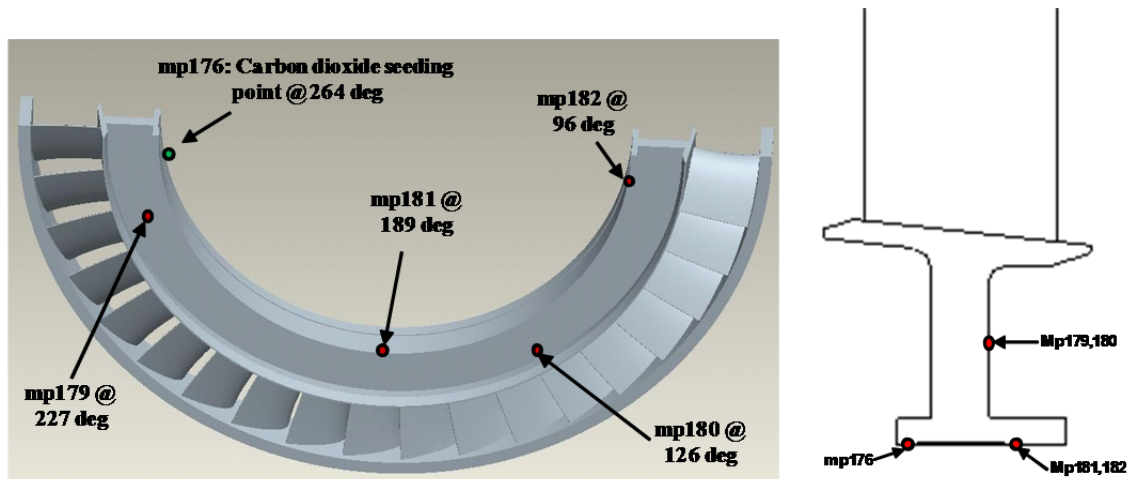


Figure 9-1: Labyrinth seal flow experimental measurement points

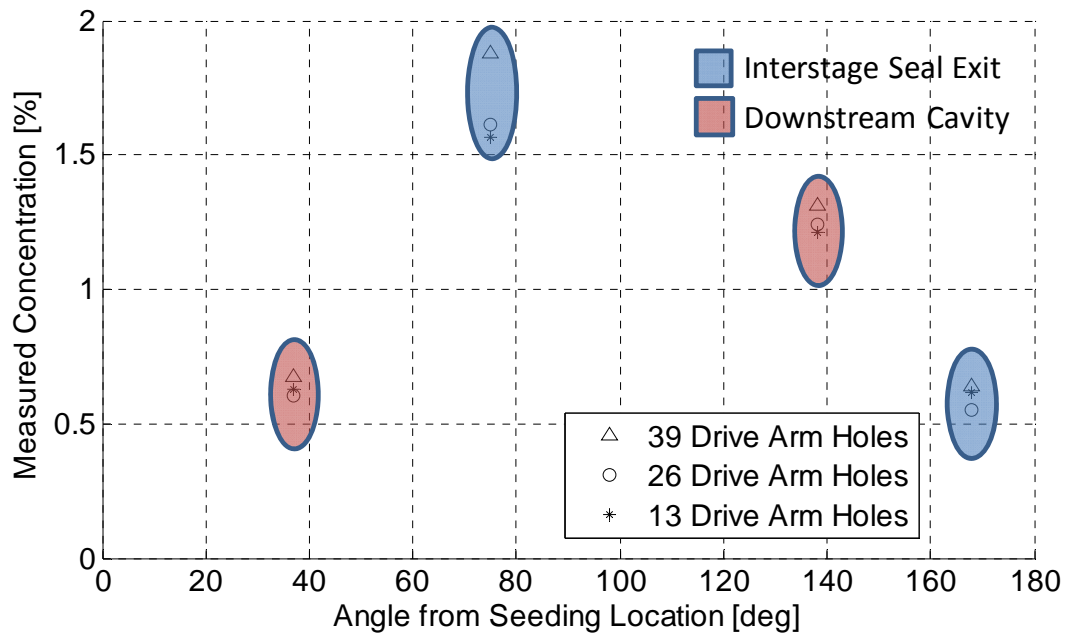


Figure 9-2: Concentration measurements made for 39 DAH, 26 DAH and 13 DAH, for 40 gs^{-1} cooling flow at interstage seal exit and downstream cavity

Where the axial velocity through the seal is of a similar or greater magnitude than the circumferential gas velocity through the seal it is unlikely that the carbon dioxide will sufficiently mix into the seal flow. This would result in areas of higher concentration, where the measurement locations could coincide with a "plume" of unmixed carbon dioxide. Figure 9-3 shows a visualisation of this effect, where a section of the rotating

surface of the seal has been unwrapped. The seeding location is shown, together with the two measurement locations immediately downstream of the seal. The figure shows how the measurement location at mp189 may be in a high concentration area, while mp182 is in a low concentration area. This would support the measurements shown in Figure 9-2.

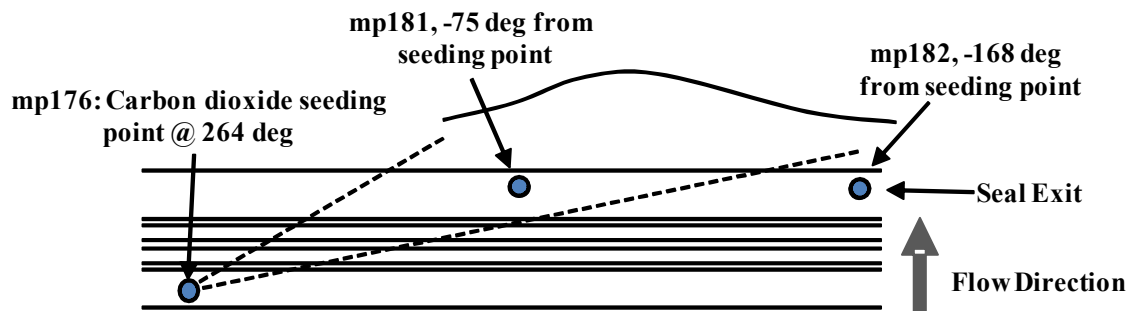


Figure 9-3: Carbon dioxide concentration plume

The failure of the interstage seal flow experiment to produce suitable results was discovered early in the experimental testing schedule. Due to the inclusion of the secondary method of obtaining seal flow, described in Chapter 7, the author was able to continue with the two main concentration experimental objectives of quantifying rim seal exchange and measuring the re-ingestion of upstream cooling flow egress. In Section 9.3.2 and Section 9.4, where these results are discussed, all quantitative results which rely on a known interstage seal flow are based on the results reported in Chapter 7.

9.3 Rim Seal Exchange

In this section results from the rim seal exchange experiment are presented. Figure 9-4 shows a review of the fundamental flows studied in this experiment. Cooling flow is delivered to the stator well, seeded with a known flow rate of carbon dioxide seeding

gas, through a number of delivery geometries presented in Chapter 3. Concentration measurements are made in both the upstream and downstream stator well cavities. Through the calculation steps, described in detail in Chapter 6, the net ingress and egress through the upstream rim seal can be calculated.

The results from the experiments are presented in two stages. Firstly in terms of dilution ratio, which is calculated using Equation 6-4. Presenting the results in this fashion allows comparison of the concentration results with normalised temperature data. The results from the summation of the calculated stator well flows are then presented and assessed for suitability of assessing rim seal exchange, as described by Equation 6-6 and Equation 6-7.

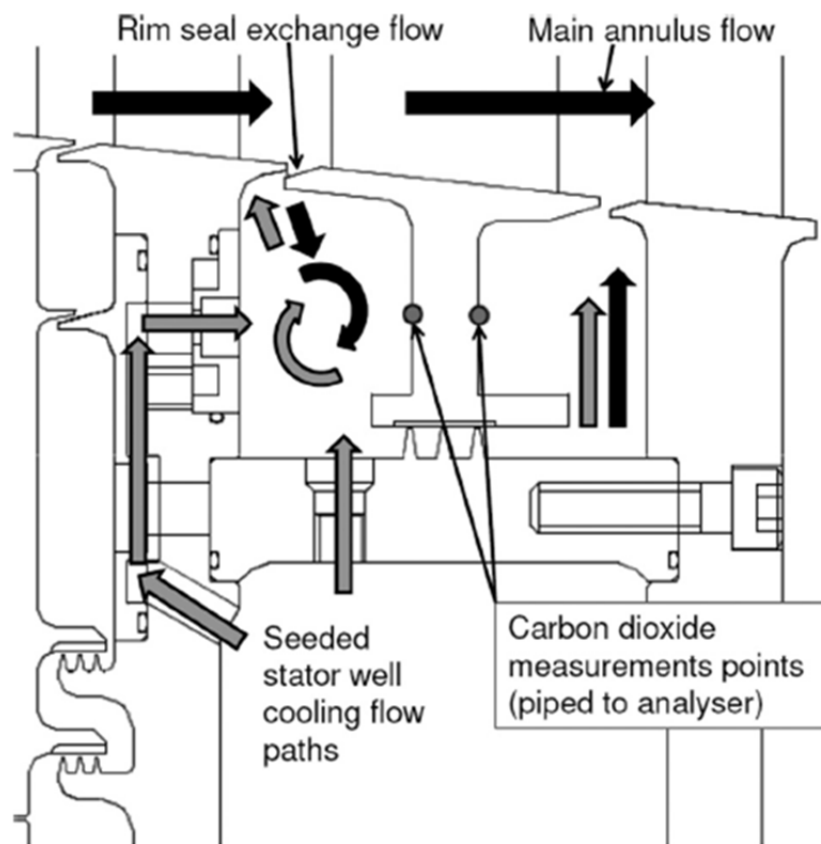


Figure 9-4: Rim seal exchange flows, Eastwood (2012)

9.3.1 Dilution Ratio Measurements

Figure 9-5 shows the dilution ratios measured for both the straight through drive arm insert geometries and the simulated lock plate slot geometries. Error bars are included which have been calculated according to the method described in Chapter 6. A dilution ratio of zero indicates that no seeded cooling air is present at the measurement point; a ratio of 1 indicates that no main annulus air is present. For both the 36 and 26 drive arm hole configurations, at the lower cooling flow rate of $\sim 42 \text{ gs}^{-1}$, a large variation was seen between the measurements taken in the upstream wheelspace and the measurements taken in the downstream wheelspace. The low dilution ratios measured at mp177 and mp178 in the upstream wheelspace indicate that the cooling air has not fully mixed with main annulus ingress into the cavity at the measurement points. A higher ratio is seen in the downstream cavity at mp179 and MP180, suggesting that the cooling air has more fully mixed with main annulus ingress air, as would be expected by the flows passing through the interstage seal. For these two geometries it appears that at low cooling flow rates the majority of the coolant directly feeds the interstage seal. The dilution ratios for the drive arm configurations at $\sim 57 \text{ gs}^{-1}$ show a similar effect, where the dilution ratio is lower for the upstream cavity. However, the difference is greatly reduced when compared to the $\sim 42 \text{ gs}^{-1}$ cases. This suggests that with increased cooling flow the coolant has more fully mixed at the upstream measurement locations, cooling at a higher radius in the cavity. This is supported by the temperature measurements obtained for the stator in Chapter 8 which showed improvements of 0.05 in normalised temperature for both the 39 and 26 drive arm insert geometries between the flow rates of 40 gs^{-1} and 55 gs^{-1} , at the concentration measurement height of $r/b = 0.86$.

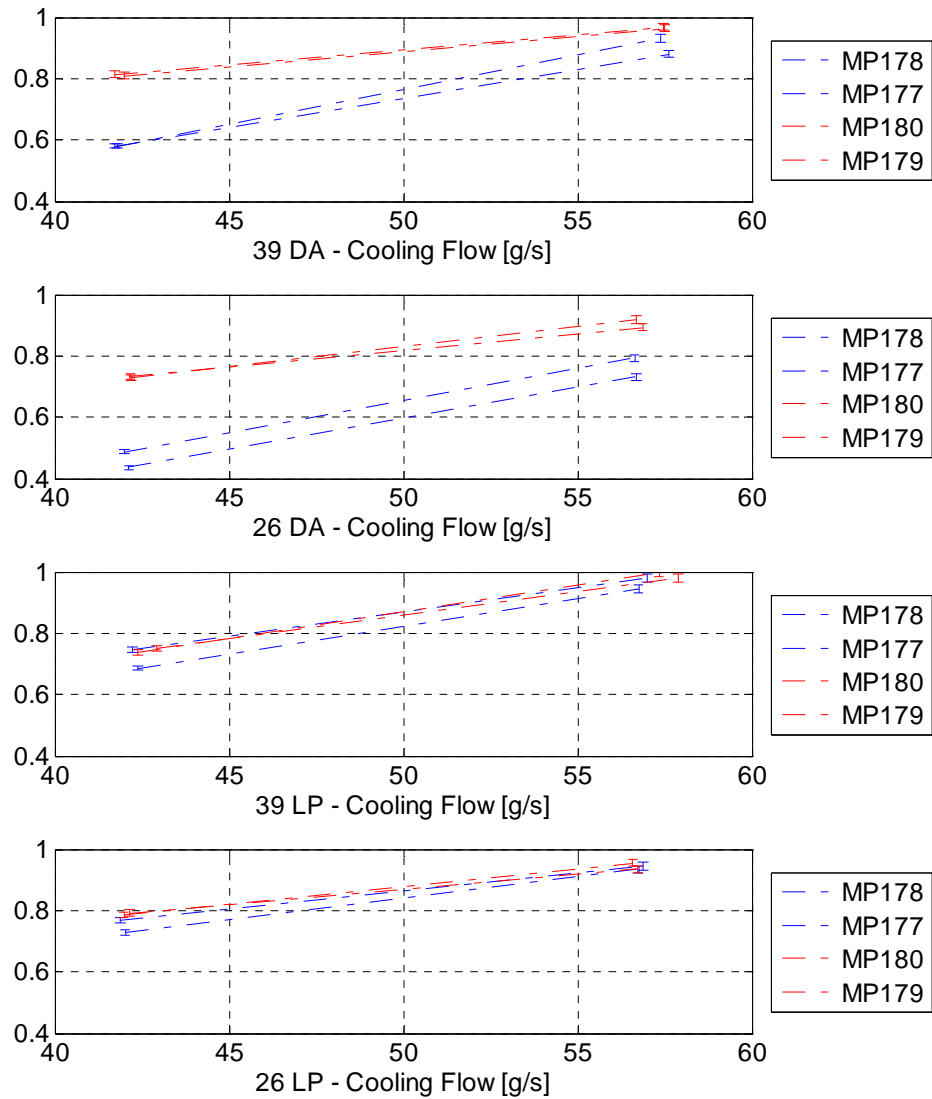


Figure 9-5: Dilution Ratio η for 39 and 26 Drive Arm Hole Geometries, & for 39 and 26 Simulated Lock Plate Slot Geometries

Coren et al (2011) considered the effect of cooling supply rate to the rotor cavity. Figure 9-6 shows stator well streamlines from a CFD study of the 39 drive arm hole geometry for two coolant flow rates of $0.63 C_{w,ent}$ and $1.08 C_{w,ent}$. For $0.63 C_{w,ent}$, where the supplied coolant flow rate is much lower than the disc entrainment it can be seen that the coolant does not penetrate to the higher radius areas of the stator well but directly feeds the interstage seal. For $1.08 C_{w,ent}$ the coolant has penetrated into the cavity.

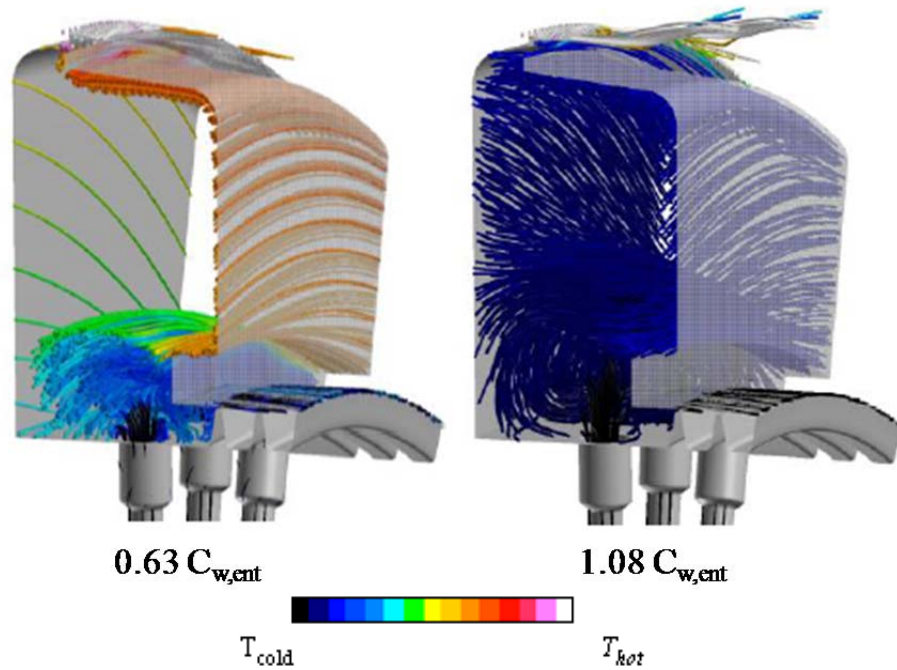


Figure 9-6: Cavity streamlines for 39 drive arm configuration coloured by normalised absolute frame total temperature, Coren et al (2011)

The results obtained for the lock plate slot geometries showed much closer agreement between the dilution values seen for the upstream and downstream measurement locations for cooling flow rates of ~ 42 g/s and ~ 57 g/s. This suggests that with lock plates the coolant has mixed fully with ingested main annulus air in both cavities as opposed to the drive arm geometries where the coolant had not fully mixed in the upstream cavity. This is due to the coolant being fed directly into the disc entrainment flow in the rotor boundary layer. This result indicates that the introduction of the cooling air through the lock plate slots has increased the amount of coolant present at the higher radius areas of the upstream stator well. As with the dilution ratios obtained for the drive arm tests, the ratios obtained for both the 26 and 39 lock plate slot geometries show an increased concentration measurement for the higher cooling flow. This shows that the higher cooling flow has reduced the ingress of main annulus gas into the upstream cavity. As expected for both 26 and 39 lock plate slots the dilution ratio is within 0.05 of being equal to 1, showing minimal ingestion through the rim seal.

This result was also supported by the temperature results reported in Chapter 8, where the rotor was seen to have significantly reduced temperatures compared to the drive arm insert geometries at the concentration measurement height. Interestingly, the temperature measurements did not show a strong corresponding reduction in temperature on the stator face. This led to the suggestion that the majority of the improvement seen for the lock plate slots was due to internal cooling of the rotor. It was also suggested that the increase in stator temperatures was due to the loss of coolant impinging on the lower radius of the stator foot which is seen for drive arm geometries, see Figure 9-6, resulting in higher conduction from the NGV platform. However, the concentration measurements show that the lock plate slots may in fact provide better sealing at the higher cooling flow rate conditions. This is discussed further in section 9.3.2.

Comparison of the drive arm and lock plate geometry downstream measurement locations, where the sampled gas has more completely mixed for both flow rates, shows that the dilution ratio increases with increased coolant flow. This indicates that for the higher coolant flow rate the upstream cavity has been more effectively sealed reducing the ingress of hot main annulus gas through the rim seal. The results also suggest generally worse sealing with fewer delivery holes. The temperature data suggested better sealing with reduced delivery holes however, when the rotor surface was considered, but showed an increase in higher radius stator temperature. This highlights one of the shortcomings of the gas sampling system used, where the limited number of sampling positions does not always give the full picture of the flow structures within the cavity.

Coren et al (2011) considered the effect of jet momentum in order to explain the variations in normalised temperature with changes in the number of flow features. It was concluded that increased jet momentum allows coolant to further penetrate into the cavity, re-distributing coolant in the cavity. Changes in normalised temperature were also attributed to the effect of the coolant jets on the core rotation of the cavity.

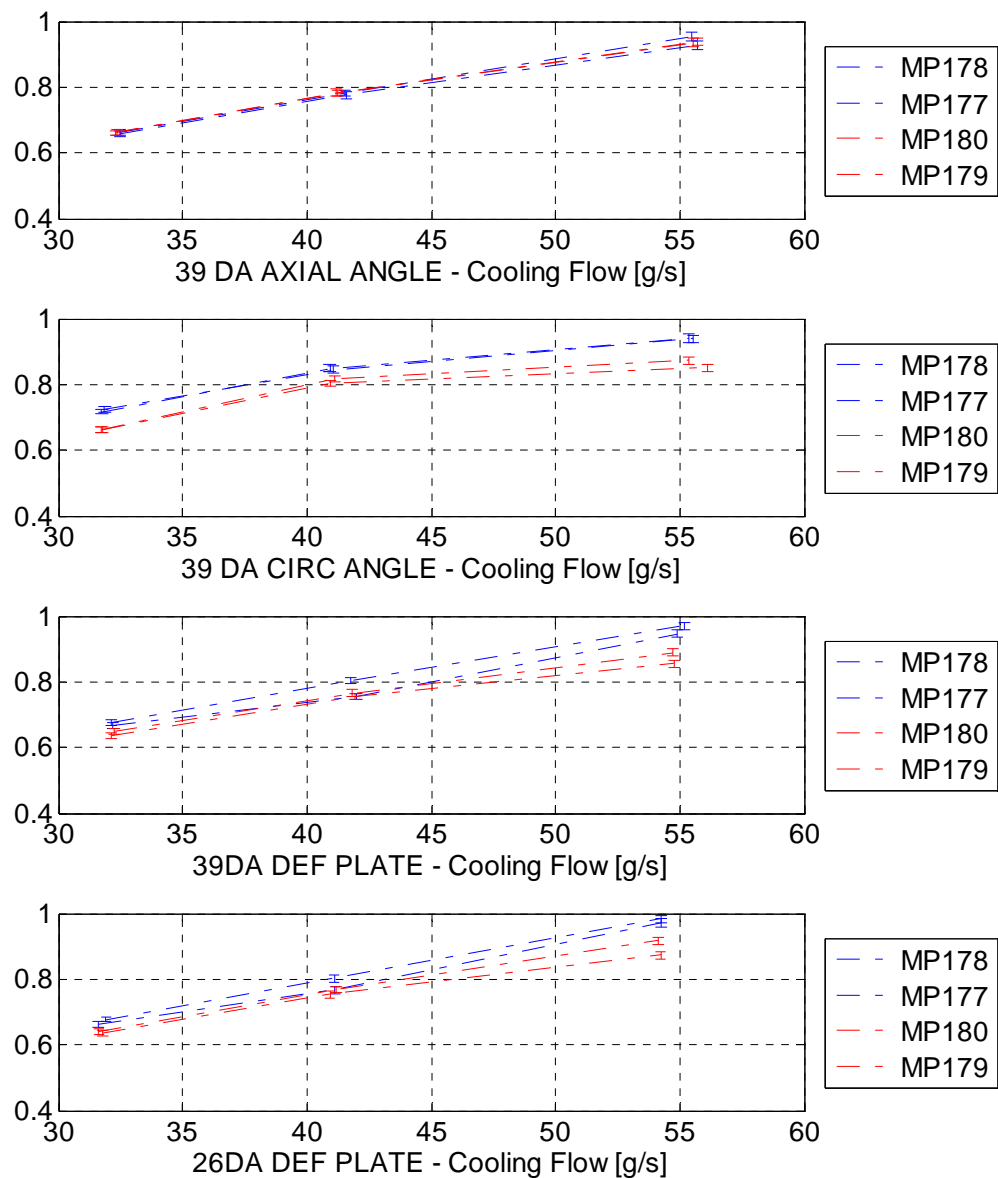


Figure 9-7: Dilution ratio η for axially angled drive arm and Deflector Plate Geometries

Figure 9-7 shows the dilution results for the 39 axial and circumferentially angled drive arm geometries, as well as the 39 and 26 drive arm geometries with the deflector plate in place. Results are shown for cooling flow rates of ~ 32 g/s, ~ 42 g/s and ~ 55 g/s. The results obtained for the axially angled drive arm inserts show very close agreement between the measurements made in the upstream stator well and the downstream stator well, the values for the higher two flow rates closely matching those seen for the downstream measurements for 39 straight drive arm inserts. This suggests that the angled inserts encourage more coolant to be entrained into the rotor boundary layer, with the coolant reaching a higher radius of the cavity. The results obtained for the circumferentially angled inserts show a similar trend however, there remains a more notable difference between the upstream and downstream measurements. This was supported by the normalised temperature measurements for the two higher flow rates, where normalised rotor temperatures indicated the axially angled inserts were the most advantageous for reducing rotor temperatures, while the circumferentially angled insert gave only a small improvement.

The results obtained for the 39 and 26 straight drive arm geometries with the deflector plate in place also show better agreement between the upstream and downstream measurements, suggesting the deflector plate increased the presence of coolant at the upstream stator well measurement positions. The temperature measurements obtained for these two geometries suggested that the higher radius of the stator was cooled. The coolant may therefore have passed “up and over” the deflector plate to the concentration measurement position. Figure 9-8 shows a study of flow aerodynamics within the stator wells conducted by Dixon et al (2012), based upon cooling effectiveness at a coolant flow rate of 30 g/s^{-1} for the deflector plate geometry. The plot shows that as the coolant enters the upstream cavity it passes to the upstream face of the deflector plate and is

then entrained onto the face of rotor 1 and pumped radially outwards to the rim seal region. The coolant then mixes with rim seal ingestion and then passes down the stator face to feed the labyrinth seal demand.

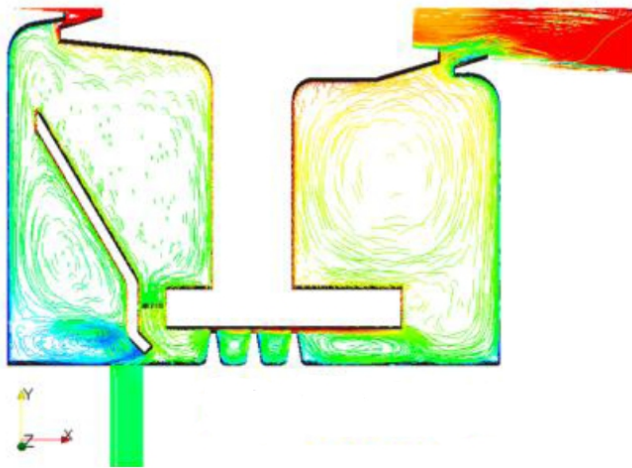


Figure 9-8: Path lines of cooling effectiveness, Deflector plate geometry, 30 gs⁻¹, Dixon et al (2012)

9.3.2 Summation Results

Although upstream dilution measurements were shown in the previous section, these only indicate the concentration of seeding gas at the upstream measurement point. Although useful for interpreting the penetration of seeded coolant into the cavity this makes the measurements less suitable for calculating the rim seal flows, as the coolant and mainstream ingress were shown not to be fully mixed at the measurement points.

Figure 9-9 shows the indicated rim seal ingress and egress rates based upon the dilution measurements made in the downstream stator well cavity. Once the coolant and any ingress has passed through the interstage seal it is can be assumed that it is homogenously mixed, making the downstream dilution measurements more suitable for use in Equation 6-6 and Equation 6-7. The ingress and egress rates are shown for each

cooling flow rate and coolant delivery geometry. It should be noted at this point that the inclusion of the interstage seal flow in the rim seal egress calculation in Equation 6-7, introduced a large uncertainty. The error bars for the egress results are seen to be of almost the same magnitude as the experimentally measured variation. The rim seal ingress, which does not use the interstage flow, shows acceptable uncertainty limits.

For all geometries tested the rate of upstream stator well rim seal ingestion, calculated using Equation 6-6, was seen to decrease with increased cooling flow supply. At the lower cooling flow rate ingress rates of between 16 gs^{-1} and 18 g/s^{-1} were measured for the four geometries tested. For the cooling flow rates at $\sim 42 \text{ gs}^{-1}$ ingestion was measured at between 9.5 gs^{-1} and 15.5 gs^{-1} . At the higher cooling flow rate of $\sim 55 \text{ gs}^{-1}$ ingestion rates were measured at between 0.6 gs^{-1} and 9 gs^{-1} . As suggested in section 9.3.1, at the higher cooling flow rate Figure 9-9 shows the 39 lock plate slot geometry to have lower ingress rates than the 39 drive arm holes geometry. The 26 lock plate slot geometry is also shown to have lower ingress rates than the 26 drive arm hole geometry.

The egress rates from the upstream stator well, calculated using Equation 6-7, show a general trend of increased wheel space egress with increased cooling flow. At the lower cooling flow rate egress rates of $\sim 6 \text{ gs}^{-1}$ were measured for the two deflector plate geometries. Higher egress rates of $\sim 13 \text{ gs}^{-1}$ were measured for the axial and circumferentially angled drive arm inserts. For both of these sets of geometries the interstage seal flow was calculated from displacement sensor measurements. The higher calculated egress rates being a product of the lower interstage seal flows, showing the sensitivity of the experiment to this flow. The intermediate flow rate results show a similar range of egress rates despite the reduced ingestion into the cavity. Again this is a

product of the interstage seal flow and the associated uncertainty. As the cooling flow is increased and the drive arm is cooled the clearance of the seal increases giving rise to higher interstage seal flows and lowering the measured egress. The higher cooling flow rates show an increase in egress, with flow rates in the range of 12 gs^{-1} to 24 gs^{-1} . Again however, the increase in egress rate is less pronounced than the decrease in ingestion due to opening of the interstage seal gap which in turn is due to cooling of the drive arm.

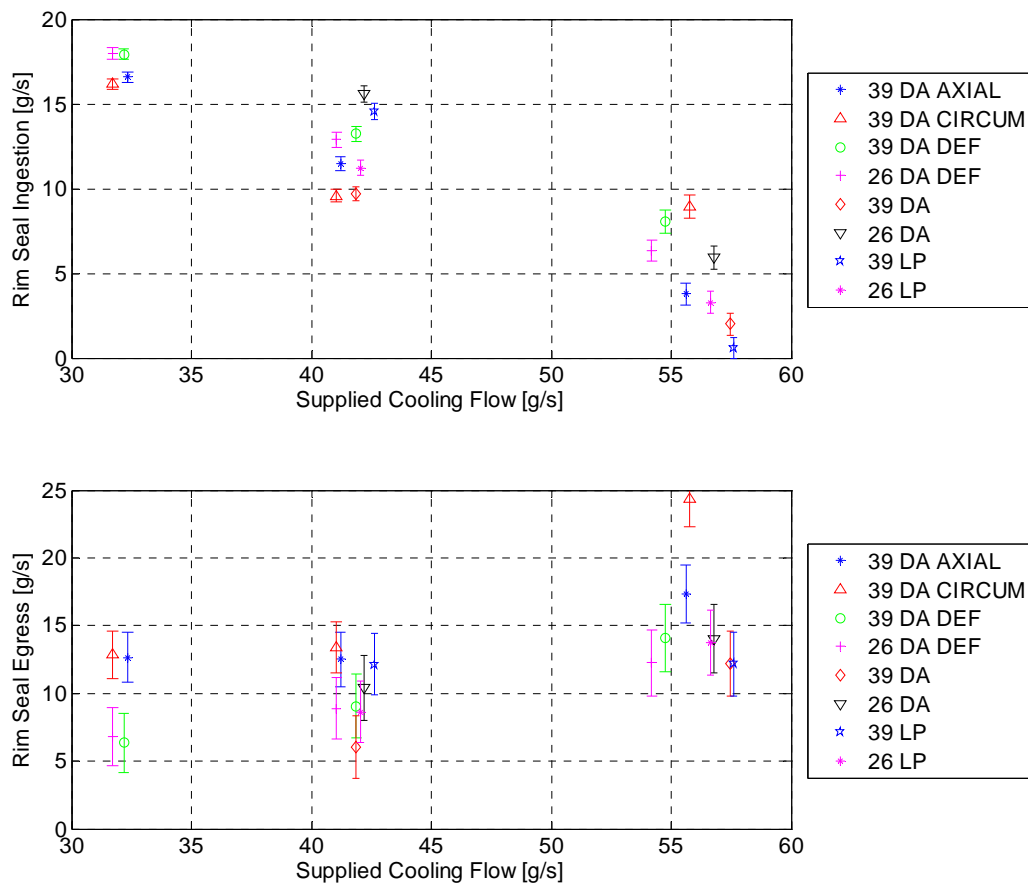


Figure 9-9: Indicated upstream stator well rim seal ingestion \dot{m}_i and egress rates \dot{m}_e

9.4 Re-Ingestion Experimental Results

In this section the results from the re-ingestion gas concentration experiment are presented. Figure 9-10 shows a brief review of the fundamental flows studied in this

experiment. The egressed cooling flow from the upstream wheelspace consists of both cooling air and carbon dioxide seeding gas. As part of the experimental procedure concentration measurements are made within the upstream and downstream stator well, in order to detect the re-ingestion of the wheelspace egress. By calculating the interstage seal flow, the mass flow rate of the re-ingestion can be determined. This method is discussed in detail in Chapter 6.

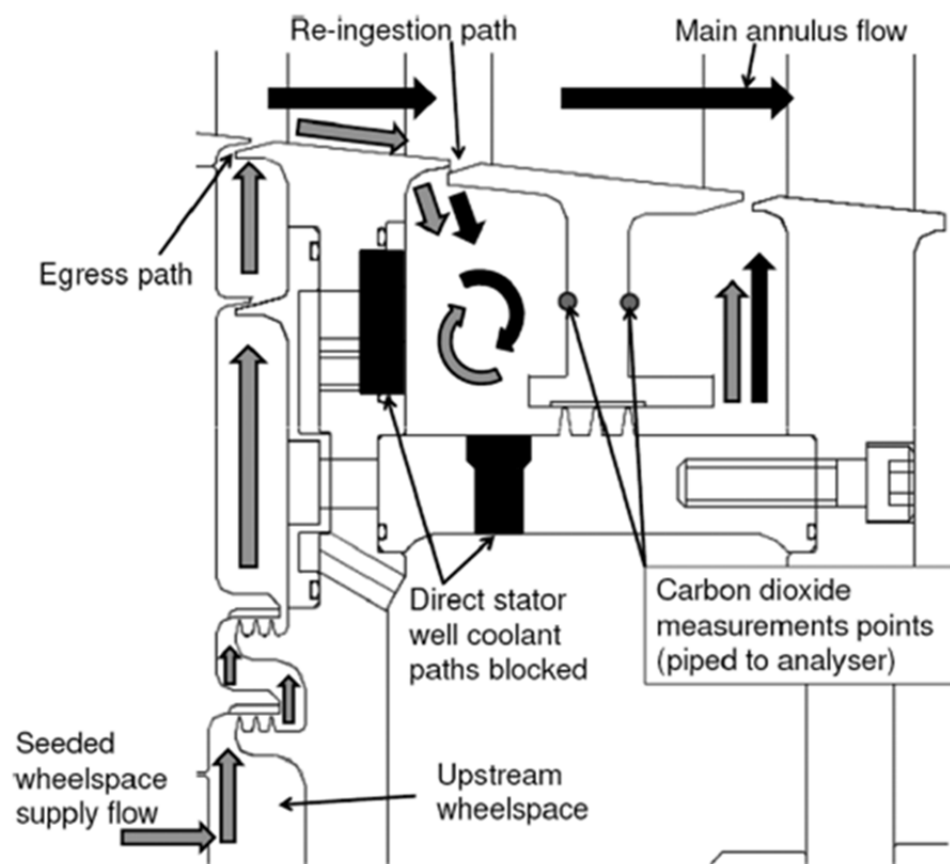


Figure 9-10: Re-ingestion experimental flows

Figure 9-11 shows the re-ingestion rates calculated from both the upstream and downstream measurement locations, using interstage seal mass flow rates calculated from displacement measurements made at the operating conditions. The calculated re-ingestion rates are plotted against the total wheelspace supply rate, including the mass

flow rate of both cooling flow and seeded gas flow. The results presented include two repeated test points conducted during a separate test run. Re-ingestion at a measureable rate was detected during the experimental runs at all measurement locations. The re-ingestion mass flow rate seems to increase with increased wheelspace egress across the tested range; however this is close to the bounds of uncertainty.

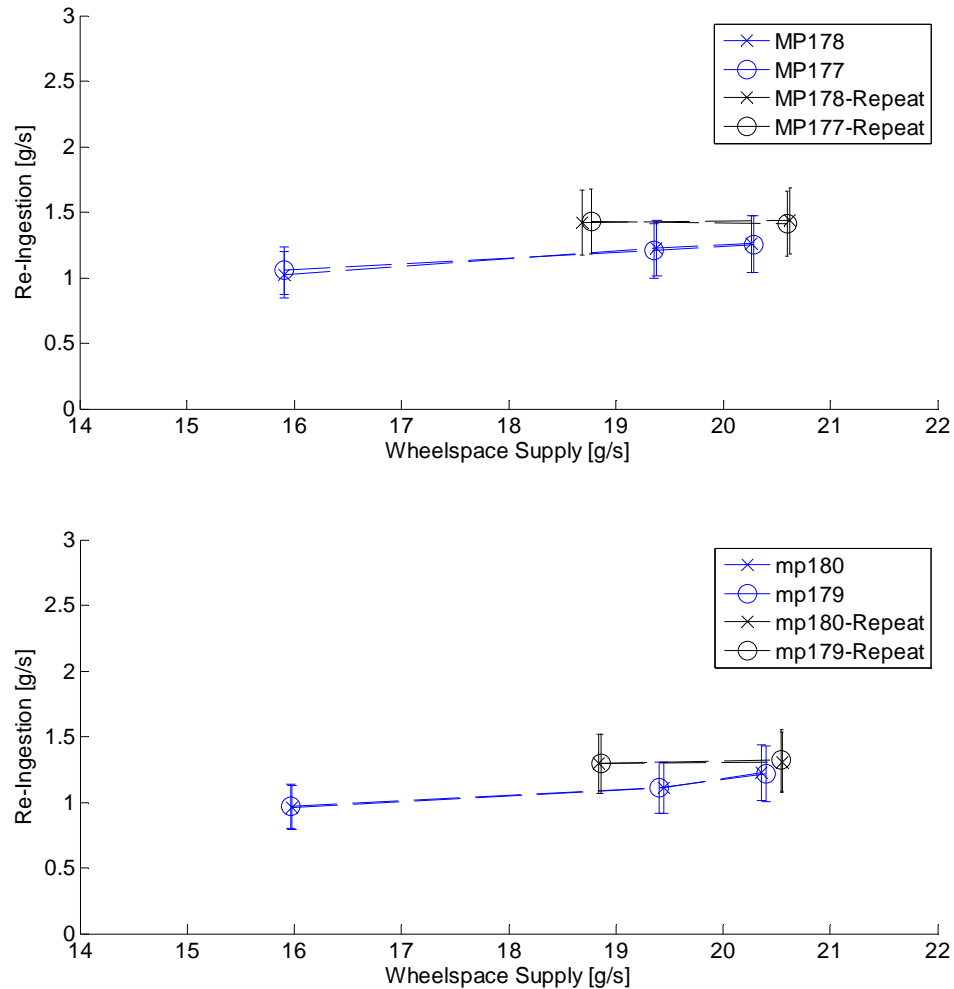


Figure 9-11: Re-ingestion rates \dot{m}_r calculated from concentration measurements made in the upstream and downstream stator wells

Figure 9-12 shows the re-ingestion results for the same runs and measurement locations as the data shown in Figure 9-11. The data has been non-dimensionalised, where the re-ingestion rates and wheelspace supply rates are presented as fractions of the calculated interstage seal flow. As the interstage seal demand can directly influence the ingress of gas into the stator well the re-ingestion rates can be re-evaluated when presented in this

manner, where the gradient of the repeat data appears to more closely match the first series of experimental data points. Again care must be taken due to the uncertainties introduced by the interstage seal flow.

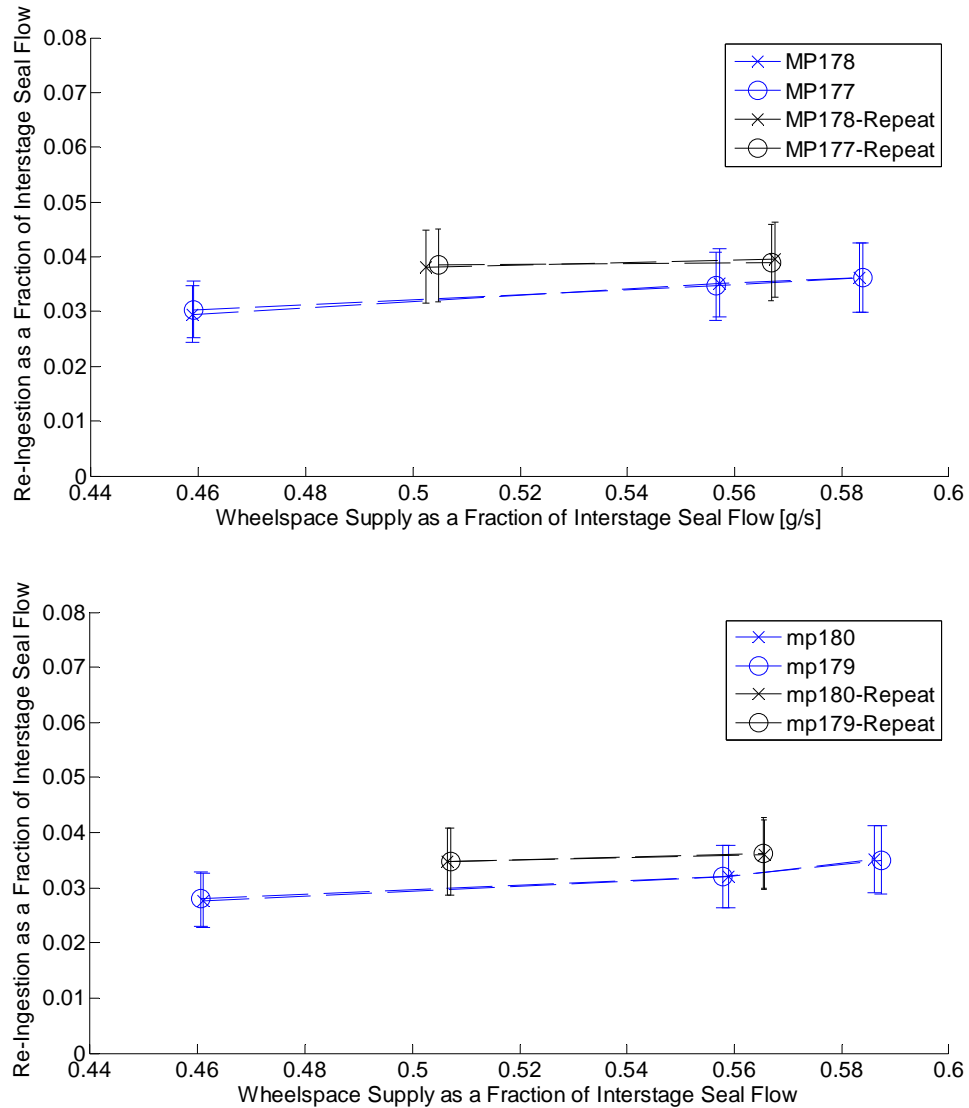


Figure 9-12: Re-ingestion as a fraction of interstage seal flow, \dot{m}_r/\dot{m}_l

Figure 9-13 shows the re-ingestion rates as a fraction of wheelspace supply rate, plotted against wheelspace supply rates as a fraction of interstage seal flow. The previous figures show that the amount of re-ingested air detected in the stator wells seems to increase with increased wheelspace egress. When the re-ingestion rates are presented as

a fraction of the wheelspace egress, the re-ingestion appears to be a constant fraction of the egress within the bounds of measurement uncertainty.

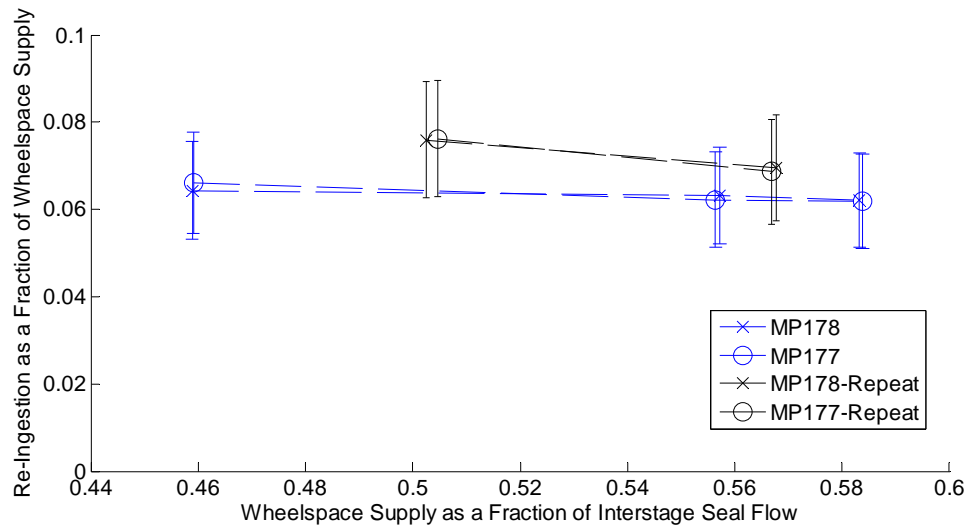


Figure 9-13: Re-ingestion as a fraction of wheelspace supply rate, \dot{m}_r/\dot{m}_w

However if the measurement uncertainty could be reduced, by means of an alternative seal flow measurement, yet the trends observed in Figure 9-13, which appear to show a negative gradient remained unchanged, then the results could be interpreted as suggesting that the proportion of egress which is re-ingested reduces as the rate of wheelspace egress increases. This could be attributed to higher radial momentum of the coolant as it exits the wheelspace rim seal, allowing some to coolant to pass through the main annulus boundary layer into the main flow from where it cannot then be re-ingested.

Figure 9-14 shows a CFD solution displaying streamlines which are seeded at the point of egress from the wheelspace. The wheelspace has not been modelled. The streamlines suggest that the coolant is initially entrained directly onto the blade foot boundary layer. The low momentum of the fluid causes it to be drawn up onto the blade suction surface as the gas approaches the tail of the blade and mixes with secondary flows. The CFD streamlines then suggest that the egressed coolant begins to lift from the foot into the

main annulus. This results in pockets of mixed coolant and main annulus gas, and areas of pure main annulus gas above the rim seal. The gas re-ingested into the stator well is drawn from these two gas mixtures. This would indicate that more coolant could mix out into the main annulus air as the momentum of the coolant through the wheelspace rim seal increases. This would reduce the amount of egressed gas present above the rim seal, therefore the gas drawn into the stator well would contain a lower concentration of coolant. This warrants further investigation.

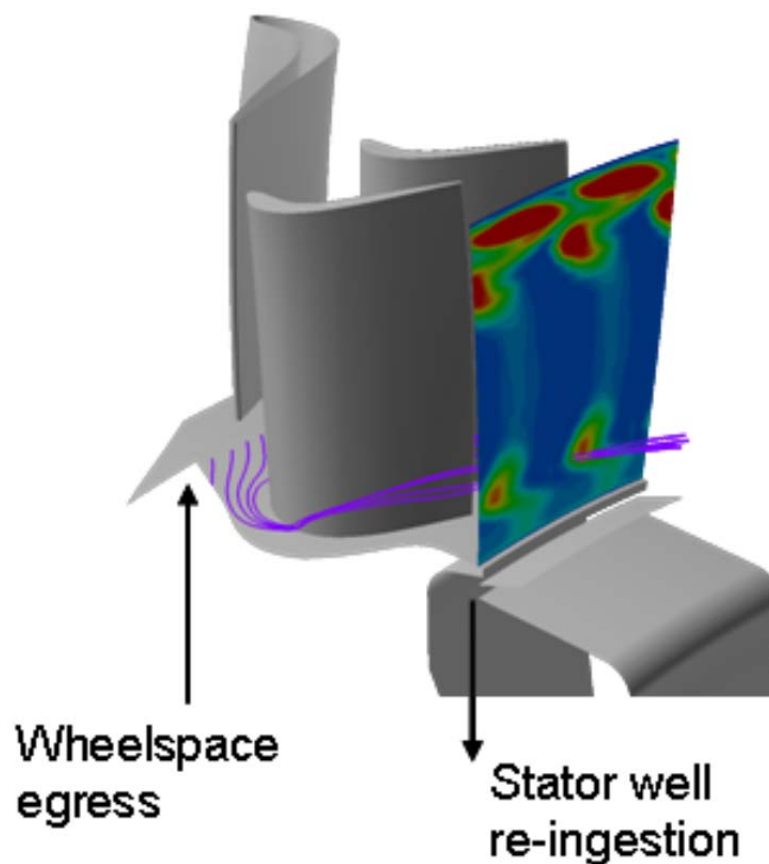


Figure 9-14: Streamlines of wheelspace egress, Eastwood et al (2012)

Guijarro Valencia et al (2012), conducted a review of the numerical analysis methods used by the MAGPI work package 1 partners to try to capture this effect. Each partner conducted CFD studies on a geometry comprising of a 1/39 section of the rig

comprising of the two rotor rows of the rig, the intermediate NGV row and the upstream and downstream cavities.

Table 9-1 shows the range of solutions run by the work package partners. These include a number of steady and unsteady industry standard solvers using a number of turbulence models. Flow rate fractions of between 0.46 and 0.59 of the interstage seal flow were modelled, corresponding to the ranges shown in Figure 9-12 and Figure 9-13. For each of the steady solutions, little or no re-ingestion was indicated, the highest being found with the Turbomeca solution which indicated 0.0417% of the wheelspace egress being re-ingested, compared to the values of around 6.5% seen in the experimental measurements. The low values calculated obtained from CFD analysis were attributed to two solver issues. Firstly we see in Figure 9-15 streamlines of main annulus and seeded egressed coolant. The egressed coolant, shown as turquoise streamlines was seen to pass over the rim seal boundary and fail to mix with the air being ingested into the upstream stator well.

	Rolls-Royce	SIEMENS	University of Florence	Turbomeca
Grid	PADRAM Hexa	ICEM Hexa	ICEM Hexa	ICEM Tetra
Grid Size	11.4 M	26.12M (fluid) 1.92 M (solid)	2.5 M	3.4M
Solver	HYDRA 6.1	CFX 12.0	CFX 12.1	Fluent 6.3
Turb. model	S-A wf k- ω SST	k- ω SST	k- ϵ standard with wf	k- ϵ realized with wf
y+ range	~1	2-3	30-300	30-100
Interface	Steady Mixing plane	Steady Mixing plane	Steady Mixing plane	Steady Mixing plane
	Unsteady Sliding plane		Unsteady Sliding plane	
Heat transfer	Adiabatic	CHT	Adiabatic rotor CHT stator	Adiabatic
Air Egress (Fraction interstage seal flow)	0.59	0.46	0.59	0.46 0.59

Table 9-1: Work package partner CFD solution details, Guijarro Valencia et al (2012)

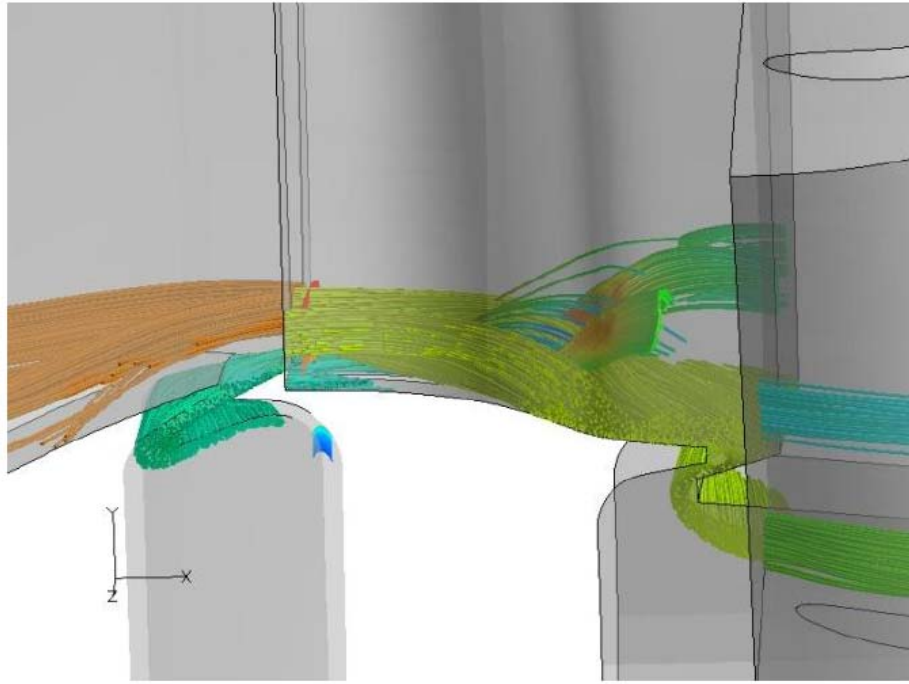


Figure 9-15: Streamlines of seeded coolant, Guijarro Valencia et al (2012)

Secondly, the egressed air was seen to be drawn into the vortices from the trailing edge of the first row of rotor blades and into the main annulus flow. Although this effect most likely accounts for a large percentage of the coolant loss into the main annulus and the low re-ingestion rates measured experimentally, the steady state CFD solvers showed almost total loss through this mechanism. The unsteady solutions run by two of the industrial partners however, detected higher levels of re-ingestion, where levels corresponding to 1-2% of wheelspace egress were found. Although of the same magnitude as the levels found experimentally, the CFD solutions were still significantly lower than 6.5%. Figure 9-16 shows streamlines of re-ingested coolant entering the upstream stator well cavity. The image on the left being for a steady solution where no coolant ingress is detected and the image on the right being for an unsteady solution where ingress is detected. The increase in ingress seen with the unsteady solutions was attributed to better modelling of the asymmetric pressure regions above the rim seal, the mechanism of re-ingestion suggested by the image shown in Figure 9-14.

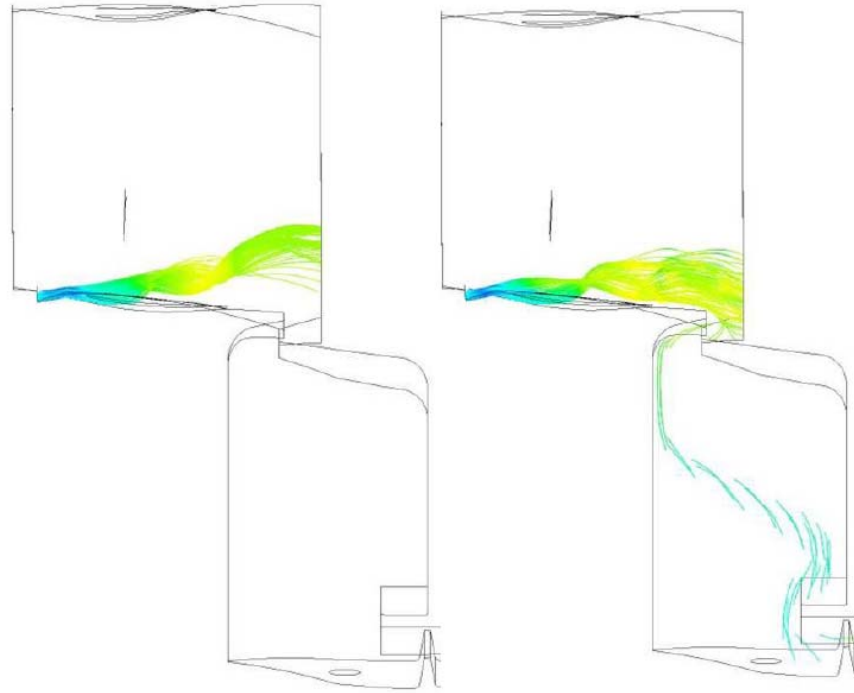


Figure 9-16: Upstream stator well ingress streamlines for steady and unsteady solutions, Guijarro Valencia et al (2012)

9.5 Summary

The results of the three gas concentration experiments have been described and where appropriate compared to experimental and numerical data. The results of the interstage seal experiment were considered unsatisfactory due to variation in the concentration measurements made at the seal exit. In order for the experimental procedure to be valid full mixing of the tracer gas was required with the seal flow.

Dilution ratio measurements from the rim seal exchange experiment were presented and compared to normalised temperature data. The general cavity sealing trends inferred from the dilution results were found to support the findings of the normalised temperature measurements.

The results obtained from displacement and thermo mechanical modelling techniques described in Chapter 7 were used to provide the necessary interstage seal flow rates for the rim seal and re-ingestion experiment. This did however introduce larger uncertainties into the mass flows calculated for rim seal egress and re-ingestion, limiting the conclusions that could be made about these flow rates in terms of trends with varied imposed cooling flows. The rate of re-ingestion of upstream coolant egress measured by the re-ingestion experiment gave levels of re-ingestion significantly higher than those found from CFD studies conducted by industrial partners. Although unsteady models were shown to predict some ingestion, it was suggested by Guijarro Valencia et al (2012) that an LES approach would improve numerical results for re-ingestion by better predicting diffusion of the coolant flow in the main annulus. Use of a 360° unsteady solution may also yield benefits by improving prediction of the tracer gas distribution above the rim seal, however both this technique and an LES approach would be extremely costly in computation time.

10 Conclusions

This body of work describes the contribution of the author to experimental investigations conducted on an aero engine representative, two stage axial turbine test facility at the University of Sussex. The objectives of the research conducted by the author included: investigation of the extent to which gas concentration measurements could be used to describe and quantify interstage labyrinth seal flow, rim seal exchange flows and coolant re-ingestion; provide experimental data for the calibration and development of cavity modelling techniques; provide hot running clearances of test facility internal seals; provide data to quantify interstage seal flows for a range of rig operating conditions and coolant supply geometries; provide data to determine rim seal exchange flows for both bulk ingress and egress conditions for a range of rig operating conditions and coolant supply geometries; and, provide data to quantify the extent to which egressed cooling air is re-ingested into downstream cavities.

10.1 Interstage Seal Flow

The concentration measurements made to determine interstage seal flow rates were found to be unsuitable for the calculation method. Full mixing of the tracer gas with the interstage flow was required in order for this calculation to be successful. However, the concentration measurements made at the seal exit were found to vary circumferentially by $\pm 50\%$ of the mean concentration value.

A secondary method of obtaining interstage seal flow, including the use of displacement measurements and thermo mechanical modelling was implemented. The thermo

mechanical model was found to predict clearance changes to within 2.5% of nominal seal clearance. Calculated interstage seal flows based on measured and modelled seal displacement values were found to be within 2%. An uncertainty of $\pm 5\%$ was applied to seal flow values obtained using this method.

10.2 Rim Seal Exchange Experiment

The rim seal exchange experiment provided concentration data suitable for comparison with normalised temperature measurements and numerical models, for cooling flow rates of $30 \text{ gs}^{-1} \leq \dot{m}_0 \leq 55 \text{ gs}^{-1}$, corresponding to in cavity Reynolds numbers of $1.71 \times 10^6 \leq Re_\phi \leq 1.86 \times 10^6$ and $Re_w = 1.75 \times 10^5$.

The mass flow of ingress \dot{m}_i was shown to reduce from a mean value across all geometries of $\sim 17 \text{ gs}^{-1}$ to $\sim 9 \text{ gs}^{-1}$ as the cooling flow rate was increased, where the uncertainty of each geometry was found to be of the order of $\pm 0.5 \text{ gs}^{-1}$.

Egress rate \dot{m}_e was seen to increase from a mean value across all geometries of $\sim 10 \text{ gs}^{-1}$ to $\sim 18 \text{ gs}^{-1}$ however, due to high uncertainties of $\pm 2.5 \text{ gs}^{-1}$ associated with the calculation of the interstage seal flow, the results for egress rate were inconclusive.

10.3 Re-Ingestion Experiment

The re-ingestion experiment produced results showing re-ingestion rates of $\sim 6.5\%$ of the upstream wheel-space egress. Despite the uncertainty introduced by the use of calculated interstage seal flow to obtain this result, uncertainty in the measurement was

found to be $\pm 1\%$. Numerical solutions obtained by industrial partners failed to recreate this level of re-ingestion by some margin. The highest values of re-ingestion were obtained with unsteady models and were of the order of 1-2%.

The results suggested a trend of reduced percentage re-ingestion with increased wheelspace egress. This was attributed to increased momentum of the coolant and a higher associated loss of coolant to the main annulus. However, this trend was within the bounds of uncertainty for the measurement.

10.4 The Use of Concentration Measurements

The use of concentration measurements to derive rotor cavity sealing effectiveness is a well established technique which is often used in experimental facilities of this type. The dilution ratios presented in this thesis from the rim seal exchange experiment use the same methodology and provide a data set suitable for comparison to numerical modelling techniques.

The adaption of this method to directly measure rim seal exchange flow rates where an interstage seal flow also contributes to the cavity flow regime has been attempted by the author. The method has been shown to produce viable results for cavity ingress. Although egress has been shown and flow rates have been arrived at the, uncertainty in the measurement has made the result inconclusive. The technique however, is valid and with the implementation of the author's recommendations for further work the uncertainty in the measurements could be easily reduced.

10.5 Recommendations for Further Work

Concentration and normalised temperature data for a large range of sealing flow rates and coolant supply geometries has been provided in this thesis. It is recommended that this data be compared to CFD and numerical models to further enhance design methods for predicting turbine disc cooling. Both the lock plate slot and deflector plate geometries show promise in reducing disc temperatures by increasing entrainment of cooling flow to the rotor surface and improving sealing characteristics. The lock plate geometry achieves this by means of injecting the coolant at a higher cavity radius directly into the disc boundary flows, while the deflector plate actively redirects the coolant within the stator well towards the rotor disc. Both of these geometries could be further explored and developed for use in future engine design.

The concentration experiments provided a methodology for direct measurement of net rim seal ingress and egress flows. The deficiency in this technique was shown to be the measurement of the interstage seal flow. This could be improved upon by including features to improve mixing of the tracer gas with the seal flow before the seal entrance, allowing direct measurement of the seal flow to be made. This could be achieved by injecting the tracer at multiple locations or using a diffuser upstream of the seal. However care must be taken not to disturb the flow physics or the inlet boundary conditions at the seal. To achieve this it is important to introduce tracer gas upstream of the seal to allow this to mix with the natural flow demanded by the pressure differential across the seal.

If successful concentration measurement of the seal flow could be achieved it would greatly reduce the complexity of both the rim seal exchange and re-ingestion experiments.

11 References

- [1] Abe, T., Kikuchi, J., and Takeuchi, H., 1979, "An Investigation of Turbine Disk Cooling (Experimental Investigation and Observation of Hot Gas Flow into a Wheel Space)," ASME Paper GT30.
- [2] Bayley, F. J., Owen, J. M., 1970, "The Fluid Dynamics of a Shrouded Disc System with Radial Outflow of Coolant", ASME Paper 70-GT-6
- [3] Bohn, D., Rudzinski, B., Suerken, N., and Gaertner, W., 2000, "Experimental and Numerical Investigation of the Influence of Rotor Blades on Hot Gas Ingestion into the Upstream Cavity of an Axial Turbine Stage", ASME Paper 00-GT-284.
- [4] Chew, J. W., 1998, "The Effect of Hub Radius on the Flow Due to a Rotating Disc" ASME Journal of Turbomachinery., 110, pp. 417–418.
- [5] Childs, P.R.N., 2011, "Note on the Turbine Stator Well Rig Thermocouple Measurement Uncertainty", Internal Communication, University of Sussex.
- [6] Coren, D.D., Atkins, N.R., Turner, J.R., Eastwood, D.E., Davies, S., Childs, P.R.N., Dixon, J., Scanlon, T.S., 2010, "An Advanced Multi-Configuration Stator Well Cooling Test Facility", ASME Paper GT2010-23450.
- [7] Coren, D.D., Eastwood, D.E., Long, C.A., Atkins, N.R., MAGPI, 2010, "D1.8: Phase Two Test Rig Commissioning", EC Framework 6 Program, Project AST5-CT-2006-0.0874, Report-D1.8-ISS01.
- [8] Coren, D.D., "MAGPI Turbine Stator Well Test Rig, Link Call, December 2010", Communication between University of Sussex and Rolls Royce plc.
- [9] Coren, D.D., Atkins, N.R., Long, C.A., Eastwood, D., Childs, P.R.N., Guijarro-Valencia, A., Dixon, J.A., 2011, "The Influence of Turbine Stator Well Coolant Flow Rate and Passage Configuration on Cooling Effectiveness", ASME Paper GT2011-46448
- [10] Dadkhah, S., Turner, A. B., and Chew, J. W., 1992, "Performance of Radial Clearance Rim Seals in Upstream and Downstream Rotor Stator Wheelspaces," ASME Journal of Turbomachinery, 114(2), pp. 439-445.

- [11] Daily, J. W., and Nece, R. E., 1960, "Chamber Dimension Effects on Induced Flow and Frictional Resistance of Enclosed Rotating Discs," *Journal of Basic Eng.*, 82, pp. 217–232.
- [12] Daily, J. W., Ernst W. D., Asbedian V. V., 1964 "Enclosed Rotating Disks with Superposed Throughflow", Report no. 64, M.I.T., Department of Civil Engineering.
- [13] Dorfman, L. A., 1963, *Hydrodynamic Resistance and Heat Loss of Rotating Solids*, Oliver and Boyd, Edinburgh.
- [14] Dixon, J. A., Guijarro Valencia, A., Coren, D. D., Eastwood, D., Long, C. A., 2012 "Main Annulus Gas Path Interactions - Turbine Stator Well Heat Transfer", ASME Paper GT2012-68588
- [15] Dunn, D.M., Zhou, D.W., Saha, K., Squires, K.D., Roy, R.P., Kim, Y.W., Moon, H.K., 2010, "Flow Field in a Single-Stage Model Air Turbine Rotor-Stator Cavity with Pre-Swirled Purge Flow", ASME Paper GT2010-22869.
- [16] Eastwood, D., Coren, D.D., Long, C.A., Atkins., N.R., Childs, P.R.N., Scanlon, T.J., Guijarro Valencia, A., 2012, "Experimental Investigation of Turbine Stator Well Rim Seal, Re-Ingestion and Interstage Seal Flows Using Gas Concentration Techniques and Displacement Measurements", *Journal of Engineering for Gas Turbines and Power*, Vol 134 / 082501-1 - 082501-9.
- [17] Egli, A., 1935, "The Leakage of Steam Through Labyrinth Seals", *ASME Transactions*, Volume 57, p. 115-122.
- [18] Ertas, B.H., 2005, "Rotordynamic Force Coefficients of Pocket Damper Seals", Ph.D. dissertation, Mechanical Engineering Department, Texas A&M University, College Station, TX.
- [19] Gamal, A.M., Ertas, B.H., Vance, J.M., 2006, "High-Pressure Pocket Damper Seals: Leakage Rates and Cavity Pressures", AMSE Paper GT2006-90858.
- [20] Gamal, M.A., Vance, J.M., 2007, "Labyrinth Seal Leakage Tests: Tooth Profile, Tooth Thickness, and Eccentricity Effects", ASME Paper GT2007-27223.
- [21] Gentilhomme, O., Hills, N. J., Turner, A. B., and Chew, J.W., 2003, "Measurement and Analysis of Ingestion Through a Turbine Rim Seal," *ASME Journal of Turbomachinery*, 125(3), pp. 505-512.

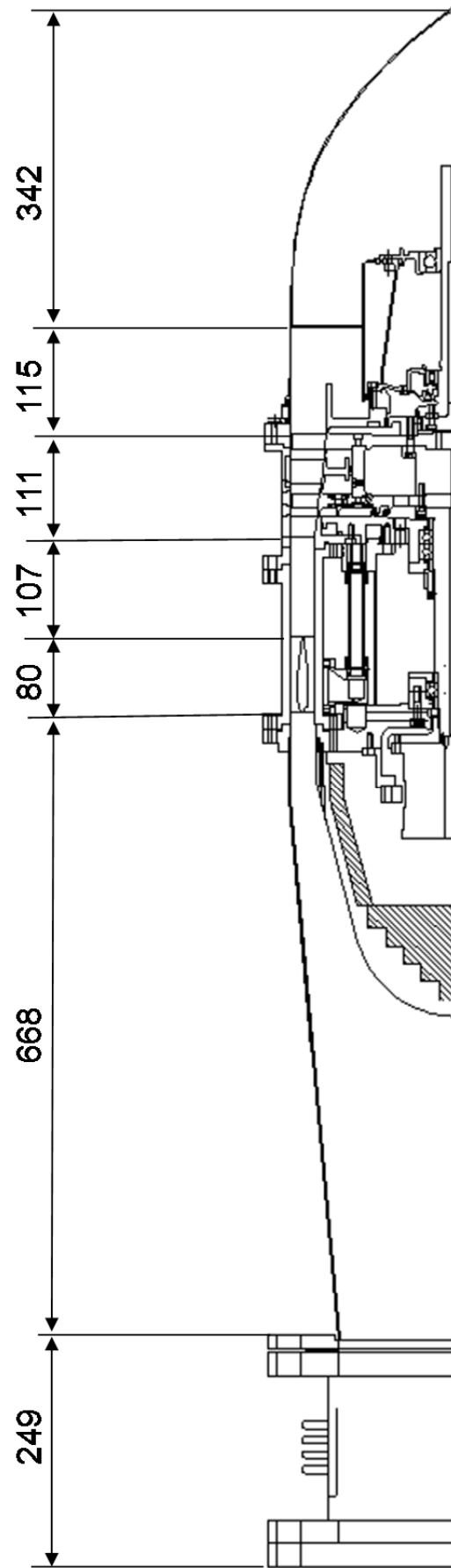
- [22] Georgakis, C., Whitney, C., Woolatt, G., Stefanis, V., and Childs, P., 2007, "Turbine Stator Well Studies: Effect of Upstream Egress Ingestion," ASME Paper GT2007-27406.
- [23] Graber, D. J., Daniels, W. A and Johnson, B V., 1987, "Disk Pumping Test, Final Report"; Air Force Wright Aeronautical Laboratories, Report No. AFWAL-TR-87-2050.
- [24] Green, T., and Turner, A. B., 1994, "Ingestion Into the Upstream Wheelspace of an Axial Turbine Stage," ASME Journal of Turbomachinery, 116(2), pp. 327-332.
- [25] GuijarroValencia, A., Dixon, J.A., Soghe, R.DA., Facchini, B., Smith, P.E.J., Munez, J., Eastwood, D., Long, C.A., Coren, D.D., Atkins, N.R., 2012 "An Investigation into Numerical Analysis Alternatives for Predicting Re-Ingestion in Turbine Disc Rim Cavities", ASME Paper GT2012-68592
- [26] Johnson, B.V., Jakoby, R., Bohn, D.E., Cunat, D., 2006, "A Method for Estimating the Influence of Time-Dependent Vane and Blade Pressure Fields on Turbine Rim Seal Ingestion" ASME Paper GT2006-90853.
- [27] Johnson, B.V., Cheng-Zhang Wang and Roy, P.R., 2008, "A Rim Seal Orifice Model with Two Cds and Effect of Swirl in Seals" ASME Paper GT2008-50650.
- [28] Karman, T., von., 1921, "Uber Laminare and Turbulente Reibung", z. angew. Math. Mech. vol 1.
- [29] Kim, T.S., Cha, K.S., 2009, "Comparative Analysis of the Influence of Labyrinth Seal Configuration on Leakage Behaviour", Journal of Mechanical Science and Technology 23 (2009) 2830-2838.
- [30] Mirzamoghadam, A.V., Heitland, G., Morris, M.C., Smoke, J., Malak, M., Howe, J., "3D CFD Ingestion Evaluation of a High Pressure Turbine Rim Seal Disk Cavity", ASME Paper GT2008-50531
- [31] Owen, J. M. and Rogers, R. H., 1989, "Flow and Heat Transfer in Rotating Disc Systems, Volume 1 - Rotor-Stator Systems"; Research Studies Press, UK; John Wiley, N.Y.
- [32] Owen, J.M., 2009a, " Prediction of Ingestion Through Turbine Rim Seals Part 1: Rotationally-Induced Ingress", ASME Paper GT2009-59121

- [33] Owen, J.M., 2009b, " Prediction of Ingestion Through Turbine Rim Seals Part 2: Externally-Induced and Combined Ingress", ASME Paper GT2009-59121
- [34] Owen, J.M., Zhou, K., Pountney, O., Wilson, M. and Lock, G.D., 2010, "Prediction of Ingress through Turbine Rim Seals. Part 1: Externally-Induced Ingress"; ASME Paper GT2010-23346.
- [35] Phadke, U.P., and Owen, J.M., 1980, "An Investigation of Ingress for a Simple Shrouded Rotating Disk System with a Radial Outflow of Coolant", ASME Paper 80-GT-49
- [36] Phadke, U.P., and Owen, J.M., 1983, "An Investigation of Ingress for an 'Air Cooled' Shrouded Rotating Disk System with Radial Clearance Seals"; ASME Journal Eng Gas Turbines & Power, 105, pp 178-183.
- [37] Phadke, U.P., and Owen, J.M., 1988a, "Aerodynamic Aspects of the Sealing of Gas-Turbine Rotor-Stator Systems Part 1: The Behavior of Simple Shrouded Rotating-Disk Systems in a Quiescent Environment," Int. J. Heat Fluid Flow, 9(2), pp. 98-105.
- [38] Phadke, U.P., and Owen, J.M., 1988b, "Aerodynamic Aspects of the Sealing of Gas-Turbine Rotor-Stator Systems : Part 2: The Performance of Simple Seals in a Quasi-Axisymmetric External Flow," Int. J. Heat Fluid Flow, 9(2), pp.106-112.
- [39] Phadke, U.P., and Owen, J.M., 1988c, "Aerodynamic Aspects of the Sealing of Gas-Turbine Rotor-Stator Systems : Part 3: The Effect of Nonaxisymmetric External Flow on Seal Performance," Int. J. Heat Fluid Flow, 9(2), pp. 113-117.
- [40] Rabs, M., Benra, F.-K., Dohmen, H.J., Schneider, O., 2009, "Investigation of Flow Instabilities Near the Rim Cavity of a 1.5 Stage Gas Turbine", ASME Paper GT2009-59965.
- [41] Rolls-Royce plc 2005, "The Jet Engine", 5th edition, ISBN 0 902121235
- [42] Roy, R.P., Zhou, D.W., Ganesan, S., Wang, C.Z., and Paolillo, R.E., 2007, "The low Field and Main Gas Ingestion in a Rotor-Stator Cavity", ASME Paper GT2007-27671.
- [43] Sangan, C.M., Pountney, O.J., Zhou, K., Wilson, M., Owen, J.M., Lock, G., 2011a, "Experimental Measurements of Ingestion Through Turbine Rim Seals. Part 1: Externally-Induced Ingress", ASME Paper GT2011-45310.

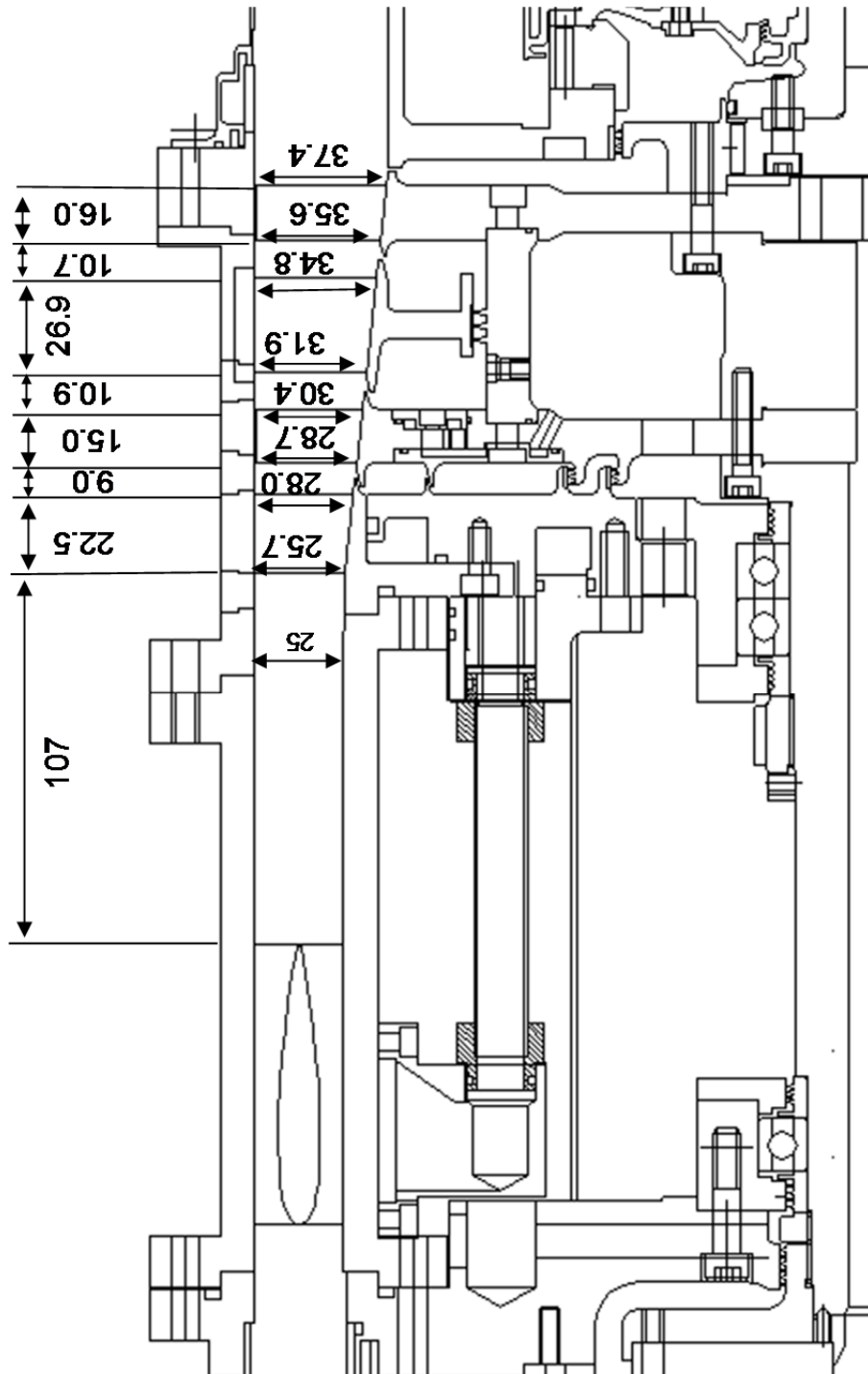
- [44] Sangan, C.M., Pountney, O.J., Zhou, K., Wilson, M., Owen, J.M., Lock, G., 2011b, "Experimental Measurements of Ingestion Through Turbine Rim Seals. Part 2: Rotationally-Induced Ingress", ASME Paper GT2011-45313.
- [45] Schlichting, H., 1979, "Boundary-Layer Theory" , ISBN 9780070553347
- [46] Shultz, R.R., 1996, "Analytical and Experimental Investigation of a Labyrinth Seal test Rig and Damper Seals for Turbomachinery", M.S. thesis, Mechanical Engineering Department, Texas A&M University, College Station, TX.
- [47] Smith, E. J., Mugglestone, J., Tham, K. M., Coren, D. D., Eastwood, E., Long, C. A., 2012, "Conjugate Heat Transfer CFD Analysis in Turbine Disc Cavities", ASME Paper GT2012-69597.
- [48] Stefanis, V., 2007, "Investigation of Flow and Heat Transfer in Stator Well Cavities of a Two-Stage Axial Turbine", D.Phil thesis, Thermo-Fluid Mechanics Research Centre, Department of Engineering and Design, University of Sussex.
- [49] St Venant, B., 1871, "Theorie du mouvement non-permanent des eaux avec application aux crues des rivières et à l'introduction des marées dans leur lit. Comptes rendus Acad Sci Paris", 73:148-154, 237-240
- [50] Touloukian, .Y.S, Kirby, .R.K., Taylor, R.E., Desai, P.D., 1975, "Thermophysical Properties of Matter, Volume 12, "Thermal Expansion - Metallic Elements & Alloys", ISBN 0-306-67032-1.
- [51] Turner, A. B., Davies, S. J., Childs, P. R. N., Harvey, C. G., Millward, J. A., 2000, "Development of a Novel Gas Turbine Driven Centrifugal Compressor", Proc. Instn. Mech. Enngs. Vol. 214, Part A, pp. 423-437.
- [52] Turner, J.R., Eastwood, D.E., Coren, D.D., Atkins, N.R., MAGPI, 2008, "D1.5: Turbine Rig Set-up and Commissioning", EC Framework 6 Program, Project AST5-CT-2006-0.0874, Report-D1.5-ISS01.
- [53] Waschka, W., Wittig, S., Kim, S., 1992, "Influence of High Rotational Speeds on the Heat Transfer and Discharge Coefficients in Labyrinth Seals", ASME Journal of Turbomachinery, Vol 114, pp. 462-468.
- [54] Wittig, S., Schelling, U., Kim, S., Jacobsen, K., 1987, "Numerical Predictions and Measurements of Discharge Coefficients in Labyrinth Seals", ASME paper 87-GT-188

- [55] Woollatt, G., 2001, "Aerodynamic design of the 2 stage ICASGT2 turbine", Technical Report B21000/1, Alstom Power Technology Centre
- [56] Zhou, D.W., Roy, R.P., Wang, C.Z., Glahn, J.A., 2009, "Main Gas Ingestion in a Turbine Stage for Three Rim Cavity Configurations", ASME Paper GT2009-59851.
- [57] Zhou, K., Wood, S., Owen, J.M., 2011a, "Statistical and Theoretical Models of Ingestion Through Turbine Rim Seals", ASME Paper GT2011-45139.
- [58] Zhou, K., Wilson, M., Lock, G., Owen, J.M., 2011b, "Computation of Ingestion Through Gas Turbine Rim Seals", ASME Paper GT2011-45314.
- [59] Zimmerman, H., Wolff, K.H., 1998, "Air System Correlations Part 1: Labyrinth Seals", ASME Paper 98-GT-206

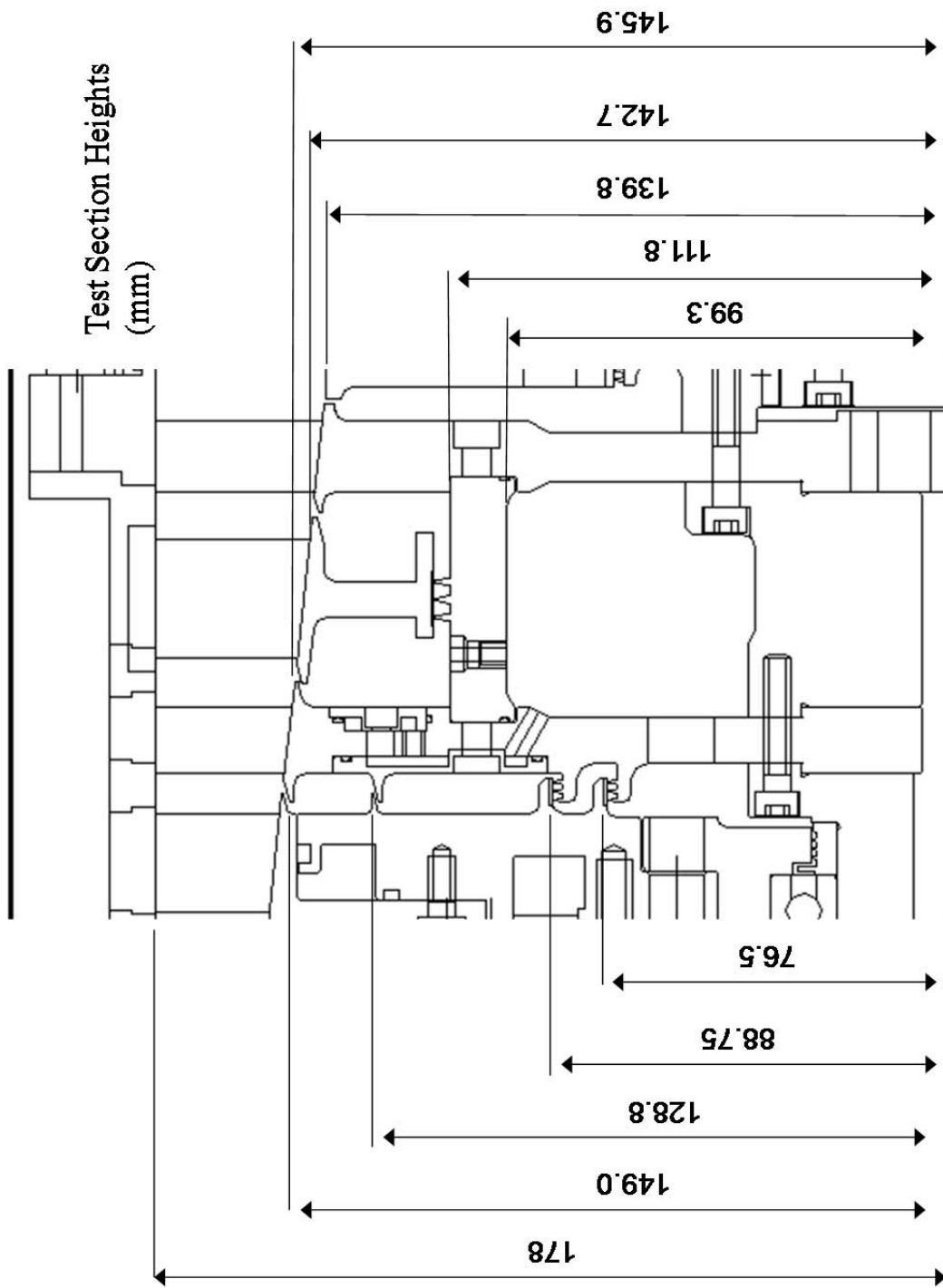
Appendix A



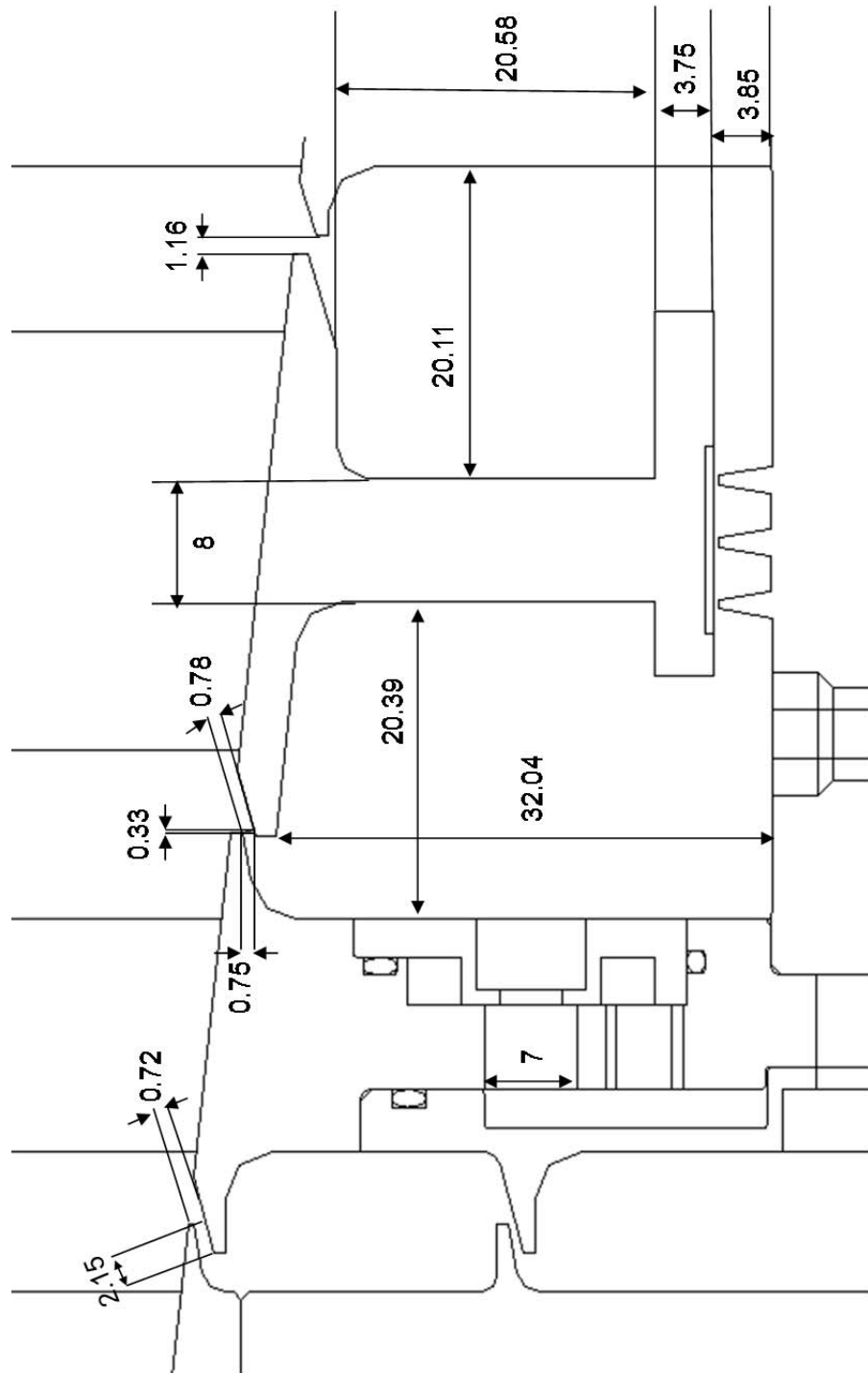
Major Rig Dimensions
(mm)



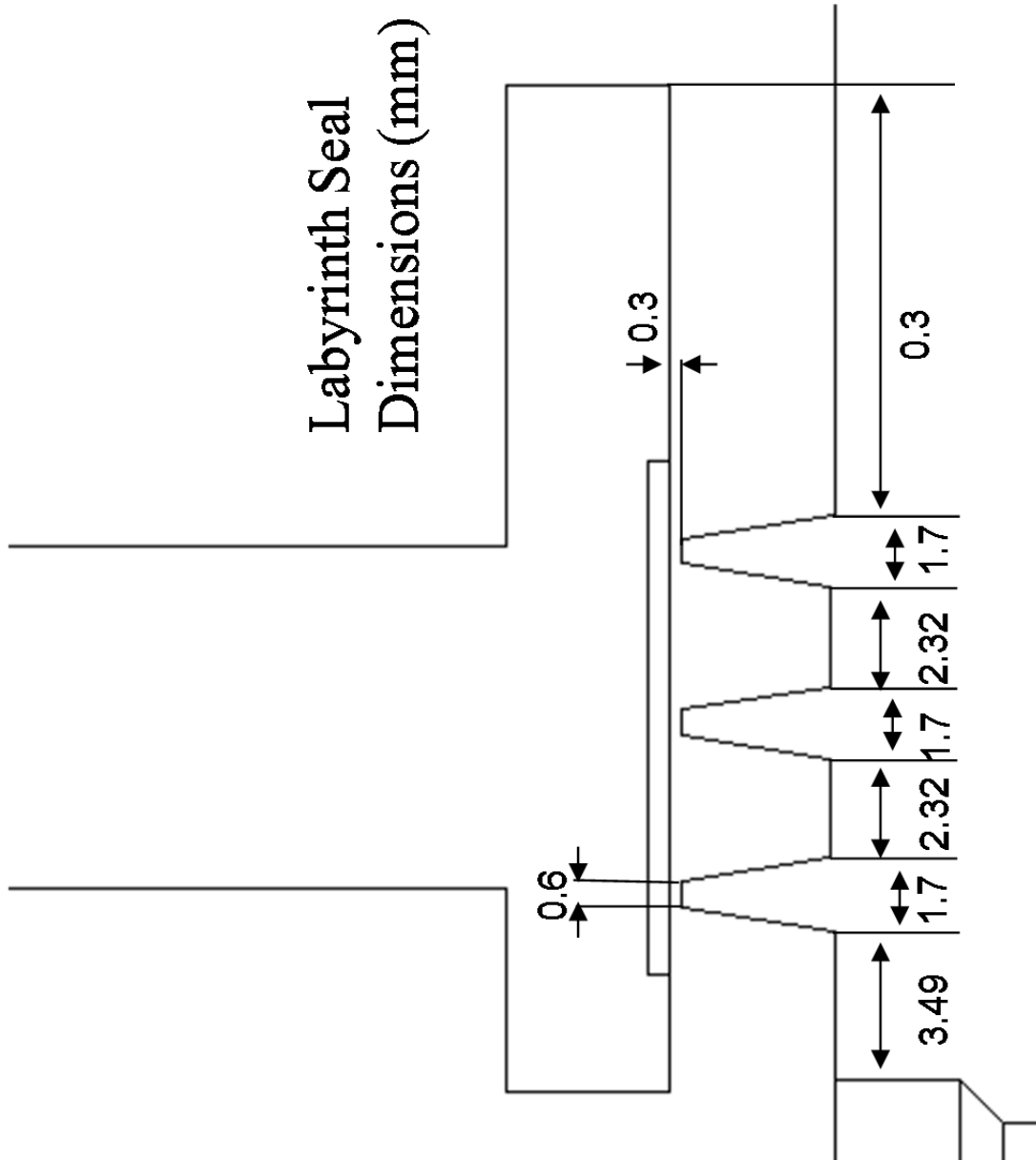
Test Section Dimensions
(mm)



Stator Well & Rim Seal
Dimensions (mm)



Labyrinth Seal Dimensions (mm)



Appendix B

TSW Test Rig Start-up Procedure

Test Number:

Date:

This guide is intended to describe the operations required to prepare the TSW test rig for operation where the main annulus air is supplied by the Dart compressor. The start up procedure for the Dart may be found elsewhere.

Preliminaries

Power up measurement systems and visual checks in Test Cells 3 and 4.

- Record atmospheric pressure using Laboratory barometer
- Test Cell 3 Data logging equipment switched on – visual check for any loose leads
- Test Cell 3 Air conditioning unit switched on and set to 20°C
- Test Cell 4 extractor fan switched on to position 3
- Test Cell 4 console switched on
- Turn rig by hand

Hydravane Compressor

This compressor is located in the compressor room and provides the air required to drive the Test Cell 4 Dynamometer oil spray system, Test Cell 4 Main Cooling air valve and the Dart bypass valve located in Test Cell 3.

- Check that ¼ turn valve in far corner of Test Cell 1 is closed (TC1HV14)
- Check that air supply valves in test Cell 3 and 4 are closed (TC3HV9-10)(TC4HV2-5)
- Check that Rotameters outside Test Cell 4 are closed
- Check Potentiometer on the Test Cell 4 control panel is set fully anticlockwise for fully closed
- Check / empty oil and water separators at exit of reservoir tank
- Check Hydravane outlet pipe valve is closed (CRV17)
- Switch Isolator on
- Switch Hydravane on using green button
- Wait a few seconds for compressor note to change then fully open valve (CRV17)
- Bleed of excess water from Yellow reservoir tank by cracking valve open and allowing water to escape through window via flexible tube – which must be held tightly.

- Open air valve in Test Cell 4 (TC4HV2)
- Open Telemetry Cooling Rotameter to an indicated 200 L/min
- Open airline drain valve in Test Cell 4 (TC4HV5)
- Partially open airline valve, when excess water has drained, close drain valve (TC4HV4)
- Fully open air valve and set regulator to 4 bar (TC4HV6)
- Check Dynamometer oil mist system is at 1 bar, use regulator if adjustment required
- Check Dart line blow off valve in Test Cell 2 is closed.

Atlas Copco Compressor

This compressor provides the cooling air to the TSW Test Rig.

- Open water valve for inlet air cooler
- Check that any Atlas pipeline valves in test Cell 1, 2, 3 and 5 are closed (TC1A7-10) (TC2A5-6) (TC3A4,9) (TC5A1-2)
- Fully open water valve in Cell 3 for cooling air heat exchanger
- Check that Atlas line Butterfly valve in Test Cell 4 is closed (TC4A3)
- Check that TSW main annulus inlet and exhaust valves are fully open DL8(TC4) DL6(O)
- Plug in remote Atlas bypass controller and set fully anticlockwise for fully open
- Check that Atlas Air Dryer valves in Compressor room are closed (CRV5-6,10-11)
- Switch dryer on using green switch
- Open compressor room doors
- Check Atlas hot (insulated) outlet is closed (CRV1) and cool outlet is open (CRV2)
- Check Atlas line valves so air diverted to dryer. (CRV3,12,18 = closed) (CRV7,8,9 = open)
- Set compressor room extractor fan to 5, press on and then reset buttons to switch on
- Switch Atlas Isolator on
- Switch Atlas on using green button on control panel, Atlas will start up and air exits via bypass
- In test cell 5, switch on small extract fan adjacent to window
- Open dryer inlet slowly – leave to stabilize for 5 minutes (go to Dynamometer section)
- Open dryer outlet slowly, then close CRV7.
- Open dryer drain valve at rear of unit – *repeat this every 20 minutes while running*
- Use potentiometer on control panel to open cooling air supply valve – approximately 7 turns to initiate opening
- Open wheelspace balance supply Rotameter to an indicated 300 L/min
- Open cooling air Rotameter to an indicated 1000 L/min (open quickly to avoid fluctuation)
- Fully open potentiometer to open main cooling air valve
- Check that Atlas output is approximately 3.2 bar when rig is running

Dynamometer

Oil lubrication and power absorbing water flow systems.

- Switch load control isolator on
- Check load and unload buttons on control panel are functioning
- Set load to mid position – leadscrew protrudes approximately 80 mm
- Switch dynamometer oil tank valve open (check that oil is dripping)
- Switch vapour extractor on
- Open dynamometer oil system water cooler valve, 1/8th turn (valve in Test Cell 3)
- Turn large red dynamometer water flow valve fully closed, then turn ¾ turns open
- Turn bypass valve fully closed, then 6 turns out
- Open valve in pipe connecting dynamometer exit to roof mounted chiller
- Open valve at base of large black reservoir tank
- Open mains water supply valve
- Turn water pump on
- Turn chiller fans on (check that fans are turning – view from windows upstairs)
- Turn catch tank drain pump on
- Check for approximately 10 to psi on the dynamometer gauges – once dynamometer is above 5000 rpm (inlet pressure will be higher while dynamometer is not rotating)

Gearbox Lubrication

Oil supplies for Turbine stage and gearbox.

- Gearbox oil tank valve open
- Switch oil pump on – check that gauge reads approximately 50 psi

Special Note for Post-Test Dynamometer Water Cooler Drain-Down

In order to avoid freezing, the water remaining in the roof mounted water cooler must be drained at the end of each test. This requires gravity draining of the water followed by air purging, which requires the pressure provided by the Hydravane compressor.

- Dynamometer water pump off
- Black water tank mains water supply valve closed
- Black water tank exit valve closed
- Dynamometer water return valve closed
- Roof cooler drains open (outside and in Test Cell 4)
- Switch off Dynamometer catch tank pumps
- Wait for water to finish draining
- Ensure pressure in air line (check gauge)
- Open valve to pressurise flying lead
- Use flying lead to connect air line to water pipework to purge water from cooler

Appendix C

D. Eastwood¹

e-mail: de23@sussex.ac.uk

D. D. Coren

C. A. Long

N. R. Atkins²

Thermo-Fluid Mechanics Research Centre,
University of Sussex,
Brighton, BN1 9QT, UK

P. R. N. Childs

Department of Mechanical Engineering,
Imperial College London,
South Kensington,
London, SW7 2AZ, UK

T. J. Scanlon

Fluid Systems Group,
Rolls-Royce plc,
Derby, UK

A. Guijarro-Valencia

Thermal Systems,
Rolls-Royce plc,
Derby, UK

Experimental Investigation of Turbine Stator Well Rim Seal, Re-Ingestion and Interstage Seal Flows Using Gas Concentration Techniques and Displacement Measurements

Gas turbine engine performance requires effective and reliable internal cooling over the duty cycle of the engine. Life predictions for rotating components subject to the main gas path temperatures are vital. This demands increased precision in the specification of the internal air system flows which provide turbine stator well cooling and sealing. This in turn requires detailed knowledge of the flow rates through rim seals and interstage labyrinth seals. Knowledge of seal movement and clearances at operating temperatures is of great importance when prescribing these flows. A test facility has been developed at the University of Sussex, incorporating a two stage turbine rated at 400 kW with an individual stage pressure ratio of 1.7:1. The mechanical design of the test facility allows internal cooling geometry to be rapidly reconfigured, while cooling flow rates of between $0.71 C_{W, ENT}$ and $1.46 C_{W, ENT}$, may be set to allow ingress or egress dominated cavity flows. The main annulus and cavity conditions correspond to in cavity rotational Reynolds numbers of $1.71 \times 10^6 < Re_\phi < 1.93 \times 10^6$. Displacement sensors have been used to establish hot running seal clearances over a range of stator well flow conditions, allowing realistic flow rates to be calculated. Additionally, gas seeding techniques have been developed, where stator well and main annulus flow interactions are evaluated by measuring changes in gas concentration. Experiments have been performed which allow rim seal and re-ingestion flows to be quantified. It will be shown that this work develops the measurement of stator well cooling flows and provides data suitable for the validation of improved thermo-mechanical and CFD codes, beneficial to the engine design process. [DOI: 10.1115/1.4005967]

1 Introduction

The prevention of hot main stream gas ingress through turbine rim seals is of great interest to gas turbine manufacturers. Hot gas ingestion through rim seals into disk cavities can lead to the overheating of disks, reducing component life. It is commonly necessary to provide cool sealing air to the disk cavities to prevent or limit this ingestion of hot main annulus gas. The necessary coolant flow rate is governed by flows prevalent to stator wells and the exchange of the stator well flows with the main annulus flows at the rim seal. The cooling air is supplied from various compressor bleed locations. Since this directly affects the cycle performance it is important that the sealing air required to prevent ingestion is minimized. This paper discusses the use of gas concentration (GC) measurement techniques together with direct seal clearance measurements. The work is part of continuing investigations using the multiconfiguration Turbine Stator Well (TSW) test facility at the Thermo-Fluid Mechanics Research Centre (TFMRC) at the University of Sussex. It is part of the EU FP6 MAGPI (Main Annulus Gas Path Interactions) program, which has the purpose of improving the understanding of interactions between cooling

and main stream flows. The TSW facility at the University of Sussex was developed to study the interaction of stator well cooling and main annulus air. A detailed overview of the test facility is described by Coren et al. [1]. The rig can be run at engine representative conditions with a number of stator well geometries, allowing coolant delivery path and flow rate to be investigated. In addition to the gas concentration instrumentation discussed within this paper, the rig includes a high density of temperature and pressure instrumentation. The results from two distinct GC experiments are discussed. The first set of experiments looks at gas path interaction in the vicinity of the rim-seals by quantifying the net ingestion of main annulus flow into the upstream stator well cavity. This was carried out across a range of cooling flows and delivery geometry. The second was conducted to obtain measurements to confirm the presence of cool upstream wheel-space flows being re-ingested into stator well cavities downstream. In support of these tests displacement sensors have been installed which allows a FEA model to be validated, which enables the calculation of hot geometry.

2 Review of Flows

The stator well flow field comprises disk entrainment, rotor stator core flow, coolant, rim seal exchange and interstage seal flow. In a rotor stator configuration where $s/b > 0.1$ the rotor and stator can be assumed to have separate boundary layers with a 2D core which rotates. Daily and Nece [2] showed that the swirl ratio, β , is in the region of 0.4 relative to the rotor. Chew [3] provides a

¹Corresponding author.

²Present address: Now at the Whittle Laboratory. University of Cambridge, 1 J. J. Thomson Avenue, Cambridge, CB3 0DY, UK.

Contributed by the Industrial and Cogeneration Committee of ASME for publication in the JOURNAL OF ENGINEERING FOR GAS TURBINES AND POWER. Manuscript received June 26, 2011; final manuscript received October 8, 2011; published online June 21, 2012. Editor: Dilip R. Ballal.

relationship (Eq. (3)) which allows the flow entrained by a partial disk $C_{W,ENT}$ to be related to the free disk entrainment $C_{W,O}$ (Eq. (2)) as demonstrated by Dorfman [4]. This is useful for the TWS rig arrangement where the drive arm can be considered a disk hub.

The introduction of coolant into a stator well has a significant influence on the flow structure. In the Sussex TSW rig coolant may be introduced through either drive arm holes or bled through simulated lock plate slots. For the purpose of this paper cooling flows are given as a fraction of the disk entrainment $C_{W,ENT}$. Rotational Reynolds number is defined in Eq. (1). The density is calculated from the temperature and static pressure taken at a radius $r = 0.905b$, corresponding to the mid height of the upstream rotor stator cavity.

$$Re_\phi = \frac{\rho \omega b^2}{\mu} \quad (1)$$

$$C_{W,O} = 0.219 Re_\phi^{0.8} \quad (2)$$

$$C_{W,ENT} = C_{W,O} \left[1 - \left[\frac{a}{b} \right]^5 \right] \quad (3)$$

where: $C_{W,ENT}$ = flow entrained by a disk with inner hub, $C_{W,O}$ = flow entrained by a free disk, a and b are the inner and outer disk radii.

The flow of coolant, in particular the drive arm holes, due to their low radius entry into the stator, can affect the interstage seal inlet pressure and velocity. For cases where the supplied cooling flow is less than the disk entrainment value, the stator flows are in general dominated by entrainment flows and the interstage seal flow. As the coolant flow rate increases and becomes greater than the entrainment rate the stator flows become increasingly dominated by the resulting changes in core flow. Owen and Phadke [5] developed a correlation relating sealing coolant supply rates to main annulus conditions for a variety of rim seal geometries. Interstage seals are used to reduce the flow of air from upstream to downstream stator wells. The seal flow is largely influenced by clearance value and the pressure drop across the seal which is a function of the upstream and downstream conditions including the pressure drop over the stage in the main annulus. The seal flow is calculated using the St. Venant-Wantzell equation for the ideal flow together with a single discharge coefficient, C_D , which accounts for all of the dependent parameters.

$$\dot{m} = C_D \frac{P_1 A}{\sqrt{T_0}} \left(\frac{P_2}{P_1} \right)^{\frac{1}{\gamma}} \sqrt{\frac{2\gamma}{R(\gamma-1)} \left[1 - \left(\frac{P_2}{P_1} \right)^{\frac{\gamma-1}{\gamma}} \right]} \quad (4)$$

Zimmerman and Wolff [6], Gamal and Vance [7] and Wittig et al. [8] provided seal discharge coefficients for a number of seal clearances, geometries and pressure ratios. Rim seal flows are influenced by both the pressure drop across a stage as well as the seal geometry and pressure drop across the interstage seal. Circumferential pressure asymmetries in the main annulus which result from the flows associated with the blade rows can also have a large influence on rim seal flows. This effect was shown by Gentilhomme et al. [9]. The effect of the re-ingestion of cooling air from upstream cavities was investigated by Georgakis et al. [10]. It was shown that re-ingestion of upstream egress provided significant contribution to stator well cooling, which was quantified as improving thermal effectiveness on the downstream cavity walls.

3 Previous Gas Concentration Studies

Phadke and Owen [11] conducted studies of a rotor-stator system with seven distinct rim seal geometries, including axial, radial and mitred seals. The seals were tested over a range of clearance ratios and rotational Reynolds numbers. Tracer gas, nitrous oxide, could be supplied to the rig through either the cooling flow, or to

the external air outside the rim seal. In order to measure the minimum amount of cooling air required to seal the rotor-stator wheel-space, the cooling air was supplied with a known concentration of nitrous oxide. The rotational speed of the rig was then increased while keeping the coolant flow constant, until the concentration was seen to drop. This was considered to be due to the ingress of air into the wheel-space, and indicated the point at which the supplied cooling air was insufficient to seal the wheel-space. Dackhah et al. [12] conducted gas concentration experiments on two engine representative seals, one where the wheel-space is upstream of a rotor and a second where the wheel-space is downstream of a rotor. Gas concentration measurements were made via a traverse within the wheel-space at four radial locations, $r = 0.163b$, $0.411b$, $0.658b$, $0.905b$, using nitrous oxide as a tracer gas seeded into the cooling air. The concentration measurements were used to determine the amount of main annulus gas ingested as well as the distribution of the ingested gas in the wheel-space. The study showed that where ingestion was present, the ingested gas entering the wheel-space was entrained onto the stator, where it then proceeded downwards. The ingested gas then moved across the core of the wheel-space into the rotor boundary layer. The study also showed that the highest dilution levels occurred at the higher radius of the wheel-space. Ingress mass flows were estimated by integration of the mean gas concentration levels. As part of an investigation into ingestion through rim seals, Gentilhomme et al. [9] seeded cooling air with nitrous oxide and carbon dioxide and then made concentration measurements within the stator well. The results were compared to unsteady CFD solutions and a basic ingestion model. It was also shown through gas concentration results that the ratio of seal to annulus flow velocity was useful when correlating ingestion rates. Green and Turner [13] used gas concentration techniques to investigate ingestion into the upstream wheel-space of an axial turbine. Using nitrous oxide as a tracer, gas concentration measurements were used together with pressure measurements to determine the level and distribution of ingestion. It was found that ingestion was present, even at sealing flow rates where the supplied sealing flow was greater than the disk entrainment. Dunn et al. [14] used measurements of concentration, static pressure and velocity together with numerical simulation to investigate the flow fields in a single-stage model air turbine rotor-stator cavity. Results showed circumferential static pressure variation in the main annulus caused by large scale flow structures directly affected the rim seal flow structure.

4 Facility Overview

The test facility at the University of Sussex consists of a two stage axial turbine test section, rated to 400 kW, with an engine representative geometry, at an overall design pressure ratio of approximately 2.7:1. Hot main annulus air is supplied to the test section by an adapted Rolls Royce DART 3 MW aero engine. The air passes through a settling chamber and bellmouth to reduce pressure asymmetry and swirl in the test section. A hydraulic dynamometer and 3:1 reduction gearbox are used to absorb the power transmitted by the turbine. Cooling air is supplied to the test section via an Atlas Copco ZT250 oil free compressor. Flow control valves allow adjustments of $\pm 0.1 \text{ gs}^{-1}$ to be made during a test run. Both the annulus flow and cooling flow lines are insulated. The cooling air supplied to the rig, including both the main cooling flow and the balance flow, as well as the seal vent air coming from the rig are measured by hot film flow meters. These were calibrated to an accuracy of $\pm 1.3\%$ for the range of mass flow for intended measurements. The main annulus mass flow is measured using an upstream venturi. The stationary components of the test section contain 73 K-type thermocouples at various locations including both metal and air measurements. The rotating assembly contains 81 K-type thermocouples at 27 distinct locations. A Datatel radio telemetry system provides noncontact transmission of the signals. The rig includes a number of pressure measurements, which are used to monitor main annulus conditions

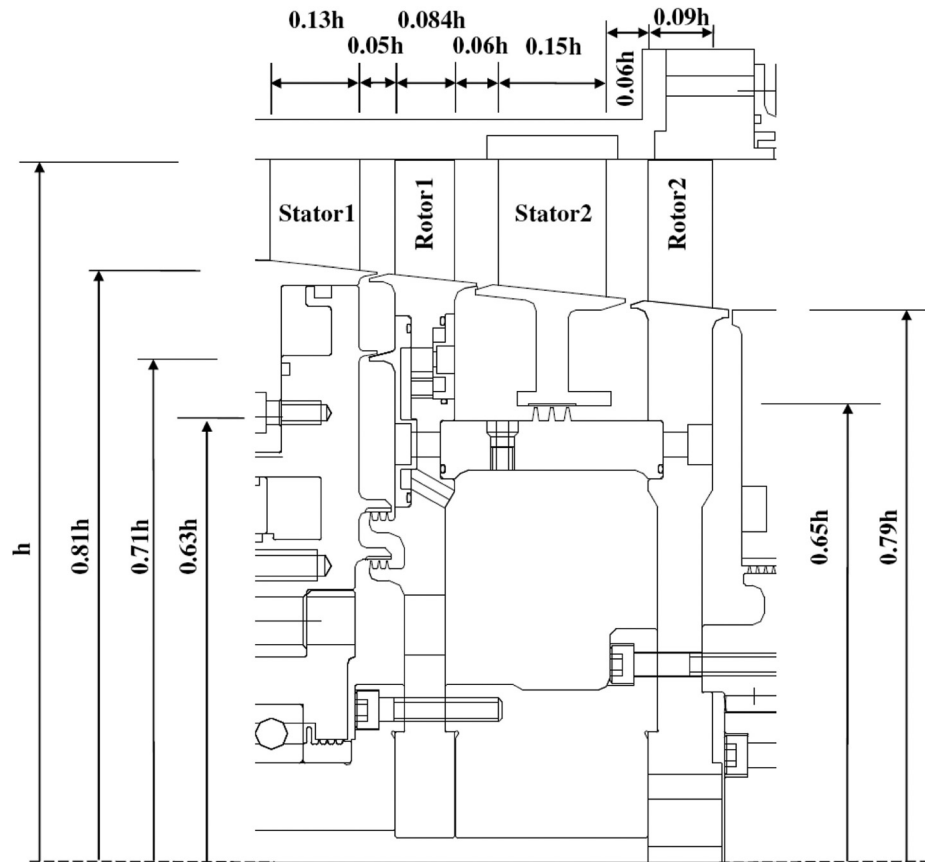


Fig. 1 Test section geometry

and aid in the balancing of cooling system seals. The accuracy obtained after calibration is within 0.017% of span for 0 to 3.5 bar. Figure 1 shows the major dimensions of the test section (at the request of industrial partners these have been nondimensionalized). The dimensions are presented in terms of h , the radial distance from the rotor shaft to the outer radius of the main annulus. Table 1 gives the blade and nozzle parameters of each stage.

5 Experimental Objectives

The GC measurements on the turbine stator well rig are designed to satisfy two measurement objectives:

- obtain measurements of main annulus rim seal exchange
- obtain measurements of flow re-ingested into the stator well cavities

The measurement of the rim seal exchange was conducted with geometry used as part of the cooling effectiveness studies. The re-ingestion experiment however required a bespoke geometry to be tested where the coolant delivery paths to the stator well were blocked.

6 Gas Concentration Instrumentation

The development of the GC measurement system used for the experiments described here required a dual species gas delivery, sample handling and measurement system. Carbon dioxide was selected due to its non corrosive property, having no detrimental effect on the rig or piping materials. The carbon dioxide is delivered from a 25 kg supply at 50 bar. The carbon dioxide passes through an inline heater to ensure the gas delivery temperature to the seeding supply flow meter is within ± 10 K of temperature at which the meter was calibrated. This results in a seeding flow rate uncertainty of $\pm 0.01 \text{ gs}^{-1}$. The metered seeding gas is then

Table 1 Blade and nozzle parameters

	Stator 1	Rotor 1	Stator 2	Rotor 2
Pitch/chord	0.6806	0.7791	0.7301	0.7512
Height/axial chord	1.199	2.188	1.233	2.568
Inlet mach number	0.1885	0.2763	0.2570	0.3014
Exit mach number	0.6563	0.6001	0.6529	0.6143
Inlet flow angle (deg)	0.00	36.68	19.02	23.32
Exit flow angle (deg)	70.07	65.36	64.60	59.33

introduced to the main cooling supply flow to provide a homogeneous gas mixture. Gas samples are taken from four locations within the rig, two located in the upstream wheelspace and two in the downstream wheelspace, each located at $r = 0.905b$.

Figure 2 shows the stator well dimensions, including the major dimensions of the interstage seal and the upstream and downstream rim seals. The location of the drive arm inserts and simulated lock plate coolant supply routes are also shown. The locations of the gas concentration measurements are shown on the stator foot as black dots, with the circumferential location noted. The dimensions are presented in terms of s , the upstream rotor-stator spacing. The gas samples are taken at a flow rate of less than $0.002 C_{W,ENT}$ which approached isokinetic conditions. Each of the sampling locations are pressure taps during normal running of the rig. A solenoid system allows the measurement to be switched between gas sampling or pressure measurement. When the solenoids are in the position to allow gas samples, the gas is piped to the gas analyzer. The gas analyzer consists of two NDIR infrared units run in series, having ranges of 0–1% and 0–10% carbon dioxide content by volume. Due to the transport time of the gas through the system the measurements are time averaged values.

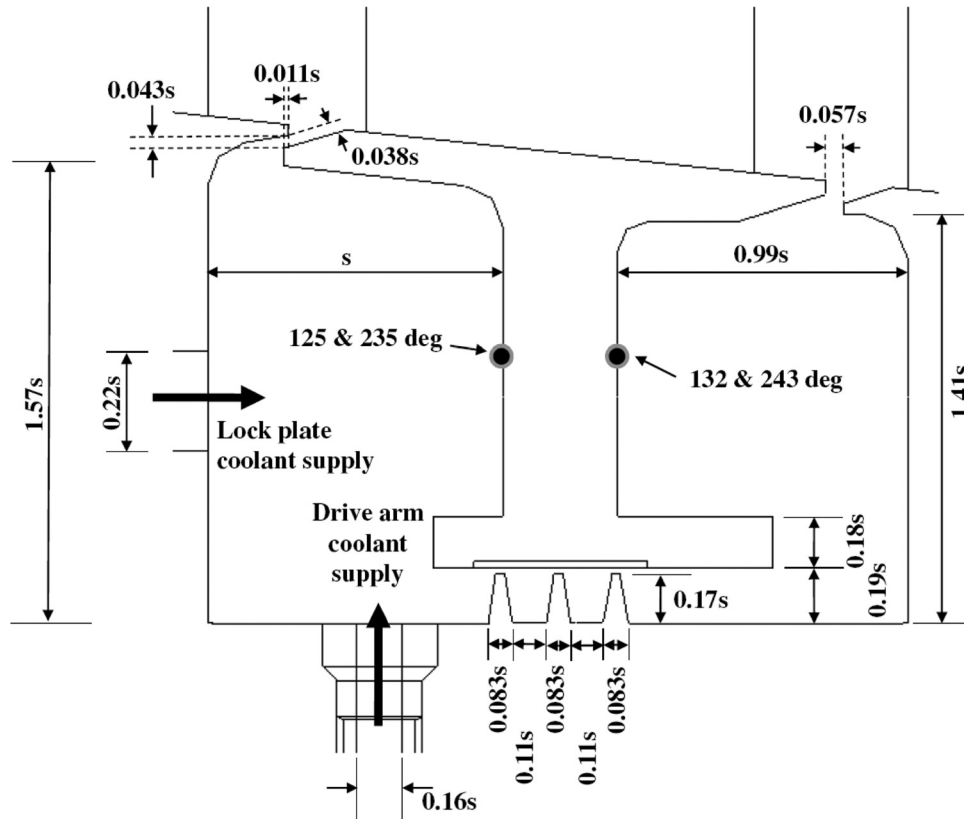


Fig. 2 Stator well and seal dimensions

7 Measurement Validation

Before the installation of the instrumentation on the TSW rig an external test was undertaken to prove the measurement method. Metered ambient air was supplied to a length of pipe. A known mass flow of carbon dioxide was then used to seed the ambient air. Both of these mass flows were measured using the flow meters to be used in the rig. A sample of the gas mixture was then taken 100 diameters downstream to ensure fully mixed flow, which was then passed to the gas analyzers. The measured concentration was compared to the ideal concentration calculated from the known mass flows of air and carbon dioxide introduced to the pipe. This was repeated with a variety of air to carbon dioxide ratio's of rates expected within the TSW rig. The measured data was found to be within 1% of the calculated data across the seeding range. Once installed in the TSW rig the entire GC seeding and sampling system was tested on the rig. The test was conducted with the rotating assembly stationary and with the rig inlet and outlet closed. This allowed the rig to be pressurized, giving a pressure drop from the rig to the gas analyzers of the magnitude that would be seen during a full test matrix run. This also ensured a homogenous mix of ambient air to carbon dioxide throughout the TSW rig. As with the pipe test, a metered amount of ambient air and carbon dioxide seeding gas was then supplied to the TSW rig. This was supplied via the main cooling air path. Once the pressure in the rig had reached the desired level, samples were taken from the rig measurement points. The test was conducted at three seeding flow rates. For each condition the measurement points showed the sampling system to give repeatable results within 2%. This represents the uncertainty of the system.

8 Rim Seal Exchange Experiments

The rim seal exchange experiments were designed to provide information on the interaction of main annulus and cooling air across the upstream stator well rim seal. The gas flows being

investigated are shown in Fig. 3. For these experiments, coolant with a known concentration of carbon dioxide was introduced to the test section through either drive arm holes or simulated lock plate slots. Concentration measurements in the stator well were then made. From the supplied and measured concentration, a dilution ratio is calculated. This, together with a known interstage seal flow can be used to calculate the net rim seal exchange. Due to the pressure ratio of the downstream stator well to the main annulus it is assumed that there is no/minimal ingress through the

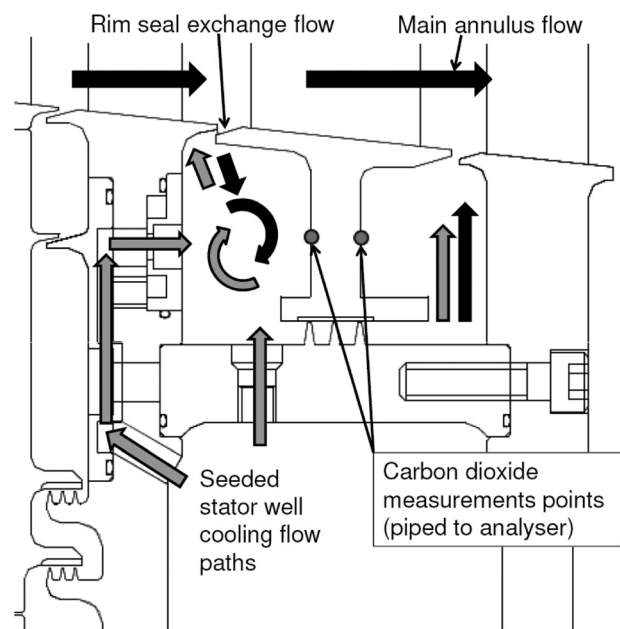


Fig. 3 Rim seal exchange experimental flows

downstream stator well rim seal. Therefore, gas samples taken from the downstream cavity give the concentration of the gas mixture which has passed through the interstage seal and therefore can be used to inform concentration measurements taken upstream of the interstage seal.

Although it would be possible to measure the coolant delivery rate, calculate the interstage seal flow and from summation alone determine an average rim seal flow, this would not take into account the possibility of a rim seal exchange. The technique used here was developed to overcome the inherent uncertainties of a direct summation approach to determining the rim seal flow. The difference in the concentration measured in the stator wells as compared to the delivery rate allows the total amount of main annulus air entering the stator well to be calculated. Where the addition of this value to the supplied cooling flow exceeds the interstage seal flow, a rim seal exchange is indicated. This is shown in the following analysis. The carbon dioxide is mixed with the cooling air before entering the test section. The total mass flow rate is then calculated.

$$\dot{m}_{SC} = \dot{m}_C + \dot{m}_{SG} \quad (5)$$

From the known mass flows of carbon dioxide and cooling air the concentration of the supplied coolant is calculated, taking into account the ambient carbon dioxide level.

$$GC_{SC} = \left[\frac{100}{\dot{m}_{SC}} \right] \times \left\{ \dot{m}_{SG} + \left[\frac{\dot{m}_C}{100} \right] \times \text{Ambient } CO_2 \right\} \quad (6)$$

From the calculated delivery concentration and the concentration measured in the stator well a dilution ratio is calculated.

$$DR = \left[\frac{GC_{SW}}{GC_{SC}} \right] \quad (7)$$

The dilution ratio is then used to calculate the total flow into the cavity, which includes the supplied coolant and ingested main annulus gas.

$$\dot{m}_{USW} = \left[\frac{\dot{m}_{SC}}{DR} \right] \quad (8)$$

From this value, the rim seal exchange values for seal ingress and egress can be calculated

$$\dot{m}_{ING} = \dot{m}_{USW} - \dot{m}_{SC} \quad (9)$$

$$\dot{m}_{EGR} = \dot{m}_{USW} - \dot{m}_{IS} \quad (10)$$

9 Re-ingestion Experiment

Quantifying the re-ingestion of coolant gas is often difficult or impossible with temperature and pressure measurements alone. The main obstacle to this measurement is differentiating between re-ingested and normally supplied cooling air to a cavity. In order to address this, a specific experiment was devised. This is shown in Fig. 4. Both the drive arm holes and simulated lock plate slots were blocked ensuring the direct coolant supply paths to the stator-well cavity were closed. The upstream wheelspace was then supplied with seeded cooling air. With the rig in this configuration, all the seeded cooling flow passes up the wheelspace and directly into the main annulus flow. This ensures that the only path for coolant to reach the stator-well is by re-ingested from the main annulus. The data reduction equations are outlined below.

Cooling air seeded with a known mass of carbon dioxide is supplied to the upstream wheelspace. The total wheelspace supply is calculated from these measured values.

$$\dot{m}_{WS} = \dot{m}_C + \dot{m}_{SG} \quad (11)$$

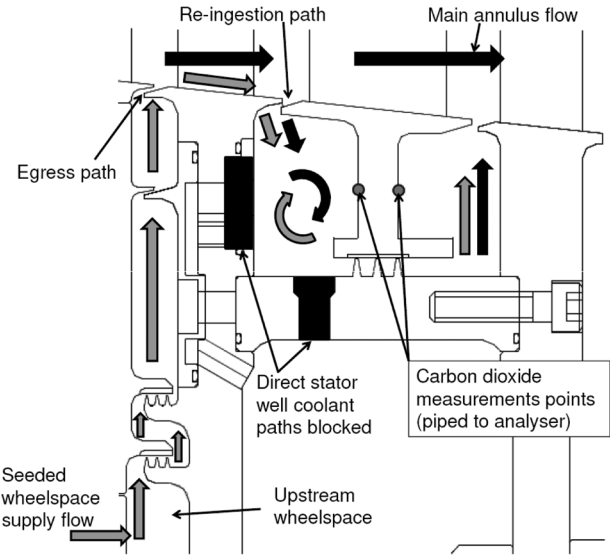


Fig. 4 Re-ingestion experimental flows

The concentration of the wheelspace supply can then be calculated

$$GC_{WS} = \left[\frac{100}{\dot{m}_{WS}} \right] \times \left\{ \dot{m}_{SG} + \left[\frac{\dot{m}_C}{100} \right] \times \text{Ambient } CO_2 \right\} \quad (12)$$

Concentration measurements are then taken in the stator wells. As the coolant delivery paths are blocked total rim seal ingress into the upstream stator well is equal to the interstage seal flow.

$$\dot{m}_{USW} = \dot{m}_{IS} \quad (13)$$

The ratio of the supplied wheelspace coolant flow concentration and the measured stator-well concentration can then be calculated.

$$DR = \left[\frac{GC_{SW}}{GC_{WS}} \right] \quad (14)$$

The wheelspace flow which has been re-ingested into the upstream stator-well can then be calculated

$$\dot{m}_{RE} = \dot{m}_{USW} \times DR \quad (15)$$

10 Interstage Labyrinth Seal Flow Estimation

The TSW interstage labyrinth seal is a three fin straight through seal with a 0.3 mm cold build clearance, set so that the seal demand is lower than disk entrainment flow and coolant delivery. It will be shown later that the hot running clearance is 0.4 mm. This results in a clearance that is scaled down from typical engine values, giving low rotational Reynolds numbers when compared too much of the data in open literature. For the purpose of this work, the 2D, nonrotating data of Wittig et al. [8] has been used to estimate a C_D . Their tightest clearance tested, 0.5 mm, (together with 2.5, 1.5 and 1.0 mm) is close to the TSW seal and the geometry is similar. Specifically, the estimation of the C_D value has been derived from an extrapolation of the 6 and 1 fin data, too 0.3 mm clearance. An estimate for the 3 fin C_D was derived from the numerical modeling of the Wittig et al. data by Kim and Cha [15]. Equivalent 2, 3, 4 and 5 fin predictions were made together with the 1 and 6 fin cases. Based on their results, the 3 fin C_D is expected to be approximately 45% worse than the 6 fin value in comparison to the single fin datum, which gives a C_D estimate of 0.48.

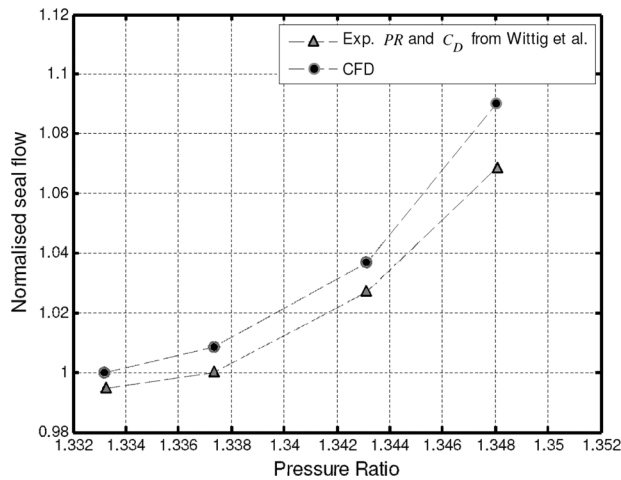


Fig. 5 Comparison of CFD and calculated seal flows using $C_D = 0.48$. Upstream to downstream seal pressure ratios = 1.333–1.348.

Figure 5 shows a comparison of seal flows calculated using a C_D of 0.48 with the St. Venant-Wantzell equation, with seal flow results from CFD. The pressure ratio is the upstream to downstream seal pressure. The normalized seal flow is seal flow/ $C_{W,ENT}$. The CFD results are within 2% of the calculated values. The effect of rotation has been shown to reduce the discharge coefficient. The TSW seal is at the borderline between the axial and rotationally affected regimes, so the effect is not expected to be significant.

11 Displacement Instrumentation

An experimental method was devised to measure hot running geometry changes using eddy current displacement sensors. A sensor for measuring axial movement in the rig is located downstream of rotor 2, while a second sensor is located on the stator foot downstream of the interstage seal. This sensor measures the change in radial gap of the seal which is of particular importance when quantifying interstage seal flows. The space available and operating environment dictated that a non contact system was essential, which removes the possibility of contact errors and frictional heating of the measurement surface. It was necessary to complete the sensor calibration before rig assembly, meaning the sensors could not be calibrated while subject to operating temperature and pressure. In order to quantify the possible uncertainty of calibrating at ambient conditions rather than operating conditions an isothermal box was created in which each sensor could be placed and output changes due to changes in temperature measured. For each sensor the resultant measurement uncertainty due to temperature change from ambient to operating temperature was less than the dynamic resolution of the sensor. The radial sensor calibrations were found to be repeatable to within ± 0.02 V, corresponding to a measurement uncertainty of ± 0.001 mm over the 0.5 mm range.

Data from the radial sensor gives a direct measurement of the net interstage seal movement. Figure 6 shows the seal movement for a typical rig commissioning run as well as the associated rig speed. Stator and rotor temperatures for the run are also shown. The cooling flow rate has been kept constant so that the dominant factor in the increasing rig temperatures seen are the result of increasing hot main annulus flow. As the rig begins to rotate an initial spike is seen in the seal gap as the blades load and the rotating assembly settles (point a). The seal gap can then be seen to close as the stator temperatures initially drop (point b). However the gap then begins to open as rig temperatures increase (point c). The stator material has a coefficient of thermal expansion almost 40% greater than that of the rotor material. The higher radius part

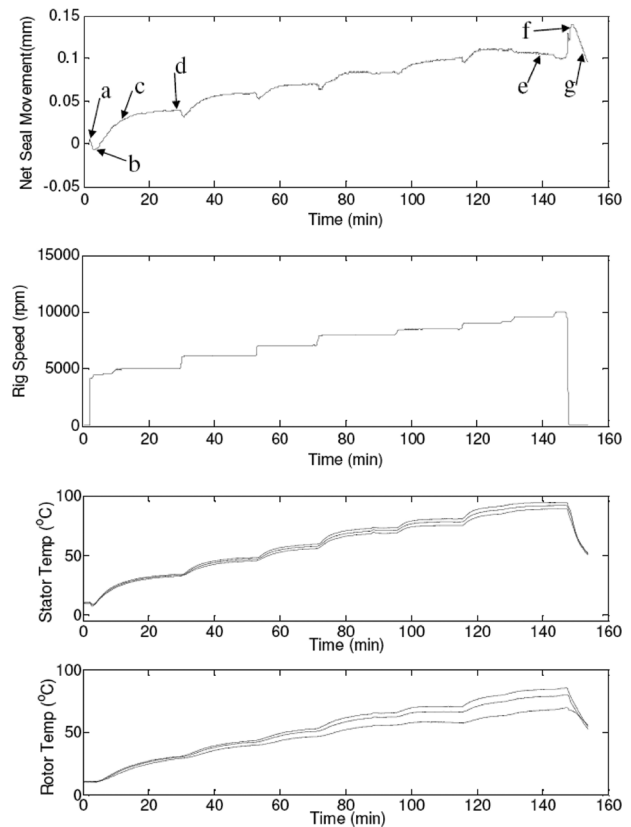


Fig. 6 Radial sensor output, rotational speed and rotor-stator temperatures for a full test cycle

of the seal where the sensor is mounted therefore expands more than the lower radius rotating part of the seal despite the similar temperature of the rotor and stator at a similar radius to the seal. The seal gap can then be seen to settle once the temperatures stabilize (point d). This pattern can be seen to repeat with each speed increase up to 10,000 rpm where the seal gap has increased by 0.1 mm (point e). The seal cold build clearance of 0.3 mm has therefore seen an increase of 33% highlighting the importance or accurately predicting the hot geometry of such seals and the influence on the flows within the stator well. At the end of the run, a sudden increase in seal gap is seen as the main annulus supply is removed and the rotating assembly slows (point f). At this point any centrifugal growth has been removed causing the rotating assembly to reduce in radius, moving away from the stationary assembly. The gap then begins to close up as the rig rapidly cools (point g). The radial sensor was not installed for the duration of the test matrix. In order to provide seal clearance values across the TSW test matrix, a thermo-mechanical modeling capability has been developed. A model constructed using the Rolls-Royce in-house code SC03, was matched thermally by using test data temperatures to inform model boundary conditions. The resulting seal movement was then compared to the experimental values of displacement taken from the radial sensor. The model was found to predict the change of seal clearance to within 0.009 mm.

12 Rim Seal Exchange Experimental Results

Rim seal exchange GC measurements were taken with four rig geometries at cooling flows of $0.77 C_{W,ENT}$ and $1.04 C_{W,ENT}$ corresponding to in cavity rotational Reynolds numbers of $1.76 \times 10^6 < Re_\phi < 1.86 \times 10^6$. The four geometries studied, including 26 and 39 drive arm holes and 26 and 39 simulated lock plate bleed slots, are shown in Fig. 7.

The dilution ratios for the four measurement locations for both drive arm configurations are shown in Fig. 8. A dilution ratio of

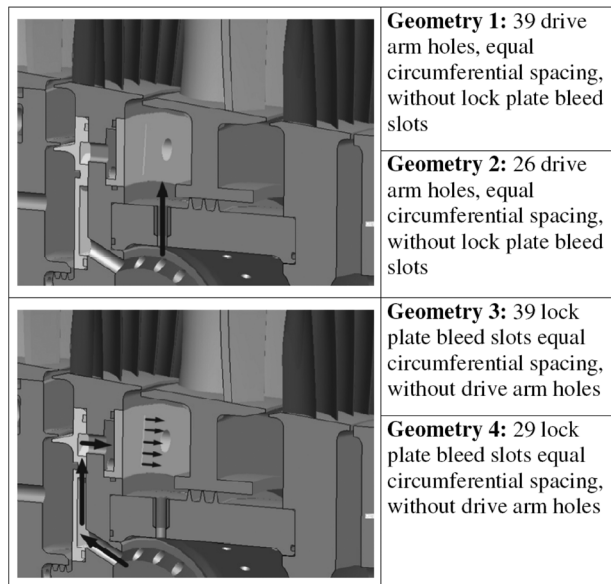


Fig. 7 Cooling supply geometries

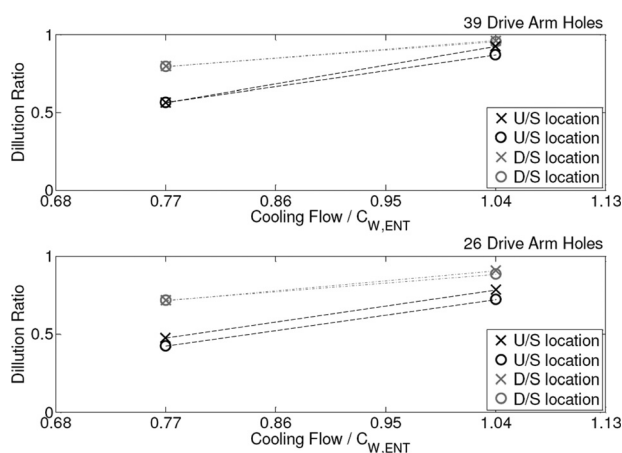


Fig. 8 Measured dilution ratios for 39 and 26 drive arm holes, at cooling flow rates of $0.77 C_{W,ENT}$ and $1.04 C_{W,ENT}$, $1.76 \times 10^6 < Re_\phi < 1.86 \times 10^6$

zero indicates that no seeded cooling air is present, a ratio of 1 indicates that no main annulus air is present. For both drive arm hole configurations at $0.77 C_{W,ENT}$ a large variation was seen between the measurements taken in the upstream wheelspace and the measurements taken in the downstream wheelspace. The lower dilution ratio in the upstream wheelspace indicates that the cooling air has not fully mixed with main annulus ingress into the cavity. The higher ratio in the downstream cavity suggests the cooling air directly feeds the interstage seal, so a higher concentration is measured in the downstream cavity.

The dilution ratios for the measurement locations at $1.04 C_{W,ENT}$ show a similar effect, where the dilution ratio is lower for the upstream cavity. However the difference is greatly reduced when compared to $0.77 C_{W,ENT}$. This suggests that with increased cooling flow the coolant has more fully mixed at the upstream measurement locations, cooling at a higher radius in the cavity. This increase in cooling effectiveness at higher cavity radius is in agreement with the findings of Coren et al. [1] which indicated cavity sealing in the vicinity of $1.04 C_{W,ENT}$. Fig. 9 shows stator well streamlines from a CFD study of the 39 drive arm hole geometry for two coolant flow rates of $0.58 C_{W,ENT}$ and $0.77 C_{W,ENT}$. For $0.58 C_{W,ENT}$, where the supplied coolant flow

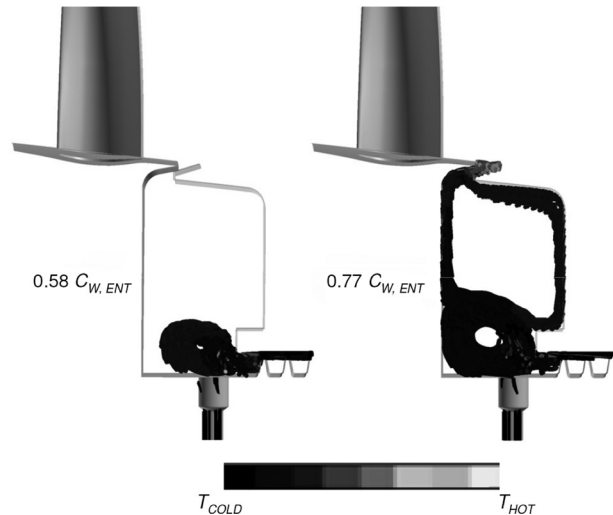


Fig. 9 Cavity streamlines for drive arm configuration colored by normalized absolute frame total temperature, interstage seal flow = $0.9 C_{W,ENT}$

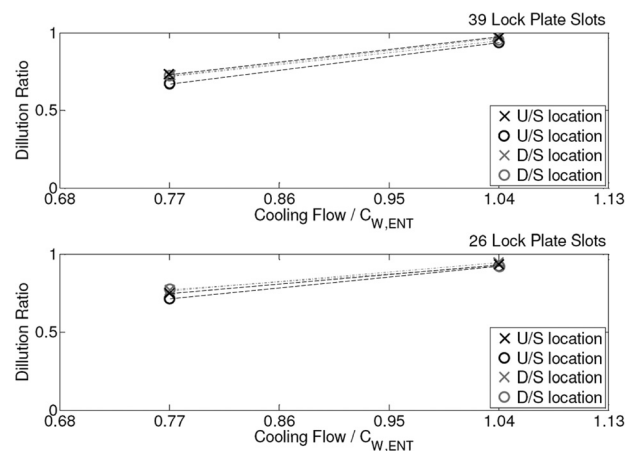


Fig. 10 Measured dilution ratios 39 and 26 lock plate slots, at cooling flow rates of $0.77 C_{W,ENT}$ and $1.04 C_{W,ENT}$, $1.76 \times 10^6 < Re_\phi < 1.86 \times 10^6$

rate is much lower than the disk entrainment it can be seen that the coolant does not penetrate to the higher radius areas of the stator well but directly feeds the interstage seal. For $0.77 C_{W,ENT}$ the coolant has penetrated into the cavity. A detailed overview of this study can be found in Coren [16]. Comparison of the downstream measurement locations, where the sampled gas has more completely mixed for both flow rates, shows that the dilution ratio increases with increased coolant flow. This indicates that for the higher coolant flow rate the upstream cavity has been more effectively sealed reducing the ingress of hot main annulus gas through the rim seal. The results also suggest generally worse sealing with fewer delivery holes. This is not yet fully understood.

The dilution ratios for the four measurement locations for both lock plate slot configurations are shown in Fig. 10. The results for the lock plate slot geometries showed much closer agreement between the dilution values seen for the upstream and downstream measurement locations for $0.77 C_{W,ENT}$ and $1.04 C_{W,ENT}$. This suggests that with lock plates the coolant has mixed fully with ingested main annulus air in both cavities as opposed to the drive arm geometries where the coolant had not fully mixed in the upstream cavity. This is due to the coolant being fed directly into the disk entrainment. This result indicates that the introduction of

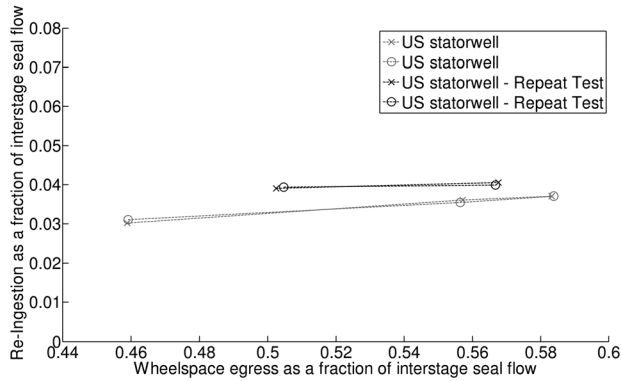


Fig. 11 Measured re-ingestion rates for wheelspace egress rates of 0.46IS to 0.59IS, $Re_\phi = 1.65 \times 10^6$

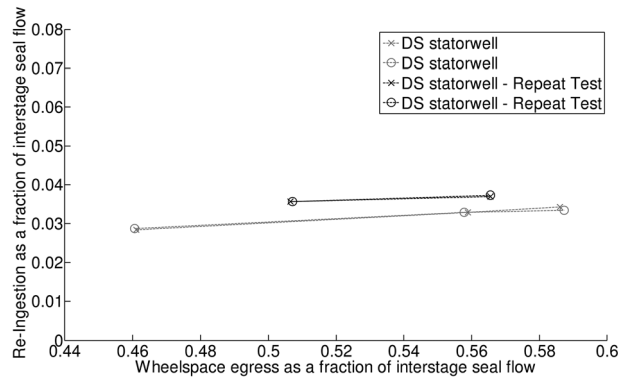


Fig. 12 Measured re-ingestion rates for wheelspace egress rates of 0.46IS to 0.59IS, $Re_\phi = 1.65 \times 10^6$

the cooling air through the lock plate slots has increased the amount of coolant present at the higher radius areas of the upstream stator well. This result is corroborated by the findings of Coren et al. [16] which indicate greater upstream cavity mixing with lock blade bleed slots when compared to drive arm hole delivery. As with the dilution ratios obtained for the drive arm tests, the ratios obtained for both the 26 and 39 lock plate slot geometries show an increased concentration measurement for the higher cooling flow. This shows that the higher cooling flow has reduced the ingress of main annulus gas into the upstream cavity. As expected for both 26 and 39 lock plate slots the dilution ratio is within 0.05 of being equal to 1, showing minimal ingestion through the rim seal. The increased sealing of the cavities for both the drive arm and lock plate slots shown by the concentration measurements are supported by the temperature measurements discussed in Coren et al. [16]. Cooling effectiveness was seen to increase with increased cooling flow. Temperature measurements also support the findings from the lock plate slot tests where coolant is thought to have penetrated further into the cavity and increased cooling on the stator face when compared to similar flow rates through drive arm hole geometries.

13 Re-Ingestion Experimental Results

The re-ingestion experiment was conducted at three wheelspace egress rates, where $Re_\phi = 1.65 \times 10^6$. This value is lower than would be expected under normal rig conditions due to the lack of cooling air being directly supplied to the rotor stator cavity. Results are shown in Fig. 11 and Fig. 12 based on upstream and downstream measurement locations. These results are based upon interstage seal flows calculated with a hot running clearance calculated using displacement sensor measurements and a C_D of 0.5,

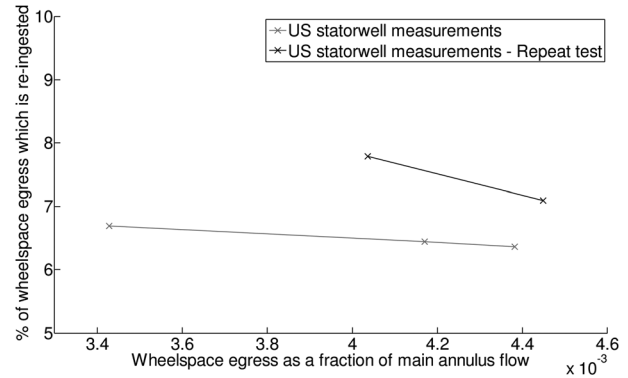


Fig. 13 Percentage re-ingestion rates for wheelspace egress expressed as a fraction of main annulus flow, $Re_\phi = 1.65 \times 10^6$

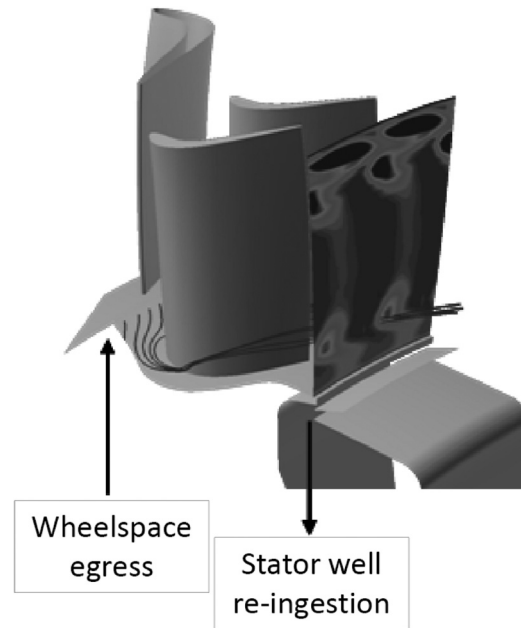


Fig. 14 Streamlines of wheelspace egressed coolant

the C_D value being increased from 0.48 to account for the increase in seal area under hot running conditions. The egress and re-ingestion rates are shown as fractions of interstage seal flow. Following publication of Paper GT2011-45874 [17] a minor leak was found between the lock plate covers. In order to address this, the seal gaps were sealed and the re-ingestion experiments repeated. This activity included two tests between which the rig was stripped in order to confirm the new seals had remained in place. The new results show a lower rate of re-ingestion than previously seen, however the trends remain the same as shown in Paper GT2011-45874 [17].

Figure 13 shows the percentage of wheelspace egress which is re-ingested into the stator cavity against the egress rate, where the egress rate is given as a fraction of the main annulus flow. It can be seen that although re-ingestion increases with increased egress the percentage of the re-ingestion decreases. Figure 14 shows a CFD solution displaying streamlines which are seeded at the point of egress from the wheelspace. The wheelspace has not been modeled. The streamlines suggest that the coolant would be initially entrained directly on to the blade foot boundary layer. The low momentum of the fluid causes it to be drawn up onto the blade suction surface as the gas approaches the tail of the blade and mixes with secondary flows. As such it is likely the coolant begins to lift from the foot in to the main annulus. This results in pockets

of mixed coolant and main annulus gas and areas of pure main annulus gas above the rim seal. The gas re-ingested into the stator well is drawn from these two gas mixtures. The reduction in percentage re-ingestion with increased egress indicates that more coolant is mixing with the main annulus air as the momentum of the coolant through the wheelspace rim seal increases, which simply reduces the concentration at the rim seal.

14 Conclusions

A two stage turbine rig with a shrouded second stage has been used to investigate ingestion in a turbine stator well. The rig enables investigation of coolant supplied by means of both coolant supply holes in the drive arm as well as coolant supplied by means of lock plate bleed slots. A noninvasive technique using tracer gas seeding and detection together with displacement sensors has been developed to provide measurements of rim seal exchange flows and re-ingestion flows within a engine representative test rig. Dilution ratio data from GC measurements has shown that as the cooling flow rate in the stator well increases, the coolant mixes more fully in the upstream stator well, providing more effective cooling at a higher radius with an effective reduction of the ingress of hot main annulus gas through the rim seal. At low flow rates the coolant is thought to pass straight through the interstage seal. Re-ingestion experiments have indicated that the percentage of wheelspace egress re-ingested is in the region of 7% for the range of realistic coolant flow rates explored, with the re-ingestion reducing with increasing coolant flow. The GC results can be used to determine the sealing effectiveness of a number of coolant flow rates. The data is suitable for the progression and validation of modern conjugate/coupled analysis tools.

Acknowledgment

The present investigations were supported by the European Commission within the Framework 6 Programme, Research Project 'Main Annulus Gas Path Interactions (MAGPI)', Grant No. AST5-CT-2006-030874. This financial support is gratefully acknowledged. The authors would like to thank J. A. Dixon (Rolls Royce Plc) and J. R. Turner. Thanks are also given to Simon Davies, Glenn Downs and Tony Martin for their assistance in the construction of the facility.

Nomenclature

a = disk inner radius (m)
 A_{SEAL} = circumferential seal area (m²)
 b = disk outer radius (m)
 C_D = seal discharge coefficient
 \dot{m} = mass flow rate (kg s⁻¹)
 P = static pressure (Pa)
 P_0 = total pressure (Pa)
 r = local radius (m)
 R = gas constant for air (J kg⁻¹ K⁻¹)
 s = axial rotor-stator spacing (m)
 T = static temperature (K)
 T_o = total temperature (K)
 μ = dynamic viscosity (kg m⁻¹ s⁻¹)
 v_ϕ = tangential velocity component (ms⁻¹)
 ρ = density (kg m⁻³)
 γ = ratio of specific heats
 ω = rotational speed (rad s⁻¹)

Dimensionless

C_W = nondimensional throughflow, $m b^{-1} \mu^{-1}$
 Re_ϕ = rotational Reynolds number, $\rho \omega r^2 \mu^{-1}$
 β = swirl ratio, $v_\phi r \omega^{-1}$

Subscripts

0 = free disk flow value
 1 = upstream of interstage seal
 2 = downstream of interstage seal
 C = cooling air
 EGR = rim seal egress
 ENT = disk with inner hub flow value
 ING = rim seal ingress
 IS = interstage seal flow
 RE = re-ingested flow
 SC = seeded cooling air
 SG = seeding gas
 SW = stator well (either up or downstream)
 USW = upstream stator well
 WS = wheel space

Abbreviations

CFD = computational fluid dynamics
 DR = dilution ration
 GC = gas concentration
 NDIR = nondispersive infrared sensor

References

- Coren, D. D., Atkins, N. R., Turner, J. R., Eastwood, D., Davies, S., Childs, P. R. N., Dixon, J. A., and Scanlon, T. S., 2010, "An Advanced Multi-Configuration Stator Well Cooling Test Facility," *ASME Paper No. GT2010-23450*.
- Daily, J. W., and Nece, R. E., 1960, "Chamber Dimension Effects on Induced Flow and Frictional Resistance of Enclosed Rotating Discs," *J. Basic Eng.*, **82**, pp. 217–232.
- Chew, J. W., 1998, "The Effect of Hub Radius on the Flow Due to a Rotating Disc," *J. Turbomach.*, **110**, pp. 417–418.
- Dorfman, L. A., 1963, *Hydrodynamic Resistance and Heat Loss of Rotating Solids*, Oliver and Boyd, Edinburgh.
- Owen, J. M., and Phadke, U. K., 1980, "An Investigation of Ingress for a Simple Shrouded Rotating Disc System With a Radial Outflow of Coolant," *ASME Paper No. 80-GT-49*.
- Zimmermann, H., and Wolff, K. H., 1998, "Air System Correlations, Part 1: Labyrinth Seals," *ASME Paper No. 98-GT-206*.
- Gamal, A. M., and Vance, J. M., 2007, "Labyrinth Seal Leakage Tests: Tooth Profile, Tooth Thickness, and Eccentricity Effects," *ASME Paper No. GT2007-27223*.
- Wittig, S., Schelling, U., Kim, S., and Jacobsen, K., 1987, "Numerical Predictions and Measurements of Discharge Coefficients in Labyrinth Seals," *ASME Paper No. 87-GT-188*.
- Gentilhomme, O., Hills, N., and Turner, A. B., 2003, "Measurement and Analysis of Ingestion Through a Turbine Rim Seal," *ASME J. Turbomach.*, **125**, pp. 505–512.
- Georgakis, C., Whitney, C., Woolatt, G., Stefanis, V., and Childs, P., 2007, "Turbine Stator Well Studies: Effect of Upstream Egress Ingestion," *ASME Paper No. GT2007-27406*.
- Phadke, U. P., and Owen, J. M., 1988, "Aerodynamic Aspects of the Sealing of Gas Turbine Rotor-Stator Systems Part 1: The Behavior of Simple Shrouded Rotating-Disc Systems in a Quiescent Environment," *Int. J. Heat Fluid Flow*, **9**, pp. 98–105.
- Dadkhah, S., Turner, A. B., and Chew, J. W., 1992, "Performance of Radial Clearance Rim Seals in Upstream and Downstream Rotor-Stator Wheelspaces," *ASME J. Turbomach.*, **114**, pp. 439–445.
- Green, T., and Turner, A. B., 1994, "Ingestion Into the Upstream Wheelspace of an Axial Turbine Stage," *ASME J. Turbomach.*, **116**, pp. 327–332.
- Dunn, D. M., Zhou, D. W., Saha, K., Squires, K. D., Roy, R. P., Kim, Y. W., and Moon, H. K., 2010, "Flow Field in a Single-Stage Model Air Turbine Rotor-Stator Cavity With Pre-Swirled Purge Flow," *ASME Paper No. GT2010-22869*.
- Kim, T. S., and Cha, K. S., 2009, "Comparative Analysis of the Influence of Labyrinth Seal Configuration on Leakage Behavior," *J. Mech. Sci. Technol.*, **23**, pp. 2830–2838.
- Coren, D. D., Atkins, N. R., Long, C. A., Eastwood, D., Childs, P. R. N., Guizarro-Valencia, A., and Dixon, J. A., 2011, "The Influence of Turbine Stator Well Coolant Flow Rate and Passage Configuration on Cooling Effectiveness," *ASME Paper No. GT2011-46448*.
- Eastwood, D., Coren, D. D., Long, C. A., Atkins, N. R., Childs, P. R. N., Scanlon, T. J., and Guizarro Valencia, A., 2011, "Experimental Investigation of Turbine Stator Well Rim Seal, Re-Ingestion and Interstage Seal Flows Using Gas Concentration Techniques and Displacement Measurements," *ASME Paper No. GT2011-45874*.

GT2011-46448

THE INFLUENCE OF TURBINE STATOR WELL COOLANT FLOW RATE AND PASSAGE CONFIGURATION ON COOLING EFFECTIVENESS

D. D. Coren*, N. R. Atkins[†],
C. A. Long, D. Eastwood

Thermo-Fluid Mechanics Research Centre
University of Sussex
Brighton, BN1 9QT, UK

P. R. N. Childs
Dept. of Mechanical Engineering
Imperial College London
South Kensington
London, SW7 2AZ, UK

A. Guijarro-Valencia,
J. A. Dixon
Thermal Systems
Rolls-Royce plc
Derby, UK

ABSTRACT

Market competitiveness for aero engine power plant dictates that improvements in engine performance and reliability are guaranteed *a priori* by manufacturers. The requirement to accurately predict the life of engine components makes exacting demands of the internal air system, which must provide effective cooling over the engine duty cycle with the minimum consumption of compressor section air. Tests have been conducted at the University of Sussex using a turbine test facility which comprises a two stage turbine with an individual stage pressure ratio of 1.7:1. Main annulus air is supplied by an adapted Rolls-Royce Dart compressor at up to 440 K and 4.8 kg s⁻¹. Cooling flow rates ranging from 0.71 to 1.46 $C_{w, ent}$, a disc entrainment parameter, have been used to allow ingress or egress dominated stator well flow conditions. The mechanical design of the test section allows internal cooling geometry to be rapidly re-configured, allowing the effect of jet momentum and coolant trajectory to be investigated. An important facet to this investigation is the use of CFD to model and analyse the flow structures associated with the cavity conditions tested, as well as to inform the design of cooling path geometry. This paper reports on the effectiveness of stator well coolant flow rate and delivery configurations using experimental data and also CFD analysis to better quantify the effect of stator well flow distribution on component temperatures.

NOMENCLATURE

a	Disc inner radius [m]
A	Cross sectional area
b	In-cavity disc outer radius [m]
C_D	Discharge coefficient
C_p	Specific heat at constant pressure [J kgK ⁻¹]
d	Inner Diameter [m]
D	Outer diameter [m]
N	Turbine speed [rpm]
m	Mass flow rate [kg s ⁻¹]

P	Static pressure [Pa]
P_0	Total pressure [Pa]
r	Local radius [m]
R	Universal gas constant
s	Axial rotor-stator spacing [m]
T	Static temperature [K]
T_0	Total temperature [K]
v_ϕ	Tangential velocity component [ms ⁻¹]
v_z	Axial velocity component [ms ⁻¹]
ω	Rotational speed [rad s ⁻¹]
ρ	Density [kg m ⁻³]
μ	Dynamic viscosity [Pa s]

Dimensionless

C_w	Non-dimensional throughflow, $m b \mu^{-1}$
G	Cavity aspect ratio, sb^{-1}
Re_ϕ	Rotational Reynolds number, $\rho \omega b^2 \mu^{-1}$
Re_z	Annular seal Reynolds number, $\rho v_z (D-d) \mu^{-1}$
β	Swirl ratio, $v_\phi r \omega^{-1}$
λ_T	Flow parameter, $C_w Re_\phi^{-0.8}$

Subscripts

0	Free disc flow value
1	Station upstream of Stator 1, <i>main annulus</i>
2	Station upstream of Rotor 1, <i>main annulus</i>
3	Station upstream of Stator 2, <i>main annulus</i>
4	Station upstream of Rotor 2, <i>main annulus</i>
<i>cold</i>	Cold Reference value
<i>coolant</i>	Coolant condition
<i>ent</i>	Disc entrainment flow
<i>hot</i>	Hot reference value
<i>inlet</i>	Inlet condition
<i>metal</i>	Metal condition
<i>s</i>	Superposed flow value

Abbreviations

CFD	Computational Fluid Dynamics
-----	------------------------------

*Correspondence to d.d.coren@sussex.ac.uk

[†] Now at the Whittle Laboratory, University of Cambridge

INTRODUCTION

This paper reports an experimental investigation into turbine stator well cavity cooling. Optimisation of the coolant and sealing flows in stator well cavities has potential benefits for both overall cycle efficiency and component life. As such, these themes provide the focus for the research here. In particular, the relationship between superposed cooling flow and rim seal ingestion, and the influence of coolant delivery geometry on cavity wall temperature distribution, is discussed here. Experimental findings are quantified in terms of a thermal effectiveness parameter, while CFD code has been used to reinforce understanding of the associated flow structures.

The flow and heat transfer within the cavities adjacent to the hub of a turbine stage has a significant effect on the durability of the neighbouring components. Stator well flows are characterised by regions of entrainment, cores of highly two dimensional rotationally dominated flow, and shear driven mixing regions both within the cavity and at the rim seals. Superposed cooling flows are required in order to ensure that engine components are kept within their rated working temperatures, either by direct cooling or by means of pressure sealing wheelspace and stator well cavities to avoid ingestion from the hot main gas path. These cooling flows influence the flow structures otherwise prevalent in rotor-stator cavities.

These phenomena represent the limits of Reynolds-Averaged Navier Stokes (RANS) approaches. More computationally expensive Large Eddy Simulation (LES) and hybrid techniques hold much promise, in particular for the prediction of mixing and interactions in the shear dominated regions. With the increased adoption of conjugate methods, the requirement for high quality validation data is clear.

Rig testing is often limited to a small number of geometrical variations before significant rebuild or re-instrumentation becomes necessary. The experimental data presented have been obtained using the Turbine Stator Well (TSW) test facility at the Thermo-Fluid Mechanics Research Center (TFMRC) at the University of Sussex. This facility is described in more detail by Coren *et al.* [1]. The Sussex Turbine Stator Well test rig comprises a two stage turbine with an overall pressure ratio of 2.7:1 at design conditions. It features an easily configurable working section which can be modified in a matter of hours. A brief overview of the test facility is given here, including description of the main annulus and internal cooling geometries, their control and supply system, and instrumentation specifications.

This work is part of the EU FP6 MAGPI (Main Annulus Gas Path Interactions) programme, which has the remit of improving current understanding of the interaction of cooling and main stream flows.

Since investigations related to the flows in the vicinity of turbine stator wells requires discussion of the flow physics associated with rotor-stator cavities, a brief review is included.

Rotor-Stator Flows

A disc rotating in the presence of a quiescent viscous fluid will entrain fluid and drive it radially outward in a three

dimensional viscous dominated boundary layer until it exits via the disc periphery. This is commonly referred to as the free disc case and provides useful reference for the study of rotating flows.

Daily and Nece [2] showed that for a rotor-stator arrangement with an aspect ratio, $G \leq 0.1$ and a circumferential sealing shroud, the working fluid recirculates around the cavity. Entrained flow pumped radially outward on the rotor surface is supplied by a radial inflow along the stator wall. These viscous boundary layer flows are separated by a two dimensional core which behaves inviscidly, and in the absence of circumferentially periodic protrusions, rotates at $\beta \approx 0.4$.

The rate at which the inviscid core rotates is a result of the rotor and stator boundary layers which form a viscous coupling and transmit a retarding force between the rotor and the stator. This was investigated by Owen and Rogers [3] who used a momentum integral approach to analyse this effect. The resultant relative tangential velocities that exist between the wall surfaces and the rotating core are proportional to the rate of frictional heating that occurs, which was investigated experimentally by Coren *et al.* [4].

The rate of entrainment for a free disc is given by the relation of Dorfman [5] for turbulent flow, Equation 1, while entrainment for partial rotors, as commonly found in turbomachinery, may be related to this by the fit of Chew [6], Equation 2.

$$C_{w,0} = 0.219 Re_{\phi}^{0.8} \quad \text{Equation 1}$$

$$C_{w,ent} = C_{w,0} \left[1 - \left[\frac{a}{b} \right]^5 \right] \quad \text{Equation 2}$$

Where: $C_{w,ent}$ = Flow entrained by a disc with inner hub

$C_{w,0}$ = Flow entrained by a free disc

and a and b are the inner and outer disc radii

The importance of accounting for disc pumped flow physics when modelling rotor-stator flows was demonstrated by Da Soghe *et al.* [7] who developed a design tool for solving steady one dimensional axisymmetric rotating cavity flows. The solutions predicted by the model were seen to more closely match experimental data and CFD predictions after developing correlations for disc friction.

Superposed Cooling Flows

Superposed cooling flows are required in order to provide direct cooling of critically loaded turbine components and to prevent bulk rim seal ingestion by pressure sealing the hub region cavities and wheelspaces from the hot gas path.

The minimum superposed throughflow required to achieve cavity sealing and avoid ingestion from the hot mainstream gas path may be estimated using correlations such as that of Owen

and Phadke [8]. The correlation of Owen and Rogers [3] provides such relation while accounting for circumferential pressure gradients in the main annulus, which were shown by Bunker *et al.* [9] to strongly influence rim seal flow exchanges. This was also investigated by Dixon *et al.* [10] using CFD.

The superposed cooling rate required for cavity sealing is generally found to exceed the entrainment rate. Such rates of superposed flow alter cavity flow structures strongly. The flow regime may be conveniently evaluated using a non-dimensional relation. The following is appropriate for turbulent flow:

$$\lambda_T = C_w Re_\phi^{-0.8} \quad \text{Equation 3}$$

The entrainment capacity of the rotating disc is exceeded when $\lambda_T \geq 0.219$, and radially dominated flow prevails. For values below this, flow may be considered to be rotationally dominated.

Daily *et al.* [11] related the rate of superposed cooling flow and the resulting core rate, β , to the core rate in the absence of superposed flow, β^* . Gartner [12] showed similarly that the presence of a two dimensional core was diminished as superposed flow was increased beyond the rate of disc entrainment. For these investigations, coolant was supplied axially from a non rotating source, such that increased coolant flow reduced core rates, ultimately flooding them with radial outflow dominated flow until free disc like flow structures and moment coefficients occurred.

However, as applied to the case of turbine stator well cooling where the coolant is supplied from a hub mounted passage rotating at rotor rate, a radial outflow, where relative tangential velocities across the rotor boundary layer are reduced is of benefit; after consideration for the work required to bring the coolant up to rotor rotational rates via pre-swirl nozzles incorporated into a rotating hub, as investigated by Karabay *et al.* [13], the relationship between cooling flow and the core rate becomes advantageous. This was demonstrated by Andreini *et al.* [14] who performed CFD analysis to investigate the effect of angled coolant passages.

Seal Flows

In an idealised environment, cavity flows would be isolated from the main annulus. In practice, high speed rotor-stator systems employ non-contact seals with finite clearance. This is set as small as possible, while accounting for thermal and rotational loads throughout the engine duty cycle, chiefly in order to reduce the superposed coolant required to achieve cavity sealing.

Rim seal flows, in simplified terms, are affected by pressure gradients acting across them, the running clearance; and also circumferential pressure gradients in the main annulus, as described by Owen and Rogers [3] and Scanlon *et al.* [15]. Interstage labyrinth seals provide means of containing upstream cavity flows prior to them exiting via either the rim or interstage seals themselves. Interstage seal flow rates are

dominated by the main annulus stage pressure drop and the effective area of the seal. Flow rates through rotor-stator labyrinth seals have been the attention of many studies, including that of Wittig *et al.* [16] who provided empirical correlation of seal geometries to standard seal flow equations, and Kim and Cha [17] who used the experimental data of Wittig to validate CFD models for rotating seal geometries.

Summary

Designing for cooling system effectiveness requires accurate prediction of the ingress and egress regime limits. For a given application, this requires consideration for superposed cooling flows, entrainment flows, interstage seal flows, and estimates of the minimum coolant required for cavity sealing. These flows are depicted, in simplified form in Fig. 1.

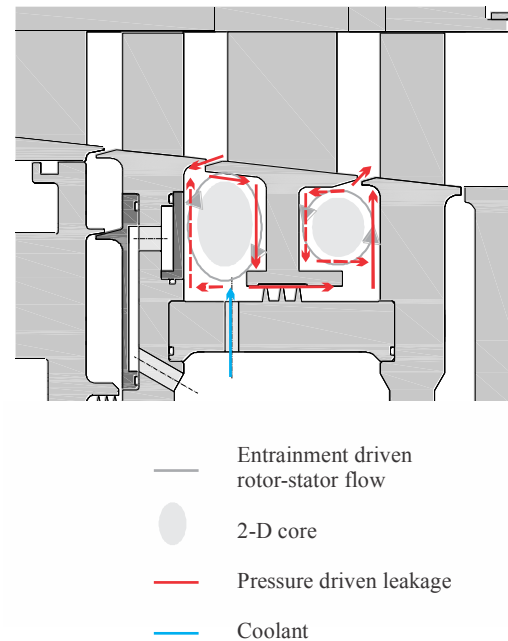


Figure 1: Rotor-Stator Flow Structure Schematic

In response, this paper presents data resulting from investigations carried out to determine the influence of the following cooling flow parameters; flow rate, cooling jet momentum, and flow trajectory. The experimental facility allows:

Coolant flow rates to be set below the disc entrainment and interstage seal demand to allow bulk ingestion, or set sufficiently high as to flood and seal the cavity to allow bulk egress.

The effective flow area of the coolant delivery passages to be altered such that, for a given rate of coolant, the momentum with which the flow enters the stator well cavity is increased, influencing cavity flow paths.

The use of angled coolant delivery passages, in order to impart the coolant flow with a particular trajectory, with the aim of improving the cooling of targeted components.

TEST FACILITY OVERVIEW

The test facility features a bespoke two stage turbine rated at 400 kW with blade geometry representative of modern gas turbines. A diagram of the test rig is given in Fig. 2. The rotor stages have 78 blades and the stators 39, which gives a convenient 2:1 repeat ratio for CFD.

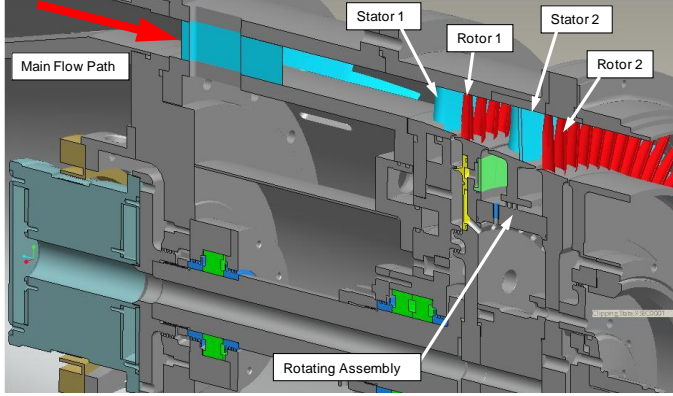


Figure 2: Schematic of the Test Rig Working Section

The main annulus flow is provided by an adapted aero engine plant driven compressor as developed by Turner *et al.* [18]. Flow enters the test rig via a settling chamber and large bellmouth inlet to reduce circumferential non-uniformity and swirl. The mass flow rate is measured using a BS1042 standard venturi meter. The turbine power is absorbed by a hydraulic dynamometer via a 3:1 reduction gearbox. The main annulus operating conditions are given in Table 1.

Overall Pressure Ratio	< 2.7
Power Output	< 400 kW
Mass flow rate	1 to 4.8 kgs ⁻¹
Cooling flow rate	0.6 to 1.65 $C_{w,ent}$
T_{inlet}	300 – 450 K
P_{inlet}	< 3.3 bar
N (at design condition)	10,630 rpm

Table 1: Test Rig Main Annulus Operating Conditions

Of central importance to the design of the test rig is the ability to readily reconfigure the cooling system geometry. This is provided by a split main casing design which allows rapid access to the stator well cavities.

Internal Air System

The stator well cavity geometry has been designed to provide a nominal in-cavity Reynolds number of $Re_\phi = 2.0 \times 10^6$ at the main annulus design condition. Cooling flow rates have been specified to encompass the ingestion point, the selection process having been informed by a review of cavity sealing correlations. The maximum rate of superposed cooling flow allows the equivalent of 2.8 greater than the minimum suggested for cavity sealing by the correlations of Owen and Phadke [8]. The interstage labyrinth seal geometry has been set such that the seal flow may be exceeded by superposed cooling

flow, allowing cavity flow conditions to be controlled by superposed coolant. The maximum cooling flow rate is equivalent to 1.8 times the interstage labyrinth seal flow requirement as predicted using the correlation of Wittig *et al.* [16] and the study of Kim and Cha [17]. This particular aspect of this work is presented in more detail by Eastwood *et al.* [19]. Taken together, this allows interstage seal demand to be satisfied and rim sealing to be achieved, with a safety factor included to account for the variation between the correlations used. Importantly, this allows cavity flow conditions from bulk ingestion to bulk egress to be tested.

Non-dimensioning of the superposed cooling flow is useful in widening the range of applicability of the results obtained. The rate may be related to the minimum required to seal the cavity, or to the interstage seal demand, using one of the many correlations available from the literature. However, there is much variation between the results of these correlations, indeed this present work seeks to further clarify the conditions required for cavity sealing. Also, the interaction of superposed coolant with entrainment flows is of particular interest to this study. For these reasons, the superposed coolant has been defined here in terms of a disc entrainment parameter, using Equations 1 and 2. The data presented here relates to experiments where cooling flow is delivered in a variety of manners. Each of these different test cases results in a unique value of core rotation rate, β . As such, the free disc case, modified using Equation 2 to account for the partial disc geometry in question, is considered to provide a non-ambiguous bench marked reference case, to which the superposed coolant rates may be equated to. The cooling system has been specified to allow coolant flow, $C_{w,s}$ over the range 0.60 to 1.65 times the predicted disc entrainment, $C_{w,ent}$. For the cooling flow data presented here, rates of 0.71, 0.87, 1.13 and 1.46 $C_{w,ent}$ have been used, which accounts for augmentation due to balance seal leakage flows.

The cooling system air is supplied by an Atlas Copco ZT250 compressor and FD710 drier plant. The test rig internal air flow circuits are shown in Fig. 3. The cooling system air is ducted via aerodynamic struts into the hub region of the rig, similar ducting is used for the balance and vent flows. Coolant is delivered to the cavity first via transfer holes in the lower part of Stator 1, and then via transfer holes in the hub region of Rotor 1. A pressure balanced, double sided claw seal is used to reduced leakage of coolant flow up through the Stator 1 wheelspace. The balance cavity is continuously monitored during tests to account for thermal growth of the claw seals. The balance supply is vented from a buffer cavity to maintain upstream wheelspace egress. Although the rig design permits both radial and axial delivery of coolant, radially administered coolant is the focus of this paper. The radial coolant passage design features 39 threaded holes equi-spaced around a hub ring, into which inserts drilled to form coolant passages may be installed. The air paths are insulated from the main annulus temperatures by Rohacell HF insulation. Bosch HFM 5 series hot-film air mass meters are used to measure the coolant, wheelspace balance and vent flows. They operate over the

range 0 to 100 gs^{-1} and were calibrated by a UKAS accredited third party. They give an uncertainty of $\pm 1.3\%$ of the measurement point.



Figure 3: Internal Air System Schematic

The influence of cooling flow jet momentum is facilitated by varying the number of drilled and blank radial flow passage inserts, as shown in Fig. 4. This arrangement allows 13, 26 or 39 coolant passages to be incorporated, providing means to alter the momentum of a given rate of exiting coolant by a factor of three. Removable cover plates on the downstream face of Rotor 1 allow axially delivered coolant to be similarly regulated. Regular spacing in all cases discourages non-axisymmetric cooling effects and simplifies balancing of the rotating assembly.

Description	Geometry
39 Radial Passage Inserts	
26 Radial Passage Inserts	
13 Radial Passage Inserts	

Figure 4: Radial Flow Passage Spacing Arrangements

The influence of coolant trajectory is facilitated by means of angled coolant delivery inserts, as shown in Fig. 5. Using delivery passages with an angle from a reference straight radial

outlet, the coolant may be imposed to follow a trajectory directed either axially towards the rotor face to encourage attachment with entrainment flows, or tangentially to pre-swirl the coolant against the direction of core rotation slippage. For the purposes of this study, axially directed coolant is considered. An angle of 25° has been used, which was informed by design phase CFD.

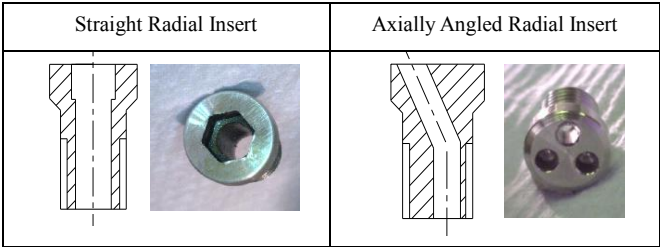


Figure 5: Straight and Axially Angled Radial Flow Passage Inserts

Ensuring that the inserts are installed with the angled passage aligned in the correct direction is performed by means of bespoke alignment jigs. Through this process, a maximum angular deviation of 0.3° is achieved.

Temperature Instrumentation

The measurement locations of the thermocouples within the main test section of the rig are given in Fig. 6. In total, 81 K-type thermocouples at 27 radial locations have been installed within the rotating assembly, including two air thermocouples used for coolant temperature measurements. 73 thermocouple measurement locations were used within the stationary components of the test rig, six of which are stator mounted air thermocouples. Total temperature measurements are made in the main annulus using probes set into the leading edge of Stator 1, Stator 2 and with a radial rake downstream of Rotor 2. This avoids the introduction of additional disturbances to the circumferential pressure gradients at the rim seal region.



Figure 6: Temperature Measurement Locations

Three thermocouples were used for each radial measurement location on the rotating components to mitigate thermocouple failures. In practice, a thermocouple mortality rate of 8 % has been found.

The thermocouple beads, with diameters ≤ 0.1 mm, are peened into the material surface as shown in Fig. 7. The lead-out trails, which are led at least 10 diameters circumferentially before radially to avoid conduction errors, are secured to the rotating components by means of spot welded metallic straps. Peening with similar material, and flush mounting to minimise velocity effects, helps to reduce embedding errors.

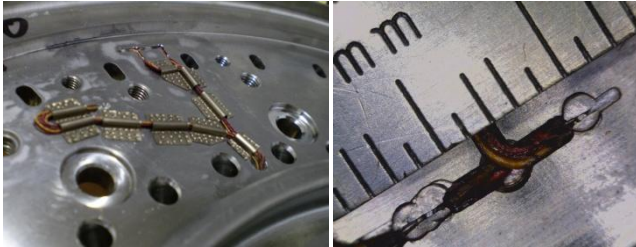


Figure 7: Thermocouple Installation Detail

A Datatel 92 channel telemetry system is used for thermocouple signal acquisition. Each unit has an in house cold junction reference module with a PRT mounted in close thermal contact to thermocouple junctions. For a given test the point to point resolution appears to be within 0.1 K. Comprehensive through-calibration techniques have reduced uncertainties to the order of 0.3 K across a 12 month period.

The stationary frame thermocouples are installed without the use of extension cables or plugs, directly into isothermal junction boxes with thick copper heat spreaders which have been fitted with PRT thermometers. These are logged using an Agilent 34970a DVM switch unit in 4-wire resistance mode. Combined with full through-calibration techniques, this reduces cold junction compensation errors to within 0.1 K.

All through-calibration is performed by comparison against Isotech Secondary Standard reference equipment with a combined uncertainty in the region of 20 mK. The test data described here have been obtained at settled conditions, defined as a change of less than 0.1 K over a five minute period.

In the interests of allowing cross comparison of test data, where small variations in main annulus and environmental conditions may be unavoidable, it is convenient to express temperature data in a normalised form;

$$\theta = \frac{T_{metal} - T_{cold}}{T_{hot} - T_{cold}} \quad \text{Equation 4}$$

This method is, however, classically ill conditioned and provides motivation for obtaining very low temperature measurement uncertainties. When the metal temperature, T_{metal} , and coolant temperature, T_{cold} , are similar, as is the case at the lower regions of the cavity, small errors will dominate. For example, a temperature difference of 10 K would yield a potential uncertainty of $\pm 3\%$ θ for an uncertainty of ± 0.3 K. Repeat testing over several months showed repeatability in normalised temperatures of approximately 1% at worst; within measurement uncertainty, suggesting that the calibration uncertainties quoted are realistic under actual test conditions.

Pressure Instrumentation

The location of the pressure measurements within the main test section of the rig are shown in Fig. 8. These are used to determine the conditions in the stator well cavities, to measure flow rates of air supplied to the rig, and to allow balancing of the upstream wheel space. Total pressure measurements are made in the main annulus using probes set into the leading edge of the NGVs. The incidence sensitivity of the total pressure measurements is minimised by recessing the tapings. All internal rig measurements use Scanivalve DSA 3217 scanner units. The orifice plate measurements use Rosemount 1151 series (differential) and Mensor 6100 (absolute) transducers.

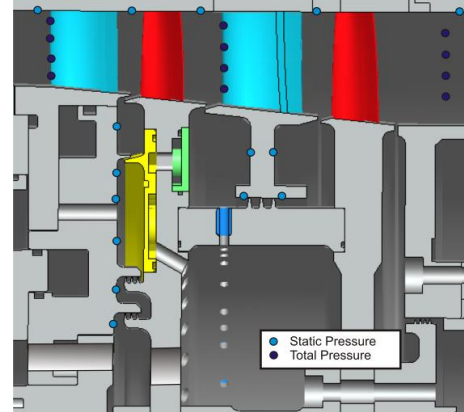


Figure 8: Pressure Measurement Locations

VISUALISATION CFD SET-UP AND ANALYSIS

The CFD analysis presented here is adiabatic and intended for flow visualisation purposes; stator well cavity streamlines representing the flow structures associated with particular cooling flow cases provide a useful aid in interpreting the measured temperature data. The domain was split into four zones separated by mixing planes between the blade rows, and an interpolation, or frozen sliding plane, between the upstream and downstream cavities. These are illustrated in Fig. 9.

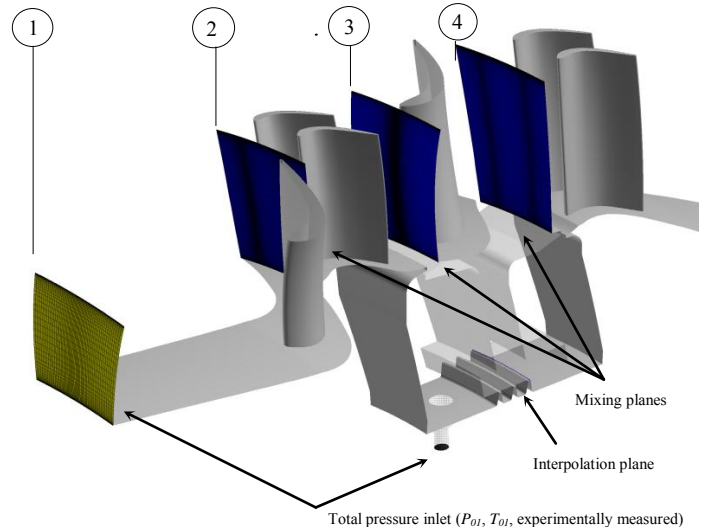


Figure 9: CFD Domain Showing Thermodynamic Stations

The multi-block structured mesh was generated using the Rolls-Royce PADRAM code and features nine Million nodes. The grid density is biased somewhat towards the cavity. The mixing plane upstream of Stator 2 is set well beyond the stationary side of the rim seal in order to model the unsteady, albeit frozen, rotor exit flow field. Grid dependency, and the effect of unsteadiness is presented by Dixon *et al.* [10].

Measured total pressure and temperature boundary conditions were used at stage inlet, and measured static pressure at the stage outlet. For the radial coolant injection, the mass flow rate is measured, but the actual total pressure is unknown.

Rim seal flows are unsteady in nature, however the unsteadiness is only likely to be dominant at the point at which the cavity is almost sealed. The steady computations presented here represent several months of computational time on a 64 CPU cluster. This work is part of an on-going study, the primary aim of which is to help validate Conjugate Heat Transfer (CHT) methods. The added fidelity of the unsteady model is considered less important than some of the other simplifications such as the use of an adiabatic solution. The steady state convergence showed oscillatory behaviour at the low coolant flow rates. The rim seal interactions are dominated by the unsteady Kelvin-Helmholtz (K-H) type interactions and the potential field of the rotor, as such the exact sealing boundary is not expected to be predicted. Also the Reynolds Averaged Navier-Stokes (RANS) approach is not well suited to the mixing and ingestion anyway. The computations are presented here simply to aid understanding of the flow.

In order to establish confidence in the cavity CFD, main annulus and interstage labyrinth seal flows have also been modelled, and are described in this section below.

Main Annulus Flow

A comparison of the predicted and total pressure and temperature at 4 discrete locations on the Stator 2 leading edge is shown in Fig. 10. Data is presented for an intermediate coolant flow test case. The plot shows total temperature T_{03} , normalised by the inlet total temperature T_{01} and total pressure P_{01} respectively, i.e. the inlet boundary conditions. The agreement at the middle two measurement locations is excellent. The worst case absolute temperature difference is ± 0.5 K for a stage temperature drop of ~ 50 K; this represents a fair comparison rather than the simple Kelvin value which would simply hide the variations. This is close to the combined measurement uncertainty of ± 0.3 K. The total pressure values at the three upper locations are within 0.2 % of the measured value. These two middle locations are away from the majority of the loss and secondary flow structures. As such the close agreement of the values suggests that the overall operation of the stage is well modelled by the grid.

At the upper and lower radial heights the CFD solution over-predicts the total temperature and pressure. At the upper radial location, the total temperature discrepancy is ~ 3 K, which represents 6 % of the stage total temperature drop. At the

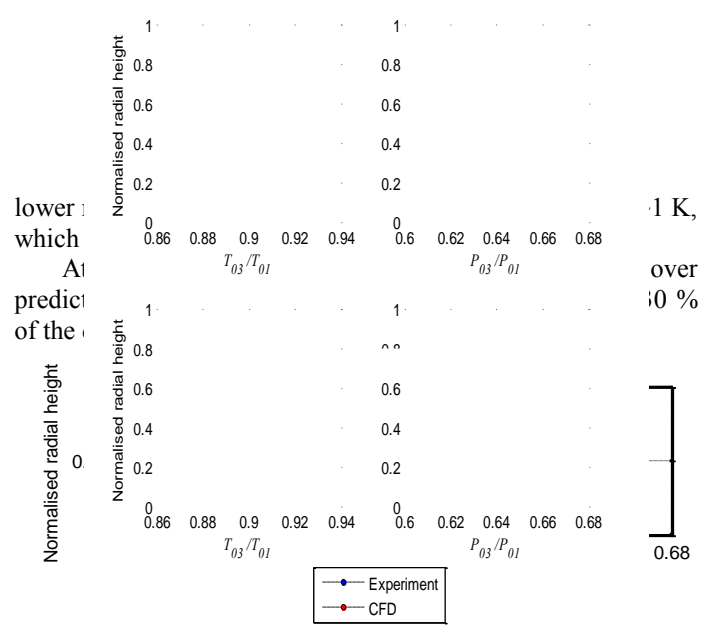


Figure 10: Total Pressure and Temperature at the Inlet to Stator 2

An area traverse of predicted total pressure and temperature ratio corresponding to a location close to the leading edge of Stator 2, but upstream of the mixing plane, is shown in Fig. 11.

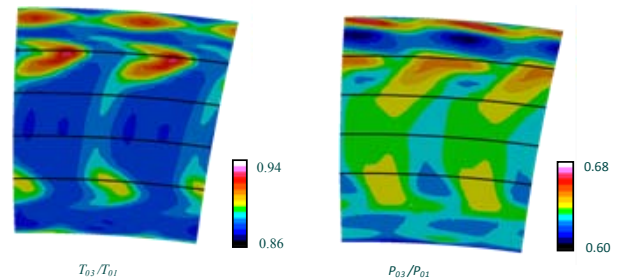


Figure 11: Total Pressure and Temperature Profiles at the Stator 2 Leading Edge Plane

The upper and lower radial heights correspond to the height at which the secondary flow structures impinge on the leading edge of the vane. As such, it is expected that the discrepancy is primarily due to the prediction of the secondary flows. The main stream grid is perhaps a little coarse, the use of a mixing plane removes all of the rotor-stator interactions, and the limitation of the Spalart-Allmaras (S-A) turbulence model to predict the mixing accurately are all likely to be significant. It should also be noted that there are steep gradients at these locations, so the predictions are also highly sensitive to the precise spatial location of the flow structures. The non-linear interactions of the upstream vane wake and vertical structures with the blade boundary layer and secondary flows are removed by the mixing plane. Blade row interactions of this type have been shown to account for 10 % of stage loss.

Another factor at the hub, where the discrepancy in total pressure is found, is the lack of the upstream wheel space cavity on the model. Although the egress is limited to approximately, 2 gs^{-1} , the presence of the cavity alone is likely to thicken the boundary layer at the very least.

These variations are local, and the excellent tie-up in the core flow shows that the model is adequate to generate the boundary conditions at the rim seal.

Interstage Labyrinth Seal Flow

Numerous articles have been published on labyrinth seal flows. The seal flow is modelled here using the St. Venant-Wantzell equation for the ideal flow together with a single discharge coefficient, C_D , which accounts for all of the dependent parameters. The discharge coefficient, C_D , for the seal is a strong function of clearance.

The TSW interstage labyrinth seal is a three fin straight through seal with a cold build clearance of 0.3 mm, which grows by approximately 30 % at the design condition. This has been set so that the seal demand is of a similar order to disc entrainment flow and also the superposed coolant, when $C_{w,s}$ is approximately $0.7 C_{w,ent}$. At the design condition, the throughflow Reynolds number, Re_z is in the order of 7×10^3 , and the ratio of axial to tangential velocity is approximately unity. For the purpose of this work, an initial flow estimate has been established using the two-dimensional, non-rotating data of Wittig *et al.* [16]. These authors considered the effects of rotation to be dominant only at low Reynolds numbers. An estimate for the three fin C_D was derived from the numerical modelling of the Wittig *et al.* data by Kim and Cha [17]. Based on their results, a C_D estimate of 0.48 has been used here.

The CFD results have been compared with results from labyrinth seal flow models, using pressure ratios representative of the experimental conditions tested. Agreement was found to be within the range 0.5 to 2 % as the pressure ratio was increased. These seal flows provide the focus of the work described by Eastwood *et al.* [19].

RESULTS AND DISCUSSION

The cooling effectiveness associated with cooling flow; rate, momentum, and trajectory are discussed here, in terms of temperature data obtained by experiment which has been normalised using Equation 4. The discussion is aided by either CFD results or flow diagrams.

The effect of core rotation rate is not included in the normalisation as the interaction of the coolant and the rotating core is a component of the performance of a particular cooling arrangement in itself, which is essentially part of this study.

As the coolant air temperature is measured at a lower radius than the cavity entry, the Euler work due to the change in radius is taken into account; ≤ 3 K for these cases, assuming the coolant enters and leaves the internal passage with little rotor relative swirl:

$$T_{0,cold} = T_{0,coolant} + \frac{1}{c_p} \Delta[(r\omega)^2] \quad \text{Equation 5}$$

Cooling Flow Rate

The effect of coolant flow rate is described here with the aid of both experimental data and CFD results for the case of 39 radial coolant delivery passages. Normalised measured metal temperatures are shown for the measurement locations on

the rear face of Rotor 1 in Fig. 12, and for the front face of Stator 2 in Fig. 13. Fig.14 shows the predicted path of main stream and coolant flow gas, for the two lowest coolant flow rates. The streamlines are seeded from the Rotor 1 aft platform boundary layer and the coolant supply jet respectively. Fig. 15 shows the rotor relative frame total temperature in the cavity at the four coolant flow rates. These figures may be used to help explain the temperature profiles observed in the measured data. The CFD predictions are used only to provide a qualitative prediction of the likely flow structure, in order to help interpret the measured profiles.

Referring to Fig. 12, it is important to note that at all four coolant flow rates the normalised temperature is approximately constant at the location on the Rotor 1 exit platform ($r/b = 1$) as would be expected. The temperature gradient between the two highest radius locations, $0.97 \leq r/b \leq 1$, is perhaps the most important part of the data set. Considering the titanium rotor, changes in temperature gradient at this location imply considerable changes in the local aerodynamic conditions, at least in terms of air temperature, if not heat transfer coefficient. At the lowest coolant flow rate, $0.71 C_{w,ent}$, there is little change in gradient across all three high radius positions shown. As the coolant flow rate is increased to $0.86 C_{w,ent}$, and $1.13 C_{w,ent}$, the gradient increases, indicating that the coolant is penetrating to higher radial locations in the cavity. This is in agreement with the CFD results in Fig. 15 which indicate significant change in cavity flows for superposed coolant rates of $\leq 0.86 C_{w,ent}$. A further increase in coolant flow rate from 1.13 to $1.46 C_{w,ent}$ yields a lower increase in temperature gradient. This indicates that the cavity is likely to be well sealed and the changes in cavity flow structure are small. At the lower extreme of the cavity, there is a larger variation in normalised temperature with coolant flow rate. This is likely to be driven by conduction, rather than differences in local adiabatic effectiveness, since this is in the vicinity of the coolant delivery passages. Even at the lowest coolant flow rate, the coolant will circulate in the lower extremes of the cavity. This is in agreement with the CFD for the low cooling flow case shown in Fig. 14. Although the spatial gradient is higher at the lower measurement points, $0.755 \leq r/b \leq 0.77$, than the outer two, $r/b = 0.97 \leq r/b \leq 1$, there is less change in gradient with increased coolant flow.

Referring to Fig. 13, an increase in the superposed cooling supply from $0.71 C_{w,ent}$ to $0.86 C_{w,ent}$ results in increased cooling at the cavity region of $0.77 \leq r/b \leq 0.945$. This is likely to be due to localised cooling of the stator foot as coolant enters the cavity. For the majority of the cavity, $0.78 \leq r/b \leq 0.99$, it is clear that the cavity is in contact with significant coolant between the supply conditions $0.71 C_{w,ent}$ and $0.86 C_{w,ent}$. This is in agreement with the CFD shown in Fig. 15. Increasing the coolant rate to $1.46 C_{w,ent}$ results in no significant additional cooling at these locations. However, at the outer most radial location, $r/b = 0.99$, which is in the main annulus, normalised temperatures can be seen to be reduced significantly at cooling rates of $\leq 1.13 C_{w,ent}$, indicating that rates sufficient for cavity sealing and bulk egress have been reached. This is in agreement with the CFD for higher coolant rates shown in Fig. 15.

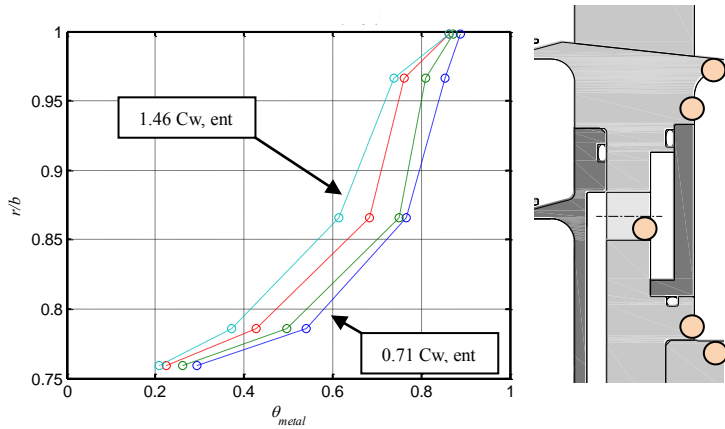


Figure 12: Rotor 1 Rear Face Normalised Metal Surface Temperatures

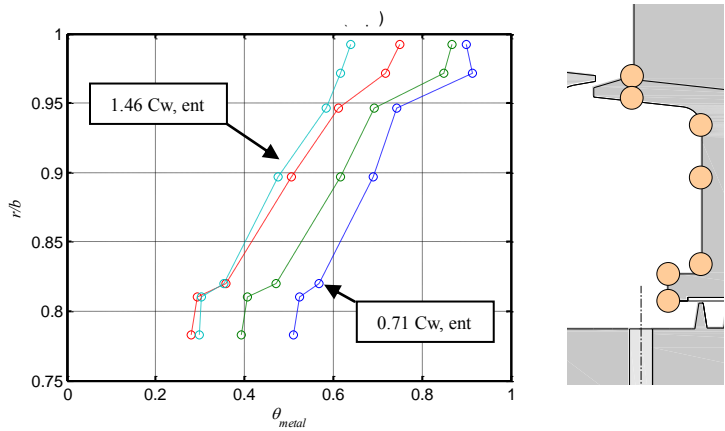


Figure 13: Stator 2 Front Face Normalised Metal Surface Temperatures

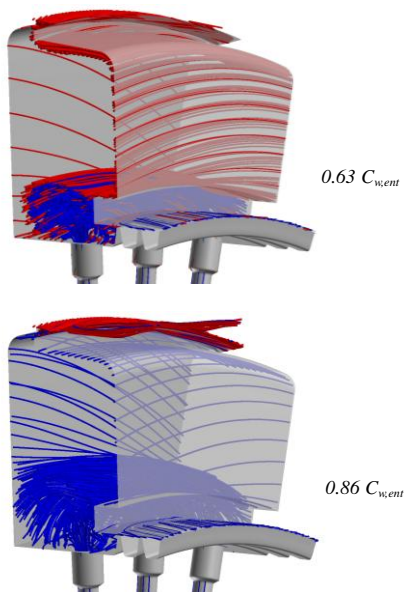


Figure 14: Comparison of Predicted Coolant (Blue) and Mainstream (Red) Streamlines.

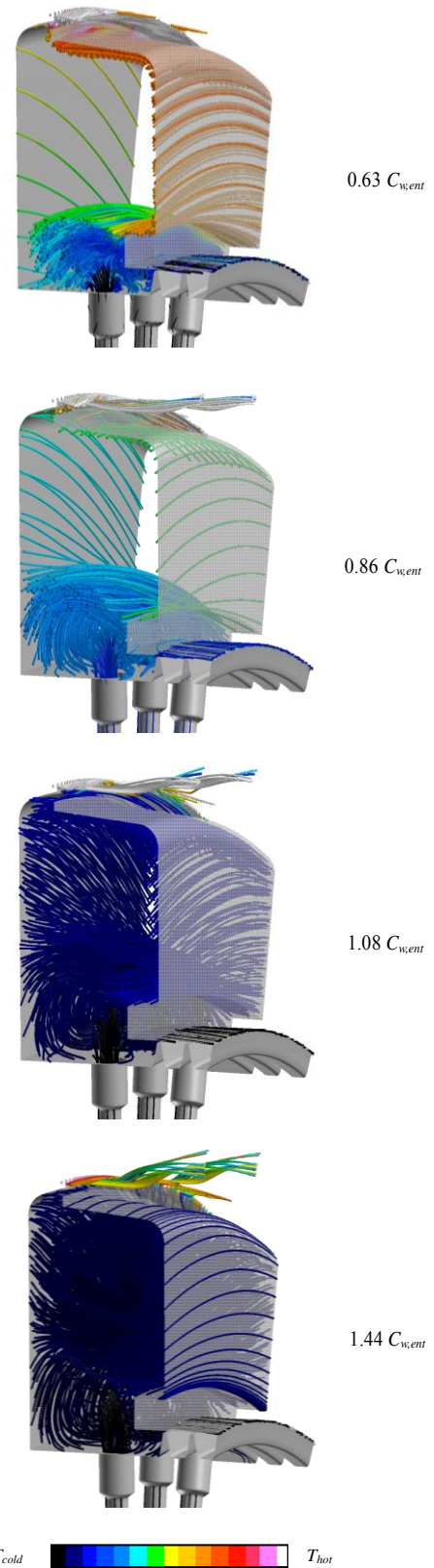


Figure 15: Cavity Streamlines, Coloured by Normalised Absolute Frame Total Temperature

Jet Momentum

Deeper penetration of the coolant streams into the cavity bears influence on the rate of core flow rotation, reducing the relative tangential velocity across the rotor boundary layers. Furthermore, for the split stator well cavities being considered here, deeper penetration encourages coolant to feed the Rotor 1 entrainment flow rather than exit through the interstage seal to the downstream cavity. This was found to be particularly evident at low cooling flow rates. Since mass flow is constant and internal cooling effects may be largely neglected, axial as well as radial delivery geometry data are considered here.

Fig. 16 shows results obtained for the downstream face of Rotor 1 in the form of normalised temperatures at a cooling flow of approximately $0.7 C_{w,ent}$ delivered radially. Reducing the effective flow area, by reducing the number of flow passages from 39 to 13, increases jet momentum threefold thereby increasing coolant flow impingement into the stator well cavity. Normalised temperatures are reduced in the vicinity of the hub region by up to 50 %, and in the region of the rotor periphery by approximately 20 %.

Measurements for the upstream face of Rotor 2 are shown in Fig. 17. In the downstream cavity, the influence of jet momentum is diluted, since the cooling air will already have mixed with ingested gas in the upstream cavity. However, as the number of flow passages is increased to 39, normalised temperatures do decrease, suggesting that cooling effectiveness has increased. This is likely to be related to the amount of heat absorbed by the coolant in the upstream cavity prior to flowing through the interstage seal.

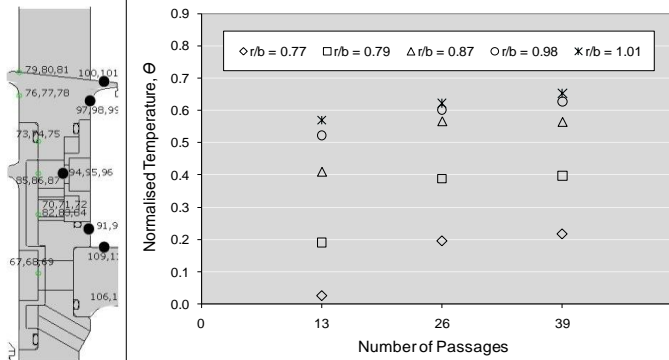


Figure 16: Rotor 1, $0.7 C_{w,ent}$, Radial Delivery

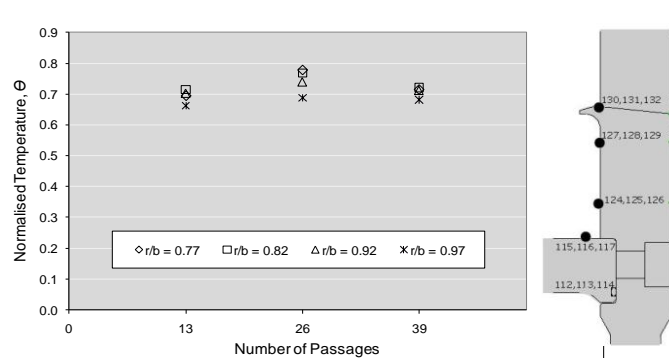


Figure 17: Rotor 2, $0.7 C_{w,ent}$, Radial Delivery

It is interesting to note that at these conditions, the reduced adiabatic viscous heating corresponding to an arbitrary change in β from 0.5 to 0.7 would equate to a 15 % reduction in the normalised measured temperatures at the rotor periphery. This equates to approximately 50 % of the total measured change between 39 and 13 coolant passages, suggesting that the temperatures measured are a result of core rate change but also re-distribution of the coolant.

Adiabatic flow visualisation CFD in Fig. 18 shows coolant delivered radially through 39 and 13 holes at $0.7 C_{w,ent}$. Streamlines indicate that the level of cavity impingement increases significantly as the number of flow passages is reduced from 39 to 13. This is likely to result in greater attachment to Rotor 1 entrainment flows, and strongly reinforces the interpretation of the experimental data.

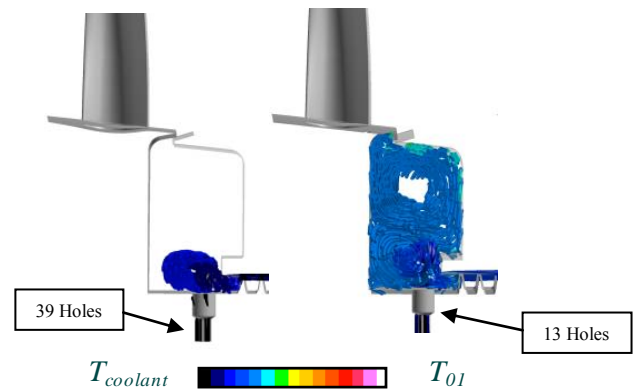


Figure 18: CFD Showing Cavity Impingement Increasing as Radial Flow Passage Number is Reduced from 39 to 13 at $0.63 C_{w,ent}$

Data also obtained at a cooling flow rate of $0.7 C_{w,ent}$ but for axially delivered coolant shows broadly similar results. See Fig. 19. Reduced benefit at the cavity periphery, as compared to the radial geometry, is considered to be a generic characteristic of axial delivery passage geometry, which supplies coolant to this region for all momentum cases. Increased cooling at the hub region for the 13 passage case may be a result of recirculation local to the rotor face.

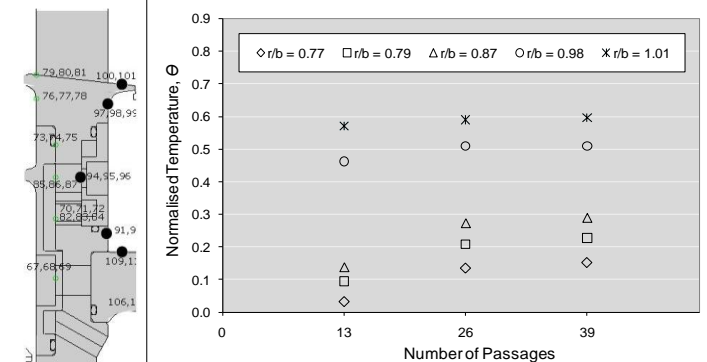


Figure 19: Rotor 1, $0.7 C_{w,ent}$, Axial Delivery

At the higher cooling flow rates of 1.13 and $1.46 C_{w,ent}$ tested for 26 and 39 passage geometries only, the cavity flows are dominated by the sheer magnitude of coolant flooding

cavity and the influence of jet momentum is less obvious. This is demonstrated in Fig. 20 by data obtained for radially delivered flow at $1.46 C_{w,ent}$.

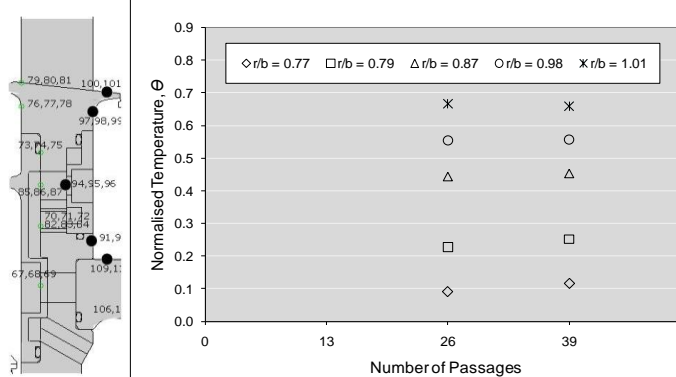


Figure 20: Rotor 1, $1.46 C_{w,ent}$ Radial Delivery

Angled Delivery Geometry

The angled insert design incorporates a flow passage inclined at 25° . This value was selected after an optimisation process involving design phase CFD investigations, which have been reported by Andreini *et al.* [14] and also a result of the angle and bore size permitted by the insert location drillings. Settled data obtained at 9800 rev/min, and also data obtained during commissioning tests at the design condition but not as well settled, have all shown improved cooling effectiveness on Rotor 1 at the cavity periphery.

Normalised temperature data for the downstream face of Rotor 1, and also for the upstream face of Rotor 2, is shown for both straight and axially angled radial insert geometries in Fig. 21. This data was obtained at a superposed cooling rate of $0.86 C_{w,ent}$. A flow schematic is also given, aiding the description of the altered flow structures associated with the geometry changes. The change in the radial temperature profiles between the results for the straight and angled geometries suggests that the coolant has successfully been re-directed; increasing the likely-hood of attachment to the rotor entrainment flows, rather than washing over the stator wall or exiting directly through interstage seal into the downstream cavity. Similarly to the jet momentum experiments, even at low cooling flow rates, the hub region is subject to effective cooling, by virtue of proximity to the coolant delivery point; this is illustrated by the CFD results shown in Fig. 14. It is of particular interest to see that for this intermediate cooling condition of $0.86 C_{w,ent}$, with the introduction of an angled passage, cooling is re-directed to the cavity periphery significantly enough to result in a 10 % reduction in the normalised rotor temperature. The likely transit mechanism for this re-distribution is carriage within the disc entrainment flows. Corroborating this, the stator temperatures, while also reduced at the cavity periphery, are actually increased at the lower radii, indicative of re-circulated coolant which has been subject to heat pick-up.

The reduction in adiabatic viscous heating corresponding to an arbitrary change in β from 0.5 to 0.7 would equate to approximately 70 % of the measured change in normalised

temperature, suggesting that the reduced temperatures are strongly related to the core rate change, but also a result of re-distribution of coolant.

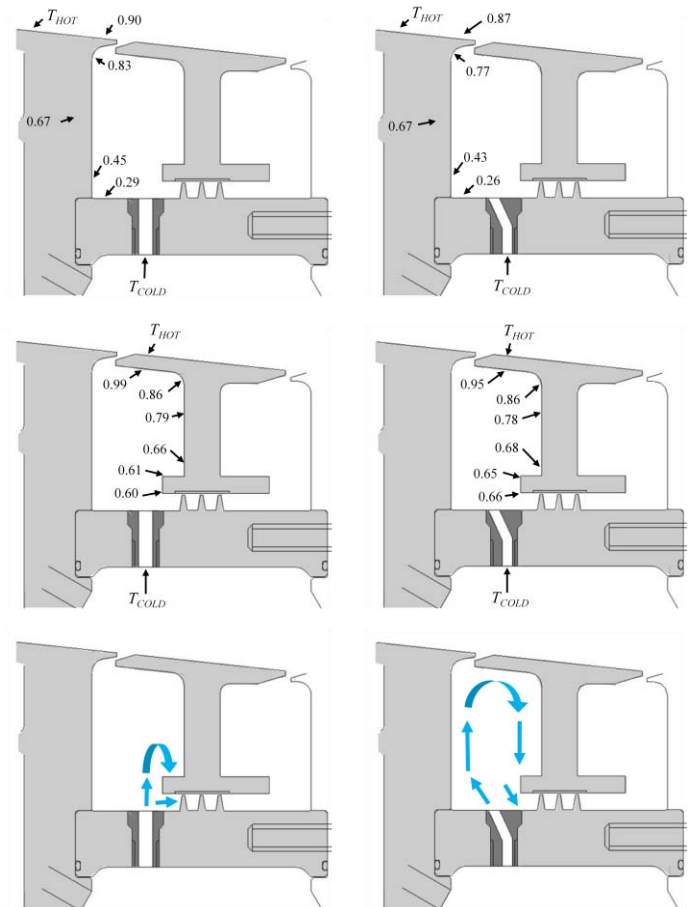


Figure 21: Normalised Temperature Data and Flow Structure Schematics for Straight and Axially Angled Radial Coolant Delivery, $0.86 C_{w,ent}$

CONCLUSIONS

Developing an effective cooling system, where bulk ingestion is prevented and critical components are adequately cooled, requires a design process informed by the geometric characteristics and the associated flow physics of the target application. This approach, where the ingestion point is identified as a result of considering the interaction of the cavity flows, is essential in the quest to develop competitive engines.

Normalised temperature data presented in this paper demonstrate that the ingestion region for turbine stator wells may be identified with respect to disc entrainment parameters when considered in conjunction with visualisation CFD and understanding of the flow physics present.

It has been shown that the relative tangential velocities, and associated heating, that the highly stressed rotor is subjected to may be reduced by employing cooling path geometry that provides increased coolant delivery momentum. It has also been shown that, by taking advantage of already present entrainment flows, the trajectory of superposed cooling

flows may be specified to deliver coolant to preferred locations by means of angled coolant passage geometry features. Both approaches have been demonstrated to improve cooling effectiveness for a given rate of coolant.

The rotor-stator cavities found in gas turbines are home to complex and composite flows during engine operation. The findings presented here demonstrate that improvements in cooling system design may be found by analysing and exploiting these flows.

ACKNOWLEDGMENTS

The authors would like to thank Rolls-Royce plc for their support and permission to publish this work. Particular thanks are also given to Simon Davies, James Turner, and Tim Scanlon for their assistance in developing the facility. The present investigations were supported by the European Commission within the Framework 6 Programme, Research Project 'Main Annulus Gas Path Interactions (MAGPI)', AST5-CT-2006-030874. This financial support is gratefully acknowledged.

REFERENCES

- [1] Coren, D. D., Atkins, N. R., Turner, J. R., Eastwood, D., Davies, S. Childs, P. R. N., Dixon, J. A., Scanlon, T. S., 2010, "An Advanced Multi-Configuration Stator Well Cooling Test Facility", Proceedings of ASME Turbo Expo 2010, Paper Number GT2010-23450
- [2] Daily, J. W., Nece, R. E., 1960, "Chamber Dimension Effects on Induced Flow and Frictional Resistance of Enclosed Rotating Discs", Journal of basic engineering, Vol.82., pp.217-232.
- [3] Owen, J. M., Rogers, R. H., 1989, "Flow and Heat Transfer in Rotating-Disc Systems: Volume 1 - Rotor-Stator Systems", Research Studies Press, John Wiley and Sons
- [4] Coren, D. D., Childs, P. R. N., Long, C. A., 2009, "Windage Sources in Smooth-walled Rotating Disc Systems", Proc. IMechE Vol.223, pp. 873-888, Part C: J. Mechanical Engineering Science.
- [5] Dorfman, L. A., 1963, "Hydrodynamic resistance and the heat loss of rotating solids", Oliver & Boyd.
- [6] Chew, J.W., 1998, "The Effect of Hub Radius on the Flow Due to a Rotating Disc", Journal of Turbomachinery, Vol. 110, pp.417-418.
- [7] Da Soghe, R., Facchini, B., Innocenti, L., Miccio, M., 2009, "Analysis of Gas Turbine Rotating Cavities by a One-Dimensional Model", Proceedings of ASME Turbo Expo 2009, Paper number GT2009-59185.
- [8] Owen, J. M., Phadke, U. K., 1980, "An Investigation of Ingress for a Simple Shrouded Rotating Disc System with a Radial Outflow of Coolant", ASME Paper 80-GT49, 1980.
- [9] Bunker, R. S., Laskowski, G. M., Bailey, J. C., Palafox, P., Kapetanovic, S., Itzel, G. M., Sullivan, M. A., Farrell T. R., "An Investigation of Turbine Wheelspace Cooling Flow Interactions with a Transonic Hot Gas Path - Part 1: Experimental Measurements", 2009, Proceedings of ASME Turbo Expo 2009, Paper number GT2009-59237.
- [10] Dixon, J. A., Brunton, I. L., Scanlon, T. J., Wojciechowski, G., Stefanis, V., Childs, P. R. N., 2006, "Turbine stator well heat transfer and cooling flow optimisation", ASME paper GT2006-90306.
- [11] Daily, J. W., Ernst, W. D., and Asbedian, V. V., 1964, "Enclosed Rotating Disks with Superposed Throughflow", Dept. of Civil Engineering, MIT, Report No.64.
- [12] Gartner, W., 1997, "A Prediction Method for the Frictional Torque of a Rotating Disc in a Stationary Housing with Superimposed Radial Outflow", ASME paper, 97-GT-204.
- [13] Karabay, H., Pilbrow, R., Wilson, M., Owen, J. M., "Performance of Pre-Swirl Rotating-Disc Systems", ASME paper, 99-GT-197.
- [14] Andreini, A., Da Soghe, R., Facchini, B., "Turbine Stator Well CFD Studies: Effects of Coolant Supply Geometry on Cavity Sealing Performance", Proceedings of ASME Turbo Expo 2009, Paper number GT2009-59186.
- [15] Scanlon, T., Wilkes, J., Bohn, D., Gentilhomme, O., 2004, "A simple method for estimating ingestion of annulus gas into a turbine rotor stator cavity in the presence of external pressure variations", ASME paper GT2004-53097.
- [16] S. Wittig, U. Schelling, S. Kim, and K. Jacobsen, 1987, "Numerical predictions and measurements of discharge coefficients in labyrinth seals", ASME, International Gas Turbine Conference and Exhibition, 32nd, Anaheim, CA, 1987, p. 1987.
- [17] Kim, T. S., Cha, K. S., 2009, "Comparative analysis of the influence of labyrinth seal configuration on leakage behaviour", Journal of Mechanical Science and Technology 23 (2009) 2830~2838.
- [18] Turner, A. B., Davies, S. J., Childs, P. R. N., Harvey, C.G., Millward, J. A., 2000, "Development of a Novel Gas Turbine Driven Centrifugal Compressor", Proc. Instn. Mech. Engrs. Vol. 214, Part A, pp. 423-437.
- [19] Eastwood, D., Coren, D. D., Long, C. A., Atkins, N. R., Turner, J. R., Childs, P. R. N., Scanlon, T. S., Guijarro-Valencia, A., 2011, "An Experimental Investigation of Turbine Stator Well Rim Seal, Re-Ingestion and Inter-Stage Seal Flows Using Gas Concentration Techniques and Displacement Measurements", Proceedings of ASME Turbo Expo 2011, Paper Number GT2011-45874.

GT2010-23450

AN ADVANCED MULTI-CONFIGURATION STATOR WELL COOLING TEST FACILITY

D. D. Coren*, N. R. Atkins†, J. R. Turner,
 D. E. Eastwood, S. Davies
 Thermo-Fluid Mechanics Research Center
 Dept. of Engineering and Design
 University of Sussex, Brighton, BN1 9QT

P. R. N. Childs
 Dept. of Mechanical Engineering
 Imperial College London
 South Kensington
 London, SW7 2AZ, UK

J. Dixon, T. S. Scanlon
 Rolls-Royce plc
 Derby
 UK

ABSTRACT

Optimisation of cooling systems within gas turbine engines is of great interest to engine manufacturers seeking gains in performance, efficiency and component life. The effectiveness of coolant delivery is governed by complex flows within the stator wells and the interaction of main annulus and cooling air in the vicinity of the rim seals. This paper reports the development of a test facility which allows the interaction of cooling air and main gas paths to be measured at conditions representative of those found in modern gas turbine engines. The test facility features a two stage turbine with an overall pressure ratio of approximately 2.6:1. Hot air is supplied to the main annulus using a Rolls-Royce Dart compressor driven by an aero-derivative engine plant. Cooling air can be delivered to the stator wells at multiple locations and at a range of flow rates which cover bulk ingestion through to bulk egress. The facility has been designed with adaptable geometry to enable rapid changes of cooling air path configuration. The coolant delivery system allows swift and accurate changes to the flow settings such that thermal transients may be performed. Particular attention has been focused on obtaining high accuracy data, using a radio telemetry system, as well as thorough through-calibration practices. Temperature measurements can now be made on both rotating and stationary discs with a long term uncertainty in the region of 0.3 K. A gas concentration measurement system has also been developed to obtain direct measurement of re-ingestion and rim seal exchange flows. High resolution displacement sensors have been installed in order to measure hot running geometry. This paper documents the commissioning of a test facility which is unique in terms of rapid configuration changes, non-dimensional engine matching and the instrumentation density and resolution. Example data for each of the measurement systems is presented. This includes the effect of coolant flow rate on the metal temperatures within the upstream cavity of the turbine stator well, the axial displacement of the rotor assembly during a commissioning test, and the effect of coolant flow rate on mixing in the downstream cavity of the stator well.

NOMENCLATURE

Symbols

a	Disc inner radius [m]
b	Disc outer radius [m]
N	Turbine speed [rpm]
p	Static pressure [Pa]
P	Total pressure [Pa]
r	local radius [m]
s	Axial rotor-stator spacing [m]
\dot{m}	Mass flow rate [kg s^{-1}]
v_ϕ	Tangential velocity component [ms^{-1}]
T_m	Metal surface temperature [K]
ω	Rotational speed [rad s^{-1}]
ρ	Density [kg m^{-3}]

Dimensionless

Re_ϕ	Rotational Reynolds number, $\rho\omega b^2\mu^{-1}$
C_w	Non-dimensional mass flow, $\dot{m}(b\mu)^{-1}$
β	Swirl ratio, $v_\phi(r\omega)^{-1}$

Subscripts

0	Free disc value at equal Re_ϕ , stagnation value
s	Superimposed flow value
ent	Entrained flow value
$seal$	Hot reference value
hot	Hot reference value
$cold$	Cold reference value

Abbreviations

CFD	Computational Fluid Dynamics
PRT	Platinum resistance thermometer
TSW	Turbine Stator Well
R1	First stage rotor
R2	Second stage rotor
S1	First stage stator
S2	Second stage stator

*Correspondence to d.d.coren@sussex.ac.uk

†Now at the Whittle Laboratory, University of Cambridge

INTRODUCTION

This paper documents the design, development, and testing of an advanced multi-configuration Turbine Stator Well (TSW) test facility at the Thermo-Fluid Mechanics Research Center (TFRMC) at the University of Sussex.

This particular work is part of the EU FP6 MAGPI (Main Annulus Gas Path Interactions) programme, which has the remit of improving current understanding of the interaction of cooling and main stream flows. The test facility described in this paper marks the evolution of existing apparatus described by Dixon [1]. Although many of the techniques used are the development or refinement of existing methods, a complete revision of internal geometry, coolant flow control, and instrumentation and logging systems has resulted in a highly exploitable experimental resource and represents a significant step forward in data density and quality for a facility of its type.

Within this paper, a brief review of works related to the flows in the vicinity of turbine stator wells is given. Specifications for the main annulus and internal cooling geometries and their control and supply systems are described. Details of instrumentation type, location and calibration are given, along with examples of data obtained for each measurement.

The flow and heat transfer within the cavities adjacent to the hub of a turbine stage has a significant effect on the durability of the neighboring components. Optimisation of the coolant and sealing flows in these cavities has potential benefits for both overall cycle efficiency and component life.

Regardless of these benefits, accurate a priori prediction of the flow and heat transfer within these cavities is of considerable importance in itself. Stator well flows are characterised by regions of entrainment, cores of highly two dimensional rotationally dominated flow, and shear driven mixing regions both within the cavity and at the outer seals. These phenomena represent the limits of Reynolds-Averaged Navier Stokes (RANS) approaches, particularly simple isotropic turbulence modeling. More computationally expensive Large Eddy Simulation (LES) techniques hold much promise, in particular for the prediction of mixing and interactions in the shear dominated regions. However, wall bounded flows are inherently problematic. In addition, with the increased adoption of conjugate methods, the requirement (and the potential benefit) for high quality validation data is clear. However, it is perhaps most useful to know where less computational costly methods deliver sufficiently accurate results for engine design purposes.

A justifiable criticism of more representative experimental test facilities is the often lengthy time scales which are required to build, commission and finally acquire useful data. Furthermore; there is an inherent trade-off between the degree of approximation to real engine conditions and the level of instrumentation density and accuracy which is achieved in practice. Finally, testing is often limited to a single or small number of geometrical variations without significant rebuild or re-instrumentation.

The redesign and re-instrumentation of the Sussex Turbine Stator Well Facility (TSW) attempts to address these issues through a highly configurable working section which can be modified in a matter of hours, combined with a unique level of instrumentation density and resolution.

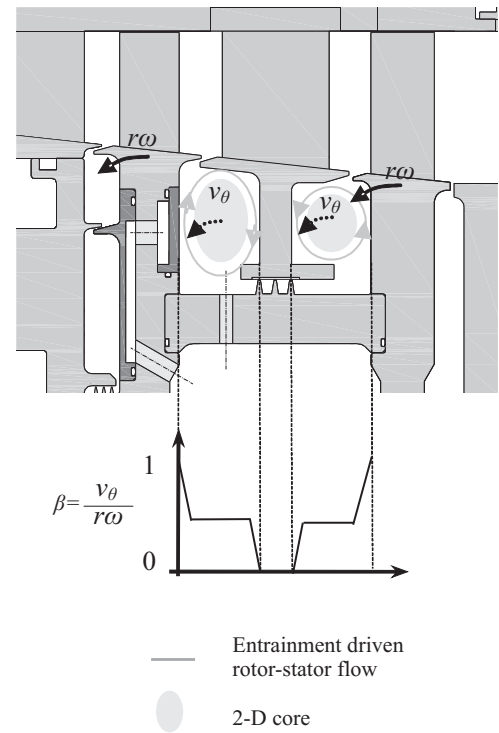


Figure 1. Schematic showing disc entrainment and 2-D core flow.

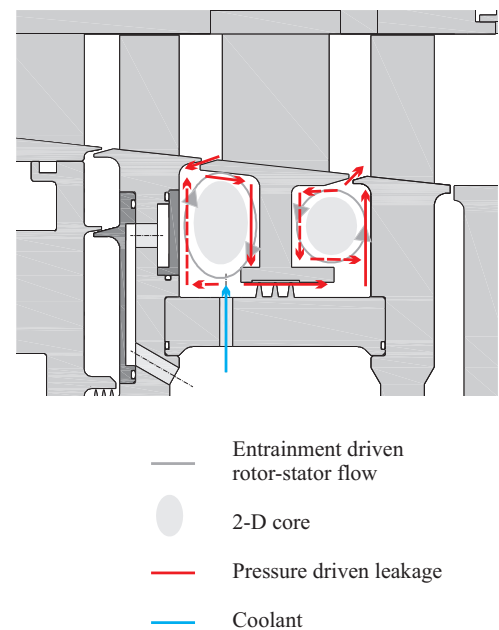


Figure 2. General stator-well flow field.

GOVERNING FLOW PHYSICS

This section gives a brief summary of the dominant flow physics in a typical turbine stator well combined with a review of relevant research. Stator well flows are strongly influenced by disc entrainment, rim and inter-stage seal geometry, coolant supply rate and orientation. An attempt has been made to examine each factor in turn; however, in reality, the actual flow field is an interaction of them all.

Disc Entrainment The viscous boundary layer of rotating disc entrains and pumps flow radially [2]. In a rotor-stator cavity, this leads to a recirculation as shown schematically in Fig-

ure 1. In general, disc entrainment flows can be considered in relation to the flow which would be pumped by a free disc (Equation 1), at the same rotational Reynolds number, Re_ϕ . The flow pumped by a partial disc with an inner hub was derived analytically by Chew [3], who also presented a simple fit to express the reduced flow in relation to that which would be pumped by a free disc (Equation 2).

$$C_{w,0} = 0.219Re_\phi^{0.8} \quad (1)$$

$$C_{w,ent} = C_{w,0} \left[1 - \left(\frac{a}{b} \right)^5 \right] \quad (2)$$

The need to accurately predict disc pumped flow in models was demonstrated by Soghe et al. [4] who developed a design tool for solving steady one dimensional axi-symmetric rotating cavity flows. The solutions predicted by the model were seen to more closely match CFD data after developing correlations for disc friction, which was also investigated by Coren et al. [5].

2-D Core Flow Owen and Rogers [6] showed that rotational equilibrium damps fluid motion other than that tangential to the axis of rotation (Taylor-Proudman Theory). For a sufficiently wide spaced rotor-stator arrangement, the viscously dominated near wall regions are separated by a core which rotates at an intermediate velocity between the rotor and stationary stator wall, this is shown schematically by the hatched regions in Figure 1. This core (or slip) velocity is described by the swirl ratio, β , relative to the rotor. The effect of rotation and cavity aspect ratio was investigated experimentally by Daily and Nece [7] who showed that for geometry where $s/b > 0.1$, β is in the region of 0.4. A highly simplified schematic of the swirl ratio expected in a two cavity TSW is shown in the lower section of Figure 1 (the thickness of the viscously dominated boundary or Eckman layers is exaggerated). The important feature of the 2-D core is that the disc pumped recirculation is confined to the near wall region. As such, small changes in the level of superposed coolant flow may have a significant effect on the flow field within the cavity. The presence of the hub, outer shroud, and coolant injection are all expected to affect the swirl ratio.

Interstage Seal Flow Neglecting the coolant and entrainment flows for a moment, the flow through a stator well cavity is driven by the static pressure drop across the stator vane. Given this pressure drop, the leakage flow is governed by the labyrinth seal demand. This leakage flow can be considered to be superposed onto the disc driven re-circulation, as mentioned above, radial flow is damped by the rotational equilibrium, so this superposed leakage flow feeds (or interrupts) the viscously dominated near wall recirculation. This is shown in simplistic terms by the dotted lines in Figure 2.

Rim Seal Leakage Flow High speed rotor-stator systems require non-contact rim seals to accommodate complex thermo-mechanical movements. The effective area of the rim is dependent on the main-stream and cavity flow as well as the ac-

tual geometry. The blade potential fields produce a circumferential pressure gradient at the rim seals. The presence of non-axisymmetric main annulus flow was shown by Gentilhomme et al. [8] to reduce cavity sealing effectiveness by inducing circumferentially separated regions of local ingestion.

A method for predicting circumferential pressure variation and also ingestion rates was developed by Scanlon et al. [9] calibrated using data from two experimental facilities. It was shown that accurate rim seal flow modeling is dependant upon capturing pressure asymmetries which exist in the vicinity of the rim seals.

Velocity maps for a turbine rotor-stator cavity were produced by Roy et al. [10] using PIV and supported by CFD. Both high and low tangential velocity flows were measured around the cavity rim seal. It was concluded that the high tangential velocity flow was ingested main stream gas, whilst the low tangential velocity fluid was cavity air. Bunker et al. [11] conducted studies on a non-rotating wheelspace sector cascade into the effect of buffer and trench cavities on the ingestion in the rim seal area, showing that vane wake, blade bow wave, and local rim seal geometry all have a dominant affect on the rim seal ingestion. Zhou et al. [12] performed experiments using PIV to obtain velocity maps around the rim seal area for a series of cavity geometries. Ingestion was found to be decreased for narrow aspect cavities. Investigations into the reduction and control of ingestion by Mirzamoghadam et al [13], using CFD found that even at relatively high sealing flow rates, ingress was strongly related to pressure asymmetry in the main annulus.

For the effect of increased cooling air to be fully understood, the presence of re-ingested air from upstream cavities must also be considered. This was investigated by Georgakis et al. [14] conducting CFD studies to investigate the effect of upstream coolant injection into the mainstream flow being ingested into a turbine stator well. The egress flow released upstream was shown to be ingested into the stator cavity, improving the thermal effectiveness at the cavity walls. The facility has also been instrumented with gas concentration measurements in order to study re-ingestion.

Coolant Flow Finally, the presence of superposed coolant flow also strongly influences cavity flow structures, as shown by Gartner [15]. Cavity coolant flows may be supplied axially by lock plate leakage flows or radially through a drive aim as indicated in Figure 2. At low coolant flow rates, depending on the particular geometry, a portion of the coolant may supply the seal demand without interacting with the cavity. The residual coolant will be entrained into the disc pumped recirculation. When the recirculating coolant exceeds the amount required to feed the disc entrainment flow it enlarges the viscously dominated near wall region and interact with the shape and rotation of the 2-D core. With sufficient flow, the coolant floods the cavity, disrupting the rotationally dominated 2-D core.

Summary The flow field within a turbine stator well can be characterised by the comparative magnitude of the supposed flows to the disc pumped recirculation. The metal temperature, and hence life, of the components within the cavity is highly sensitive to this balance. As such, the test facility has been devised to deliver coolant flow levels which cover bulk ingestion, where the coolant is below the disc entrainment and inter-stage seal demand, through to bulk egress where the coolant is more than sufficient to flood and seal the cavity.

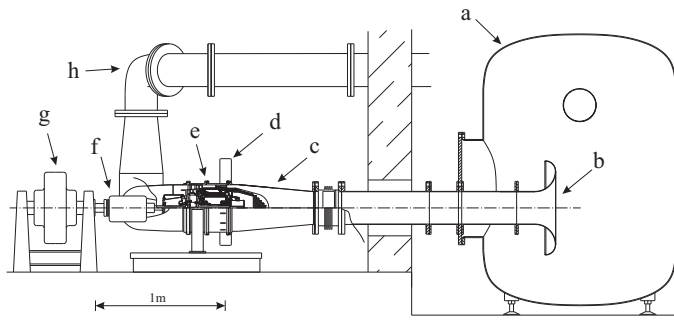


Figure 3. Schematic of the Sussex TSW test facility.

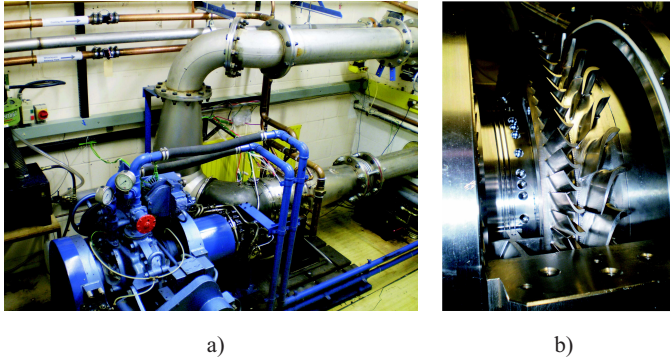


Figure 4. a) Test cell arrangement and b) rapid access rig casing

FACILITY OVERVIEW

The layout of the test facility is shown in Figure 3 and Figure 4a. The test facility features a two stage turbine rated at 400 kW with a generic blade geometry representative of modern gas turbines. The average stator exit Mach numbers are approximately 0.7 which gives a near engine representative potential field at the rim seals. The stages are approximately equally loaded and have similar geometry. The rotor stages have 78 blades and the stators 39 which gives a convenient 2:1 repeat ratio for CFD. The design speed is 10,630 rpm at a mass flow of 4.8 kg s^{-1} , inlet total pressure of 3 bar and total temperature of 165°C .

The rotating assembly is machined from Titanium-318 (4% vanadium and 6% aluminium) with both rotors (R1 and R2 in Figure 5) manufactured as a bladed disk (blik). The stators (S1 and S2 in Figure 5) were machined from stainless steel as a bladed ring (bling). Central to the design of the test rig is the ability to reconfigure the cooling system geometry and this is provided by a split main casing which allows rapid access to the stator well cavities. This is shown in Figure 4b. The stator side of the inter-stage seal is made from an abradable material. This was machined in-situ, with the two halves of the casing assembled, in order to avoid non-axisymmetric clearance. The seal has a cold build clearance of $0.3 \pm 0.1 \text{ mm}$.

The main annulus flow is provided by an adapted aero engine plant (Turner et al. [16]). All pipework is insulated to maximize the temperature difference between the main and cooling flow circuits. The mass flow rate is measured using a venturi.

The main annulus flow enters the turbine via a large settling chamber (Figure 3a) where the flow is accelerated through a bell-mouth inlet (Figure 3b) to avoid swirl and pressure asymmetry. The flow enters the tank through a showerhead distribution pipe at the top of the tank. The performance of the settling tank/bell-mouth system was checked using CFD before manufacture. The residual pressure asymmetry was measured after the inlet con-

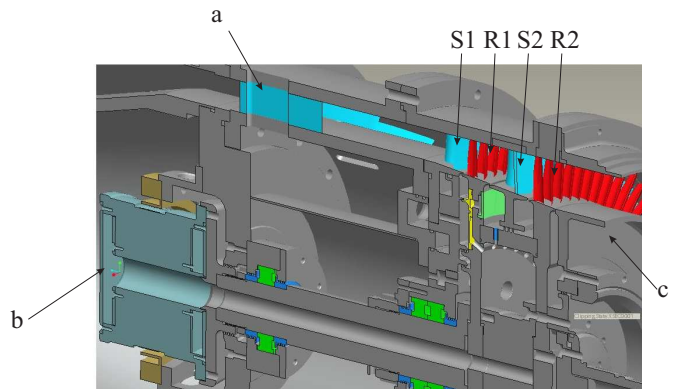


Figure 5. Detail of the TSW facility working section.

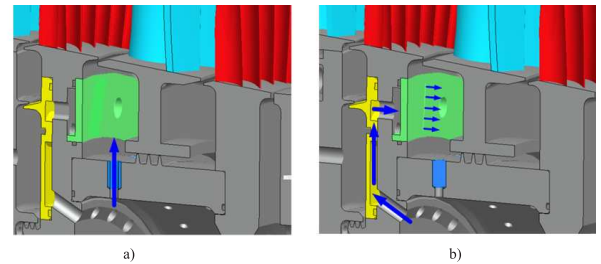


Figure 6. Detail of the Drive Arm (DA) a) and (ii) Lock Plate (LP) b) coolant configurations

traction (Figure 3c) using four circumferentially distributed total pressure rakes, with four radial tappings. Comparing equal radial heights, the total pressures are within $\pm 1.5\%$ of the dynamic head of the flow at 80 ms^{-1} . The cooling air is cooled with a water-air heat exchanger to 18°C and delivered to the turbine via a manifold (Figure 3d), and then through aerodynamic struts upstream of the turbine stage (Figure 5a). The internal cooling system air is supplied by an Atlas Copco ZT250 oil free compressor and Atlas Copco FD700 dryer plant. The internal air system is described in detail in the next section. The turbine exit flow passes over a step diffuser (Figure 5c) and then ducted through a Rolls-Royce Gnome exhaust casing (Figure 3h). After a 3.25:1 reduction gearbox, the turbine drives a Heenan and Froude DPY 590 water brake dynamometer (Figure 3f, g).

Stator Well Coolant Entry Geometry

The multi configuration approach used in the rig design provides potential for a wide range of flow features to be fitted. The MAGPI programme features two test configurations. These are shown in Figure 6. The Drive Arm (DA) geometry features a total of 39 threaded inserts (Figure 6a), which allows for 13, 26 or 39 coolant delivery holes. Similarly, the simulated Lock Plate (LP) leakage path geometry (Figure 6b) use 3 removable plates which seal against the disc with silicon o-rings. A series of slots, 0.5 mm wide by 16 mm radially, are spark eroded into the plates. Again 13, 26 and 39 flow features are possible. The flow area is equal for the DA and LP geometries. For the lock plate configuration, the coolant is fed through the R1 disc into a small annular plenum formed by a cover-plate. This in turn feeds the annular cavity behind the removable plates. Using the split main casing design, both geometries may be reconfigured in a matter of hours.

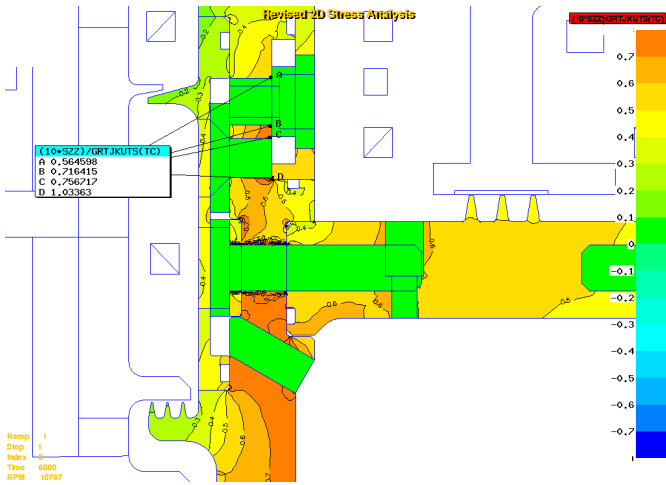


Figure 7. Contours showing 10x the hoop stress normalised by the ultimate tensile strength

Bearing Arrangement The rig has been designed with quick geometry changes in mind. For this type of application, the simplicity of grease packed bearings is highly desirable, allowing simple driveshaft and bearing housing arrangements. Off the shelf, ultra-precision bearings meet the speed and temperature, and axial load requirements. As part of the bearing selection process, shaft diameter, axial load capacity, alignment precision, temperature and speed were defined using predicted operating conditions. Bearing life calculations from a variety of manufacturers were used for life estimates. A pair of sealed angular contact bearings with phenolic cages were used at the downstream end of the shaft. They are positioned in tandem to resist the axial load from the blades and the wheelspace pressures. A single bearing with pre-load springs is used at the upstream end to ensure that the bearings races cannot relax, maintaining radial and axial alignment during start-up and shut-down transients. Several iterations of bearing arrangement have been required. This includes an increase from 15° to 25° angular contact angle. The bearing life is a function of the actual test conditions. It is reduced both by the high internal rig temperatures at low cooling flow rates, and by increased axial load at high cooling flow rates. Typical bearing life is in the region of 50 hours. The bearing temperatures are monitored constantly through the test runs and replaced as necessary. An oil lubricated bearing system, with the necessary feed and scavenge pipes would have significantly increased the re-build times and required complex and careful sealing.

Stress Analysis The structural integrity of the rotating assembly was assessed with a 2-D axis-symmetric thermo-mechanical analysis using the Rolls-Royce plc in-house finite element modeling package. The blade loading is ignored, but other non-axisymmetric features such as feed holes, bolt recesses and lands were modeling using an equivalent thickness technique. As expected, high stress regions were found in the vicinity of the various holes on R1, shown in Figure 7, but the worst case value gives a safety factor of 10 on the ultimate tensile strength.

INTERNAL AIR SYSTEM

The pressure required to deliver the coolant and balance the various cavities at a given coolant flow rate is set by the effective

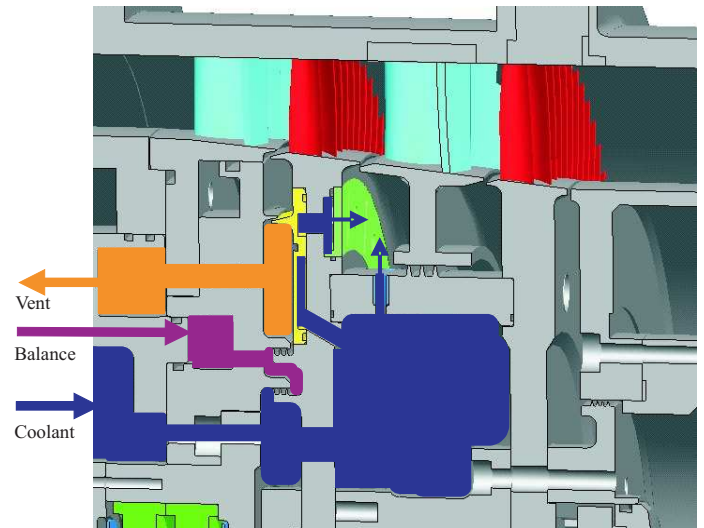


Figure 8. The turbine stator well test facility internal air system.

area of the transfer holes and the pressure loss of the coolant path into the TSW cavity. A flow network model has been used to determine the flow areas required to meet the target range of coolant flow and geometry configurations.

Inter-stage seal clearance The inter-stage seal clearance has been set so that the seal demand is of similar order, but below the rate of disc entrainment. Estimates of seal discharge coefficient from Wittig et al. [17] suggests that the inter-stage seal demand, $C_{w,seal}$, would be in the region of 85% of the disc entrainment, $C_{w,ent}$, at the cold build clearance of 0.3 mm.

Superposed coolant flow rate The maximum value of the superposed cooling flow rate was estimating using the correlation of Owen and Phadke [18], and the minimum flow rate is set below the predicted lab seal demand.

Coolant delivery pressure balance The coolant is delivered to the stator well cavity through a series of aerodynamic struts and then through a series of transfer holes at a low radius in S1. The coolant is then driven through a series of rotating transfer holes in R1 into the cavity beneath the drive arm. The coolant path is shown by the blue shaded region in Figure 8. The coolant flow rate is measured upstream of the rig. A pressure balance cavity (or blown seal) is used to seal the coolant delivery path between S1 and R1. This ensures that the coolant flow delivered to the stator well cavity is neither lost up the wheel space nor contaminated by main annulus gas. The balance cavity is shown by the purple shaded region of Figure 8. Balancing these flows is difficult in practice, however pressure differences of as low as 0.01 bar have been achieved. Under these conditions, the excess flow from the balance cavity is vented via transfer tubes such that rim seal egress into the mainstream is maintained to be within $\pm 0.5 \text{ gs}^{-1}$. The vent path is shown by the orange shaded region in Figure 8. The internal air transfer tubes are insulated from the main annulus temperatures by means of a cylindrical shield of Rohacell HF. Bosch HFM 5 series hot-film air mass meters are used to measure the coolant, wheelspace balance and vent flows. They operate

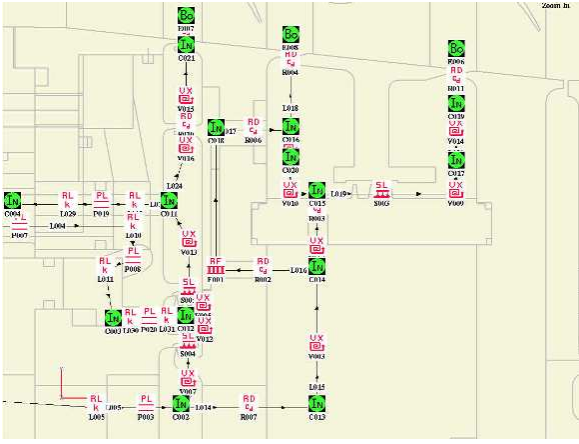


Figure 9. Internal air system network flow model.

over the range 0 to 100 gs^{-1} and were calibrated by a UKAS accredited third party. They give an uncertainty of $\pm 1.3\%$ of the measurement point.

Flow Network Modeling With the cooling flow capacity and layout determined, precise dimensions for the flow paths were defined using the Rolls-Royce in-house network analysis tool.

The tool was used to determine appropriate orifice sizes for the drive arm inserts and simulated lock plates, sufficient for the maximum flow case estimates. The seal clearances required within the upstream wheel space in order to satisfactorily pressure balance the lower cavity were also determined. The model was setup using estimated orifice discharge coefficients, vortex configurations and seal clearances. The complete flow network shown in Figure 9 below.

As a result, the upstream wheel space labyrinth seal clearances have been reduced to 0.15 mm, and the flow area of drive arm holes and lock plate slots was set at 8 mm^2 . This achieves the full range of coolant conditions whilst satisfying bearing requirements.

INSTRUMENTATION

The following sections detail the various instrumentation systems together with example data.

Main Annulus Instrumentation

Total temperature and pressure measurements are made in the main annulus using probes set into the leading edge of S1, S2 and with a radial rake downstream of R2. This avoids the introduction of additional disturbances to the circumferential pressure gradients at the rim seal flows. The incidence sensitivity of the total pressure measurements is minimized with a 2 mm diameter by 1.5 mm deep recess before the actual pressure tap. This geometry was tested using a spare NGV leading edge piece and a free jet calibration rig at representative Reynolds numbers. The yaw sensitivity is extremely low; in the region of 0.5% of a dynamic head for an incidence angle range of $\pm 10^\circ$. The total temperature measurements are made with air thermocouples which protrude from the leading of S1 and S2. Situated at the stagnation point, the recovery errors are negligible.

Pressure Measurement

Pressure measurements are made throughout the test rig to measure flow rates of air supplied to the rig and to balance the upstream wheel space as well as to determine the conditions in the stator well cavities. The locations are shown in Figure . All internal rig measurements use a series of Scanivalve 3217 scanner units (uncertainty of within 0.017% of span for the 0 to 50 psi units, 0.023% of span for the 0 to 100 psi units). The orifice plate measurements pressure use Rosemount 1151 series differential transducers (uncertainty of within 0.031% of span) and Mensor 6100 absolute transducers (uncertainty within 0.015% of span).

Data Acquisition System

The Data Acquisition (DAQ) system is built around a National Instruments PXI system architecture. The system utilises a combination of PXI, SCXI, Ethernet and Serial communication. A total of 280 channels are monitored, including instrumentation points and rig safety measures, and logged using a Labview 8.5 VI at approximately 0.5 Hz. A complete system schematic is shown in Figure 10. The on-line logging system is shown in Figure . The measured data is overlaid onto a graphical representation of the facility, and a tabbed window system displays the 280 channels in convenient sub groups, such as metal temperature, main annulus properties, and cavity pressures (Figure 11). All DAQ hardware is housed in temperature controlled cabinets to ensure the equipment operates close to the rated calibrated temperatures. The cabinets are located in a room adjacent to the test cell, allowing the thermocouples to be plugged in directly to the cold junction terminals without the use of thermocouple extension wires.

TEMPERATURE INSTRUMENTATION

The importance of establishing low temperature measurement uncertainty is demonstrated by considering the propagation of uncertainty in the common expressions used to derive normalised metal temperatures, θ , and metal effectiveness, ϵ :

$$\theta = \frac{T_m - T_{cold}}{T_{hot} - T_{cold}} \quad (3)$$

$$\epsilon = \frac{T_{hot} - T_m}{T_{hot} - T_{cold}} \quad (4)$$

These equations are classically ill-conditioned, which is easily seen by considering the effect of small errors as the measured metal temperature approaches either the cold or hot reference temperature. The amplification of uncertainty approaches infinity in this extreme case. In practice, the radial temperature difference down the disc has been maximised by insulating the main annulus delivery, and significant internal insulation to minimise the heat pickup of the coolant prior to the TSW entry point. However, considerable attention has been made to the reduction of temperature measurement uncertainty.

A total of 81 K-type thermocouples at 27 radial locations have been installed within the rotating assembly, while 73 thermocouple measurement locations were used within the stationary

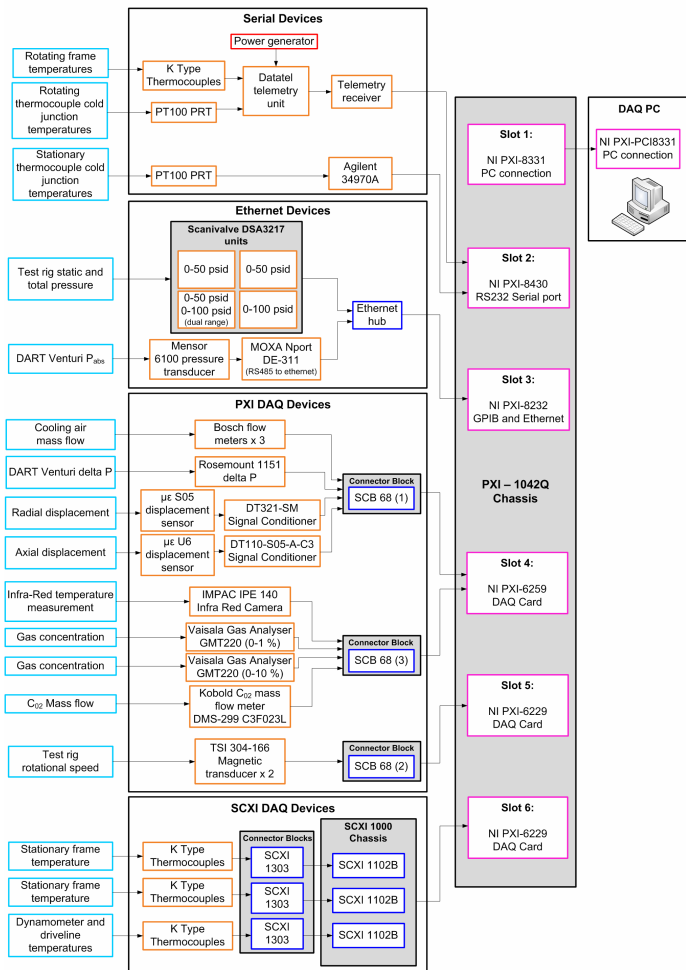


Figure 10. Schematic of the complete data acquisition system.

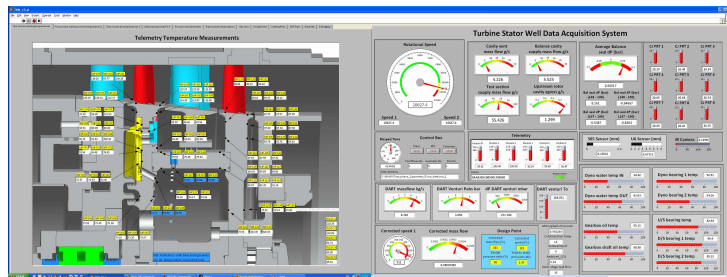


Figure 11. TSW facility control and logging panel.

components of the test rig. Six of which are stator mounted air thermocouples.

The measurement locations are shown in Figure 12, and the instrumented rotating assembly is shown in Figure 13.

Three thermocouples are used for each radial measurement location on the rotating components to give triple redundancy. In practice only 6 thermocouples out of the 81 have failed in approximately 18 months; importantly, not more than 2 at any radial location. The thermocouple beads are peened into the material surface and the thermocouple wires were secured to the rotating components by means of spot welded metallic straps. The wires are led circumferentially, along an isotherm, for at least 10 diameters. Detail of a typical installation can be seen in Figure 12. The beads themselves are ~ 0.1 mm. The peening helps to reduce embedding errors, but they have not yet been quantified.

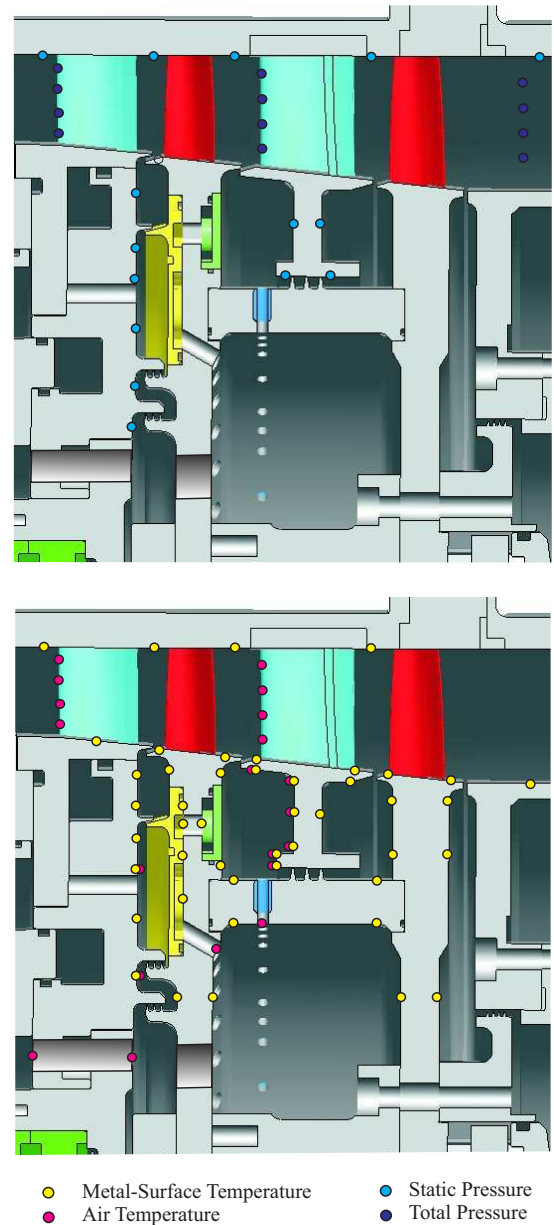


Figure 12. Schematic showing the instrumentation locations.

A 92 channel Datatel radio telemetry system (shown in Figure 5, (b)). The system comprises 6 individual units connected in a parallel bus. Each unit has an in house cold junction reference module with a PRT mounted in close thermal contact to thermocouple junctions. The resistance of the PRT is measured on a dedicated 4-wire resistance channel. This channel is normally used to enable a remote cold junction; particularly useful with high cost thermocouple extension wires. However, in this situation it reduces the rotating frame cold junction compensation errors to within 0.1 K. In addition to the metal surface temperatures, the air temperature is measured at the location of the coolant entry into the DA inserts or into the transfer holes in rear of R1 for the LP geometry.

The stationary thermocouples are installed without extension cables or plugs. Again in-house cold junction referencing has been used to reduce the uncertainty to 0.1 K. National Instruments SCXI 1303 thermocouple input cards have been modified by the addition of 5 mm thick copper heat spreader plates, monitored with 3 embedded PRTs to check for spatial non-uniformity. The

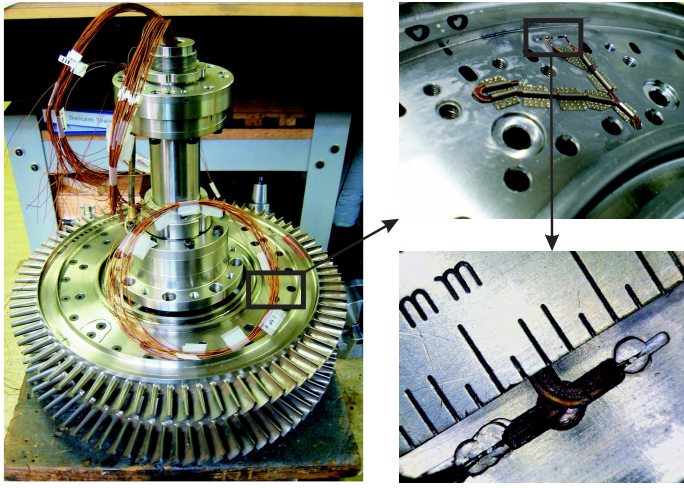


Figure 13. The rotating assembly and detail of the thermocouple installation.

units are installed within Rohacell HF insulated boxes, within a temperature stabilised instrumentation room.

A through-calibration technique has been used for the calibration of all thermocouples and cold junction referencing PRTs. The entire data acquisition chain including the thermocouples, cold junctions, amplifiers and acquisition cards are calibrated by comparison against a national laboratory standard reference system. The calibrations use an Isotech 915 parallel tube oil bath, an Isotech SPRT and a TTI-2 resistance measurement system. A custom copper equalisation block is submerged within the oil bath and enables all 81 thermocouples to be calibrated in a single batch (the calibrations take approximately 24 hours per run). This reference system gives a comparison uncertainty of ~ 20 mK which is an order of magnitude lower than the target uncertainty of the thermocouples. The calibrations show that both the thermocouples and PRT cold junctions give typically single point uncertainties in the region of 0.1 K. Once installed into the discs, recalibration to these levels is impractical. As such, spare drift check thermocouples are installed in both the telemetry, and stationary frame measurement systems. These are recalibrated between test phases to track the any system drift. Typical recalibrations after a 6 month period indicate a system drift of 0.1 K. Despite it being common practice, in reality these uncertainties cannot be considered independent *or* normal in distribution so a worst case 6 month combined uncertainty for all of the temperature measurements of 0.3 K is considered to be realistic. This propagates to a practical uncertainty in normalised temperature and effectiveness in the region of 1% for the coolant flow rate conditions discussed in the proceeding sections.

Data has been taken with the rig in the 26 DA configuration with a coolant flow rate of 55 gs^{-1} (or approximately $1.1 C_{w,ent}$) before and after a complete strip and re-assembly (approximately 3 months apart). A histogram of the difference in effectiveness, ϵ are shown in Figure 17 for the 38 distinct radial locations in and around the stator well cavity. The standard deviation gives an estimate of the 95% confidence interval $\pm 1.5\%$.

However, the resolution of local temperature differences (or gradients) on a specific test is far better. Figure 15 shows raw data from three thermocouples at the same radial location, just below the rim seal on the rear face of R1. All three locations read to within a spread of 0.1 K, which is similar in magnitude to the

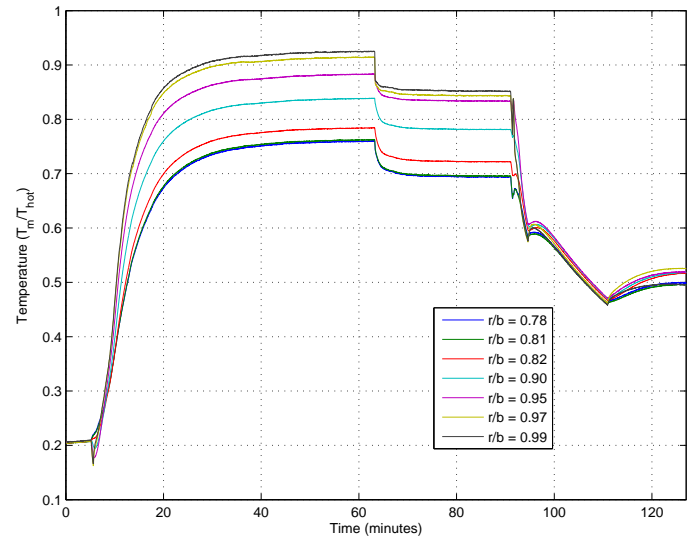


Figure 14. Typical temperature time history (S2).

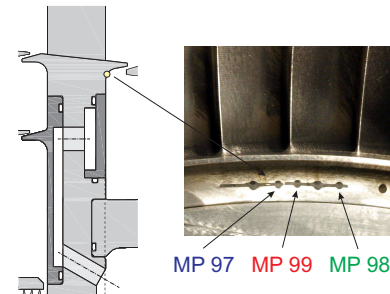
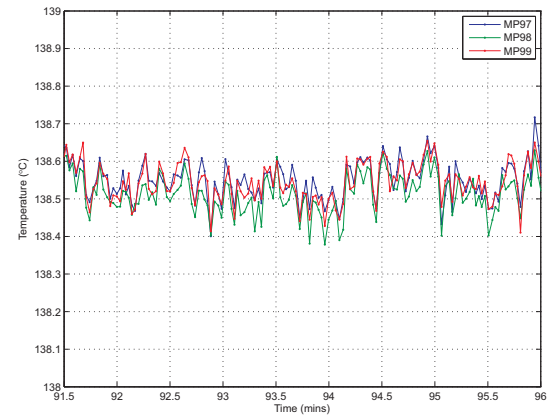


Figure 15. Temperature measurement uniformity.

noise. In fact MP97 and MP99, which are physically next to each other, show single point differences of less than 0.025 K.

Example Data

Temperature time histories for measurement points on S2 for a typical test run are shown in Figure ???. Two distinct cooling flow rate conditions are shown, 1.45 and $1.73 C_{w,ent}$. The settling criterion is for a temperature change of less than 0.1 K, over a 5 minute period, based on 1 minute long running average.

Temperature time histories during a thermal transient, typical of those performed during normal testing, where the cooling rate is decreased from 1.47 to $0.6 C_{w,ent}$, is shown for locations on the upstream face of stator 2 in Figure 16. This transient data clearly shows the different time constants at each location, and

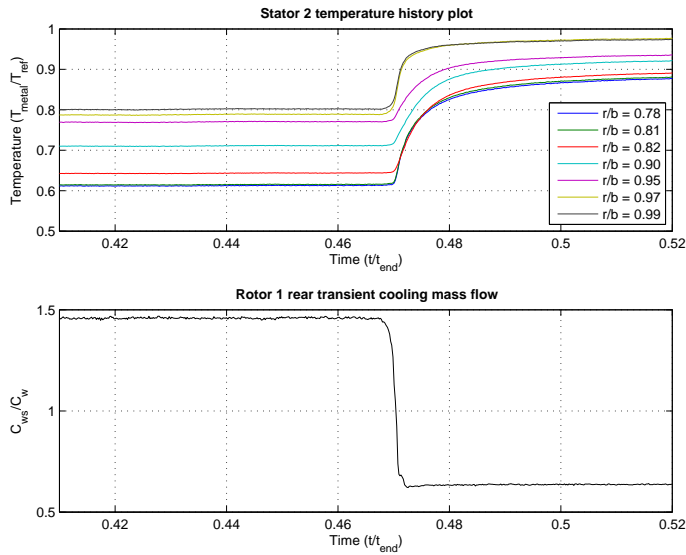


Figure 16. Detail of a temperature transient (S2).

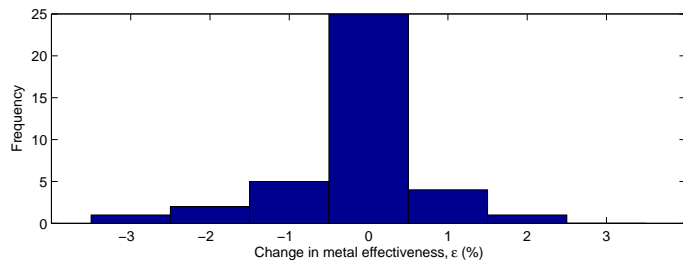


Figure 17. Histogram of the difference in effectiveness for the back to back tests.

the different radial temperature gradients at the two cooling flow rates. At the higher coolant flow rate of $1.47 C_{w,ent}$, the temperature gradient at the outer two locations indicates that the coolant is flooding the cavity. In comparison, at the lower coolant flow rate of $0.6 C_{w,ent}$, there is little temperature gradient at the outer two locations, in fact the inner location is hotter than the main stream facing location, possibly indicating windage heating of the already hot main annulus ingested gas.

The temperature profiles on the rear of R1 and front of S2 for a complete range of coolant flow, for a 39 DA hole configuration are shown in Figures 18 and 19 respectively. As the coolant flow is increased, there is a significant change in gradient at the upper two measurement locations. The temperature profile on the upstream face of S2 shows little change between the 1.1 and $1.46 C_{w,ent}$ flow rates indicating that the cavity is likely to be flooded with coolant.

HOT GEOMETRY

Displacement sensors have been installed to give accurate measurement of hot running geometry. These provide a means of determining the inter-stage and upstream wheel space labyrinth seal clearances at operating conditions. Measurement of the hot-running inter-stage seal clearance is vital to the interpretation of the data. Figure 20 shows a schematic of the sensor locations.

The sensor downstream of R2 measures axial displacement, and the sensor on the stator well foot measures the radial displacement at the drive arm. Micro-Epsilon U6 and SO5 eddy cur-

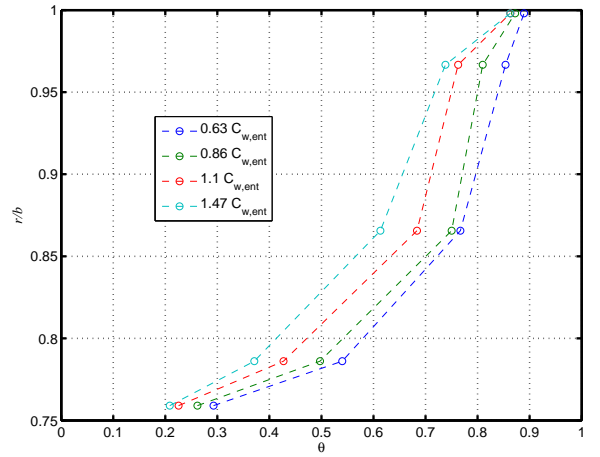


Figure 18. Normalised temperature profile on the rear face of R1 for a range of coolant flow rates.

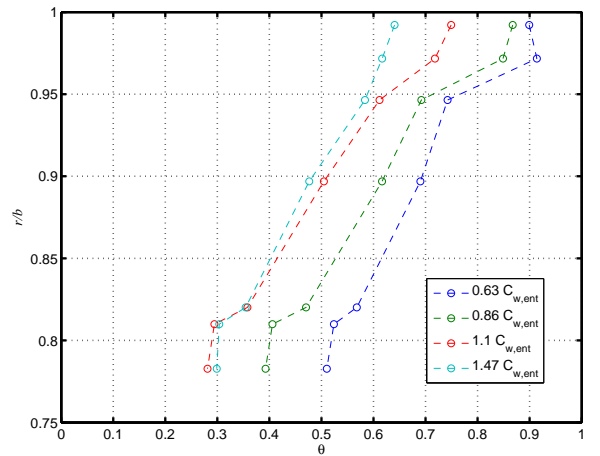


Figure 19. Normalised temperature profile on the front face of S1 for a range of coolant flow rates.

rent sensors with supporting signal conditioning electronics are used which give a resolution of $\pm 6 \mu m$. The sensors are calibrated against mock targets, and checked at representative test temperatures in a heated box. The calibration set-up for the radial sensor is shown in Figure 21.

A plot of the axial movement between R2 and the exit stage during a commissioning run can be seen in Figure 22. At point A, a small gap increase can be seen, this is due to a small thrust load exerted on the rotating part of the telemetry unit, generated due to an increase in telemetry cooling air which is not balanced until the rig is rotating. At point B a peak gap can be seen as the blade loading causes a movement due to the initial flow of main annulus air. At point C, the gap can be seen to reduce as the rig speed and pressure load on each stage increase. At point D, the rig is at design speed and inlet pressure, the gap is at its minimum running value due to the maximum load. By point E the gap has increased slightly as the hub region of the rig warms. By point F the rig has reached settled conditions and the gap is constant. Between points F and G the cooling flow is increased, causing an increase in the gap due to changes in the relative temperature of the rotor and stator. At point H, the shut down procedure is started. The gap can be seen to open up as the pressure load on the rotating assembly is reduced. As the rig comes to a complete stop at point I, the gap reduces as a step change. At point J a small spike in the

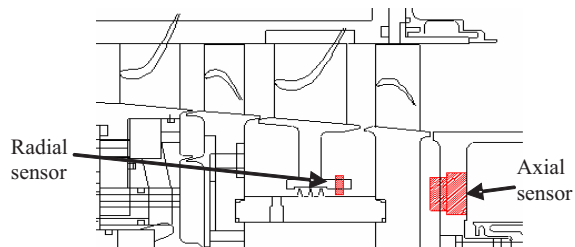


Figure 20. Displacement sensor locations.



Figure 21. Displacement sensor calibration.

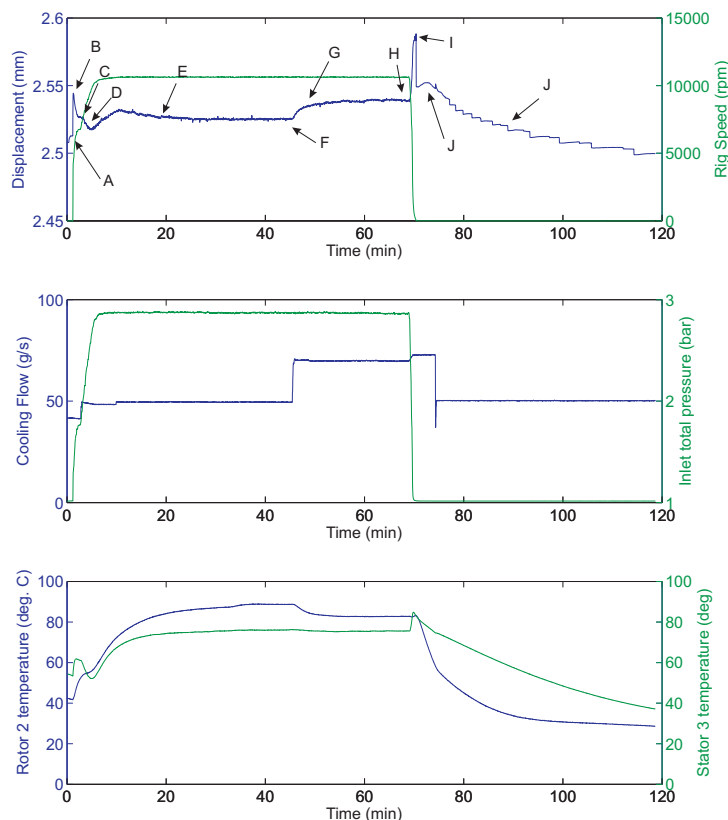


Figure 22. Axial rotor movement during a commissioning test.

gap can be seen as the cooling flow is shut off, causing a drop in the axial load on the rotor. Finally at point K, contraction of the rig can be seen in steps as the casing contracts faster than the rotating assembly. The step characteristic is the result of contraction forces being opposed by shaft bearing stiction, whilst stationary.

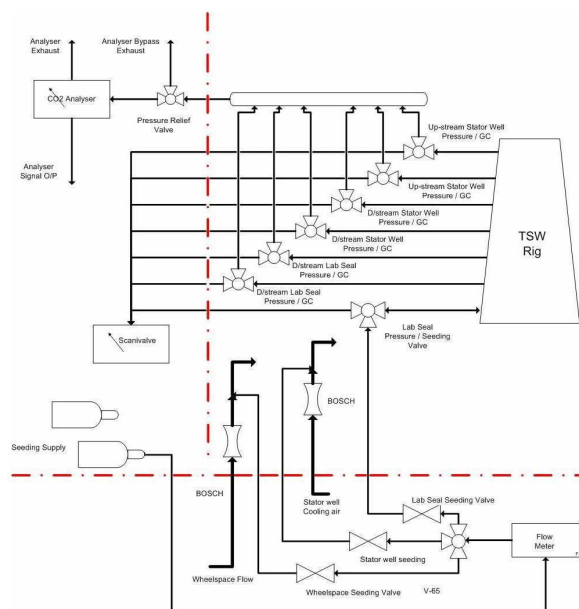


Figure 23. Gas concentration schematic.

GAS CONCENTRATION INSTRUMENTATION

The complex flow interactions that exist in the cooling flows of a gas turbine engine are difficult to quantify. In order to address this problem a carbon dioxide delivery and detection system has been installed. The work has been informed by Phadke and Owen [19] who used flow visualisation, pressure and concentration measurements to investigate the sealing of a shrouded rotor-stator system. The tests were conducted over seven geometries including axial-clearance, radial-clearance and mitred seals. The new rig system has been designed so that it can be configured for three distinct experiments:

1. The re-ingestion of cool upstream wheelspace flows into the stator well cavities;
2. Measurements of main gas path interaction in the vicinity of turbine rim seals;
3. Measurements of inter-stage labyrinth seal flows.

A schematic of the system set-up is shown in Figure 23. CO₂ may be seeded into both the main cooling flow and also the upstream wheelspace cavity balance flows. It may also allow be injected upstream of the inter-stage seal through the stator well foot.

Long pipe lines and an adjustable back pressure valve are used to provide near iso-energetic conditions at the measurement points. An in-line heater is used to maintain the CO₂ delivery temperature. The complete system is checked by flooding the rig with air seeded at a known concentration, at typical operating pressures. The location to location repeatability of the concentration measured at each point is of the order of 2%.

Example data

To investigate the rim seal exchange in the upstream stator well cavity, the stator well cooling air is seeded with CO₂ at a known rate or concentration. The concentration measured at the various tapings within the stator well indicates the dilution or mixing of the coolant with the main annulus gas. Example results obtained for two cooling flow rates are shown below in

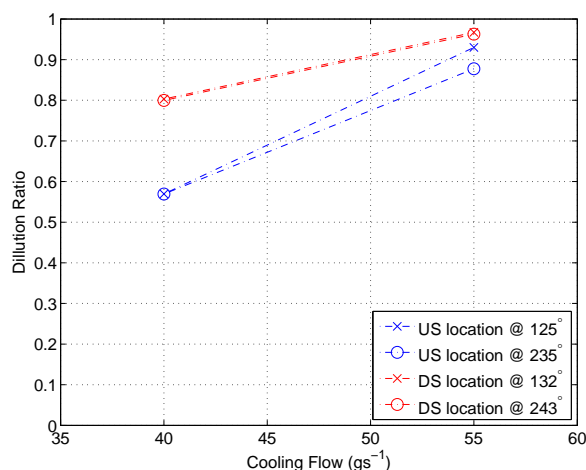


Figure 24. Dilution measurements in the upstream and down stream cavities.

Figure ?? The dilution ratio presented below is the ratio of the delivered to measured concentration. A value of 1 represents pure coolant, and 0 indicates pure main annulus gas. The coolant flow rates of 40 gs^{-1} and 55 gs^{-1} are estimated to be in the region of 90% and 110% of the disc entrainment flow respectively. Comparing the two cases, at the lower coolant flow rate, the dilution ratio shows that comparatively little coolant is present at the Upstream (US) cavity measurement points. At the lower flow rate, the Down Stream (DS) cavity measurement points indicate the presence of more coolant, which suggests that the coolant flows through the inter-seal seal to the DS cavity with little mixing. At the higher flow rate, the coolant is expected to exceed the disc entrainment. The increased dilution ratio confirms this, showing that the coolant penetrates into the cavity with greater mixing with the main stream ingestion before it gets to the DS cavity. The variation in concentration measured in the US cavity at the higher flow rate indicates a highly complex 3-D flow structure. This non-axisymmetric variation is fully mixed out by the time the mixture of ingress and coolant reaches the DS cavity.

CONCLUSIONS

A test turbine test facility has been developed which allows the measurement of high resolution temperature data, hot running seal clearances and re-ingestion by means of a gas concentration system. The design of the test rig architecture and flow systems is such that a wide range of stator well flow regimes, centered around cavity sealing conditions, may be composed at will. The data available from the test rig allows the effects of a range of stator well cooling flows to be accurately quantified. The presence of cavity ingestion resulting from the rim seal flow exchanges may be quantified, as well as re-ingested flow using gas tracing techniques. This data will be useful for the validation of the next generation of conjugate/coupled analysis tools.

ACKNOWLEDGMENTS

The authors would like to thank Rolls-Royce plc and the EU FP6 programme for their support and permission to publish this work. Thanks are also given to Glenn Downs and Tony Martin for their assistance in the construction of the facility.

REFERENCES

- [1] Dixon, J. A., Brunton, I. L., Scanlon, T. J., Wojciechowski, G., Stefanis, V., Childs, P. R. N., 2006, "Turbine stator well heat transfer and cooling flow optimisation," ASME paper GT2006-90306.
- [2] Dorfman, L. A., 1963, "Hydrodynamic resistance and the heat loss of rotating solids", Oliver & Boyd.
- [3] Chew, J. W., 1998, "The Effect of Hub Radius on the Flow Due to a Rotating Disc" Journal of Turbomachinery, Vol. 110, pp. 417-418.
- [4] Da Soghe, R., Facchini, B., Innocenti, L., Miccio, M., 2009, "Analysis of Gas Turbine Rotating Cavities by a One-Dimensional Model". Proceedings of ASME Turbo Expo 2009, Paper number GT2009-59185.
- [5] Coren, D. D., Childs, P. R. N., Long, C. A., 2009, "Windage Sources in Smooth-walled Rotating Disc Systems" Proc. IMechE Vol.223, pp. 873-888, Part C: J. Mechanical Engineering Science.
- [6] Owen, J. M., Rogers, R. H., 1989, "Flow and Heat Transfer in Rotating-Disc Systems: Volume 1 - Rotor-Stator Systems", Research Studies Press, John Wiley and Sons.
- [7] Daily, J. W., Nece, R. E., 1960, "Chamber Dimension Effects on Induced Flow and Frictional Resistance of Enclosed Rotating Discs, Journal of basic engineering, Vol.82., pp.217-232.
- [8] Gentilhomme, O., Hills, N., and Turner, A. B., 2003. "Measurement and analysis of ingestion through a turbine rim seal". ASME Journal of Turbomachinery, Vol. 125, pp. pp.505-512.
- [9] Scanlon, T., Wilkes, J., Bohn, D., Gentilhomme, O., 2004, "A simple method for estimating ingestion of annulus gas into a turbine rotor stator cavity in the presence of external pressure variations," ASME paper GT2004-53097.
- [10] Roy, R. P., Zhou, D. W., Ganesan, S., Wang, C. Z., Pao-lillo, R.E., 2007, "The Flow Field and Main Gas Ingestion in a Rotor-Stator Cavity", 2007, Proceedings of GT2007, Paper number GT2007-27671.
- [11] Bunker, R. S., Laskowski, G. M., Bailey, J. C., Palafox, P., Kapetanovic, S., Itzel, G. M., Sullivan, M. A., Farrell T. R., "An Investigation of Turbine Wheel-space Cooling Flow Interactions with a Transonic Hot Gas Path - Part 1: Experimental Measurements", 2009, Proceedings of ASME Turbo Expo 2009, Paper number GT2009-59237.
- [12] Zhou, D. W., Roy, R. P., Wang, C. Z., Glahn, J. A., 2009, "Main Gas Ingestion in a Turbine Stage for Three Rim Cavity Configurations". Proceedings of ASME Turbo Expo 2009, Paper number GT2009-59851.
- [13] Mirzamoghadam, A. V., Heitland, G., Morris, M. C., Smoke, J., Malak, M., Howe, J., 2008, "3D CFD Ingestion Evaluation of a High Pressure Turbine Rim Seal Disc Cavity". Proceedings of ASME Turbo Expo 2008, Paper number GT2008-50531.
- [14] Georgakis, C., Whitney, C., Woolatt, G., Stefanis, V., Childs, P., 2007, "Turbine stator well studies: Effect of upstream egress ingestion," ASME paper GT2007-27406.
- [15] Gartner, W., 1997, A Prediction Method for the Frictional Torque of a Rotating Disc in a Stationary Housing with Superimposed Radial Outflow, ASME paper, 97-GT-204.
- [16] Turner, A. B., Davies, S. J., Childs, P. R. N., Harvey, C. G., Millward, J. A., 2000, "Development of a Novel Gas Turbine Driven Centrifugal Compressor", Proc. Instn. Mech. Engrs. Vol. 214, Part A, pp. 423-437.

[17] S. Wittig, U. Schelling, S. Kim, and K. Jacobsen, 1987, "Numerical predictions and measurements of discharge coefficients in labyrinth seals," ASME, International Gas Turbine Conference and Exhibition, 32nd, Anaheim, CA, 1987, p. 1987.

[18] Owen, J.M., Phadke, U.K., 1980, "An Investigation of Ingress for a Simple Shrouded Rotating Disc System with a Radial Outflow of Coolant", ASME Paper 82-GT-145.

[19] Phadke, U. P., Owen J. M., 1988 "Aerodynamic Aspects of the Sealing of Gas Turbine Rotor-Stator Systems Part 1: The Behavior of Simple Shrouded Rotating-Disc Systems in a Quiescent Environment". Int. J. Heat Fluid Flow, 9, pp. 98-105.